Physics | Lancaster University

Medium- and long-wavelength InAs/InAsSb strained-layer superlattices for applications in infrared nBn detectors

---

Author:
Veronica LETKA

Supervisor:
Dr Andrew R. J. MARSHALL

Thesis submitted for consideration for the award
of the degree of Doctor of Philosophy

May 2019

"We've got no money, so we've got to think."

- Ernest Rutherford

Declaration of Authorship

This thesis has not been submitted in support of an application for another degree at this or any other university. It is the result of my own work and includes nothing that is the outcome of work done in collaboration except where specifically indicated. Many of the ideas in this thesis were the product of discussion with my supervisor Dr Andrew Marshall.

Excerpts of this thesis have been published in the following conference manuscripts and academic publications:

- V. Letka, A. Bainbridge, A.P. Craig, F. Al-Saymari, A.R.J. Marshall. "Resonant cavity enhanced photodetector using a type-II superlattice to extend MWIR sensitivity" (paper in preparation)

- E. Delli, V. Letka, P.D. Hodgson, E. Repiso, J.P. Hayton, A.P. Craig, Q. Lu, R. Beanland, A. Krier, A.R.J. Marshall, P.J. Carrington. "Mid-Infrared InAs/InAsSb Superlattice nBn Photodetector Monolithically Integrated onto Silicon" *ACS Photonics*, 6, 2 (2019), pp. 538-544.

- V. Letka, J. Keen, A. Craig, A. R. J. Marshall. "Modelling and measurement of bandgap behaviour in MWIR InAs/$InAs_{0.815}Sb_{0.185}$ strained-layer superlattices" *Proc. SPIE 10433, Electro-Optical and Infrared Systems: Technology and Applications XIV*, 1043319 (2017)

- V. Letka, A. Craig, A.R.J. Marshall."Modelling and measurement of bandgap behaviour in MWIR InAs/$InAs_{0.815}Sb_{0.185}$ strained-layer superlattices" *UK Semiconductors*, Sheffield, UK (2017) (poster presentation)

- V. Letka, A. Craig, A.R.J. Marshall. "Modelling and measurement of bandgap behaviour in MWIR InAs/$InAs_{0.815}Sb_{0.185}$ strained-layer superlattices" *Workshop on Compound Semiconductor Devices and Integrated Circuits*, Las Palmas de Gran Canaria, Spain (2017) (oral presentation)

- V. Letka, A. Craig, A. Krier, A.R.J. Marshall. "Dual-colour InAs/$InAs_{1-x}Sb_x$ superlattice photodetectors" *UK Semiconductors*, Sheffield, UK (2016) (poster presentation)

- V. Letka, J. Keen, A. Craig, A. R. J. Marshall. "IR InAs/$InAs_{1-x}Sb_x$ superlattice photodetectors" *UK Semiconductors*, Sheffield, UK (2015) (oral presentation)

Veronica Letka, MPhys (Hons)

Lancaster University, UK

Acknowledgements

First of all, I would like to thank my supervisor Dr Andrew Marshall for his relentless support, knowledge, patience and energy that have made this work possible in the first place.

This project built extensively on the achievements and continued support of Dr Adam Craig, whom I would like to thank for his time spent providing training, assistance and informative discussion.

I would like to extend my thanks to the company Leonardo for providing funding for this CASE project, and in particular to Chris Maxey for his support as well as hospitality during my visit at the company.

Not all the work could have been done by myself: I would like to thank Dr James Keen from Lancaster University for providing photoluminescence spectra and Dr Richard Beanland from Warwick University for obtaining transmission electron microscopic images of my samples.

I would also like to thank Dr Michael Thompson for laying the groundwork for the MBE growth without which this project would not have been possible, for the training and support early in my PhD and for the useful discussion since.

I would also like to express my gratitude to Dr Kunal Lulla and Christopher Somerton for providing state-of-the-art the cleanroom facilities, and to the staff of the mechanical and the electronics workshops without whom this work would not be possible; and to Shonah Ion, Stephen Holden and Robin Lewsey for their excellent technical support.

I would also like to express my deepest gratitude to Dr Ofogh Tizno for just being there when things got tricky, and to Fiona Rambridge for being Fiona. I would also like to thank my office mates for their friendship and conversation: James Keen, Zhiming Jin, Laura Hanks, Denise Montesdeoca Cardenes, Eva Repiso Menendez, Marta San Juan Mucientes, Leonardo Forcieri, Angelo Lamantia and Xiao Collins.

And last but not least, I would like to thank my family without whose unquestioned support and unwavering confidence I would not be where I am today.

Abstract

Veronica LETKA

Medium- and long-wavelength InAs/InAsSb strained-layer
superlattices for applications in infrared nBn detectors

InAs/InAs$_{1-x}$Sb$_x$ type-II strained-layer superlattices (SLS) have potential applications in infrared detection, owing to their narrow tunable bandgap and decreased Auger recombination currents. Furthermore, the so-called nBn device architecture promises to suppress the majority carrier dark current and the surface current thanks to its inbuilt potential barrier, as well as the Shockley-Read-Hall (SRH) process due to the structure's lack of a depletion region. This thesis reports on the growth, modelling, and characterisation of InAs/InAs$_{1-x}$Sb$_x$ nBn devices in an effort to deliver a viable alternative to the HgCdTe-based technology. Sample growth proceeded with the use of molecular beam epitaxy (MBE) on both native GaSb substrates and lattice-mismatched GaAs equipped with GaSb and AlSb buffer layers. Excellent crystallinity of devices grown on GaSb is confirmed with the use of X-ray diffraction (XRD) and transmission electron miscroscopy (TEM) scans; the GaAs-grown samples, meanwhile, display broadened XRD peaks and dislocations largely originating at the buffer interfaces. Group V intensity data reveals a Sb segregation length of $\sim$ 0.95 nm. Temperature-dependent transmission spectra of undoped SLS samples with varying x_{Sb} are obtained using Fourier Transform Infrared (FTIR) spectroscopy, and used to derive their absorption coefficients α, which are shown to be comparable to other technologies operating in the same wavelength range. Direct fundamental optical bandgaps E_g are extracted, and incorporated into the Kronig-Penney model of the superlattice band structure. Further, several nBn device parameters are characterised. Dark current-voltage characteristics and activation energies show diffusion-limited behaviour at higher temperatures, especially in the medium-wavelength (MWIR) detectors, but voltage-dependent current mechanisms dominate at lower T and in some long-wavelength (LWIR) devices. Responsivity R of two MWIR and two LWIR devices is obtained at target operational temperatures of 160 and 77 K respectively; the peak value in the MWIR range is found to be 1.70 ± 0.11 A/W, corresponding to an external quantum efficiency of $\sim 33\%$. When the dark current density data is combined with responsivity results, the resultant specific detectivity D^* is found to be 5.3×10^{10} cmHz$^{1/2}$W^{-1} for the MWIR samples at the operational bias and temperature of -0.1 V and 160 K, while one of the LWIR samples shows 1.1×10^{10} cmHz$^{1/2}$W^{-1} at -0.2 V and 77 K.

Contents

Declaration of Authorship **ii**

Acknowledgements **iv**

Abstract **vi**

1 Introduction **1**

2 Background Theory **5**

2.1 Modelling 6

2.1.1 Effects of strain 6

Effects of strain on epilayer lattice constant 6

Critical thickness 7

Lattice constant thermal expansion 8

Vegard's law 9

2.1.2 Band structure modelling 10

Basics of the semiconductor band structure 10

Kronig-Penney model 11

Heterojunction band alignments 14

Superlattice band alignment types 17

Bandgap temperature dependence 18

$\mathrm{InAs}_{1-x}\mathrm{Sb}_x$ band bowing 19

2.1.3 Absorption coefficient, transmission and reflection 20

Absorption processes near the band edge 21

2.2 Device physics 23

2.2.1 nBn structure 23
2.2.2 Dark current mechanisms 24
Shockley-Read-Hall generation 24
Auger mechanisms 25
2.2.3 Responsivity, internal and external quantum efficiency 27
2.2.4 Relevant noise types and specific detectivity 28

3 Literature Review **31**
3.1 Thermal detectors 33
3.2 Group IV-VI: lead salts 33
3.3 Group II-VI: HgCdTe (CMT) 34
General properties 34
J_d and Rule 07 35
Manufacturing and devices 36
Challenges 37
3.4 Group III-V 38
3.4.1 Bulk InSb, $InAs_{1-x}Sb_x$ detectors 38
InSb 38
$InAs_{1-x}Sb_x$ 39
3.4.2 Strained-layer superlattices 41
InAs/GaSb strained-layer superlattices 42
$InAs/InAs_{1-x}Sb_x$ strained-layer superlattices 47
$InAs/InAs_{1-x}Sb_x$ photodiodes 50
3.5 nBn detectors 51
3.5.1 $InAs/InAs_{1-x}Sb_x$ nBn devices 52
3.6 Summary 54

4 Experimental Methods **57**
4.1 Molecular Beam Epitaxy 57
4.2 Structure characterisation 62

4.2.1 High-resolution X-ray diffraction 62
4.2.2 Transmission electron microscopy 64
4.3 Fourier Transform Infrared spectroscopy - transmission 64
4.4 Photoluminescence measurements 67
4.5 Device fabrication 68
4.5.1 Photolithography 68
Photoresist deposition and soft-bake 68
Ultraviolet exposure 69
4.5.2 Contact deposition and lift-off 71
4.5.3 Wet etching 72
4.5.4 Wire bonding 74
4.6 Device characterisation 75
4.6.1 Fourier Transform Infrared spectroscopy - spectral response . . . 75
4.6.2 Quantum efficiency and responsivity 76
4.6.3 I-V characteristics 77

5 I. Results and discussion: Design, growth and structural properties 79
5.1 Superlattice design 79
5.2 nBn device considerations 85
5.3 Molecular beam epitaxy growth recipe 87
5.4 Characterisation: X-ray Diffraction and Transmission Electron Microscopy 88
5.4.1 Sb incorporation 88
5.4.2 Buffer layer relaxation 89
5.4.3 InAs/InAs$_{1-x}$Sb$_x$ nBn growth on native GaSb 91
X-ray diffraction 91
Transmission Electron Spectroscopy 98
5.4.4 InAs/InAs$_{1-x}$Sb$_x$ growth on lattice-mismatched GaAs 103
5.4.5 Growth on a GaSb buffer layer 103
5.4.6 Growth on an AlSb buffer layer 105
5.5 Conclusions 108

5.5.1 Future work 109

6 II. Results and discussion: Optical Properties 111

6.1 Fourier Transform Infrared Spectrometry 111

6.1.1 Transmission 112

Transmission at 300 K 112

Transmission below 300 K 115

6.1.2 Analysis of absorption coefficients 119

Magnitudes and features at 300 K 119

Extraction of the fundamental bandgap E_g 121

Temperature-dependent bandgaps $E_g(T)$ 128

6.2 Spectral response 131

Extraction of bandgap values 138

6.3 Photoluminescence 141

6.4 Temperature dependence of the InAs/InAs$_{1-x}$Sb$_x$ bandgap 144

6.4.1 Temperature dependence of undoped epilayers 144

6.4.2 Temperature dependence of nBn devices 149

6.5 Band structure modelling of InAs/InAs$_{1-x}$Sb$_x$ 152

6.5.1 Conclusions 165

6.5.2 Future work 167

7 III. Results and discussion: Device Performance 168

7.1 IV characteristics 168

7.1.1 Dark current density J_d 168

Comparison with Rule 07 172

7.1.2 Arrhenius plot and activation energies 174

7.2 Quantum efficiency 180

7.2.1 Responsivity 180

7.2.2 External quantum efficiency 185

7.2.3 Internal quantum efficiency 186

7.3 Specific detectivity 188
7.4 Conclusions 190
7.4.1 Future work 192

8 Conclusions **193**
8.1 Future work 195

A Theory of strain **197**

B Sample summary **199**

Bibliography **202**

Chapter 1

Introduction

The so-called blackbody radiation characterises every object whose spectral emission lineshape and intensity are determined by its temperature T. The flux of emitted photons (irradiance S_λ) at a certain wavelength λ is also dependent on the object temperature, and these two dependencies are expressed such that[1]

$$S_\lambda \propto \frac{\lambda^{-5}}{exp\left(^{hc}/_{\lambda k_B T}\right) - 1} \tag{1.1}$$

where h is the Planck's constant, k_B is the Boltzmann constant and c is the speed of light. Normalised emission lineshapes for several T values can be seen in Figure 1.1.

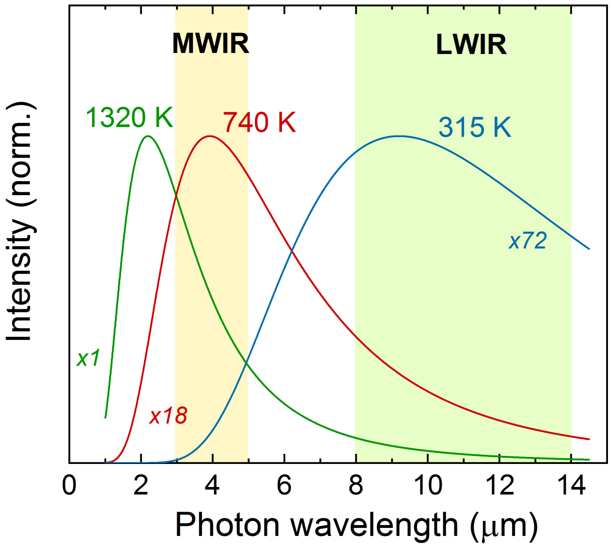

FIGURE 1.1: Theoretical blackbody emission of an object with $T = 1320$, 740 and 315 K, normalised to 1. The scale multiplying factors are also included.

The implication of this radiative phenomenon is that this thermal radiation can be used to characterise and image radiating objects using cameras with the detecting element designed to absorb photons with suitable wavelengths. In practice, however, a fundamental limiting factor for thermal detection arises from atmospheric absorption, causing certain λ ranges to be unsuitable for detection, which is illustrated in Figure 1.2.

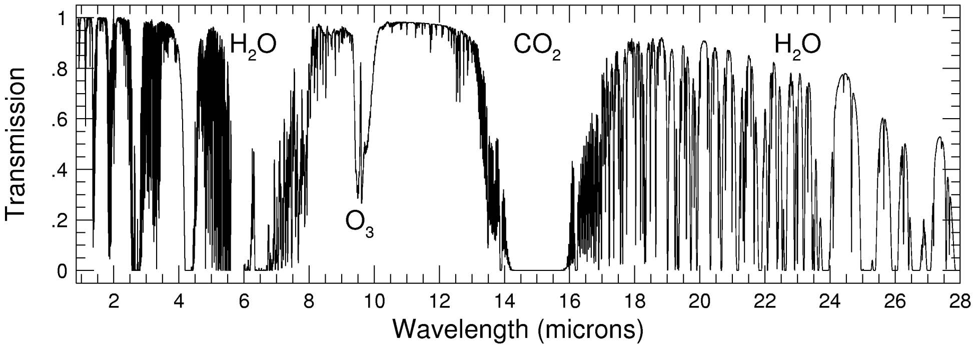

FIGURE 1.2: Atmospheric absorption as a function of photon wavelength. Two transparent infrared 'windows' are discernible: 3-5 μm (MWIR) and 8-14 μm (LWIR). Figure from osu.edu[2].

In the λ range that is broadly of interest in this work (3-14 μm), two atmospheric 'windows' are available: 3-5 μm, referred to as medium-wavelength infrared (MWIR) and 8-14 μm, denoted long-wavelength infrared (LWIR). These windows are also marked on Figure 1.1. The MWIR window is best suited for detection of objects and phenomena at temperatures of hundreds of degrees Celsius, such as hot exhausts, flames or cooler astronomical objects. The LWIR band, meanwhile, can be utilised to detect and image objects at or near room temperature, finding use in night vision and reconnaissance, security, and atmospheric imaging. Away from thermal emission, both bands are routinely used for gas detection due to the absorption spectrum lineshape of certain industrial gases such as CO_2[3] and methane[4].

The photon-sensing detector technology has been in development since the 1950's[5], and of all the materials used for photon absorption, the group II-VI semiconductor bulk alloy HgCdTe (CMT) has emerged as the dominant material[6,7,8,9]. However, in addition to several manufacturing and structural issues[10], the CMT technology now faces a legal hurdle in the form of the Minamata convention, aimed at eliminating the toxic element mercury from commercial products in the signatory countries[11]. Various group III-V detector materials, although less ubiquitous than CMT, have developed alongside it; this includes both bulk materials such as InSb and $InAs_{1-x}Sb_x$, and quantum structures such as quantum wells (QW) and strained-layer superlattices (SLS). A superlattice, which is part of the focus of this work, can be understood as a series of quantum wells and barriers that are physically thin enough (usually a few nanometers) to allow carrier tunnelling across the potential barriers. Unlike in a quantum well, whose primary mode of absorption is inter-subband transition[10], absorption in an SLS occurs via the fundamental interband transition between the first electron and heavy hole bands. Selection rules that forbid optical transitions perpendicular to the growth axis in QW structures are also relaxed in the superlattice structure, eliminating the need for scattering filters[10].

A superlattice type particularly advantageous for IR detection is called type-II, where the top of the valence and the bottom of the conduction bands are located in the two different materials, giving rise to a highly tunable optical bandgap E_g independent of the band structure of either constituent material. This also causes spatial separation of carriers which suppresses the Auger mechanism that restricts performance of bulk CMT; in addition, increased carrier effective masses reduce band-to-band tunnelling[9].

The SLS system that has seen the most research is InAs/GaSb, due to its theorised very low dark currents[9] and increased carrier effective masses[12]. However, the system is believed to suffer from decreased minority carrier lifetimes due to the presence of anti-site defect centres in GaSb; furthermore, when molecular beam epitaxy (MBE) is used for growth, the optimal SLS growth temperature also correlates with decreased lifetimes in GaSb[13]. Interface engineering has also been a challenge[12,14]. As such, the $InAs/InAs_{1-x}Sb_x$ superlattice has emerged as a potential Ga-free alternative, and has already been shown to possess superior minority carrier lifetimes of about 400 ns at 77 K[15], which compares favourably with those of LWIR InAs/GaSb superlattices, measured to be 31 ns at 77 K[16].

In addition, one of the narrow-bandgap device structures that have emerged as an alternative to the common photodiode is the so-called barrier detector[17,18], of which the nBn - which stands for n-doping/barrier/n-doping - is a variant. Here, both the n-doped absorber and the n-doped contact layer are narrow-bandgap materials that surround a wide-bandgap undoped barrier layer, whose role is to block the flow of electron majority carriers (which constitute dark current) by introducing a large conduction band offset, while a minimised valence band offset ensures the passage of minority holes. Unlike the p-n junction-based diode, the nBn eliminates the depletion region and so suppresses the Shockley-Read-Hall (SRH) current mechanism that tends to limit the diode performance[18]. A superlattice-based nBn detector is expected to combine this SRH suppression mechanism with the Auger-limiting characteristic of a type-II SLS.

The aim of this CASE project, funded and supported in part by the technology company Leonardo, is to understand and develop $InAs/InAs_{1-x}Sb_x$ nBn detectors for applications in the MWIR and LWIR absorption regimes. While these structures are routinely grown on the native GaSb substrate, the work presented here is conducted with the goal of extending it to growth on buffer layers deposited on the cheaper lattice-mismatched GaAs substrates. Chapter 2 summarises the theoretical background necessary to design high quality crystalline devices, to model and characterise their electronic band structures and to assess the performance of an nBn device. In Chapter 3, a review of the most relevant MWIR and LWIR detector technologies is presented. Finally, Chapter 4 briefly outlines the sample growth and characterisation methods, the device processing steps and the optical and current measurement procedures. This is next followed by three result Chapters. The design principles and the structural characterisation of samples are presented in Chapter 5. The optical and absorptive characteristics of undoped SLS are analysed and then modelled in Chapter 6. Finally, the dark current performance as well as several figures of merit for the nBn detectors are presented in Chapter 7.

Chapter 2

Background Theory

This Chapter is divided into two main parts: Section 2.1 introduces the most important concepts related to understanding, designing and modelling InAs/InAs$_{1-x}$Sb$_x$ strained-layer superlattices (SLS), and Section 2.2 outlines the current mechanisms and figures of merit relevant to nBn devices.

Pseudomorphic growth is a key requirement for fabrication of high-quality crystalline structures for detector purposes. Section 2.1.1 summarises the most important factors affecting crystallinity of MBE-grown lattice-mismatched epilayers: strain, critical thickness h_c, and thermal expansion of lattice constants.

In order to be able to predict the optical properties of the superlattice and SLS-based detectors, band structure modelling is introduced in Section 2.1.2. The Kronig-Penney model is used to predict the shape and the position of carrier minibands within the SLS structure. The heterojunction band alignment at the InAs/InAs$_{1-x}$Sb$_x$ interface is discussed next, followed by a summary of different possible SLS band alignments. Next, two different temperature dependence models of the bandgap E_g are discussed. Because InAs$_{1-x}$Sb$_x$ is a ternary alloy material, the interpolation schemes of its parameters from InAs and InSb are explained. Finally, in order to relate the measured optical characteristics of a sample to its band structure, the mechanisms of absorption, transmission and reflection are outlined.

Relevant nBn device physics are summarised in the last section, starting with the general properties of the nBn structure in Section 2.2.1, followed by the most relevant dark current mechanisms (Shockley-Read-Hall or SRH, and Auger) in Section 2.2.2. Responsivity R and internal and external quantum efficiency QE are outlined in Section 2.2.3 and finally, in Section 2.2.4 it is shown how to combine dark current density (J_d) with responsivity to obtain the specific detectivity D^* of a device.

2.1 Modelling

2.1.1 Effects of strain

When one epilayer deposited on top of another one has a different native lattice constant, this mismatch is initially accommodated by strain. Strain is a major design consideration in any system where crystalline quality needs to be ensured in order to avoid degradation of the system's electronic properties. When strain due to lattice mismatch exceeds certain critical limits, it can lead to a creation of defects and dislocations (most notably threading dislocations) in the crystal, which in turn introduces additional energy states in the bandgap, promoting the flow of dark current[19]. In addition, strain has non-negligible effect on a heterojunction's band alignment: it splits otherwise degenerate heavy- and light-hole valence bands, and shifts all the bands upwards or downwards depending on whether the strain is compressive or tensile[20,21].
The following analysis is valid only for {001} crystal orientations, as face-centred cubic zinc blende (001) is the only configuration used in the systems considered in this work.

Effects of strain on epilayer lattice constant

Mismatched lattice (pseudomorphic) growth results in strain arising in both in-plane (biaxial, x-y) and out-of-plane (uniaxial, z) directions, and which can be either compressive or tensile. This has a twofold effect on the InAs/InAs$_{1-x}$Sb$_x$ system: first, hydrostatic and shear strains induce additional band shifts at the heterojunction (see Section 2.1.2); furthermore, it places practical limits on superlattice layer thicknesses, total superlattice thickness as well as the d_{InAs} and d_{InAsSb} ratio. Biaxial $\epsilon_{\|}$ and uniaxial strain $\epsilon_{\perp}$ can be parametrised by[22]

$$\begin{aligned}\epsilon_{\parallel} &= \frac{a_{\parallel}}{a} - 1 \\ \epsilon_{\perp} &= \frac{a_{\perp}}{a} - 1\end{aligned} \tag{2.1}$$

where a refers to the unstrained lattice constant of the epitaxial material in question, and, for thin layers grown on a substrate, $a_{\parallel} = a_0$ is the lattice constant of the substrate. Because of the strain tensor form for a {001} crystal (see Appendix A), $a_{\perp}$ is obtained from

$$a_{\perp} = a\left[(1 - 2\frac{c_{12}}{c_{11}}\left(\frac{a_0}{a} - 1\right)\right)\right] \tag{2.2}$$

where c_{11} and c_{12} are elastic constants. The behaviour of $a_{\perp}$ and $a_{\parallel}$ in response to strain due to a mismatched a_0 can also be understood by referring to Figure 2.1.

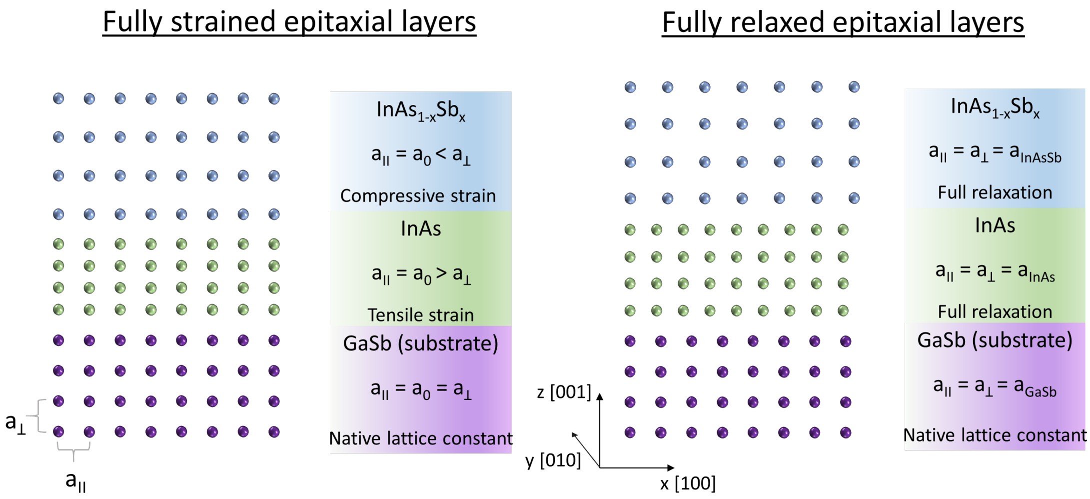

FIGURE 2.1: Visual demonstration of the effect of the compressive and tensile strain on epilayer constants due to growth on a substrate with a native lattice constant (left), and a fully relaxed buffer layer (right).

Critical thickness

The other strain-related design consideration is the critical thickness of a single epitaxial layer. It has been shown that lattice mismatch of up to 7% will be accommodated by elastic strain until a certain thickness is reached[23], beyond which it becomes energetically favourable to relieve some of the strain through dislocations instead, which compromises the electronic properties of the crystal. The Matthews-Blakeslee model of critical thickness[23] considers the balance of two mechanical forces on already existing dislocation lines - the force exerted by the strain due to lattice mismatch, and the tension in the dislocation line. Beyond a certain value of the force due to misfit strain (proportional to layer thickness) the dislocations move in a way that reduces strain and damages interface coherence. The critical thickness at which this occurs is[24]

$$h_c = \frac{a_0 \left[ln \left(\frac{\sqrt{2} h_c}{a_0} \right) + 1 \right] \left(1 - \frac{1}{4}\nu\right)}{\sqrt{2}\pi f \left(1+\nu\right)} \tag{2.3}$$

where ν is the epilayer's Poisson's ratio equal to $c_{12}/(c_{11}+c_{12})$, and f is its strain factor:

$$f = \frac{|a_0 - a|}{\frac{1}{2}(a_0 + a)} \tag{2.4}$$

In an alternative model People and Bean[25] consider lowest energy density balance instead of a mechanical one: their system is initially free of misfit dislocations, which are created when the strain energy density exceeds the self-energy of a dislocation. As one consequence of their approach, they conclude that the Matthews-Blakeslee model underestimates h_c below 1.4% lattice mismatch, and increasingly overestimates it beyond that value. Because the lattice mismatch in the systems discussed in this work (InAs/InAs$_{1-x}$Sb$_x$ grown either on GaSb substrates, or on GaSb or AlSb buffer layers) tend to stay well within or near the 1.4% mismatch limit (see Section 5.1), the Matthews-Blakeslee model is employed at the design stage as a matter of caution.

Lattice constant thermal expansion

Just like any solid, InAs and InSb crystals are subject to linear expansion due to temperature change. The zinc blende InAs linear expansion coefficient is[26] $4.52 \times 10^{-6}\ \mathrm{K}^{-1}$, and that of InSb is[27] 5.37×10^{-6} K^{-1}. Together with their 300 K lattice constant values, these coefficients translate into the following temperature dependencies[28]:

$$\begin{aligned} a_{InAs}(T) &= 6.0583 + 2.74 \times 10^{-5}(T - 300) \\ a_{InSb}(T) &= 6.4794 + 3.48 \times 10^{-5}(T - 300) \end{aligned} \tag{2.5}$$

where a is the lattice constant in units of Å and T refers to temperature in K. The InAs$_{1-x}$Sb$_x$ lattice constant is then obtained with linear interpolation using Vegard's law. The fact that the two lattice constants respond to temperature at different rates (see Figure 5.2) has to be kept in mind when designing strain-balanced superlattices: this will affect the critical thickness calculated using Equation 2.3.

In nBn devices barrier layers represent a complication for the balancing of the top contact superlattice; additionally, pseudomorphic strain arising from lattice mismatch will cause a valence band shift at the superlattice-barrier heterojunction, an important parameter for device optimisation. Temperature-dependent lattice constants for both the substrate and constituent barrier binaries can be seen in Appendix A.

Vegard's law

Vegard's law is a well-established method of estimating physical parameters of alloys from the parameters of their constituent materials, on the assumption of constant temperature and the same crystal structure. For example, given the lattice constants a_{InAs} and a_{InSb} at a certain temperature are known, the corresponding lattice constant of of InAs$_{1-x}$Sb$_x$ can be linearly interpolated as

$$a_{InAsSb} = xa_{InSb} + (1 - x)a_{InAs} \tag{2.6}$$

In the work presented here, the same linear treatment is also applied to the InAs$_{1-x}$Sb$_x$ hydrostatic and shear deformation potentials a_v, a_c and b. Other InAs$_{1-x}$Sb$_x$ parameters, notably the spin-orbit splitting parameter Δ_0 and the bandgap, are additionally affected by non-linear bowing; for example, E_g at a given temperature is calculated according to

$$E_g = xE_g(InSb) + (1-x)E_g(InAs) - x(1-x)b_g(T) \tag{2.7}$$

where the bandgap bowing parameter $b_g(T)$ has an additional temperature dependence calculated via Equation 2.31.

2.1.2 Band structure modelling

This section focuses on the theoretical underpinning of the band structure of a semiconductor, the derivation of relative band positions in a superlattice, and the different band alignment types possible in an SLS.

Basics of the semiconductor band structure

Qualitatively speaking, a semiconductor is a material 'halfway' between a conductor and an insulator: the bandgap (or the energetic distance between the lowest point on the conduction band and the highest point on the valence band) is non-negligible, but small enough to promote thermally excited carriers from the valence band into the conduction band at temperatures above 0 K. A related property is the Fermi energy, E_F, defined as the energy level at 0 K below which all states are occupied and above which all states are empty. Beyond 0 K Fermi energy is redefined as a 'chemical potential' μ whose value defines the probability of occupation equal to 0.5. Otherwise, the occupation of available states is determined by Fermi-Dirac probability distribution

$$f(\epsilon) = \frac{1}{e^{\left(\frac{\epsilon-\mu}{k_B T}\right)} + 1} \tag{2.8}$$

where ϵ is the state energy and T is the temperature of the system. For an intrinsic (undoped) semiconductor Fermi energy/chemical potential lies in the middle of the bandgap, and can be shifted upwards (downwards) with an appropriate n-doping (p-doping). Figure 2.2 gives some insight into the usefulness of using n-dopants to lift μ towards the conduction band: because the majority of electrons are more likely to occupy the states under μ even at temperatures above 0 K, any mid-bandgap states due to defects are filled and therefore unavailable for non-radiative recombination, which contributes to noise in photodetectors.

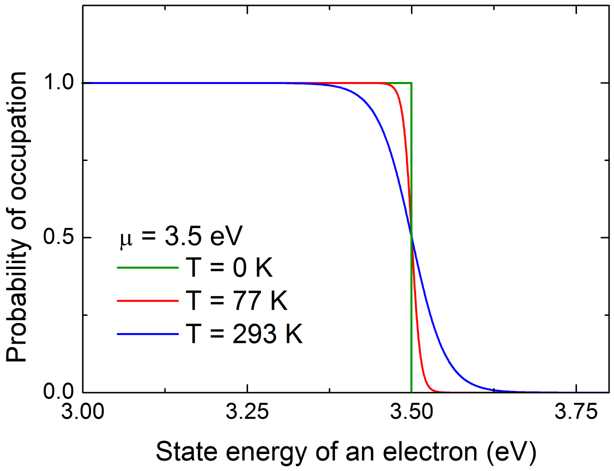

FIGURE 2.2: The Fermi-Dirac distribution for an arbitrary semiconductor at several temperatures.

Kronig-Penney model

When Fourier-transforming the primitive cell of a crystal from real space to reciprocal (momentum) space, one derives the Brillouin zone of the crystal: a volume in the momentum space whose boundary defines all the values of electron wavevectors (k) that can be Bragg-reflected by the crystal[29]. The actual form of carrier dispersion relation, $E(k)$, depends on the potential profile of the structure in question. Figure 2.3 shows an example band structure for an InAs crystal[30]. The Γ point refers to the centre of the zone (k=0), and the other letters refer to other points of interest on the face-centered cubic cell. Because InAs is a direct semiconductor, the electron (red) dispersion relation and the degenerate heavy and light holes (blue) have their minimum (maximum for holes) at the same point Γ, resulting in a direct bandgap.

The Kronig-Penney model is suitable for calculating the band structure in the vicinity of the Γ point, ie. $k = 0$, of a superlattice-like structure of periodic one-dimensional square potentials (see Figure 2.4). The Schrödinger's equation across the width $d =$

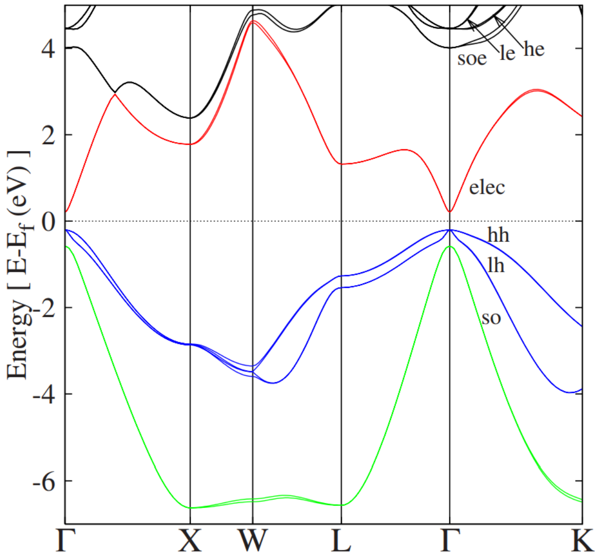

FIGURE 2.3: The electronic band structure of bulk InAs in the first Brillouin zone. Figure from Kim et al[30].

$b + w$ (where b and w are the barrier and well widths as per Figure 2.4) of the superlattice cell is[29]

$$\Psi = \begin{cases} Ae^{ik_w x} + Be^{-ik_w x} & \text{for} \quad 0 \leq x \leq w \\ Ce^{k_b x} + De^{-k_b x} & \text{for} \quad w \leq x \leq b \end{cases} \tag{2.9}$$

where k_w and k_b are wavevectors inside the well and the barrier respectively, x is the distance along the superlattice growth axis and A, B, C and D are constants.

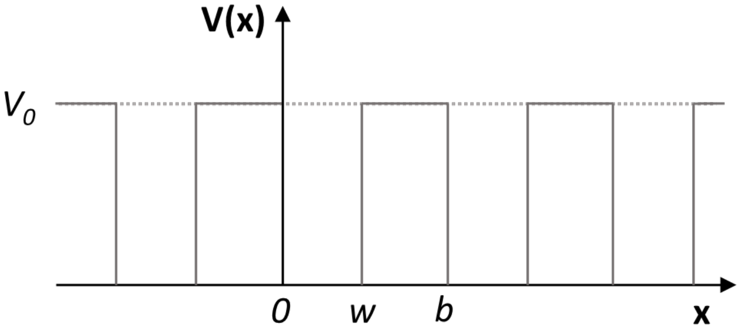

FIGURE 2.4: The one-dimensional array of finite square potential wells that serves as a basis of the Kronig-Penney superlattice model.

The wavevector of a carrier propagating normal to the barriers with height V_0 is

$$k_w = \sqrt{\frac{2m^*}{\hbar^2}E} \tag{2.10}$$

when the carrier is located in the potential well, and for an electron or hole inside the barrier

$$k_b = \sqrt{\frac{2m^*}{\hbar^2}(E - V_0)} \tag{2.11}$$

where E is the energy of the carrier as measured from the bottom of their potential well, m^* is the effective mass and $\hbar$ is the reduced Planck's constant. 'Effective mass' is the mass of the carrier in the crystal modulated by the periodic potential of the crystal, and here it is taken to be[31]:

$$m^*{}_{e,InAs} = 0.023m_0 \quad ; \quad m^*{}_{hh,InAs} = 0.41m_0 \quad ; \quad m^*{}_{lh,InAs} = 0.26m_0 \tag{2.12}$$

where m_0 is the free electron mass. For InAs$_{1-x}$Sb$_x$, the expressions (in terms of m_0) are[32]

$$m^*{}_{e,InAsSb} = 0.03 - 0.01x_{As} + 0.025x_{As}^2 \tag{2.13}$$

where x_{Sb} is the Sb fraction in the alloy. For the heavy holes it is[32]

$$m^*{}_{hh,InAsSb} = 0.4 - 0.18x_{As} + 0.18x_{As}^2 \tag{2.14}$$

and light holes[31]

$$m^*{}_{lh,InAsSb} = 0.026 - 0.011x_{Sb} \tag{2.15}$$

Just as in the case of quantum wells, continuity conditions at the well and barrier boundary apply to the constants A, B, C and D (Equation 2.9). For an infinite superlattice, Bloch theorem also demands that the wavefunctions defined in Equation 2.9 in different superlattice cells must be the same except for a phase shift e^{-ikd}, where k is the Bloch wavevector defined over the first Brouillin zone, and $d = w + b$[33]. Shen et al[34] use the 2×2 transfer matrix method to derive the following dispersion relation for a superlattice:

$$k = \frac{1}{d} arccos \left(\frac{Q}{2} \right) \tag{2.16}$$

where, for a superlattice cell with $M = 2$ layers, Q is defined to be

$$Q = \prod_{h=1}^{M} cos(k_h d_h) - \sum_{h=1}^{M-1} \times \sum_{j=h+1}^{M} \left[\left(\frac{w_h}{w_j} + \frac{w_j}{w_h} \right) sin(k_h d_h) sin(k_j d_j) \times \prod_{l(\neq h,j)=1}^{M} cos(k_l d_l) \right] \tag{2.17}$$

where h, j and l are integers and $w_i = k_i / m_i$ for the ith layer. The above is valid for k_b where $E \geq V_0$ (see Equation 2.11); when the carrier energy is below V_0, $k_b = ik'_b$ and the following substitutions are made to the above equation:

$$\begin{aligned} sin(k_b d_b) &= isinh(k'_b d_b) \\ cosh(k_b d_b) &= cosh(k'_b d_b) \end{aligned} \tag{2.18}$$

Heterojunction band alignments

If a superlattice structure is to be successfully integrated into a photodetector, it is critical to be able to predict and engineer its bandgap. When attempting to calculate the relative band offsets of two separate bulk materials, one is faced with the problem of forming a common reference level for the energy levels. Although there exist theoretical approaches to deriving a common reference point for all crystals, this work uses the approach from Vurgaftman et al[28], to define the position of all bands in the system with respect to the valence band (VB) of InSb, where VB_{InSb} is normalised to 0 eV.

Once a common band position reference point is established, band positions can be defined. The starting point is the average unstrained valence band energy which is equal to[22,35]

$$E_{v,av} = \frac{1}{3}\left(E_{hh} + E_{lh} + E_{so}\right) + \frac{\Delta_0}{3} \tag{2.19}$$

where the first three subscripts correspond to heavy holes, light holes and the spin-orbit split-off band. Note that unlike all other $\text{InAs}_{1-x}\text{Sb}_x$ parameters, which are calculated or otherwise derived, $E_{v,av,InAsSb}$ is used as a free parameter in model fitting. Spin-orbit interaction Δ_0 arises due to the interaction of an electron's spin with its own motion around the nucleus. This effect splits E_{hh} and E_{lh} upwards from the split-off band E_{so}[35], and its value is added from experimental data[28]. Under conditions of no strain, E_{hh} and E_{lh} are degenerate.

Adding the temperature-dependent bandgap $E_g(T)$ to Equation 2.19 results in the unstrained conduction band position:

$$E_c = E_{v,av} + \frac{\Delta_0}{3} + E_g(T) \tag{2.20}$$

where binary $E_g(T)$ values are first defined according to Equation 2.29, and then any ternary values are found using Equation 2.7.

The shift of the conduction and valence band edges under strain is parametrised with deformation potentials. Hydrostatic deformation is the volume change of the crystal, and its effect on the conduction and heavy hole valence band positions is such that[35] (see Appendix A):

$$\begin{aligned} \Delta E_c^{hy} &= a_c(2\epsilon_{\parallel} + \epsilon_{\perp}) \\ \Delta E_{v,av}^{hy} &= a_v(2\epsilon_{\parallel} + \epsilon_{\perp}) \end{aligned} \tag{2.21}$$

Nonhydrostatic shear strain is the cause of relative changes of energies of different electronic states in the system and leads to splitting of degenerate bands. Like the hydrostatic strain component, this can also be described in terms of a deformation potential. All three valence bands constituting $E_{v,av}$ are affected differently, but in all cases the splitting arises from the interaction with Δ_0. In a tetragonal (zinc-blende) (001) system, the additional shifts are:

$$\Delta E_{hh}^{sh} = -\frac{1}{2}\delta E^{sh} \tag{2.22}$$

$$\Delta E_{lh}^{sh} = -\frac{1}{2}\Delta_0 + \frac{1}{4}\delta E^{sh} + \frac{1}{2}\left[\Delta_0^2 + \Delta_0 \delta E^{sh} + \frac{9}{4}\left(\delta E^{sh}\right)^2\right]^{1/2} \tag{2.23}$$

$$\Delta E_{so}^{sh} = -\frac{1}{2}\Delta_0 + \frac{1}{4}\delta E^{sh} - \frac{1}{2}\left[\Delta_0^2 + \Delta_0 \delta E^{sh} + \frac{9}{4}\left(\delta E^{sh}\right)^2\right]^{1/2} \tag{2.24}$$

where the shift δE^{sh} is equal to

$$\delta E^{sh} = 2b(\epsilon_\perp - \epsilon_\parallel) \tag{2.25}$$

where b is the deformation potential itself.

Collecting all the terms together: the positions of both the conduction and heavy hole valence bands are defined with respect to the valence band of unstrained bulk InSb, and are given by

$$E_v = \underbrace{E_{v,av} + \frac{\Delta_0}{3}}_{\text{unstrained}} + \Delta E_{v,av}^{hy} + max(\Delta E_{hh}^{sh}, \Delta E_{lh}^{sh}) \tag{2.26}$$

whereas the conduction band position is

$$E_c = \underbrace{E_{v,av} + \frac{\Delta_0}{3} + E_g(T)}_{\text{unstrained}} + \Delta E_c^{hy} \tag{2.27}$$

where the unstrained terms comprise of the average valence band energy $E_{v,av}$, spin-orbit splitting Δ_0 and the temperature-dependent bandgap $E_g(T)$. Additionally, the valence band position is subject to hydrostatic (hy) and shear (sh) strain; the conduction band at Γ (the region under consideration) is subject only to the former one.

Superlattice band alignment types

One of the proposed advantages of the InAs/InAs$_{1-x}$Sb$_x$ system as a candidate for LWIR detectors is its tunable bandgap. But this could not be successfully implemented without an appropriate type of superlattice band alignment present: in a type-I alignment, for example (see Figure 2.5), the band positions of the narrow-bandgap material are located 'inside' the bands of the wide-bandgap material, which leads to both electron and hole confinement within the same physical layer and as a result, the fundamental bandgap of the superlattice would approach that of bulk InAs$_{1-x}$Sb$_x$. Another alternative is referred to as type-II superlattice (T2SL), where the carriers are physically separated in the two layers. Two type-II alignments are possible: type-IIa, where the holes are confined in wide-bandgap material and the electrons are in the narrow-bandgap material, and type-IIb where the opposite is true. There also exists a variation of type-II alignment called 'broken gap', which arises when the relative valence band offset (VBO) of the two materials is large enough to push the valence band of one material above the conduction band of the other.

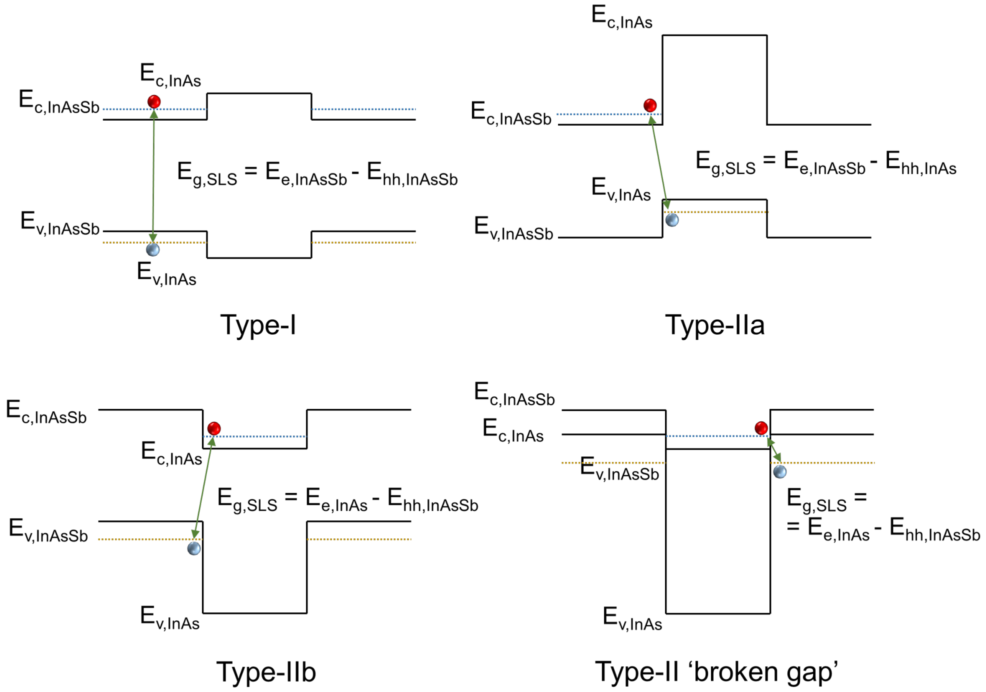

FIGURE 2.5: Possible superlattice band alignment types.

The type of superlattice band alignment of InAs/InAs$_{1-x}$Sb$_x$ is strongly tied to the nature of bandgap bowing b_g in InAs$_{1-x}$Sb$_x$, and (less importantly) epitaxial strain. In general, calculated and observed narrowing of the InAs/InAs$_{1-x}$Sb$_x$ bandgap compared to constituent bulk materials conclusively supports[36,37,38,39,40] presence of type-II alignment, and because the most recently reported large bowing parameters tend to have a strong valence band bowing component (as discussed in Section 3.4.1), including the one adopted for modelling in this work (Section 2.1.2), the result is a type-IIb alignment with strong heavy hole confinement in the alloy[41,40,36]. Type-I alignment is expected from Sb fractions lower than any discussed in this work[42], and is generally suppressed by epitaxial strain and lack of ordering in the alloy[38].

Bandgap temperature dependence

Group III-V semiconductors all demonstrate a decrease in bandgap with increasing temperature due to decreased binding energy between constituent atoms, as well as electron-phonon interaction. The relation most widely used to predict this behaviour is the empirically-derived Varshni fit:

$$E_g(T) = E_0 - \frac{\alpha T^2}{\beta + T} \tag{2.28}$$

where E_0 is the 0 K bandgap of the material, T is temperature in K and α and β are fitting parameters loosely corresponding to gap entropy at $T \to \infty$ and to Debye temperature respectively[43]. Varshni equation, however, is first and foremost an empirical fit to experimental results without a strong theoretical underpinning; it also predicts a quadratic relation at very low temperatures, contradicting existing data[42,44,45].

One proposed alternative to the Varshni relation is the Einstein single-oscillator model[42,46], which has the form

$$E_g(T) = E_0 - \frac{S_g k T_E}{exp(T_E/T) - 1} \tag{2.29}$$

where $T_E = h\omega_{ph}/k$ is the Einstein temperature of the solid, related to the average oscillation frequency of the phonons ω_{ph}. $\frac{1}{2}T_E$ denotes the onset of the flat low-temperature region. S_g is a dimensionless coupling parameter and k is the Boltzmann constant; their product $S_g k$ describes the bandgap reduction rate in the high-temperature region. Finally, the product $\frac{1}{2}S_g k T_E$ is the bandgap reduction due to the zero-point motion of the lattice[42]. This model has consistently been found to predict the low ($T \lesssim 50K$) temperature bandgaps more accurately[42,44,46] in that it predicts them to be relatively temperature-independent.

$InAs_{1-x}Sb_x$ band bowing

While linear interpolation is a correct and sufficient approach for a number of alloy parameters (see Section 2.1.1), the bandgap of most ternary zinc-blende structures is calculated using an additional quadratic term (see Equation 2.7). b_g can be defined to be

$$b_g = b_{CB} - b_{VB} \tag{2.30}$$

where b_{CB} and b_{VB} stand for conduction band and valence band bowing parameters respectively. The b_g value most commonly reported[28,47,48] in literature is 670 meV for fully relaxed bulk $InAs_{1-x}Sb_x$. Svensson et al[49], however, propose an increased value of 870 meV based on low-temperature photoluminescence studies of $InAs_{1-x}Sb_x$ carried out by Yen et al[48] and Kurtz et al[50], as well as their own. Webster et al[42] goes further in proposing a temperature-dependent double-oscillator model for $b_g(T)$:

$$b_g(T) = b_0 - \frac{S_1 k T_1}{exp(T_1/T) - 1} + \frac{S_2 k T_2}{exp(T_2/T) - 1} \tag{2.31}$$

where the corresponding parameters can be seen in Table 2.1. No physical explanation, however, is offered for this approach.

For the case of the $InAs/InAs_{1-x}Sb_x$ system in particular, the value of b_{VB} is of crucial importance as it determines the heavy hole ground-state bandgap. A number of

TABLE 2.1: Double-oscillator model parameters for InAs and $InAs_{1-x}Sb_x$[42].

	b_0 (meV)	S_1	T_1 (K)	S_2	T_2 (K)
$InAs_{1-x}Sb_x$	938	22.98	115.8	18.80	275.6

studies have reported on the spread of b_g between the conduction and valence bands, a summary of which is presented in Section 3.4.1.

2.1.3 Absorption coefficient, transmission and reflection

In order to calculate internal quantum efficiency (see Section 2.2.3) it is necessary to be able to calculate surface reflection from as well as transmission of the sample. Both of these calculations first require obtaining the absorption coefficient of the superlattice. The absorption coefficient α of a material is defined in the context of the light intensity I, which is absorbed as it travels through thickness x and undergoes multiple internal reflections due to reflectivity R_s:

$$\frac{I}{I_0} = \frac{(1-R_s)^2 exp(-\alpha x)}{1-R_s^2 exp(-2\alpha x)} \tag{2.32}$$

where I_0 is the normal incident intensity[51,52]. Defined in the above way, the left-hand side of the equation is equivalent to the transmittance of the sample.

The air-superlattice interface dominates the amount of total reflection due to the relative differences in the refractive indices of the two media, and is calculated using

$$R_s = \frac{(1-n_{SLS})^2 + k_{SLS}^2}{(1+n_{SLS})^2 + k_{SLS}^2} \tag{2.33}$$

where the extinction coefficient k_{SLS} is derived from the absorption coefficient α_{SLS} of the superlattice using the relation

$$k_{SLS} = \frac{\lambda \alpha_{SLS}}{4\pi} \tag{2.34}$$

where λ is the light wavelength. n_{SLS} is the effective refractive index of the superlattice according to[53]

$$n_{SLS}^2 = \frac{n_w^2 + n_b^2}{1+r} \tag{2.35}$$

where n_w is the refractive index of the electron well (InAs), n_b that of the barrier (InAs$_{1-x}$Sb$_x$) and $r = n_w/n_b$. The InAs refractive index spectrum was taken from Refractive Index Database[54], while the InAs$_{1-x}$Sb$_x$ spectrum was extrapolated from the calculated spectra found in Paskov et al[55] depending on the Sb content of the sample. It is important to point out that in order for Equation 2.33 to be polarisation-independent, the incoming light must be at normal incidence.

Absorption processes near the band edge

In a perfectly crystalline intrinsic semiconductor, the lowest allowed energy transition would correspond to the energetic distance between the bottom of the parabolic conduction band and the top of the valence band. The behaviour of the absorption coefficient α_g at the onset of this optical gap depends on whether the material is direct or indirect, and can be described by[56,57]

$$\alpha_g \propto \begin{cases} (h\nu - E_g)^{1/2} & \text{for a direct bandgap} \\ \frac{(h\nu - E_g + E_{ph})^2}{exp(E_{ph}/(kT))-1} + \frac{(h\nu - E_g - E_{ph})^2}{1-exp(E_{ph}/(kT))} & \text{for an indirect bandgap} \end{cases} \tag{2.36}$$

where E_{ph} is the energy of the phonon that assists in the transition between the indirect minima of the bands, while the temperature term emerges due to the phonons' dependence on lattice vibrations. Both phonons with $+E_{ph}$ (phonon absorption) and $-E_{ph}$ (phonon emission) can assist in the transition, which is reflected in the numerators of the two terms of the indirect α_g equation. It must be noted these relationships assume parabolicity of the bands, which is a sufficient approximation near band minima of a superlattice[40,58] as per Equations 2.10 and 2.11, but should not be assumed for the higher-energy regions of the bands. A simplified visual illustration of the α_g behaviour as a function of photon energy $h\nu$, devised for an arbitrary semiconductor with a fixed bandgap of 0.20 eV and a phonon energy of 0.01 eV, can be seen in Figure

2.6. Although the example is highly artificial, the temperature dependence of the magnitude of indirect α_g is evident, as well as the different functional forms of the direct and indirect regimes.

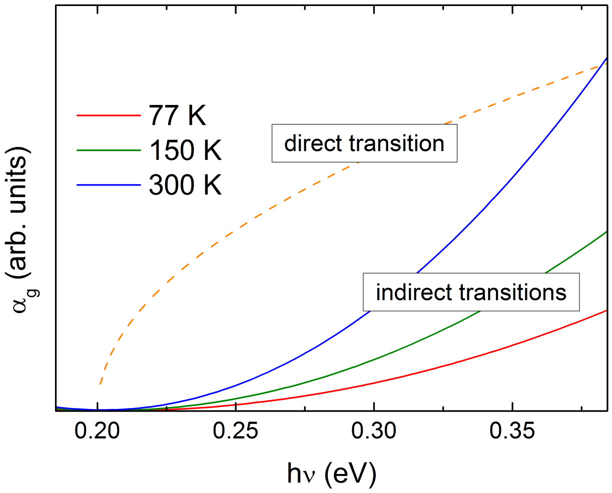

FIGURE 2.6: The idealised behaviour of the absorption coefficient α_g near the band edges of the conduction and valence bands of a semiconductor with $E_g = 0.20$ eV and $E_{ph} = 0.01$ eV. The solid lines show the $h\nu$ and the temperature difference of an indirect material, and the dashed line corresponds to a direct one.

In the case of a real material, the periodicity of conduction and valence bands is perturbed by the introduction of impurities and their associated energy levels. Their presence results in a mostly localised 'tail' of states that can extend below the minimum of the band, and whose nature depends on the type of the impurity in question. First, introducing dopants results in additional states near the edge of the relevant band that, for a sufficiently high doping density, will broaden into an impurity band. Any Coulomb interaction between an ionised donor/acceptor and carriers in the bands will also perturb the bands. In the case more relevant to the low-doped structures discussed in this work, dislocations and their relevant states will also contribute to absorption by broadening both bands. Finally, localised accommodation of strain and stress due to impurities will decrease the optical bandgap in the case of the former (eg. due to vacancies), and increase it for the latter (eg. due to interstitials), essentially shifting the parabolic bands to various energies. The sum of these perturbations acts to broaden the band edges of the material[51,57].

The contribution of these near-band states to absorption manifests itself as the so-called Urbach tail, a region of non-zero α in the spectrum just below the onset of band-to-band absorption. This sub-bandgap absorption α_U rises exponentially with photon energy such that[46,59]

$$\frac{1}{E_U} = \frac{\mathrm{d}ln(\alpha_U)}{\mathrm{d}h\nu} \tag{2.37}$$

where E_U is the the characteristic width of the absorption edge (Urbach energy).

2.2 Device physics

This section details the principles of operation of a superlattice nBn structure, its relevant dark current mechanisms and several figures of merit used to characterise IR photodetectors.

2.2.1 nBn structure

The nBn device structure is a type of a unipolar barrier detector - so called because the inbuilt wide-bandgap barrier impedes the flow of majority carriers while permitting the passage of the minority carrier photocurrent. A number of different barrier structures have been proposed in literature[18], however nBn is by far the most common one[17]. In this variant, compared in Figure 2.7 to a conventional photodiode, both the narrow-bandgap contact and absorber layers are n-doped, while the wide-bandgap barrier is intrinsic.

The main engineering requirement for the barrier is minimised or no valence band offset at barrier interfaces; in addition, the conduction band offset must be large enough to suppress thermal excitation of electrons above it, and thick enough to prevent tunnelling (50-100 nm)[60]. A well-designed barrier, when located away from the absorption region and near the minority current collector, suppresses majority carrier dark currents and the surface current, while allowing minority carrier photocurrent to pass through[61]. Blockage of surface current is particularly useful from a processing point of view - the

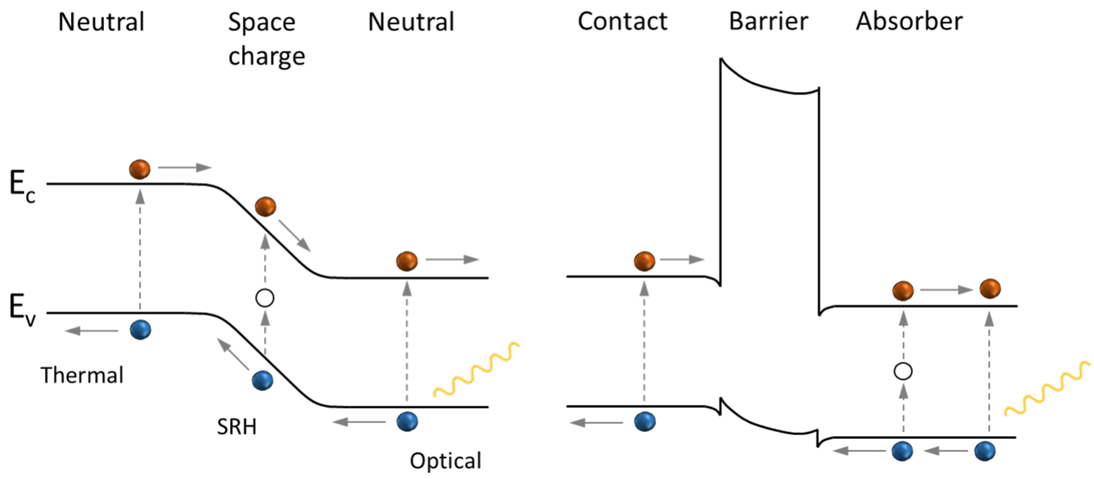

FIGURE 2.7: Photodiode (left) and nBn (right) structures under negative bias. Some idealised types of current generation processes are represented for both structures. Figure adapted from Martyniuk et al[17].

presence of barrier essentially acts as a passivation layer[62]. Unlike a photodiode, an ideal nBn device has no space charge region, and so Shockley-Read-Hall generation in response to bias does not occur. Auger-induced diffusion currents, however, are not naturally suppressed by the structure[61], but it is a feature that can be achieved by incorporating a superlattice into the contact and absorber layers.

2.2.2 Dark current mechanisms

Any current component inside a photodetector material that is not due to photon absorption impedes its performance, and is referred to as a dark (or leakage) current. Dark currents can occur due to a number of physical processes and considerable effort is spent on limiting their occurrence in semiconductor devices. Below are described the current mechanisms most relevant to an nBn detector.

Shockley-Read-Hall generation

Generation-recombination of carriers that is enabled by deep traps embedded in the material bandgap is referred to as a Shockley-Read Hall (SRH) current. The occurrence of SRH generation/recombination under reverse bias is a design flaw inherent in photodiodes due to the presence of a depletion region where the Fermi level is located in the middle of the bandgap, which facilitates carrier flow in the inbuilt electric field[18,63] and makes this mode of recombination dominant. The SRH current is directly proportional to intrinsic carrier density n_i according to

$$J_{SRH} \propto n_i \propto T^r e^{\frac{-E_{tr}}{kT}} \tag{2.38}$$

where n_i is the intrinsic carrier concentration, E_{tr} is the deep trap energy level, T is the temperature and r is a factor related to Moss-Burstein energy[64].

Unlike a p-n junction, an ideal nBn detector is proposed to have no SRH element due to two design factors: the effective lack of depletion zones in the structure[18,17,60], and the shift of the Fermi level above the midgap states due to n-doping of the absorber[65], which helps fill these states according to Equation 2.8. In such a structure, the total current would instead be diffusion-limited. Figure 2.8 demonstrates the difference in current characteristics between a conventional diode and an ideal nBn structure: the SRH current, which has a weaker temperature dependence than the diffusion current, dominates at lower temperature values, while the diffusion component becomes dominant beyond a certain 'crossover' temperature T_0. However, without the SRH component, the total dark current continues dropping in accordance with the diffusion temperature dependence, which offers an advantage over conventional diodes.

Auger mechanisms

The diffusion current in an ideal nBn device is primarily due to the band-to-band Auger 1 generation-recombination process[66]. The Auger mechanism is a three-particle process wherein a particle in conduction/valence band recombines with a particle in the valence/conduction band, but the energy emitted during recombination is transferred as a phonon to another particle in either conduction or valence band, which promotes it to a higher energy level. As such, it is a non-radiative process. The classification of a particular Auger mechanism depends on which carriers are involved at each stage; the

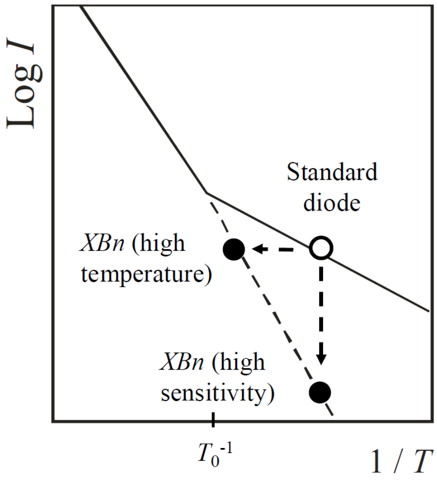

FIGURE 2.8: A model Arrhenius plot for a diode and an XBn structure (including nBn). In an ideal nBn device no Shockley-Read-Hall generation takes place at lower temperatures, and the dark current density keeps falling according to $\sim E_g$. Figure from Klipstein et al[18].

Auger 1 variant, which can be seen in Figure 2.9, consists of an electron transferring its energy to another electron as it recombines with a heavy hole.

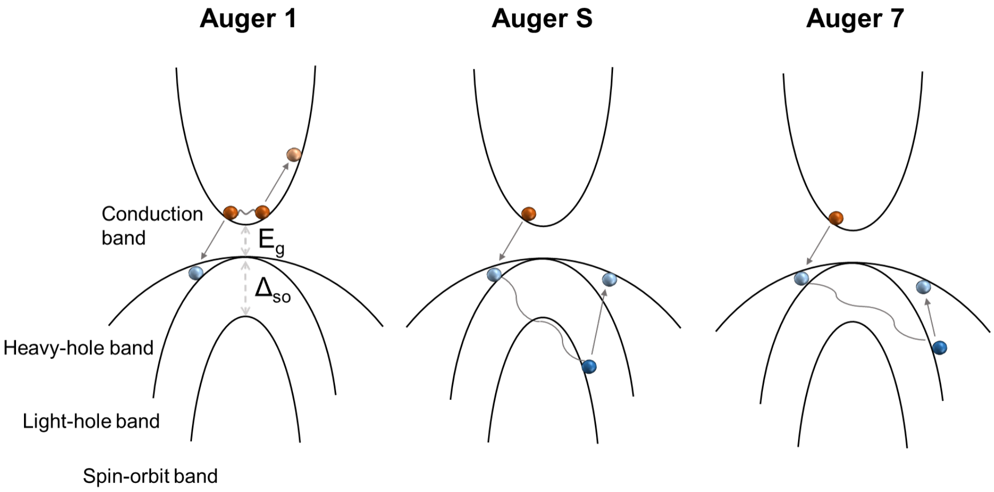

FIGURE 2.9: Auger mechanisms. Auger 1: an electron in the conduction band transfers its energy to another electron, promoting it to a higher band, then recombines with a hole. This process is dominant in an ideal bulk nBn structure. Auger S: an electron recombines with a heavy hole, followed by an energy transfer to and a promotion of a carrier from the spin split-off band to the heavy-hole band. This mechanism is suppressed by large Δ_{so}. Auger 7: an electron recombines with a heavy hole, with the resultant energy transferred to a light hole, subsequently promoted to the heavy hole band. This process can be minimised by strain. Diagram adapted from Rogalski et al[67].

This variant is dominant in narrow-bandgap nBn structures due to their n-doping, and also the fact that their spin-orbit splitting energy Δ_{so} tends to be much larger than the bandgap E_g, which suppresses the so-called Auger S mechanism[67]. The diffusion current density due to Auger generation rate is proportional to[18]

$$J_{diff} \propto n_i^2 \propto T^r e^{\frac{-E_{diff}}{kT}} \tag{2.39}$$

where E_{diff} is roughly equal to the bandgap E_g due to the band-to-band nature of the transition. It is important to point out, however, that a significant proposed advantage of type-II strained-layer superlattices is that they naturally suppress both Auger 1 and 7 mechanisms. The suppression of Auger 1 arises when the width of the electron miniband is smaller than the bandgap, which makes the maximum allowed energy transfer too small for the transition to proceed[68,6]. Suppression of Auger 7 relies on the presence of strain in the superlattice, which shifts the light- and heavy-hole bands away from each other and so increases the energy threshold for allowed transitions[69].
Figure 2.8 is a theoretical example of the so-called Arrhenius plot, where the total current density in a device is plotted in a logarithmic form as a function of $1000/T$. Fitting the equations 2.38 and 2.39 to various sections of the resultant graph can give insight into the dominant current mechanism of the device in a given temperature range.

2.2.3 Responsivity, internal and external quantum efficiency

Responsivity and quantum efficiency are important figures of merit used to characterise the performance of a photodetector. External quantum efficiency describes a device's ability to convert incident photons into useful electric signal, and is defined as the ratio of the two:

$$\eta_e = \frac{\text{number of generated electron-hole pairs}}{\text{number of incident photons}} = \frac{I_p}{P_0}\frac{hc}{\lambda q} \tag{2.40}$$

where I_p is the photocurrent, P_0 is the incident optical power, q is electron charge and λ is the incident photon wavelength. The magnitude of the photocurrent is strongly modulated by the geometry of the device, including (but not limited to) the use of double-pass architecture and the reflection R_s at the surface of the detector. Accounting for R_s using Equation 2.33 yields internal quantum efficiency:

$$\eta_i = \frac{\text{number of generated electron-hole pairs}}{\text{number of photons entering the absorber}} = \frac{1}{(1-R_s)} \frac{I_p}{P_0 \lambda} \frac{hc}{q} = \frac{\eta_e}{(1-R_s)} \tag{2.41}$$

In addition, not all radiation entering the active region is absorbed, due to the finite width of the layer and the dependence of the absorption coefficient on the photon wavelength (Equation 2.32). As such, further dividing η_i by $e^{-\alpha w}$ (where α is the absorption coefficient at given wavelength λ, and w is the absorber thickness) results in the generated photocurrent that reaches out the readout electronics as a fraction of the total photocurrent generated in the absorber volume.

Responsivity (spectral response) is a figure of merit that is directly related to quantum efficiency, and is defined as

$$R = \eta_e \frac{q\lambda}{hc} \tag{2.42}$$

with units of AW^{-1}. As such, it is fundamentally defined as the ratio of photocurrent reaching the read-out electronics and incident optical power.

2.2.4 Relevant noise types and specific detectivity

A useful figure of merit in photodetector technology is detectivity D, which is fundamentally defined as the reciprocal of noise-equivalent power: the minimum incident power required to lift the resultant signal above the noise floor of the device. This can be cast in terms of detector responsivity R and root mean square of the noise current $< I_n >$[33] as

$$D = {}^{1}/_{NEP} = {}^{R}/\sqrt{< I_n^2 >} \tag{2.43}$$

The above definition, however, incorporates area dependence of the device and so in order to allow for direct comparisons between different-sized detectors, specific (ie. normalised) detectivity D^* is defined such that

$$D^* = D \times (A_d \Delta f)^{1/2} = \frac{R}{\sqrt{< I_n^2 >}} (A_d \Delta f)^{1/2} \tag{2.44}$$

where A_d is the area of the device and Δf is the output bandwidth of the circuit, here normalised to 1 Hz. Noise current I_n is a composite value of the total of the noise components in the detector, and in an ideal nBn structure it can be approximated as the root mean square of the sum of the thermal noise I_T and the so-called shot noise I_{sh}, such that

$$\sqrt{< I_n^2 >} = \sqrt{< I_T^2 > + < I_{sh}^2 >} \tag{2.45}$$

Thermal noise of a resistor R_d arises due to the fundamentally random thermal fluctuation of carriers in the material. For circuit frequencies much lower than the term ${}^{k_bT}/_{h}$ (which can be assumed to be the case for all devices in this work) the mean squared value of thermal current is

$$< I_T^2 > \approx \frac{4k_bT}{R_{dyn}} \Delta f \tag{2.46}$$

where R_{dyn} is the dynamic resistance of the device, defined as $\mathrm{d}V/\mathrm{d}I$.

Shot noise of a device is a consequence of the particle nature of charge carriers. The collection of a DC current I_{DC} by external circuitry can be considered a series of independent random events (ie. carrier arrivals) with a fixed mean - ie. a Poisson distribution. For a large enough number of events, Poisson distribution approaches Gaussian distribution, and so the standard deviation of the current becomes the square root of the average DC current. The shot noise is thus defined

$$< I_{sh}^2 > = 2qI_{DC}\Delta f \tag{2.47}$$

where the factor of 2 arises from the derivation of the spectral density function in terms of frequency[33,62].

It is important to note that the R_0A product, related to shot noise in photodiodes and so commonly used to characterise their dark current performance, is not an appropriate figure of merit for nBn detectors since their zero-bias resistance shows little correlation with defect density[66]. Because of this, dark current-related performance reported in this work is characterised using Arrhenius fits and detectivity instead.

Chapter 3

Literature Review

This chapter summarises general trends in medium- (3-5 μm) and long-wavelength (8-14 μm) infrared detector technology, beginning with a short summary of thermal detectors. Photon detection is achieved with the use of semiconductors, which can be broadly divided into group II-VI, IV-VI and III-V materials, and whose relationship between the optical bandgap and the crystalline lattice constant is presented in Figure 3.1.

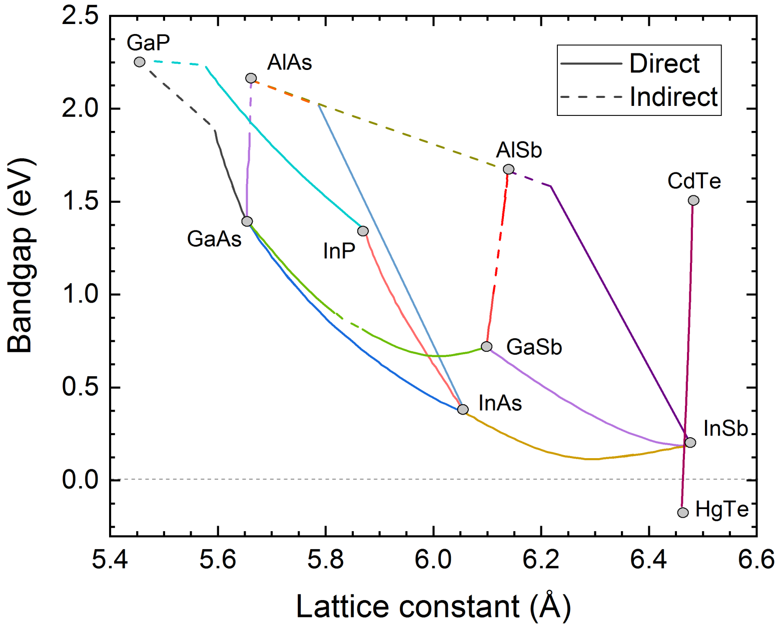

FIGURE 3.1: The bandgap of various III-V binaries (grey dots) as a function of their lattice constant. HgTe and CdTe belong to the II-VI group. The lines correspond to their ternary alloys including any band bowing. Data adapted from Walters et al[70] and Rogalski et al[7].

Special consideration is given to the II-VI HgCdTe technology which currently dominates the infrared detection field[6]. Because InAs/InAs$_{1-x}$Sb$_x$ is a III-V group system, bulk materials from the same group that are the most relevant for MWIR and LWIR detection purposes are also introduced. A brief history of the strained-layer superlattice (SLS) structure is outlined and special attention is given to the III-V InAs/GaSb type-II superlattice (T2SL), which has so far received the most attention as an SLS detector material[10]. The InAs/InAs$_{1-x}$Sb$_x$ superlattice has been proposed as a direct alternative to InAs/GaSb and its progress as detector material is outlined. Finally, the progress and status of the nBn structure is summarised, with special attention given to structures incorporating the Ga-free superlattice.

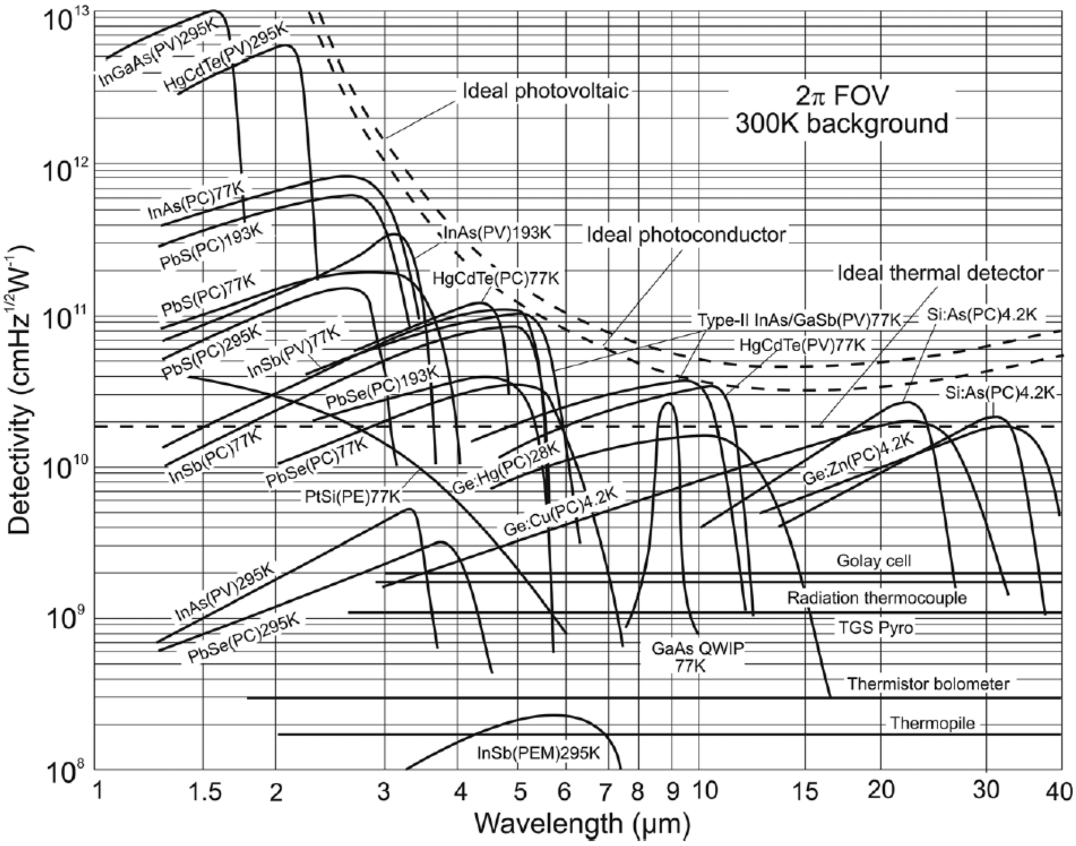

FIGURE 3.2: Specific detectivity (D^*) of various commercially available infrared detection technologies as a function of photon wavelength. Figure from Rogalski et al[62].

3.1 Thermal detectors

Detection technologies for infrared light date back to the 19th century. The very first IR detectors were thermal - relying on heating effects rather than detection of radiation - and consisted of structures such as thermopiles[71], exploiting the thermoelectric effect, followed by the earliest bolometers, wherein absorption of thermal radiation causes change in the absorber's electrical resistance. Since then, thermal detector technology has developed mostly around these two physical phenomena as well as the pyroelectric effect[5], which exploits the spontaneous electrical polarisation (and the resultant voltage) of certain crystals in response to a temperature gradient. Because thermally induced processes show no (or very little) wavelength dependence, signal quality is generally flat across the absorption spectrum and instead is primarily driven by the magnitude of temperature change in response to incident flux intensity[5]. It is due to this primary mechanism that thermal detectors are much slower than photon ones, characterised by responses measured in milliseconds as well as low detectivity, especially at higher frequencies[72]. Despite these limitations, however, thermal detectors have found widespread use in applications where low cost, simple design and room temperature operation are more important than high speed performance and signal quality; in addition, more recent developments in 2D array technology have seen improvements to some of their figures of merit[5].

3.2 Group IV-VI: lead salts

The development of intrinsic lead salt (eg. sulphide and selenide) single-element detectors in the first half of the 20th century signalled the ascent of IR photon detector technology. These photoconductive systems, whose wavelength range has eventually been extended to 1-7 μm[73], with corresponding D^* values of up to $\sim 10^{12}$ cmHz$^{1/2}$W^{-1} in the SWIR region (Figure 3.2), have nevertheless suffered from several drawbacks, such as poor uniformity of photoresponse and significant $1/f$ noise[74], although they also offer the advantage of low cost, simple design and high-T background-limited performance[73]. Theoretical understanding of lead salt structures[73] as well as improved manufacturing methods of linear arrays aimed at addressing performance issues[74] continue to be developed.

3.3 Group II-VI: HgCdTe (CMT)

The HgCdTe (cadmium-mercury-telluride, or CMT) material was first manufactured in the late 1950's and was the first intrinsic, direct-bandgap alloy with a highly tunable wavelength of 0.7-25 μm (see Figure 3.1), spanning all useful atmospheric windows[8] (see Figure 1.2). Because of its considerable advantages over other technologies available at time, the CMT system has seen major investment ever since and has evolved into the most widespread and best-performing IR technology in the industry[7,75].

General properties

The alloy has a number of favourable properties that directly arise from its zinc-blende structure, such as the aforementioned extremely tunable direct bandgap, the resultant sharp onset of the absorption coefficient above E_g (see Figure 3.3), and Auger-limited dark current behaviour that leads to high operating temperatures[7]. HgCdTe photodiodes demonstrate background-limited (BLIP) operation at temperatures higher than other materials and structures[7]. In addition, unlike the lead salt systems, the CMT alloy does not suffer from large thermal expansion coefficients (which would compromise crystal quality) and has a moderately low relative permittivity ϵ[8]. The effect of the latter means that HgCdTe has an average index of refraction, as well as competitively short integration times and low junction capacitances compared to other materials[10]. Compared to most other IR-sensitive alloys, the bandgap of HgCdTe shows remarkable sensitivity to the lattice constant (as can be seen when comparing group III-V alloys to HgCdTe in Figure 3.1): a change in a of about 0.3% (at a given T) is sufficient to shift the cut-off wavelength from SWIR to the VLWIR regime. Because HgTe is semi-metallic (ie. its valence band is marginally elevated above the conduction band), in theory the CMT bandgap can be arbitrarily small, however this has not been significantly exploited beyond 25 μm[8]. The electron mobility of CMT is a function of composition and temperature, and behaves favourably when compared to other detector materials. The minority carrier lifetime τ due to different mechanisms in HgCdTe is doping- and temperature-dependent, but is generally of the order of 10^{-6} to 10^{-5} s, with typical $\tau_{SRH} > 5$ μs and $\tau_{SRH} > 30$ μs reported respectively for LWIR and MWIR n-doped high quality HgCdTe[6].

The absorption coefficient α of a number of samples spanning the SWIR-LWIR range collated by Li et al[76] can be seen in Figure 3.3. Although there is some evidence of sub-bandgap absorption due to tail in density of states[77], the overall behaviour and magnitude of α_{HgCdTe} is typical of direct narrow-bandgap semiconductors.

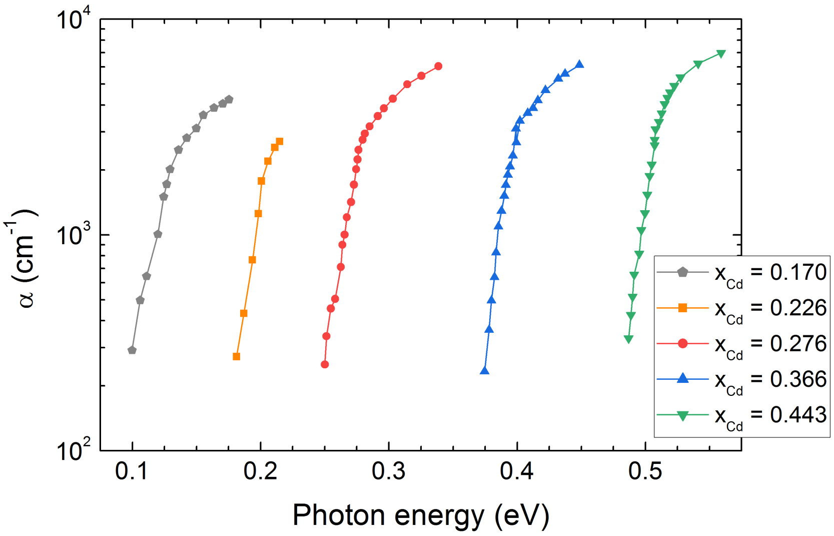

FIGURE 3.3: HgCdTe absorption coefficients as a function of x_{Cd} at $T =$ 300 K (data adapted from Li et al[76]).

J_d and Rule 07

High-quality intrinsic CMT material is naturally diffusion-limited with the Auger 1 and 7 mechanisms responsible for the recombination-generation processes. Because of the extensive development of CMT manufacturing and growth techniques, CMT detectors have become a benchmark for dark current (J_d) performance, and in order to enable convenient comparison of a given detector technology to that of CMT, Tennant et al[78] have derived the so-called Rule 07: a heuristic dependence of the Auger-limited diffusion current in a high-quality n-doped ($\sim 10^{15}$ cm^{-3}) HgCdTe on its cut-off wavelength $\lambda_{cut-off}$ and temperature. The fit was empirically derived from state-of-the-art Teledyne process evaluation chip (PEC) diodes and focal plane arrays (FPA) and has since been adopted as a popular reference for dark current performance[62,79]. This J_d is calculated using

$$J_d = J_0 exp\left(C\frac{1.24q}{k\lambda_e T}\right) \tag{3.1}$$

where fit parameters (here rounded to 4 s.f.) are $J_0 = 8367$ Acm^{-2} and $C = -1.163$. λ_e is conditional such that

$$\lambda_e = \begin{cases} \lambda_{cut-off} & \text{for } \lambda_{cut-off} \geq \lambda_{threshold} \\ \frac{\lambda_{cut-off}}{1-(\lambda_{scale}/\lambda_{cut-off}-\lambda_{scale}/\lambda_{threshold})^P} & \text{for } \lambda_{cut-off} < \lambda_{threshold} \end{cases} \tag{3.2}$$

where the second condition is specifically set up to fine-tune the fit below $\lambda_{threshold} = 4.635$ μm, with $\lambda_{scale} = 0.201$ μm and $P = 0.5441$ being additional fit parameters. Since its implementation, Rule 07 was reviewed by its author in 2010 in comparison to other extant HgCdTe technologies as well as Sb-based superlattices and nBn detectors, and concluded that it remains a robust performance benchmark[80].

Manufacturing and devices

Because of the stringent uniformity requirements, high-quality HgCdTe materials are necessarily manufactured using epitaxial methods, that is molecular beam epitaxy (MBE), metal-organic vapour phase epitaxy (MOVPE) and liquid phase epitaxy (LPE)[6,5], with the latter two being generally preferred for industrial growth[10]. The substrate of choice is the lattice-matched CdZnTe[81], however high costs, thermal incompatibility with the Si ROIC, and upscaling difficulties present challenges. Growth on Si, CdTe and sapphire has been reported[7] however dislocation density remains an obstacle for LWIR applications[6].

A photodiode (p-n junction) remains the main structure of choice for all CMT applications, and is compatible with both frontside and backside-illuminated focal plane arrays (FPAs). As can be appreciated from Figure 3.2, HgCdTe detectors tend to have detectivities approaching ideal performance; quantum efficiencies can reach 90% without anti-reflective coating[8]. Surface currents are suppressed by a combination of internal electric fields and appropriate passivation techniques, and junction tunnelling is controlled with appropriately low base (absorber) doping. In the highest-quality CMT p-n junctions at operating temperatures (77 and 200 K) the defect-induced SRH currents were considered all but eliminated two decades ago[7] thanks to progress in processing technologies, with dark current performance limited by Auger 1 diffusion and radiative recombination, the former of which is further suppressed in wider-bandgap SWIR and MWIR structures. However, under certain other conditions (eg. unoptimised doping, sub-77 K operation, metallurgical defects or high bias), non-fundamental current mechanisms such as trap-assisted and band-to-band tunnelling still emerge as the dominant current components[6,7].

Challenges

Despite its dominant position in the industry and very well established theory, the HgCdTe technology faces several limitations and hurdles for which other materials and systems have been proposed as solutions.

From a commercial standpoint, perhaps the most important challenge arises from the implementation of the United Nations' 2013 Minamata Convention, which seeks to restrict and eventually eliminate the toxic element Hg from industrial and commercial use, and of which the European Union is one of the signatories. Corresponding EU-level legislation has since been drafted and put into force in January 2018[11], increasing the attractiveness of non-Hg-based technologies for long-term investment, especially for non-military applications.

From a manufacturing point of view, one of the main difficulties is a side-effect of the otherwise highly advantageous bandgap tunability - because the bandgap shows extremely strong dependence on the lattice constant and therefore on x_{Cd} (see Figure 3.1), composition control becomes much more crucial as the cut-off wavelengths progress from MWIR to LWIR and VLWIR. As shown by Rogalski[7], a $x_{Cd} \pm 0.2\%$ variation results in a cut-off uncertainty of 0.023 μm for SWIR applications, and increases to 0.51 μm for LWIR; this poses an issue both for the uniformity of large area LWIR FPAs and any potential multi-colour devices[10,7]. Also, as mentioned before, the upscaling of FPAs is impeded by the large mismatch in thermal coefficients between the most commonly used CdZnTe substrate and the Si read-out circuits, which results in structural fatigue following multiple thermal cycles[7].

3.4 Group III-V

Group III-V semiconductors are a broad group of materials that present a number of potential alternatives to HgCdTe. A useful general property lies in the covalent nature of their atomic bonds[5,40,62], which are stronger than the ionic bonds characteristic of group II-VI, making group III-V materials more structurally robust[17].

3.4.1 Bulk InSb, $InAs_{1-x}Sb_x$ detectors

InSb

The narrow-bandgap InSb was one of the first III-V binaries to be developed in the 1950's for IR detection purposes[5]. InSb is an inherently MWIR material with a maximum response in the region of 5.0 μm at the standard operational temperature of ~ 80 K[72,82,83]; photovoltaic (PV) diodes achieve a D^* of about 10^{11} cmHz$^{1/2}$W^{-1} (as per Figure 3.2). The most popular method of InSb photodiode fabrication involves bulk n-type single-crystal wafers where a p-n junction is further created by ion implantation. This process results in a large (when compared to epitaxy) density of dislocations, making the best currently available InSb photodiodes SRH-limited[62]. In an effort to eliminate the implantation-induced damage, work has been done to demonstrate the viability of

MBE-grown InSb p-n junctions resulting in a factor of 17 decrease in J_d at the operational temperature[84].

InAs$_{1-x}$Sb$_x$

InAs$_{1-x}$Sb$_x$ is a direct-bandgap zinc-blende material with the smallest possible bandgap of all bulk III-V semiconductors[62], as can be seen in Figure 3.1. When examining the behaviour of InAs$_{1-x}$Sb$_x$ and HgCdTe on the same graph, it can be appreciated that InAs and InSb have much closer bandgap values than HgTe and CdTe, with the practical consequence that the InAs$_{1-x}$Sb$_x$ bandgap is far less sensitive to material composition and non-uniformity, making it an attractive alloy from the manufacturing standpoint. As explained in Section 2.1.2, compound alloys experience atomic displacement and bond angle relaxation which is not present in their constituent binaries and which has a non-negligible effect on bandgap energy[85]; as a result, simple linear interpolation is insufficient to calculate a compound bandgap and an additional band bowing parameter b_g is needed, as per Equation 2.7. The accepted value of b_g for InAs$_{1-x}$Sb$_x$ has evolved since the early reports of 0.58-0.60 eV, eventually understood to be underestimated due to a linear extrapolation of data taken only above 100 K[28]. Theoretical considerations have led to a value of 0.7 eV, recommended by Rogalski et al[86] derived using a k.p model, while a pseudopotential calculation by Wei et al[38] finds 0.65 eV, attributing most of the bowing to CB and using $E_{VB,InAs} = -0.50$ eV, a value that is generally no longer in use[28,40,42,68]. Experimental results by Fang et al[47] obtained from 10 K photoluminescence on a varied x_{Sb} sample series find $b_g = 0.67$ eV, but also note that a room temperature optical absorption measurement carried out by Stringfellow et al[87] was lower, about 0.6 eV. Elies et al[88] make a more explicit report of a temperature dependence of bowing parameters based on PL analysis. Other works similar to Fang from the period[28] put the overall range as $b_g = 0.64 - 0.69$ eV, which has resulted in Vurgaftman et al[28] recommending $b_g = 0.67$ eV as a composite value. This value, however, has since continued to creep upwards in a number of reports; Razeghi et al[89] reports 77 K bandgaps derived from photoconductive spectra that are consistently lower than the theoretical prediction. Lin et al[90] fit the bandgaps of a series of $x_{Sb} = 0.2 - 0.46$ PL samples grown on GaSb substrates with $b_g = 0.87$ eV. Svensson et al[49] extracted $b_g = 0.83$ eV from PL data reported by Yen et al[48], and presented evidence that the samples analysed by Lin et al are free from bandgap-reducing phase separation effects, supporting Lin's findings. This atomic ordering effect has been shown to decrease the overall bandgap of the alloy[38]; also, band filling effects and unaccounted-for residual strain and relaxation effects in the earlier reported samples could have contributed to the b_g spread, before lattice-matching and strain-relieving buffer layers were taken into account[62]. Webster et al[42] presented a temperature-dependent double-oscillator model to describe $b_g(T)$ between 4 and 300 K, derived based on PL data for a lattice-matched $InAs_{0.91}Sb_{0.09}$ structure and explicitly related it to its valence and conduction band positions with respect to $E_{v,InSb} = 0$ eV, which is why it is incorporated into the superlattice band alignment model used in this work, as discussed in Section 2.1.2.

From a technological standpoint, $InAs_{1-x}Sb_x$-based detectors suffer a number of setbacks. The same weak dependence on lattice constant that makes the bandgap resistant to variation in composition also means that lattice-matching $InAs_{1-x}Sb_x$ to a commercially viable substrate is not trivial. The cheap Si and GaAs substrates cannot be matched at any x_{Sb}, while GaSb is naturally lattice-matched at $x_{Sb} = 0.09$, with the resultant bandgap of 325 meV at 77 K, or about $\lambda_{cut-off} \approx 4$ μm. The emergence of ternary substrates such as InGaSb and AlInSb could alleviate this issue[62,91], however these are not yet commercially available. Nevertheless, a number of photodiode devices have been demonstrated. One of the most significant developments was the broadband MWIR $InAs_{1-x}Sb_x$ homojunction diode grown on GaSb using liquid phase epitaxy (LPE), as reported by Bubulac et al[92], with $R_0A \sim 10^9$ Ωcm^2 at 77 K (indicating low dark currents), and external quantum efficiency of $\sim 65\%$. Other architectures have been introduced since, such as 3-5 μm p-i-n diodes, where the narrow-bandgap $InAs_{1-x}Sb_x$ absorber is 'sandwiched' between heavily doped wide-bandgap materials; Remennyy et al[93] report a $D^* \sim 2 \times 10^{11}$ cmHz$^{1/2}$W^{-1} at room temperature. A series of InAsSbP/$InAs_{0.9}Sb_{0.1}$ double-heterojunction photodiodes were also LPE-grown by

Brunkov et al[94], resulting in negligible leakage currents at $T > 190$ K and D^* varying between 6×10^{11} and 8×10^{8} cmHz$^{1/2}$W^{-1} at 77 and 300 K correspondingly. Away from p-n junction variants, incorporation of $InAs_{1-x}Sb_x$ into the so-called nBn structure has also generated interest, and is further discussed in Section 2.2.1.

3.4.2 Strained-layer superlattices

Superlattices were first proposed in 1970 by Esaki and Tsu[95] as a one-dimensional periodic potential with a period shorter than the electron mean free path, which they predicted would result in the division of the dispersion relation into a number of forbidden gaps and minibands. They proposed this periodic potential could be created with varied doping or heterostructures. Type-II (see Figure 2.5 for SLS band alignment types) $In_{1-x}Ga_xAs/GaSb_{1-y}As_y$ superlattices with their highly tunable band structure were proposed a few years later[96], closely followed by the InAs/GaSb system whose bandgap was tunable via layer thicknesses rather than composition[97]. The realisation of strained-layer (rather than lattice-matched) superlattices expanded their potential applications to lattice-mismatched material configurations: strain up to 7% could be accommodated so long as the layers were kept under critical thickness h_c, and for superlattices grown beyond h_c appropriate strain-relieving buffer layers could be employed[21]. An HgTe/CdTe superlattice (so-called type III) was also proposed[98], with the associated advantages of shorter tunnelling wavelength when compared to bulk HgCdTe (suppressing junction tunnelling in p-n diodes), a bandgap less sensitive to growth variations due to its dependence on layer thickness and not composition, and reduced cross-plane diffusion currents due to larger effective carrier masses. Nevertheless, the system still faces several drawbacks: high interdiffusion coefficient of HgTe could be an issue at temperatures required for high-T device processing steps, such as passivation; a critical thickness of ~ 80 nm when grown on CdZnTe; and the large effective masses in HgTe, imposing constraints on layer thicknesses required to sustain carrier transport[6]. Instead, type-II antimonides have emerged as the most promising superlattice systems[6,10,62], of which InAs/GaSb is currently the most ubiquitous[6,62], while

InAs/InAs$_{1-x}$Sb$_x$ is expected to hold a number of advantages as its development progresses.

InAs/GaSb strained-layer superlattices

The potential of the type-II superlattice as an IR detector structure was already recognised in the the 1970's. The InAs/InGaSb system originally generated a lot of interest[40,62], however it has also faced hurdles in the form of critical thickness limitations due to strain in the ternary, numerous growth and processing challenges[7] such as difficulty of controlling the In fraction, and poor carrier lifetime and quantum efficiency[62], and so since the 2000's this led to increased interest in the binary system instead[9,10]. The InAs/GaSb system is an example of a 'broken gap' band alignment: the valence band of GaSb lies above the conduction band of InAs, while the physical carrier confinement in separate layers is achieved by modulating the superlattice period, and hence the carrier minibands (see Figure 3.4).

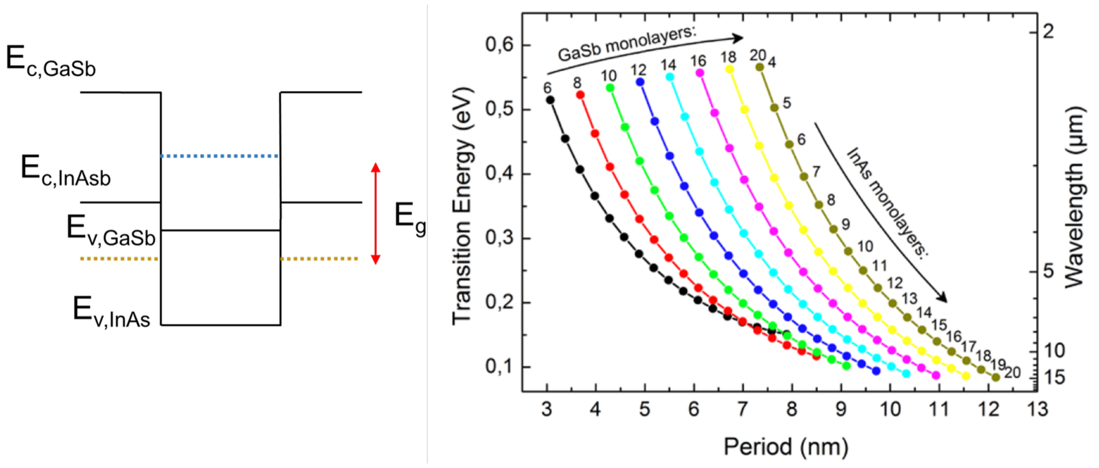

FIGURE 3.4: Left: the type-II 'broken gap' band structure of the InAs/GaSb superlattice. The orange and the blue lines denote fundamental carrier miniband positions and E_g is the corresponding transition energy. Right: the dependence of this transition energy on the superlattice period. Figure from Rutz et al[3].

The naturally small resultant bandgaps (as well as theoretically suppressed dark currents) lend themselves well to LWIR applications, and it is $\lambda = 8.3$ and 15.5 μm where most of the research has concentrated[10]. LWIR p-i-n photodiodes at 8.0 μm have been demonstrated eg. by Mohseni et al[99], who utilised AlSb barrier layers to achieve a peak responsivity of $\sim$ 1.2 A/W and thermally limited detectivity of $\sim 10^{11}$ cmHz$^{1/2}$W^{-1} at 80 K; a very similar structure (but without AlSb) was shown by the same author[100] to achieve $D^* \sim 10^8$ cmHz$^{1/2}$W^{-1} at room temperature, with the R_0A product two orders of magnitude higher than that of equivalent HgCdTe. High wafer uniformity and LN_2-cooled LWIR performance are desirable properties for large FPAs used in space applications; to that end, Plis et al[101] implemented a PbIbN architecture resulting in $R = 1.8$ A/W at $V = -0.25$ V, $J_d = 1.2$ mA/cm^2 and a QE of 23%. In the same publication, a dual-colour (5 and 10 μm) pBp detector is demonstrated at 77 K with QE of 39 and 17% respectively.

FIGURE 3.5: Dual-colour (4/5 μm) image from an InAs/GaSb SLS camera, identifying a CO_2 leak. Image from Rutz et al[3].

Tuning the InAs/GaSb bandgap for MWIR applications requires increasingly thinner periods, which can cause interface degradation: Haugan et al[102] show that as the period thickness of MBE-grown superlattices reduces from 50 to 17 Å, the FWHM of PL peaks increases and TEM shows more poorly defined interfaces. Nevertheless, development of single-pixel devices followed the LWIR work, resulting in photodiodes with $\lambda_{cut-off} = 5.3$ μm and $D^* \sim 10^{13}$ cmHz$^{1/2}$W^{-1} at 77 K[103], and room-temperature MWIR devices with $D^* \sim 10^9$, $R \sim 1$ A/W and 25% QE. Proof-of-concept dual-colour MWIR-MWIR CO_2 cameras with stacked architecture have also been demonstrated[3]; a resultant image with a characteristic CO_2 trace can be seen in Figure 3.5.

A comprehensive comparison of LWIR InAs/GaSb-based devices at 77 K found in literature to Rule 07 discussed in Section 3.3 was carried out by Rhiger[79], who extracted dark current densities of non-barrier structures from their R_0A figures, and adopted the operational bias J_d of the barrier structures. This summary can be seen in Figure 3.6. The reduction in J_d in barrier structures is evident, and a testament to their current-suppressing properties. A convergence of the experimental data with Rule 07 is also observed at higher $\lambda_{cut-off}$; the author proposes that this is due to the Auger diffusion current (which varies as $\propto n_i^2$) becoming dominant at lower bandgap values (since the SRH current varies as $\propto n_i$).

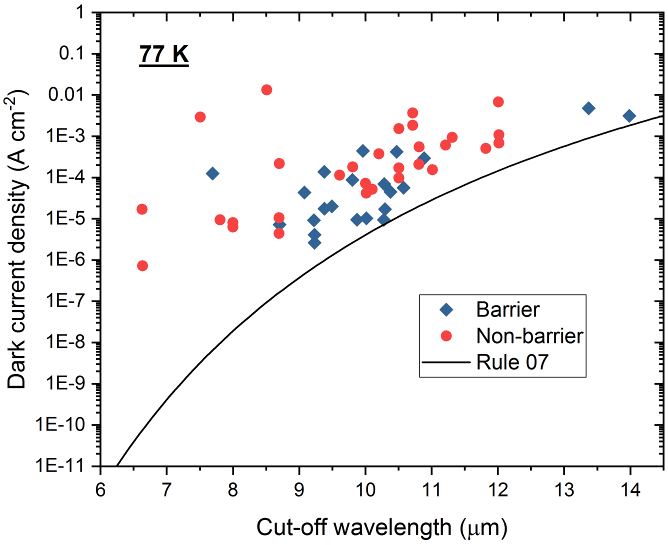

FIGURE 3.6: Dark current density of barrier and non-barrier InAs/GaSb T2SL devices found in literature, compared to Rule 07. Data collated by and adapted from Rhiger[79].

Challenges

Although the InAs/GaSb T2SL system is projected to match and even exceed the performance of bulk HgCdTe[79], in reality there are a number of issues still to be addressed. As can be appreciated in Figure 3.6, both barrier and non-barrier architectures suffer from elevated dark currents, especially when approaching the MWIR regime, which indicates presence of a non-negligible trap-assisted SRH component. According to Plis et al[9], the physical origin of this current can be understood in the context of the defect formation energy of native defects in both InAs and GaSb: Walukiewicz[104] showed that the participation of native defects in creating free carriers depends on the position of the so-called Fermi level stabilisation energy with respect to the Fermi level. This energy level is then shown to lie just above the conduction band in InAs, but in GaSb and GaAs its position is near the valence band to midgap - enabling these states to act as recombination centres. Connelly et al[105] confirm this proposition by carrying out time-resolved photoluminescence on a series of InAs/InGaSb superlattices, and establishing a presence of a native trap state in InGaSb located below the intrinsic Fermi level of the superlattice and 60±15 meV above the valence band maximum. This has direct implications for carrier lifetime in the InAs/GaSb T2SL.

Svensson et al[13] carried out an extensive investigation of InAs and GaSb minority carrier lifetimes by examining the following factors: the interface density, the substrate growth temperature for both binaries and the T2SL, and interface engineering. The first is shown to have no significant effect on the carrier lifetime, contrary to the expectation that the crystal quality would degrade the most at interfaces, as seen in Figure 3.7; instead, slight lifetime degradation is observed with increased GaSb thicknesses, suggesting that the recombination centres are located in the bulk material instead.

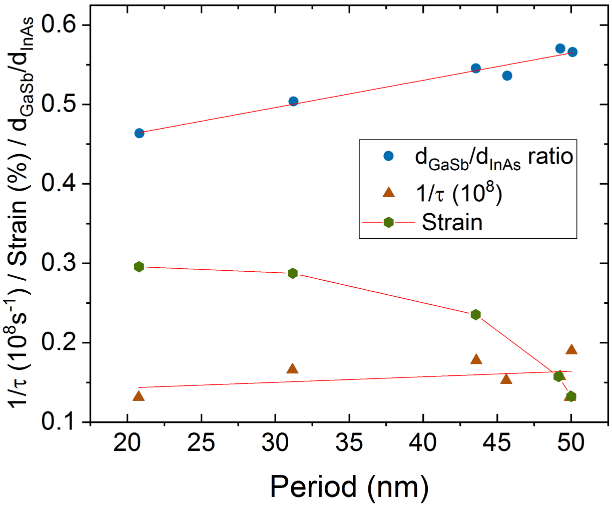

FIGURE 3.7: The effect of InAs/GaSb interface density on carrier lifetime τ and residual strain in the superlattice. Figure adapted from Svensson et al[13].

The investigation of bulk lifetimes as a function of growth temperature (Figure 3.8 top graph) supports this assertion: τ_{InAs} is about 3 times higher (typical lifetimes of the MWIR and LWIR InAs/GaSb structures are included for comparison). By using XRD FWHM as a figure of merit for the test superlattices, optimal growth temperature range is also idenfitied (Figure 3.8 bottom graph), the significance of which lying in the fact that this range does not align with the optimal binary growth temperature, represented in the graph by the dotted area.

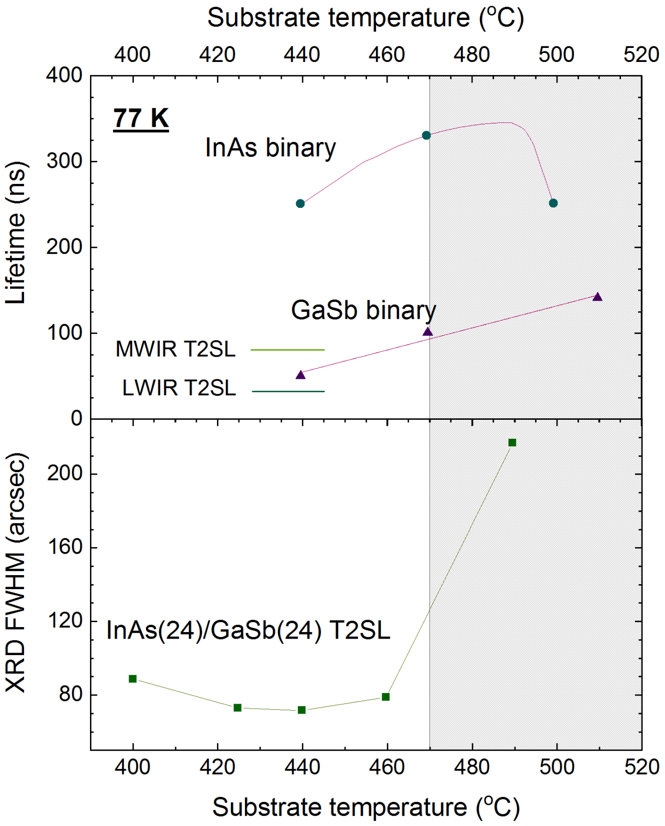

FIGURE 3.8: [The effect of substrate growth temperature on, top: the minority carrier lifetime in bulk InAs and bulk GaSb (with typical SLS lifetimes included as reference); bottom: the XRD FWHM of InAs/GaSb superlattice 0th order peaks. The dotted area represents optimal binary growth temperatures. Figure adapted from (Svensson).

Based on these findings, the authors conclude that native defects in GaSb are likely to be the primary mediator of SRH current (InAs is considered less likely due to the insensitivity of τ_{InAs} to whether it is grown with As_2 or As_4), causing the low minority carrier lifetimes observed in InAs/GaSb superlattices, ranging from 0.13[106] to about

100 ns at 77 K[16]. Photodiodes featuring InSb-based interface engineering have recently pushed this value up to 157 ns (at 6 K)[107], demonstrating the relevance of interface engineering for this system as discussed below.

Because T2LS in general relies on spatial carrier separation for its dark current performance, high quality interfaces are needed to prevent trap-assisted tunnelling[12]. Seeing that a total change in composition occurs at the InAs/GaSb interface, eliminating interfacial disorder in MBE growth is a non-trivial task and a lot of work has been dedicated to optimising the growth procedure, primarily with the goal of creating InSb and GaAs interfaces. Thibado et al[14] distinguish between roughness (variations in topography at the interface, such as islands and pits) and intermixing (like diffusion and exchange reactions), and use scanning tunnelling microscopy to study MBE-grown superlattice to conclude that surface roughness (especially on the Sb-terminated GaAs interface) causes the most disorder; they note, however, that their results are at odds with other reports, and that this is likely due to different growth conditions. This primary dependence of InAs/GaSb interface quality on specific growth parameters (rather than more fundamental principles) is a recurring observation in literature[9,13,102], a situation additionally complicated by the fact that engineered interfaces in the InAs/GaSb superlattice are also used to manage strain[108] and therefore Auger suppresion[9].

InAs/InAs$_{1-x}$Sb$_x$ strained-layer superlattices

The first Ga-free III-V superlattice to be proposed in the 1980's was InAs$_{0.40}$Sb$_{0.60}$/InAs$_{1-x}$Sb$_x$, as a LWIR alternative to bulk HgCdTe with a longer cut-off wavelength than bulk InAs$_{1-x}$Sb$_x$[109]. InSb/InAs$_{1-x}$Sb$_x$ superlattices were also demonstrated, exhibiting LWIR type-II behaviour; however, although both photoconductive and photovoltaic devices were implemented, interest was eventually shifted to the InAs/InGaSb system due to its smaller period thickness required to reach LWIR, and the resultant increased wavefunction overlap needed for enhanced absorption[40]. Strain-balancing also presented a challenge[5].

The first InAs/InAs$_{1-x}$Sb$_x$ superlattices were grown by MOCVD and MBE in the 1990's[40], reporting lower PL peak energies than that of bulk $InAs_{1-x}Sb_x$. Zhang et al[110] demonstrated the viability of $x_{Sb} = 0.09$ structures grown on InAs for use in midwave (~ 3.4 μm) infrared lasers; light-emitting diodes grown on mismatched GaAs substrates were shown to operate at room temperature at emission wavelengths up to 10 μm[111]. A proposition to utilise the superlattice as an IR detector was made by Zhang et al[112].

Advantages

The typical advantages expected from T2SL superlattices in general are also present in $InAs/InAs_{1-x}Sb_x$. Suppression of Auger 1 and 7 mechanisms (the former of which limits the performance of CMT) arises naturally from the band structure type as discussed in Section 2.2.2. Just like type-III superlattices discussed in Section 3.4.2, T2SL also demonstrates higher than bulk (including HgCdTe) effective carrier masses in the growth direction, lowering band-to-band tunnelling currents[6,75]. Because the fundamental transition in T2SL occurs between the conduction band of material 1 and the valence band of material 2, the bandgap is independent of the bulk band structure of either and can be more easily engineered. $InAs/InAs_{1-x}Sb_x$ also does not suffer from the same interdiffusion issues as HgTe/CdTe[6,62,75] (see Section 3.4.2), and can be strain-balanced on the widely available GaSb substrate.

The interest in the $InAs/InAs_{1-x}Sb_x$ system as an alternative to InAs/GaSb arose largely in response to the limited minority carrier lifetimes originating in the GaSb layers, as discussed in Section 3.4.2. This is an intrinsic property of the Ga-containing alloys due to the presence of a mid-gap trap level[105]. In contrast, pressure-dependent photoluminescence measurement of $InAs/InAs_{0.86}Sb_{0.14}$ has provided evidence for a native defect level located 180±10 meV above the InAs conduction band[113], effectively disabling it as a centre for SRH recombination. Multiple minority carrier lifetime measurements of $InAs/InAs_{1-x}Sb_x$ confirm this in practice (here, the total carrier lifetime is $\tau^{-1} = \tau_{SRH}^{-1} + \tau_{rad}^{-1} + \tau_{Auger}^{-1}$, where the subscripts refer to the corresponding mechanism). Steenbergen et al[15] carried out time-resolved photoluminescence (TRPL) measurements of a LWIR $InAs/InAs_{0.72}Sb_{0.28}$ superlattice to find a maximum lifetime of

412 ns at 77 K (a combination of both τ_{rad} and τ_{SRH}), an order of magnitude increase over comparable InAs/InGaSb structures at the time, and even bulk InAs due to T2SL suppression of radiative recombination. The mechanisms dominating τ in a MWIR superlattice were also studied by Hoglund et al[114] who observed an increase in lifetime from 1.8 to a maximum 2.8 μs between 77 and 200 K, pointing to radiative recombination; beyond 200 K, τ decreases due to the Auger mechanism. The same author also reported on lifetime dependence on carrier concentration in the superlattice, observing a decrease in τ from 3.6 to 1 μs between 2×10^{15} and 4.4×10^{15} cm^{-3} at 77 K, while associated temperature-dependent measurements confirmed once again the mostly radiative nature of the process[115]. Lin et al[116] studied the effect of p-doping on τ in LWIR superlattices at 77 K: an undoped SLS resulted in a lifetime of 450 ns , $n_p = 6 \times 10^{16}$ cm^{-3} yielded 45 ns and 3×10^{17} cm^{-3} resulted in 8 ns. It is also noted that an InAs/GaSb SLS structure with a similar bandgap reaches a lifetime of 45 ns at a doping of 1×10^{16} cm^{-3}, which means that in addition to intrinsically higher carrier lifetimes, Ga-free superlattices can be doped to higher concentrations without as significant degradation of τ.

While the natural enhancement of τ is the primary source of interest in InAs/InAs$_{1-x}$Sb$_x$, other practical advantages are also proposed. The Ga-free T2SL does not require complicated interface engineering steps in order to manage strain or interface disorder, which simplifies growth (while most of the III-V SLS growth has occurred via MBE, Huang et al[117] demonstrated that high-quality InAs/InAs$_{1-x}$Sb$_x$ is simpler to grow via MOCVD as well). InAs/InAs$_{1-x}$Sb$_x$ can also be more readily strain-balanced on GaSb through simple variation of the monolayer number ratio of the constituent materials (as can be appreciated from Figure 3.1), eliminating the need for strain-relieving layers. Finally, since E_g is primarily determined by x_{Sb}, the choice of d_{SLS} is not constrained by the required cut-off wavelength and can be decided on other merits instead, as discussed further in Section 5.1.

Challenges

While the carrier lifetime results for InAs/InAs$_{1-x}$Sb$_x$ are promising, the system also has some drawbacks when compared to InAs/GaSb. Because the band offsets in the former are much smaller while the effective carrier masses of the two are comparable, this could potentially lead to larger tunnelling currents[62]. The absorption coefficient α near the bandgap is generally projected and observed to be lower than that of an InAs/GaSb detector for the same cut-off wavelength, due to a thinner ternary layer where the hole confinement occurs, leading to a lower wavefunction overlap. Grein et al[69] use the k.p model to consider 'ideal' InAs/InAs$_{1-x}$Sb$_x$ and InAs/InGaSb detectors for LWIR applications, and find a near-bandgap α of 1500 and 2000 cm^{-1} respectively; Klipstein et al[118] simulated barrier architecture devices with $\lambda_{cut-off} = 10$ μm incorporating both superlattices to find consistently lower quantum efficiencies due to the same factor. One way of improving the absorption performance of a superlattice is to increase the ratio of the hole well thickness to d_{SLS}[119]; this ratio is normally constrained by strain-balancing considerations, and would require a different substrate to GaSb. Otherwise, the more feasible path to improving detectivity of InAs/InAs$_{1-x}$Sb$_x$-based devices lies in minimising dark currents instead.

InAs/InAs$_{1-x}$Sb$_x$ photodiodes

Compared to InAs/GaSb-based devices, incorporation of InAs/InAs$_{1-x}$Sb$_x$ into photodiode architecture has seen less interest. A MWIR InAs/InAs$_{0.65}$Sb$_{0.35}$ diode with $\lambda_{50\%} = 5.4$ μm was demonstrated by Schuler-Sandy et al[41], grown on a GaSb substrate with doping densities of 4×10^{18} cm^{-3}. The peak responsivity, reported at 77 K and -10 mV, was 0.64 A/W, corresponding to a QE of about 20%; dark current density measured under the same conditions was 2.1×10^{-4} Acm^{-2}, which the authors note to be higher than the best MWIR InAs/GaSb-based p-i-n diodes at the time. Very low activation energies were found at all temperatures, despite the expected advantage of higher carrier lifetimes. In general, the authors propose that the poorer J_d performance could

be explained by lower than InAs/GaSb band offsets, leading to tunnelling currents (although it is worth noting that at 14 ML/12 ML thickness ratio of the constituent layers, the superlattice is not strain-balanced for $x_{Sb} = 0.35$).
A VLWIR InAs/InAs$_{0.59}$Sb$_{0.41}$ photodiode was presented in 2014 by Hoang et al[120], featuring a lightly p-doped active region ($\sim 10^{15}$ cm^{-3}) with a 35 ML/12 ML thickness ratio, resulting in $\lambda_{50\%} = 14.6$ μm at 77 K. Maximum responsivity was achieved at -150 mV, saturating at 4.8 A/W which corresponded to a QE of 46%. With a dark current density of 0.06 - 0.7 A cm^{-2} for -50 and -300 mV bias respectively, the D* value was reported to be 1.4$\times$10^{10} cmHz$^{1/2}$W^{-1}. Above 50 K the device exhibited an activation energy of $\sim$ $^1/_2E_g$, indicating SRH-limited behaviour.

3.5 nBn detectors

Ever since the viability of the nBn detector structure was demonstrated in 2006 by Maimon and Wicks[60] using an InAs absorber layer, efforts have been made to incorporate it into viable MWIR and LWIR detectors. nBn devices incorporating lattice-matched MWIR InAs$_{1-x}$Sb$_x$ absorber and an 0.5 μm AlAsSb barrier, experimentally demonstrated by Klipstein et al[64], showed diffusion-limited current behaviour at biases below -0.2 V and above the lowest resolvable temperature of 150 K. At 150 K, J_d was 8×10^{-8} A cm^{-2} for a sample with a doping of 1.5$\times$10^{17} cm^{-3}; a sample with 4$\times$10^{15} cm^{-3} doping density had a comparable J_d of $\sim 10^{-7}$ A cm^{-2}, and the corresponding responsivities varied between $\sim$0.7 and 1 A/W. Based on these findings, the authors went on to incorporate InAsSb nB$_n$n architecture into 'Kinglet', a commercialised 640$\times$512 4.2 μm focal plane array with an operational temperature of 150 K[121].
The InAs/GaSb superlattice structure was first incorporated into an nBn by Rodriguez et al[122], who reported room temperature D^* of 10^9 cmHz$^{1/2}$W^{-1} and a QE of 18% for a cut-off wavelength of 4.5 μm, a value comparable to state-of-the-art InAs/GaSb p-i-n diodes at the time. Kim et al[123] demonstrated an InAs/GaSb 320$\times$256 MWIR focal plane array operating at 77 K and bias of 0.7 V, with QE approaching 50% near

$\lambda_{cut-off} \sim 4.2$ μm and a D^* of $\sim 6 \times 10^{11}$ cmHz$^{1/2}$W^{-1}. The authors note that despite lack of passivation treatment, the performance of their camera approaches state-of-the-art MWIR photodiodes that incorporate a passivation layer. This self-passivating behaviour of the nBn is more explicitly demonstrated by Bishop et al[124], who consider two InAs/GaSb nBn structures: one with the absorber exposed via wet etching, and one with a mesa etch terminating at the barrier, and show that the latter structure demonstrates dark current densities lower by two orders of magnitude.

The nBn structure is also believed to be advantageous for HgCdTe material growth, by eliminating issues associated with p-type doping[7]. Both modelling[125] and experimental work[126], however, have indicated presence of a large valence band offset at the barrier interface arising due to iodine diffusion from the surrounding layers into the barrier[125], necessitating high operational bias voltages and resulting in activation of trap-assisted and band-to-band tunnelling currents which impede the overall performance. A possible solution, which lies in p-doping the barrier, is currently under investigation[17].

3.5.1 InAs/InAs$_{1-x}$Sb$_x$ nBn devices

nBn devices incorporating both MWIR and LWIR InAs/InAs$_{1-x}$Sb$_x$ have been devised. In 2012 Kim et al[127] demonstrated the first LWIR InAs/InAs$_{62}$Sb$_{0.38}$ nBn equipped with an InAs/Al$_{0.80}$Ga$_{0.20}$As$_{0.03}$Sb$_{0.97}$ T2SL barrier. The absorber layer had a superlattice period of 13.9 nm/4.5 nm, and was only unintentionally doped. The device was characterised at 77 K with $\lambda_{50\%} = 13.2$ μm, with a responsivity of 0.24 A/W and $D^* \sim 10^8$ cmHz$^{1/2}$W^{-1}, under -0.3 V bias and at 12 μm. Together with $J_d \sim 5 \times 10^{-4}$ Acm^{-2}, this combined to a QE of 2.5%. The authors note that the dark current performance is actually better than Rule 07, but that the device's limited optical performance still needed improvement.

In 2014, Haddaddi et al[128] reported an InAs/Inas$_{0.45}$Sb$_{0.55}$ structure with a modified barrier design wherein the T2SL is repeated within the barrier, but an additional thin layer of AlAs is inserted in the middle of each InAs layer, raising the effective conduction band. The monolayer ratio for the SLS was 28/7 and the barrier thickness was 500 nm; two samples with $d_{absorber} = 2$ and 6 μm were grown, with an absorber doping of 10^{16} cm^{-3}. Optical measurements, carried out at 77 K and -90 mV, revealed $\lambda_{50\%} = 10$ μm, and peak QE (at 8 μm) of 54% for the thick absorber (corresponding to 3.47 A/W responsivity) and half that for the thinner one. Specific detectivity (calculated using shot noise only) resulted in 2.8×10^{11} cmHz$^{1/2}$W^{-1}. The corresponding J_d was 4.4×10^{-4} A cm^{-2}. A year later, the authors reported extending this structure into a dual-colour device, where the top contact was replaced with a low-Sb MWIR absorber layer[129], with performance comparable to the best reported InAs/GaSb T2SL dual-colour detectors.

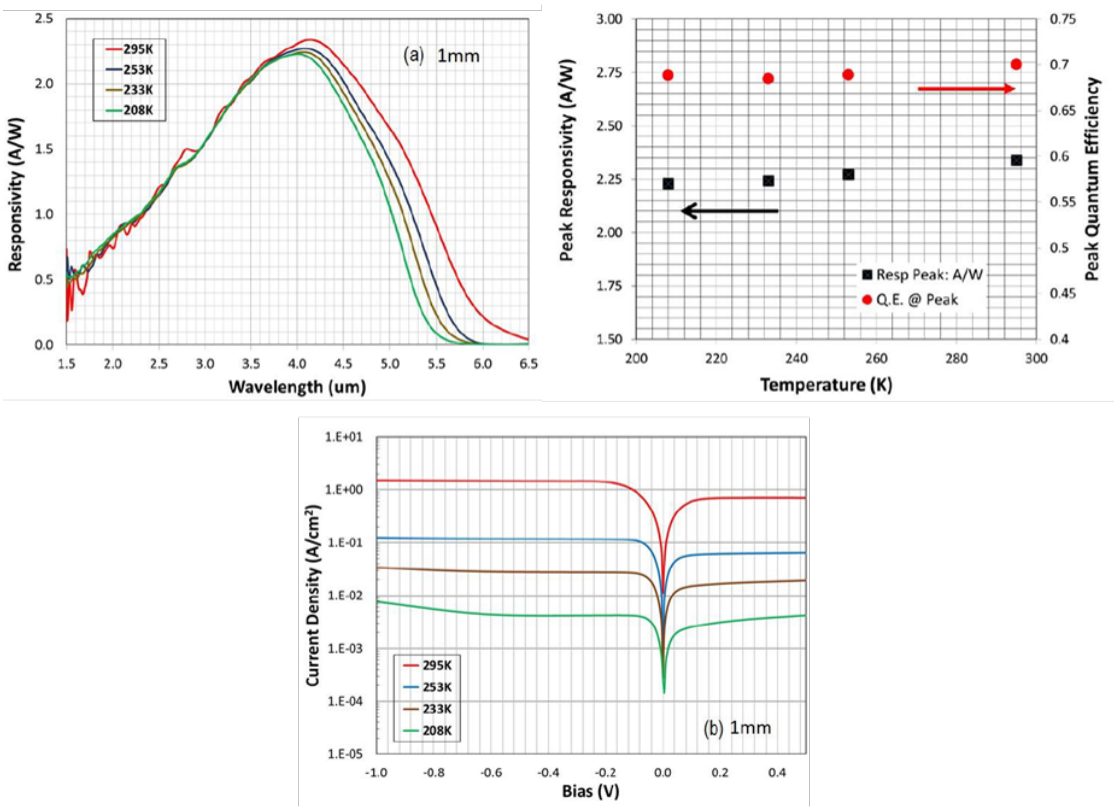

FIGURE 3.9: Responsivity, peak quantum efficiency and dark current density of MWIR InAs/InAs$_{1-x}$Sb$_x$ single-element nBn detectors by Teledyne Judson Technologies. Figures from Kim et al[130].

Recently, Teledyne Judson Technologies have proposed large-scale front-side illuminated discrete MWIR detectors based on InAs/InAs$_{0.6}$Sb$_{0.40}$ superlattices[130], showing $\lambda_{50\%} \sim 5.5$ μm at the (operational) room temperature. The demonstration devices were grown on GaSb substrates using the same monolayer number for both materials. Two detector sizes were manufactured, 0.25 and 1 mm; the former was measured to have $J_d \sim 1.48$ Acm^{-2}, and the latter demonstrated 1.17 Acm^{-2} at -0.3 V bias; diffusion-limited behaviour was achieved for temperatures above 120 K, with band-to-band tunnelling or surface leakage current dominating below that. With anti-reflection coating applied to the structures, their QE was reported as 72% derived from the peak responsivity (at 4.24 μm) of 2.47 A/W and corresponding to $D^* \sim 1.9 \times 10^9$ cmHz$^{1/2}$W^{-1} at room temperature (see Figure 3.9). The authors conclude that while the optical performance is good, the high dark currents should be minimised with further optimisation of passivation and device structure.

3.6 Summary

Historically, effective detection of light in the infrared spectrum has been mostly achieved with the use of the II-VI extrinsic semiconductor HgCdTe alloy, which became the material of choice in the 1970s after a period of competition with lead salt systems due to its favourable thermal expansion coefficient, better SRH lifetimes and lower RC constants[62]. In addition, HgCdTe is a ternary system with a band structure characterised by a direct, highly tunable bandgap spanning SWIR to VLWIR regimes and high absorption coefficients, while its carrier recombination mechanisms are Auger-limited and allow for high operating temperatures. The limitations of HgCdTe systems stem from technological rather than fundamental disadvantages. The weak ionic Hg-Te bond causes structural instabilities in the bulk crystal, poor interface control due to high interdiffusion and a decrease in uniformity and yield in larger arrays[7]. Because its fundamental bandgap is extremely sensitive to the alloy composition (as per Figure 3.1), small growth variations can further compromise wafer uniformity, especially in the LWIR and VLWIR regimes. Thermal compatibility with silicon ROIC also presents a challenge for the LWIR technologies. Finally, a major legal challenge emerges in the form of the United Nations 2013 Minamata Convention, which seeks to restrict and eliminate mercury from non-military applications[11].

In contrast to II-VI, III-V semiconductor crystals are characterised by the stronger covalent bonds leading to improved material robustness as well as finer interface and surface control enabling the use of heterostructures. Also, because of the considerable yield and pixel outage issues in HgCdTe focal plane arrays (caused by the aforementioned structural problems) which significantly increase their manufacturing costs, III-V-based IR detectors are projected to be cheaper[81]. The group of III-V materials suitable for MWIR to VLWIR detection is broadly termed antimonides, as the InSb and $InAs_{1-x}Sb_x$ are the binary and ternary alloys with the lowest optical bandgaps, where the latter can achieve LWIR operation. A manufacturing advantage of $InAs_{1-x}Sb_x$ is that its bandgap demonstrates a markedly lower (when compared to HgCdTe) sensitivity to the lattice constant, improving the optical uniformity of the wafer. A corollary to this, however, is that bulk $InAs_{1-x}Sb_x$ for LWIR applications presents a strain-balancing challenge due to a lack of suitable substrates beyond GaSb.

A strained-layer superlattice is a quantum heterostructure that addresses the strain-balancing issue (as strain is moderated by layer thicknesses) as well as a number of others. A type-II superlattice features physical carrier separation, leading to suppression of the Auger process (the natural limit of HgCdTe); increased carrier effective mass limiting band-to-band tunnelling; and tunable bandgaps independent of the bulk bandgap values. InAs/GaSb is a system that has generated interest due to its expected low dark currents and increased carrier effective masses; however, it has also encountered a fundamental hurdle in the form of low carrier lifetimes arising due to intrinsic defects in GaSb, as well as complex growth issues. The Ga-free superlattice $InAs/InAs_{1-x}Sb_x$ has been proposed as an alternative that simplifies interface engineering in MBE growth, and has also shown to possess increased carrier lifetimes thanks to elimination of the Ga-related defect centre.

The proposed benefits of the superlattice can be further extended by incorporating it into the nBn (n-doped-barrier-n-doped) structure. The unipolar architecture of the nBn eliminates the depletion region intrinsic to the diode structure, resulting in suppression of the Shockley-Read-Hall recombination mechanism. In addition, the majority-electron barrier further acts as a natural passivation layer by blocking both the electron dark current from the contact layer and across the mesa surface. Combined with Auger suppression, this approach could help close the gap between the dark current performance of III-V systems and HgCdTe[79]. Because HgCdTe has, over the years, achieved excellent optical and device performance, in order to capitalise on the proposed advantages of III-V materials in general and InAs/$InAs_{1-x}Sb_x$ nBn's in particular, their figures of merit (such as quantum efficiency, responsivity and dark current density) are still in need of improvement.

Chapter 4

Experimental Methods

The samples presented in this work were fabricated, processed and characterised almost entirely in-house. All fabrication proceeds with the use of molecular beam epitaxy, outlined in Section 4.1. X-ray diffraction measurements are then carried out in order to assess the structure and quality of the epitaxial layers (Section 4.2.1); in addition, two selected samples (XV0161 and XV0208) were imaged with transmission electron microscopy by Richard Beanland from University of Warwick (Section 4.2.2). Absorption properties of undoped superlattices grown on semi-insulating GaAs substrates were obtained using Fourier Transform Infrared spectroscopy above 77 K as outlined in Section 4.3, and photoluminescence measurements at 4 K (Section 4.4). Before the nBn samples can be characterised, they are first processed into a series of devices using standard cleanroom procedures as described in Section 4.5. Three characterisation methods are then used on the finished samples: a Fourier Transform Infrared spectrometer is employed to measure spectral response (Section 4.6.1), a simple blackbody source setup is used to obtain quantum efficiency (Section 4.6.2), and the dark current characteristics are obtained on a cryogenic probe station (Section 4.6.3).

4.1 Molecular Beam Epitaxy

Molecular Beam Epitaxy (MBE) is a method of material growth characterised by its advanced level of control over growth conditions and the resultant material structure. Its use of ultra-high vacuum (UHV) environment and precisely controlled molecular beam fluxes allow to control layer thickness and composition to a precision of several Å, which is orders of magnitude lower than methods such as liquid phase or vapour-phase epitaxy; and to produce very sharp material interfaces, with low background doping levels, at growth temperatures generally lower than other epitaxy methods[131]. All these factors are advantageous or necessary in epitaxial growth of superlattices due to their strict requirement for repeated thin layers with clearly defined interfaces.

The samples described in this work were grown in-house using VG V80-H and Veeco GENxplore MBE reactors, with all but one sample having been grown in the latter machine. As such, the description of the MBE process in this chapter will mostly be based on the Veeco system. It has a standard stainless steel structure comprising three chambers (separated by secure gate valves) that increase in vacuum quality: the loadlock, used for loading, initial outgassing, and unloading the substrates; the buffer chamber, used for further outgassing and wafer storage, typically held at $\sim 10^{-10}$ mbar in its rest state by an ion pump; and the UHV growth chamber, with a base pressure of $\sim 10^{-11}$ mbar.

The UHV conditions in MBE machines are required for two primary reasons: first, it is necessary to ensure that the mean free path of molecules is larger than the distance from the cell to the wafer, as defined by the geometry of the chamber (see Figure 4.1).

Secondly, it is necessary to avoid incorporation of contaminants into the wafer by ensuring that the source material deposition time is many orders of magnitude shorter than that of background vapour[132]. Combining these two factors results in typical growth chamber pressure of $\sim 10^{-11}$ to $\sim 10^{-9}$ mbar. Pumping is

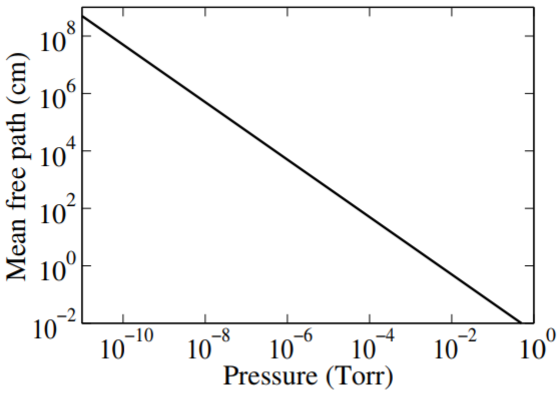

FIGURE 4.1: The mean free path of a nitrogen molecule as a function of background pressure. Figure from Rinaldi[132].

provided by ion pumps and a cryogenic pump; a cryogenic panel is also filled with liquid nitrogen during operation in order to act as particle trap for remaining background gases, and to thermally isolate the source cells.

One of the advantages of the MBE technology is that growth can be monitored in real time using a Reflection High-Energy Electron Diffraction (RHEED) system built into the growth chamber. In RHEED, a high-energy electron beam is emitted at a glancing angle towards the surface of the wafer, and its reflection is then incident upon a fluorescent screen. The condition for Bragg diffraction is fulfilled for a wafer surface with a periodic atom arrangement whose lattice constant is smaller than the wavelength of the electrons. This gives rise to a 'streak' pattern on the screen (see Figure 4.2) and indicates good crystallinity and smoothness of the layer being grown (the so-called Frank-van der Merwe growth). On the other hand, a spotty pattern indicates a rough (3D) surface for example due to cluster (Volmer-Weber) growth, relaxation, or faceting on the surface and is not a desired outcome for superlattices. It is, however, characteristic of oxide desorption in preparation for growth.

The type of crystal forming the topmost layer can be gauged from the so-called reconstruction. The crystal surface acts as a diffraction grating and so carries information about the reciprocal space structure of the surface (however, this is not equivalent to the k-space of the material because atomic bonds between surface atoms form under different energetic conditions to those inside bulk). For example, a 2×4 reconstruction pattern is characteristic of GaAs and InAs, 1×3 can be observed for GaSb and 2×3 for $InAs_{1-x}Sb_x$. The 2×3 characteristic of $InAs_{1-x}Sb_x$ growth can be seen in Fig 4.2.

As mentioned before, wafer preparation starts in the loadlock, where four quartz-lamp heaters are run at 200°C to remove contaminants introduced into the chamber and onto the wafer. The next step is to load the wafer into the heated station (using a hand-cranked lead screw for vertical movement and a magnetically coupled transfer arm for the horizontal axis), located in the buffer chamber, for further outgassing at 200-300°C. A good rule of thumb for GaAs and GaSb wafers (established by observing the ambient pressure in the buffer chamber while outgassing) is that it takes about 30-60

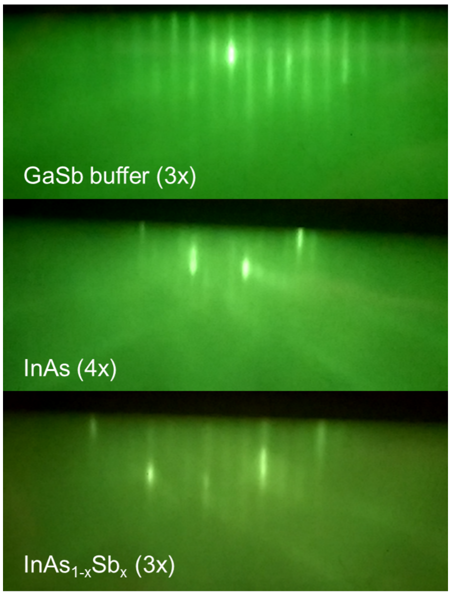

FIGURE 4.2: Example RHEED patterns obtained at various stages of growth.

minutes to outgas the wafers to a satisfactory level. Once the sample is ready for growth it is mounted on a sample holder in the growth chamber, which is typically rotated at 15 rpm to ensure uniform material deposition. The holder is made of molybdenum, which has a high melting point and a very low outgassing rate, and can accept wafers up to 3" in diameter. The final preparation step is thermal desorption of the wafer (ie. removal of the thin layer of oxide that forms on the wafer in contact with atmosphere) by briefly heating the substrate and observing a transition to a clear spot pattern on the RHEED screen, which indicates oxide removal from the surface. The samples in this work were grown almost exclusively on 1/4 n-GaSb and semi-insulating as well as n-GaAs substrates, for which actual desorption temperatures were as follows: 540°C for GaSb wafers, and 580°C for both semi-insulating and n-doped GaAs, with setpoint temperatures implemented using calibration methods described further in this Section. Solid source materials are stored in and thermally evaporated from crucibles inside effusion cells, arranged opposite the wafer holder (see Figure 4.3). For group III elements (Ga, In, Al) and the n-dopant material GaTe, flux (and therefore growth speed) is determined by cell temperature, while group V sources (As_4, Sb_4) are kept at constant temperature and instead the position of the valve is varied. However, the As_4 molecule has a low sticking coefficient of 0.5 or less, while that of the dimer As_2 approaches 1[131]; also, growth conducted with As_4 has been associated with a larger occurrence of deep electron traps in n-GaAs[133]. Because of this, a separately heated valved cracker is installed on both the arsenic and antimony cells, resulting in As_2 and Sb_2 beams. Layer thicknesses are controlled using shutters with low actuation time located in front of the cells. It is worth noting that the action of opening and closing a shutter can cause thermal transients on the group III material surface, due to the shutter acting as a reflector for thermal radiation, which in turn can affect superlattice growth rates due to their very short periods (however, it is unlikely to be an issue for group V materials, as they are thermally isolated from the shutters by their heated cracker zones).

The substrate itself is heated with the use of a radiation heater located above the wafer holder. The thermal output of the heater can be estimated with the use of a thermocouple, which is permanently bonded to a reference substrate located on its other side, albeit these setpoint readings are likely be offset from the real substrate temperature. As such, two additional calibrations are carried out: one, because desorption temperatures are known, it is possible to observe the offset between the setpoint and the real substrate temperatures. The second calibration method involves observation of the RHEED surface reconstruction pattern of GaSb transitioning from 2×5 to 1×3 under a constant Sb flux, which can be related to the absolute substrate temperature[134]. Together these two points are then fitted to create a real temperature dependence for a given substrate type.

It is worth noting that the sticking coefficients of group III materials can be approximated as 1 under the growth conditions used in this work; group V materials, however (here, As and Sb), have more complex sticking coefficients that are dependent on substrate temperature and are generally less than 1[135]. This has two implications. First, because of the complex relationship of group V sticking coefficients with growth conditions, the ratio of As to Sb in any given superlattice sample needs to be fine-tuned empirically over several repeated growths. The other consequence is that all group V-terminated surfaces require maintained group V flux whenever growth is not occuring,

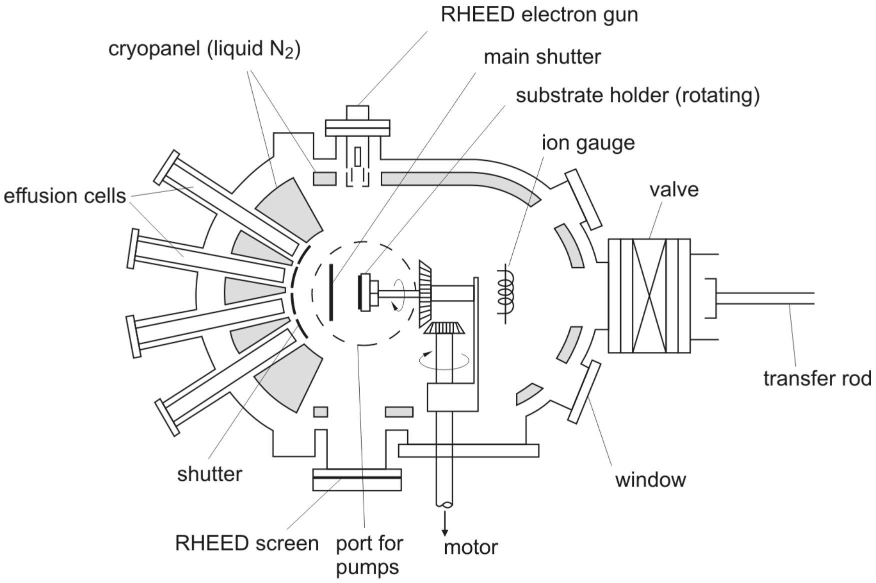

FIGURE 4.3: A top-down diagram of a generic molecular beam epitaxy growth chamber.

in order to replace any ’escaped’ molecules. For the specific case of $InAs_{1-x}Sb_x$ under AsSb flux, however, this can have the unintended consequence of slightly altering the As/Sb ratio of the surface monolayer. For a detailed description of growth optimisation of samples used in this work see Section 5.3.

4.2 Structure characterisation

This subsection details the X-ray diffraction and the transmission electron miscroscopy methods.

4.2.1 High-resolution X-ray diffraction

X-ray diffraction is a non-destructive method of characterising crystals, including compounds and heterostructures. It relies on the effect of X-ray photons being coherently (elastically) scattered off the surface of a crystal, in an effect called Bragg diffraction:

$$2d_{hkl}sin\theta_B = n\lambda \tag{4.1}$$

where d_{hkl} is the interplanar spacing of the cubic lattice (d_{004} for the symmetrical scan used in this work), θ_B is the Bragg angle (the angle between the incident beam and the lattice plane), λ is the wavelength of the incident X-ray photons and n is the diffraction order. In the so-called coupled $\omega - 2\theta$ scan, which scans parallel to the scattering vector in the reciprocal space, both the angle between the source and the sample ω, and the angle between the sample and the detector 2θ (see Figure 4.4) are varied such that $\omega = 0.5 \times 2\theta$. As such, because θ_B and λ from Equation 4.1 are known, it is possible to obtain $2d_{hkl} = a_0$ of the epilayer. Another structural parameter that can be accessed with a coupled $\omega - 2\theta$ scan is the period of the superlattice, which is calculated from the satellite peak separation arising as a result the superlattice periodicity.

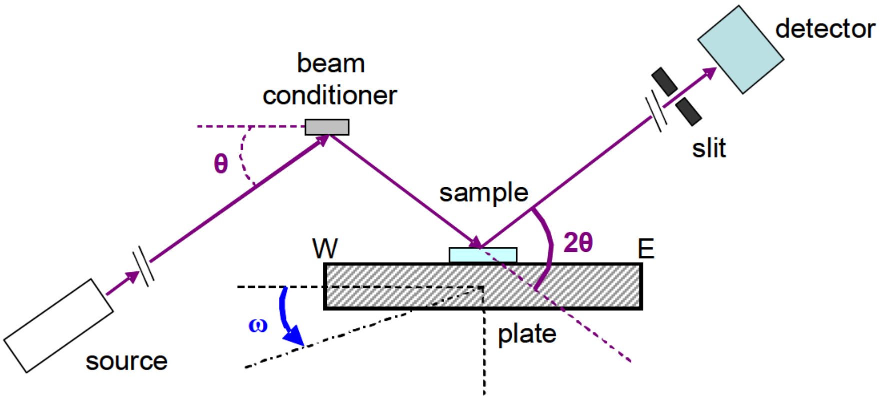

FIGURE 4.4: A side-view of the X-ray diffraction scanning apparatus.

The samples described in this work were characterised using a double-crystal Bede QC200 system. A hot filament acts as a source of electrons, which are accelerated by an electric field (usually set to $\sim$ 38 kV) and is incident on a copper target, producing two X-ray emission lines with wavelengths 1.541 Å and 1.545 Å, which are conditioned using a mirror. The scan is set up by calibrating the 2θ angle with respect to the substrate peak (here, either GaAs or GaSb), which then becomes the 0" reference point for resultant epilayer peaks. The other two calibration parameters are ω, used for further refining the substrate peak amplitude, and χ, the position of the sample stage perpendicular to the beam axis. Diffracted peak intensity is then recorded as a function of $\omega - 2\theta$, and the resultant spectrum is loaded into the RADS Mercury simulation software and compared to a model spectrum. The model input parameters, such as superlattice layer thickness, ternary and quaternary element ratios, and buffer layer relaxation (if applicable), are first estimated from growth conditions, then refined by comparing the modelled and experimental spectra. The expected structure is modelled using the Bede RADS software, while Bede PeakSplit is used to simulate the buffer layer peak positions with respect to the substrate.

4.2.2 Transmission electron microscopy

Transmission electron microscopy (TEM) is a method that uses electron diffraction across a sample to achieve sub-nanoscale image resolution. Unlike in the case of the XRD spectra described in Section 4.2.1, the result of a TEM scan is a real-space cross-sectional image of a sample with a possible resolution of individual molecules. The TEM images of several samples were obtained by Richard Beanland at University of Warwick using a JEOL 2100 LaB6 miscrocope, and employing the high-angle annular dark-field (HAADF) imaging technique which is particularly suited to resolving gradients in the atomic number Z, such as between As ($Z \sim 33$) and Sb ($Z \sim 51$). In order for a specimen to be suitable for TEM scanning it needs to be electron-transparent, ie. thin enough to transmit incident electrons with minimal energy loss. The samples analysed in this work were thinned using grinding, polishing and Ar^+ ion milling, which involves eroding the sample surface using accelerated Ar ions.

4.3 Fourier Transform Infrared spectroscopy - transmission

Fourier Transform Infrared Spectroscopy (FTIR) is a non-destructive method of measuring the spectral properties (usually absorption) of a material using a type of a Michelson interferometer. The basic principles can be understood with help of Figure 4.5: the infrared radiation, produced by a NIR or MIR source, is incident on a partially transparent beamsplitter (BMS), which coherently reflects part of the light onto Mirror 1 and passes the rest through onto Mirror 2 (both parts of the Interferometer). The feature characteristic of the rapid-scan FTIR method is that Mirror 2 is continuously moving (scanning) with respect to the beamsplitter, so that the beam travels a fixed distance to Mirror 1 but a continuously changing one to Mirror 2, dependent on the mirror speed.

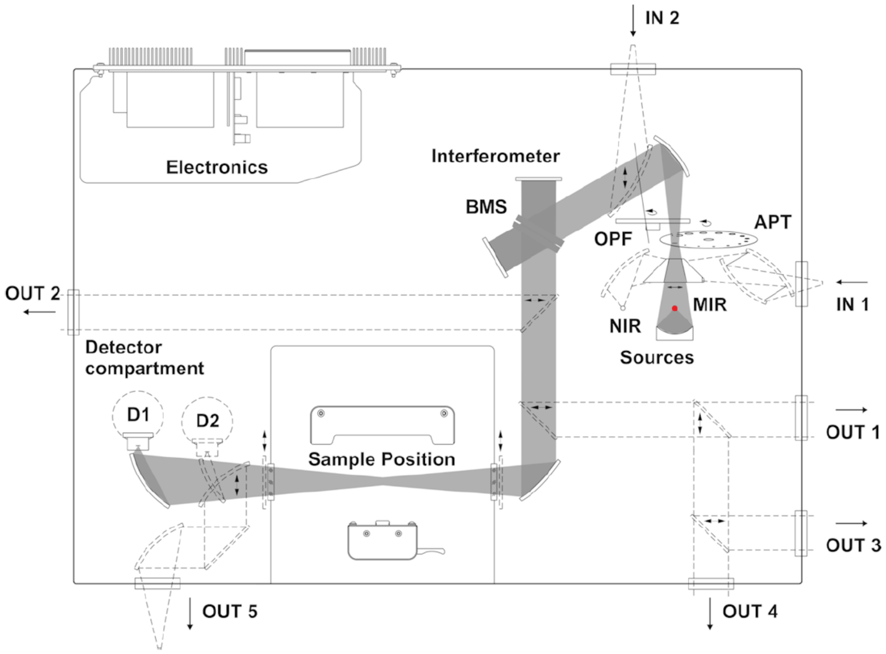

FIGURE 4.5: Top-down view of the internal structure of the Vertex 70 Fourier Transform IR spectrometer. The optical beam path for internal (transmission) measurements is coloured in solid grey, while alternative beam paths are marked with broken lines. The OUT 2 port is usually used for spectral response measurements. Figure adapted from the Vertex 70 manual[136].

The introduction of a scanning mirror is the source of the major practical advantage of FTIR: a single interferogram contains information about the entire scan spectrum, making this technique quick and efficient[137]. The difference between the two paths travelled by the split beams can be defined as optical path difference, or optical retardation δ. Subsequently, when the two beams recombine at the beamsplitter and reflect towards the specimen (and then the detector), the result is a beam intensity function with two components: a constant dependence on the wavenumber k_0 (not useful for Fourier analysis) and a signal modulated by δ

$$I(\delta) = B(k_0)cos(2\pi k_0 \delta) \tag{4.2}$$

which constitutes the interferogram. $B(k_0)$ is a compound term that accounts for the intensity of the incident beam, non-ideality of the beamsplitter, detector response, and amplifier modulation characteristics. This is a simple Fourier transform for a monochromatic light source (such as the reference HeNe laser), but a convolution of wavenumbers (eg. a continuous spectrum) needs to be analysed with the Fourier integral:

$$I(\delta) = \int_{-\infty}^{+\infty} B(k)cos(2\pi\delta k)dk \tag{4.3}$$

where

$$B(k) = 2\int_{0}^{+\infty} I(\delta)cos(2\pi\delta)d\delta \tag{4.4}$$

Although the above integrals imply an infinite spectral resolution, in practice δ has a range of no more than a few millimetres[137].

The simplicity of Equation 4.2 in the case of a monochromatic source is exploited in the use of a HeNe laser as a reference signal for the optical path difference. Because the ideal HeNe interferogram is a simple sin function, the software can count the number of generated fringes and trigger digitisation of the signal due to infrared radiation.

Transmission and spectral response measurements were performed using a Bruker Vertex 70 FTIR apparatus, equipped with a nitrogen gas purging system and a removable OptistatDNV2 LN$_2$-cooled cryostat. Figure 4.5 shows the top-down view of the internal structure of the FTIR, as used in transmission measurements. MIR radiation is produced in the source compartment, and passes through aperture and optical filter wheels (APT and OPF respectively). The aperture size is mostly determined by the sensitivity of the detector in use, and here it is customarily set to 6 mm; the optical filter is left open. The default configuration of the sample compartment only permits room temperature measurements, so it has been modified in-house to permit installation of the cryostat. The in-built room-temperature DLaTGS detector covers a spectral range from 833 nm to 40 μm, which, together with the KBr beamsplitter and the MIR source results in a detectable range from 1.25 to 28.7 μm.

In order to obtain the transmittance data, first the background measurement is taken in order to provide a reference dataset for the sample spectrum. The sample is then mounted in the sample compartment either using a simple magnetic plate, or by installing it inside the cryostat (equipped with ZnSe windows) for low-temperature measurements. In a transmittance measurement the scanning resolution is usually set to 4 cm^{-1}, which provides sufficient signal-to-noise ratio; the aperture size is determined automatically by the OPUS (ver. 7) software.

4.4 Photoluminescence measurements

Photoluminescence is a non-invasive method of assessing the optical properties of a material, e.g. the bandgap. It consists of shining a light on the surface of the material with photon energy larger than the expected bandgap, exciting electrons into the conduction band which then radiatively recombine with holes. However, the resultant emission peak position does not necessarily correspond to the fundamental bandgap transition, for example due to band filling: excited carriers occupying all available lowest energy states, increasing the effective optical bandgap. A power-dependent measurement can be carried out in order to account for this factor, however, which encompasses varying the power of the laser source (LP) incident on the sample at a constant temperature and observing the red-shift of the peak position as a function of decreasing pump power (see Section 6.3). The power-dependent photoluminescent measurements were carried out at Lancaster University by James Keen using a Bruker FTIR spectrometer equipped with either a MWIR InSb detector or a LWIR HgCdTe detector, and using a 785 nm pump laser with 2.55 W cm^{-2} power density and a spot diameter of 1 mm. The laser power was modulated with the use of lowpass filters in the range of 0.4% to 50%.

4.5 Device fabrication

A number of additional processing steps need to be taken in order to produce testable nBn photodetectors from nBn-structure wafers. These were all performed on-site at the Quantum Technology Centre in the Physics Department, Lancaster University.

As a matter of good practice, the very first step is to ensure that the surface of the sample to be processed is clean and free of debris. This is done by submerging the sample in acetone followed by high-concentration isopropyl alcohol (IPA) bath which act as solvents, then rinsing the material in de-ionised water and drying it under high-pressure nitrogen flow. Follow-up options include baking the sample on a conduction hot plate to thermally remove contaminants and water residue, and subjecting the sample to high-power (50+%) oxygen plasma treatment in a Plasma Etch Inc. PE-25 oxygen asher. Low-power plasma treatment can also be used to remove any remaining photoresist at later stages of processing.

4.5.1 Photolithography

In order to create microscale features on a thin film, precise patterning of the surface is required. Photolithography is a technique used in production of integrated circuits (IC), where a polymer-based photoresist is first deposited on the sample surface, then selectively exposed to ultraviolet light, which breaks down the photoresist molecules in the exposed area. Chemical treatment (development) then dissolves the affected molecules, leaving behind the desired IC pattern.

Photoresist deposition and soft-bake

Two resists are applied to the substrate: first LOR 3A and then the positive photoresist S1813 (a positive photoresist breaks down in response to UV radiation; the opposite applies to a negative resist). For the purposes of processing, the main difference lies in their development rates: by developing at a faster rate than S1813, LOR 3A creates an undercut beneath the S1813 layer, allowing lift-off to proceed as intended (see Section

4.5.2). First, the sample is positioned on a chuck inside the SUSS MicroTec LabSpin spin-coating equipment, then fixed in place with vacuum. The liquid resist is deposited statically with a pipette, then the sample is spun at a speed and for a time chosen to produce the desired resist thickness (this thickness is also a function of resist viscosity and a number of other parameters such as ambient humidity, so a recommended spin program needs to be established experimentally). For LOR 3A, 3000 rpm for 30 seconds is enough to produce a layer of about 300 nm.

Once the coating is applied, the wafer is baked on a hot plate for a certain time and temperature in order to drive out any solvent remaining in the resist and to stabilise the surface. For LOR 3A, the optimum result is achieved after 5 minutes at 180 °C.

Once the lift-off resist deposition is finished, S1813 is applied by following the same steps but varying the optimal parameters: the spin is carried out at 6000 rpm for 45 seconds, achieving a thickness of $\sim$1300 nm, followed by a soft-bake at 115 °C for 2 minutes.

Ultraviolet exposure

The equipment used for exposure is a SUSS MicroTec MJB4 mask aligner. It is a design-replicating machine with exposure uniformity of $\leq$3% and several possible contact modes. The UV wavelength used for S1813 and LOR 3A exposure is 365 nm, corresponding to the I-line of the mercury lamp source. First, the prepared wafer is loaded onto a stage, with the mask secured above with the use of vacuum. The next step is to perform the so-called wedge error compensation on the position of the sample surface with respect to the plane of the mask, which ensures parallel alignment of the two. Any other alignment of the mask features with the sample surface is performed using a microscope and x, y and θ controls.

The contact mode used for all the samples in this work is Soft Contact, where only mechanical pressure keeps the sample and the mask aligned. This offers a maximum resolution of $\sim$2 μm, sufficient for this work, and minimises damage to the mask and sample surface[138]. Suitable exposure time is periodically adjusted due to parameter drift, but is usually within 1-2.5 second range.

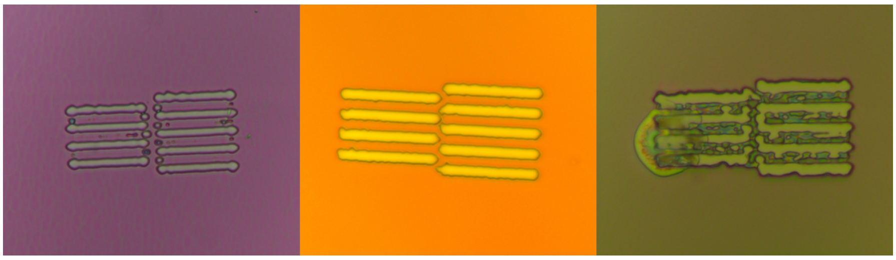

FIGURE 4.6: A feature of the photolithographic mask called exposure fingers, used to gauge the quality of exposure and resist development. Left: underdeveloped/underexposed, middle: appropriately developed/exposed, right: overdeveloped/overexposed. Note: the colours are artefacts of microscope lighting.

Note that the reflection of UV light off the surface of the sample can imprint standing wave patterns in the resist. The usual recommendation is to use a post-exposure bake to thermally diffuse them; however, because the device features used in this work are much larger than the UV wavelength, this effect can be ignored without affecting device characterisation. Therefore, once exposed, the resist is immediately developed in MF-CD-26, which specifically targets the resist sections broken down by the UV radiation. The quality of exposure and development can be assessed under a microscope by inspecting a mask feature called exposure fingers, which can be seen in Figure 4.6. LOR 3A develops at a faster rate than S1813, so it creates an undercut for the following thermal evaporation step (see Figure 4.7). Before evaporation, however, it is necessary to ensure that all the LOR resist is removed from the surface, as it can cause poor metal adhesion; also, a layer of left-over resist can render the metallic contacts non-ohmic by introducing stray potential barriers. Therefore, this left-over resist is dealt with by exposing the sample to low-power (20 - 30 %) plasma in the oxygen asher for 15-25 seconds.

4.5.2 Contact deposition and lift-off

In order to form an electrical circuit between the devices and the external electronics it is necessary to equip the devices with ohmic contacts. An ohmic contact is a non-rectifying metal-semiconductor interface with a linear I-V dependence, and an ideally negligible voltage drop (ie. one that minimises the Schottky barrier present at the junction).

The contacts are thermally evaporated in a Moorfield Minilab 060 deposition reactor, equipped with a turbo-molecular pump. It employs resistive evaporation, where the metal to be evaporated is placed in a highly resistive coil ('source' or 'basket') through which a high current is passed in order to melt and eventually evaporate the source materials.

The standard titanium/gold (Ti/Au) combination is used for the InAs/$\mathrm{InAs}_{1-x}\mathrm{Sb}_x$ surface. It is recommended that the sources are first heated to evaporation temperature if they are in use for the first time, and that similarly the source materials should undergo an acetone bath before being placed in the growth chamber. The growth rate is monitored using a quartz crystal microbalance, which exploits the piezoelectric property of quartz: a crystal is resonated at a known frequency, which is modulated in a known way by mass coming in contact with the surface of the crystal. The QPod control software requires three inputs: the source material density, the tooling factor (a parameter calibrated in situ that accounts for the difference in position between the sample and the monitor) and the Z-ratio (a correction parameter accounting for the change of frequency in response to deposited mass)[139]. This monitor is located in a close proximity to the samples.

Titanium, which is deposited first, acts as an intermediary layer and serves two functions: it prevents gold from diffusing into the semiconductor and acting as a dopant, and promotes surface adhesion in order to counteract gold's poor chemical reactivity. The high reactivity of titanium has another useful property: a sudden drop in chamber pressure at high coil power signals the start of Ti sublimation, as impurities are trapped by the Ti coating the chamber. About 30 nm of Ti is a sufficient thickness. Note that gold evaporation needs to immediately follow that of titanium as Ti quickly oxidises when exposed to atmosphere. The recommended thickness of gold is at least 200 nm to ensure that the contacts are robust enough for wire bonding and characterisation; however, care needs to be taken that the total contact thickness does not overtake that of the LOR 3A resist (see Figure 4.7).

The lift-off is performed by submerging the sample in a bath of Shipley 1165 remover for ∼10 minutes. This is usually sufficient to remove all gold-coated resist from the sample, but should any gold remain, the surface of the sample can be agitated by squirting the remover onto it using a pipette (the sample needs to be submerged at all times to avoid van der Waals forces binding dislodged metal flakes to the surface permanently). Agitation via a sonic bath is usually not employed due to the potential structural damage to the epitaxial films.

4.5.3 Wet etching

Wet etching refers to the removal of epilayers in a chemical solution. This removal can be applied selectively to sample areas patterned with resist to produce specific device structures. First, the sample is patterned with resist, which is not reactive with the acid solution, using the techniques described in Section 4.5.1 (S1813 alone is sufficient if the etching is not followed by thermal evaporation). A standard wet etching process involves three components: an oxidising agent, an oxide-stripping compound, and a solvent (water).

Anisotropic wet etching of the InAs/$InAs_{1-x}Sb_x$ superlattice is achieved using a 2:1 solution of citric acid (which is $C_6H_8O_7$ dissolved in deionised water in 1:1 ratio) with hydrogen peroxide (H_2O_2), where H_2O_2 oxidises the surface of the material while citric acid acts as the solvent for the resulting oxides. The etch rate of a solution has a pronounced temperature dependence described by the Arrhenius equation[140], as well as mechanical agitation and concentration. However, because the barrier layer (AlGaSb, AlAsSb or AlGaAsSb) acts as a natural etch stop, it is sufficient to assume an etch rate of 200 nm/min. Similarly, the superlattice absorber layer is thick enough (at least 3-4

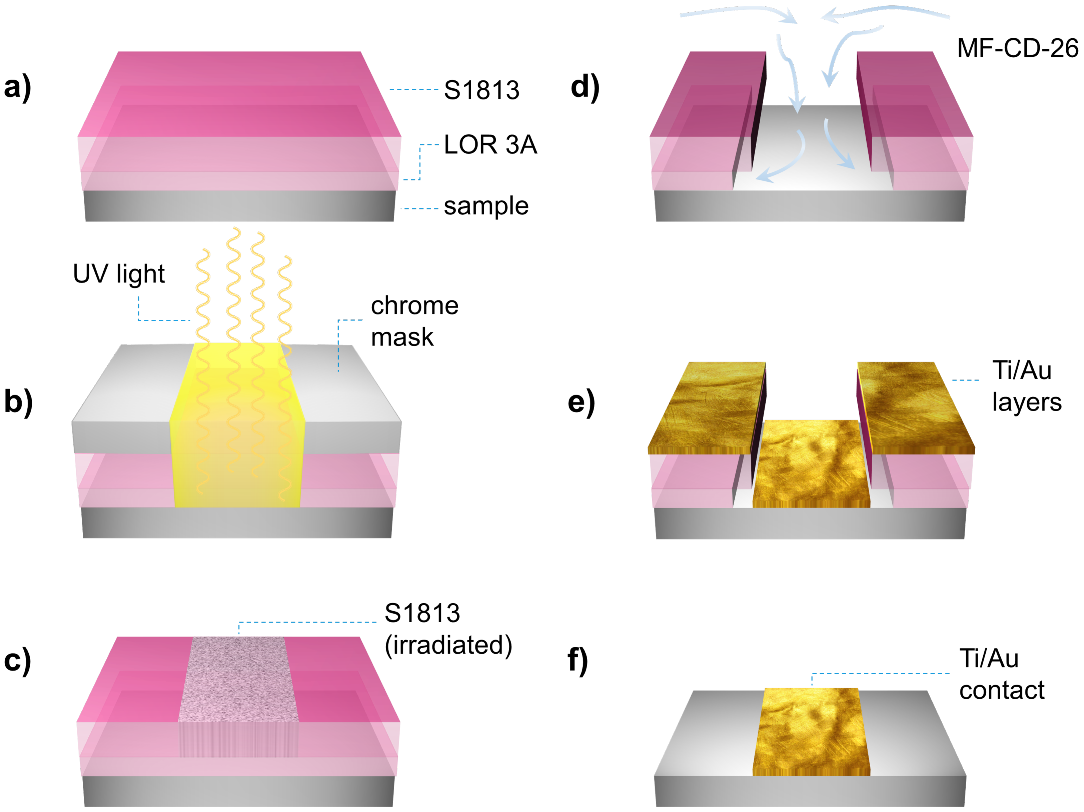

FIGURE 4.7: The process of photolithography and thermal evaporation as used in creating top contacts: a) deposited and baked resists, b) UV exposition, c) the area of resist decomposed by UV, d) development in MF-CD-26, which creates an undercut, e) a sample after Ti/Au evaporation, f) a sample after lift-off in the 1165 remover.

μm) to allow for a controlled etching process without knowing the exact etch rate.

In order to etch the barrier material, an aggressive non-selective $HCl{:}H_2O_2{:}H_2O$ (1:1:5) solution is briefly used (∼35 s) before immediately transferring the sample to an $C_6H_8O_7{:}H_2O_2$ bath to stabilise the etch surface. The etch depth and profile is controlled with a KLA Tencor Alpha Step IQ surface profiler.

Figure 4.8 shows a sketch cross-section of a finished nBn device, with the most important parts denoted with labels. The top ohmic contact is created using photolithography, evaporation and lift-off; the mesa (contact SLS) is fabricated with photolithography and citric acid wet etching; the barrier layer uses photolithography and HCl wet etching, followed by a citric acid etch into the absorber to achieve sufficient depth for the ground ohmic contact (grid), created with evaporation and lift-off.

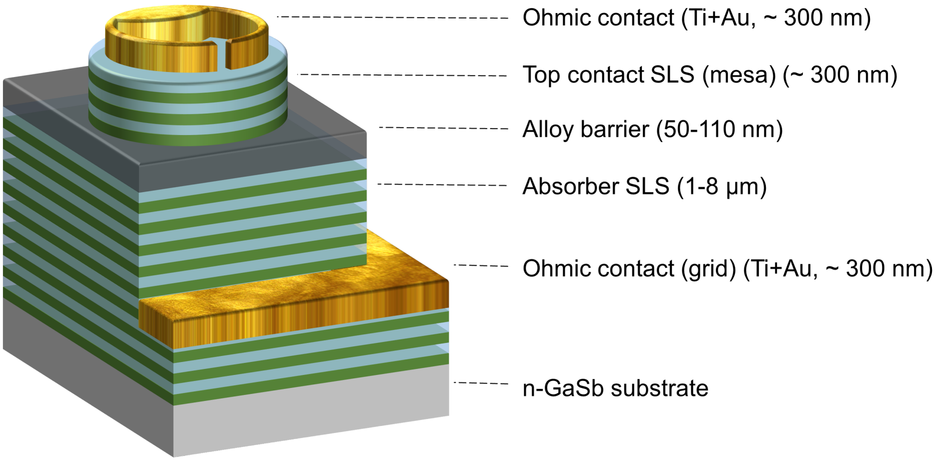

FIGURE 4.8: Cross-section of a mixed area device with relevant components labelled.

4.5.4 Wire bonding

Ultrasonic wire bonding is a cold-welding technique used for connecting a device to external read-out electronics. This method does not require melting of the surface metal to create a bond; instead, an application of ultrasonic energy to the bond and the contact surfaces promotes metal-to-metal coupling via excitation of electrons in the outer valence levels of the two metals[141]. Wire bonding is carried out in situ using a TPT HB05 apparatus.

One drawback of on-device contacts becomes evident when comparing the current-voltage characteristics of bonded and unbonded devices: the ultrasonic energy and the bond force are both strong enough to damage the crystalline structure of the device and raise the total current magnitude (see Figure 4.9).

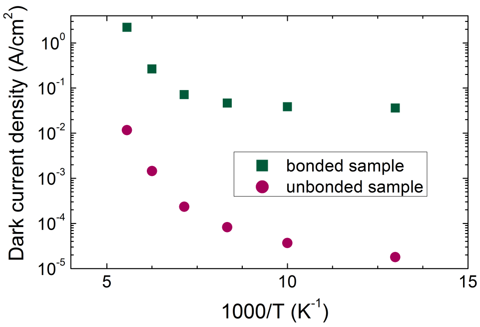

FIGURE 4.9: An Arrhenius plot for two devices on the same sample. The squares correspond to a device with wire-bonding damage.

4.6 Device characterisation

This Section details the experimental procedures for optical characterisation of nBn devices, comprising spectral response (SR) using the FTIR, quantum efficiency (QE) obtained on a blackbody setup, and the use of a cryogenic probe station to measure dark current density J_d.

4.6.1 Fourier Transform Infrared spectroscopy - spectral response

The behaviour of spectral response as a function of incident IR light can be characterised using a Fourier Transform IR spectrometer as the light source and the device sample as the detector. The experimental setup can be seen in Figure 4.10. The sample is mounted in the OptistatDN-V2 cryostat and carefully aligned with the output beam of the FTIR (which is redirected through of either OUT 2 or 3 port seen in Figure 4.5) using a visible NIR (tungsten) source as a reference, then cooled down to the temperature of interest. External read-out electronics connect it to a Stanford Research Systems SR570 preamplifier which provides a bias of -0.1 V. The preamplifier gain allocation mode is set to Low Noise to reduce the Johnson noise at the output terminal, and the gain value (the ratio of the outgoing to incoming signal, expressed in A/V) is adjusted at each temperature to obtain a suitable signal-to-noise ratio. This signal is further processed by a Bruker digitiser and sent to the OPUS software.

The resultant single-channel data does not contain information about background conditions or the lineshape of the blackbody source; instead, the spectral response can be normalised to a theoretical blackbody curve (computed using the temperature of the MIR source, 1320 K) to recover the response characteristics of the detector. However, in order to obtain numerical values of responsivity it is necessary to know the total optical power incident on the device, which would be prohibitively difficult to calculate due to the complicated geometry of the FTIR beam path. An alternative technique is discussed in Section 4.6.2.

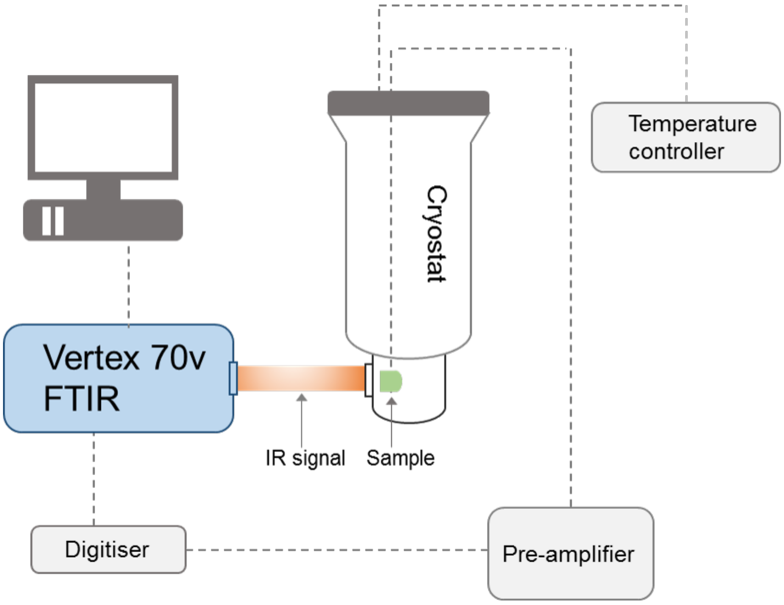

FIGURE 4.10: The experimental setup in spectral response measurements, where the Fourier Transform IR spectrometer (blue) is used as the light source.

4.6.2 Quantum efficiency and responsivity

External quantum efficiency of the device samples is measured using a Landcal P550P blackbody emitter rather than a single-wavelength source. First, the sample is mounted and cooled inside the OptistatDN-V2 cryostat, and connected to the SR570 pre-amplifier, which is operated according to the same principles described in Section 4.6.1. The pre-amplifier output is further connected to an SRS SR830 lock-in amplifier, which uses phase-sensitive methods to detect a very small signal against a background of noise which can be orders of magnitude larger. This is done by providing a reference frequency (here sourced from a chopper separating the blackbody source from the sample; see Figure 4.11 for the complete set-up) at which the amplifier looks for the relevant signal, and discards any signal outside of it.

Responsivity is defined as the ratio of the photocurrent I_p generated in the absorber to the total incident optical power P_{BB} (see Section 2.2.3). P_{BB} is emitted from a blackbody element and is equal to

$$P_{BB} = \frac{\sigma}{\pi}(T_{BB}^4 - T_d^4)\Theta W \Gamma \tag{4.5}$$

where σ is the Stefan-Boltzmann constant, W is the transmission of the ZnSe cryostat window equal to ~0.65 across the 0.6 - 16 μm range, T_{BB} is the temperature of the blackbody equal to 550°C, and T_d that of the device. System throughput Θ parametrises the active area of the absorber under illumination, and is equal to[142]

$$\Theta = \pi^2 r_a^2 F \tag{4.6}$$

where r_a is the radius of the aperture in Figure 4.11 and F is the form factor calculated using

$$F = \frac{1}{2}\left(\frac{(r_a^2 + r_d^2 + d^2) - \sqrt{(r_a^2 + r_d^2 + d^2)^2 - 4r_a^2 r_d^2}}{r_a^2}\right) \tag{4.7}$$

where r_d is the device radius and d is the distance from the aperture to the device. Care needs to be taken when defining effective r_d when an opaque top contact is present.

The dimensionless bandpass filter transmission factor Γ quantifies the fraction of the total blackbody flux that passes through the bandpass filter, and is obtained by multiplying the normalised blackbody spectrum for a given T_{BB} and the transmission spectrum of the bandpass filter, and calculating the integrated area of the resultant curve. The filter transmission spectrum was obtained using the method described in Section 4.3.

4.6.3 I-V characteristics

Leakage current characteristics were obtained using a Lake Shore TTPX cryogenic probe station and Keithley 2430 and 2350 sourcemeters, controlled remotely with a LabVIEW program. The probe station offers accurate control of the device temperature in the

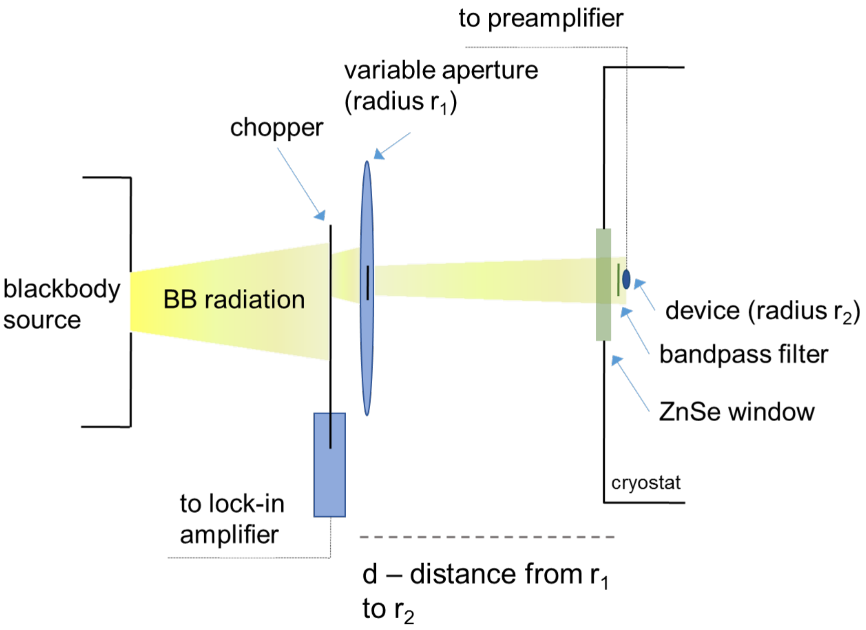

FIGURE 4.11: Side-view of the experimental setup used in external quantum efficiency measurements.

liquid nitrogen regime via a cooled copper sample stage, an inner radiation shield preventing thermal radiation effects, and probe arms that are thermally anchored to the stage. A 1.55 μm Thorlabs fiber DFB laser, mounted on the third probe arm, is also positioned above each device. Measurements are taken at 20 K increments starting at 77 K, and each one involves the following steps. First, the sample is left idle for a few minutes to allow it to reach thermal equilibrium with the stage. The probes are then lowered down on the device under consideration, and the optic fibre of the laser is positioned above it. It is commonly found in our superlattice nBn devices that once the probes are contacted to the device, a gradient in dark current is observed even under constant bias, temperature and illumination, which settles with time. However, it has been found that applying a laser burst of ∼10 seconds to the sample prior to the measurement helps the dark current to settle almost instantly, which implies that trap centres in the wide-bandgap barrier play a role in this process. Once the current reaches a plateau, a voltage sweep between -0.5 V and 0.5 V is applied in steps of 0.01 V.

Chapter 5

I. Results and discussion: Design, growth and structural properties

In terms of sample structure, two types of specimen were produced. The first type was undoped superlattice epilayers, usually grown on buffer layers on GaAs substrates, produced with the intent of studying optical properties of the SLS using transmission and photoluminescence methods. The second type was the n-doped nBn device, with superlattices constituting the absorber and the top contact layer. Section 5.1 deals with the principles of designing a superlattice layer (both for undoped and device samples), Section 5.2 details how the properties of the nBn device structures are decided, Section 5.3 outlines a typical MBE recipe, and Section 5.4 presents the results of structural characterisation using X-ray diffraction and transmission electron microscopy.

5.1 Superlattice design

This section outlines the design procedure of the InAs/InAs$_{1-x}$Sb$_x$ superlattices, and the way different structural variables affect each other and the final performance of the detectors.

When designing an infrared detector, the primary parameter that defines its scope of operation is the desired cut-off wavelength ($\lambda_{cut-off}$). $\lambda_{cut-off}$ is usually defined at a fraction of the maximum spectral response of the detector, and as such its position is dependent on the strength of absorption near the fundamental band edge, which determines the gradient of spectral response. This absorption strength, in turn, is strongly dependent on absorber thickness and other practical choices made during growth and processing of the sample. Because of this, when designing a device from scratch, it is simpler to first choose the value of the fundamental bandgap near the desired $\lambda_{cut-off}$, carry out the design procedure outlined below, characterise the device as necessary, then iteratively fine-tune the design parameters until the correct shape of spectral response is achieved.

The fundamental bandgap of the absorber superlattice (E_g) is the dominant structural parameter that determines the majority of subsequent design choices. In a type-IIb superlattice (see Section 2.1.2) the bandgap is strongly dominated by the valence band offset between InAs and InAs$_{1-x}$Sb$_x$, making the antimony fraction x_{Sb} the variable of interest. Originally, the valence band position of InAs$_{1-x}$Sb$_x$ with respect to that of InSb (a common reference point recommended by Vurgaftman et al[28]) or a theoretical zero-energy asymptote[22] was calculated using values found in literature[28,22,42], but that led to a routine overestimation of the bandgaps obtained from transmission and spectral response data (for an example see Figure 5.1). Because of this, as an alternative approach, the InAs$_{1-x}$Sb$_x$ valence band position was subsequently estimated and used as a fitting parameter based on previous sample data, which is discussed in detail in Section 6.5.

Once the desired Sb fraction is known, it is necessary to choose an appropriate substrate for the sample: a native GaSb substrate, a GaAs substrate with a GaSb buffer layer, or one with an AlSb buffer. This choice is crucial as it determines the crystalline quality and the strain-balancing conditions of the structure, i.e. the ratio of the thicknesses of InAs and InAs$_{1-x}$Sb$_x$ across a single superlattice cell that results in the least possible residual strain. The ideal ratio is obtained using the following relation:

$$\epsilon_{\parallel,InAs_{1-x}Sb_x} \times ML_{InAs_{1-x}Sb_x} + \epsilon_{\parallel,InAs} \times ML_{InAs} = 0 \tag{5.1}$$

where $\epsilon_{\parallel}$ is the in-plane strain defined in Section 2.1.1 and $ML_{InAs,InAs_{1-x}Sb_x}$ are the

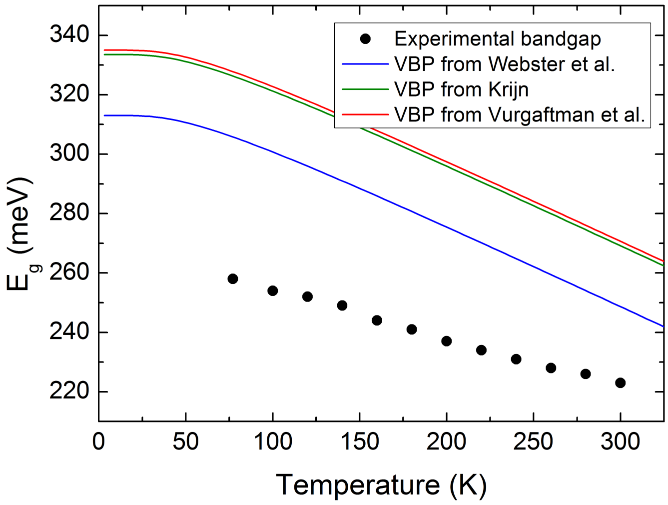

FIGURE 5.1: Fundamental bandgap values obtained from an InAs/InAs$_{0.824}$Sb$_{0.176}$ superlattice transmission data (black dots) compared to theoretical predictions (continuous lines) using different valence band position (VBP) values from literature. The temperature dependence is modelled using single-oscillator parameters from Webster et al[42].

numbers of respective monolayers in a single superlattice cell. In practice, this calculation is iterated for different monolayer numbers until the right-hand side is minimised, which results in some amount of residual strain always being present. It is also important to note that strain is temperature-dependent due to the different expansion coefficients of InAs and InAs$_{1-x}$Sb$_x$ (see Figure 5.2). During its lifetime a sample goes through a temperature range of at least 600 K between the MBE growth conditions and the cryogenic testing temperatures, therefore care needs to be taken that critical thickness is not reached at any point. As such, in this work the appropriate monolayer ratio is customarily found at 300 K, which is believed to be an acceptable middle ground between these temperature extremes. As an example, the behaviour of critical thickness of an arbitrary 14 ML/ 14 ML InAs/InAs$_{0.82}$Sb$_{0.18}$ superlattice on GaSb in response to temperature can be seen in Figure 5.2. All critical thickness calculations in this work are carried out using the Matthew and Blakeslee's model introduced in Section 2.1.1. It can be shown that the model's condition for a lattice mismatch of 1.4% or less is fulfilled for the majority of samples discussed here (see Figure 5.2), so the h_c values calculated using this model can be taken as reliable.

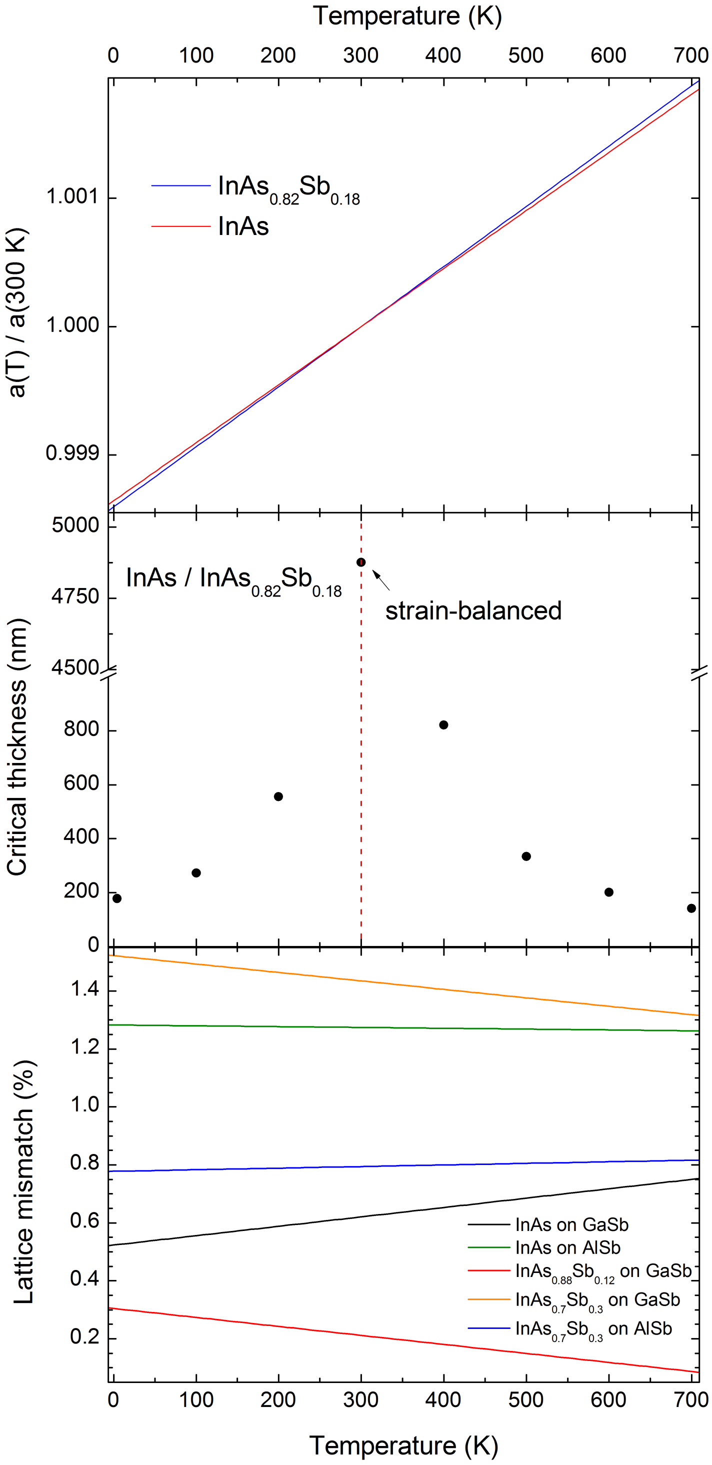

FIGURE 5.2: Top: the behaviour of the InAs and $InAs_{0.82}Sb_{0.18}$ lattice constants in response to temperature. The different rates of lattice constant changes have implications for designing strain-balanced heterostructures. Middle: calculated critical thickness of an $InAs/InAs_{0.82}Sb_{0.18}$ superlattice cell grown on GaSb, designed to be strain-balanced at 300 K using the Matthew and Blakeslee model. The FWHM of $h_c(T)$ here is $\sim$ 60 K (note the axis break). Bottom: calculated lattice mismatch for different combinations of epilayers and substrates, validating the use of the Matthew and Blakeslee model for their critical thicknesses.

Regarding the bottom graph of Figure 5.2, however, it should be noted that in a real scenario involving growth on a buffer layer, the response of a_{AlSb} would be at least partially determined by the thermal expansion of the underlying GaAs substrate.

The strain-balanced monolayer ratio is also dependent on the substrate lattice constant. GaSb, with its native lattice constant, offers the smallest dislocation density of the three so it is a suitable choice for MWIR device samples. The advantage of a buffer layer acting as a 'virtual' substrate is that the strain-balancing conditions of the superlattice are no longer dependent on the lattice constant of the substrate, as the superlattice is strained to the buffer layer instead. This is a significant consideration for superlattices with Sb fractions appproaching 0.3 and above on GaSb: at this value, the strain-balanced ratio of InAs$_{1-x}$Sb$_x$ to InAs quickly falls to 0.5 and below (see Figure 5.3), in practice requiring the hole barrier layer (InAs) to be much thicker than the hole well layer, which decreases the wavefunction overlap between the electron (e1) and fundamental heavy hole (hh1) bands, which impedes absorption; heavy hole tunnelling and subsequently photocarrier extraction from the absorber are also affected. Very thin InAs$_{1-x}$Sb$_x$ layers could also potentially suffer from a Sb gradient existing across the entire layer thickness, as discussed in Section 5.4.3.

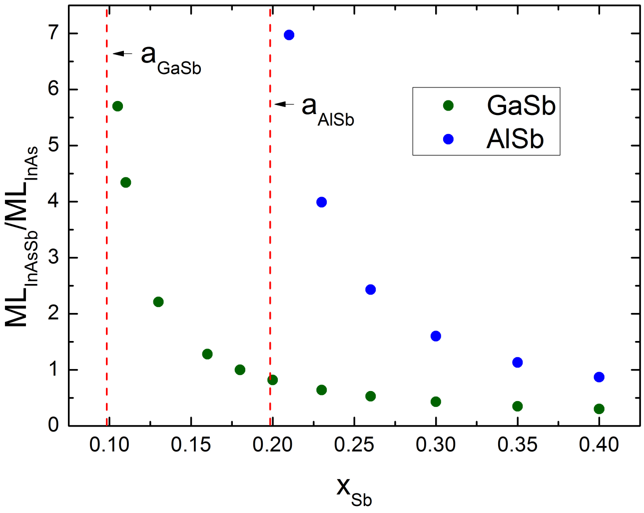

FIGURE 5.3: The strain-balanced ratios of InAs$_{1-x}$Sb$_x$ and InAs monolayer numbers at 300 K as a function of Sb fraction, calculated either for the GaSb or AlSb lattice constants.

For layers grown on AlSb, on the other hand, the high-Sb monolayer ratio remains in the range of 0.9-1.6 across the entire LWIR range, potentially mitigating both of these issues.

Furthermore, if the sample is being grown on a mismatched-lattice substrate, then the buffer layer thickness also needs to be chosen. This choice is supported by the known percent relaxation as a function of buffer thickness, the details of which are discussed in Section 5.4.2.

Once the strain-balanced monolayer ratio is known, it is necessary to choose the actual superlattice layer thicknesses. TEM images taken of an $InAs/InAs_{0.824}Sb_{0.176}$ SLS nBn grown on a GaSb substrate (discussed in more detail in Section 5.4.3) show a gradient in Sb incorporation that spans about 2 nm near the layer interface. This will affect the band structure and therefore the optical properties of the superlattice in the case the quantum well layer is thin enough that this gradient spans its entire width. As such, $InAs_{1-x}Sb_x$ thicknesses above 2 nm are generally recommended. However, increasing quantum well thickness requires widening the barrier by the same ratio, which has implications for the heavy-hole wavefunction overlap between the wells, because it increases photocarrier confinement and potentially affects carrier extraction due to reduced tunnelling probability. This issue is particularly pronounced for high-Sb superlattices strained on GaSb: for example, an $x_{Sb} = 0.35$ superlattice requires a barrier that is 2.9 times thicker than the well, while one strained on AlSb necessitates a barrier 0.9 times the thickness of the well (as per Figure 5.3). Nevertheless, thicker superlattice cells offer an additional advantage when interface roughness occurs between InAs and $InAs_{1-x}Sb_x$, because the affected area around the interface constitutes a smaller fraction of the total layer thickness. Counter-intuitively, increasing the superlattice cell thickness also decreases the MBE growth times due to the additional growth interrupt stages (see Section 5.3). Finally, it is worth noting that the position of carrier minibands within a quantum well has a non-negligible dependence on the well's thickness, according to the Kronig-Penney model discussed in Section 2.1.2; for discussion of a study of this effect see Section 6.5. A qualitative summary of these considerations can be seen in

TABLE 5.1: A qualitative summary of the consequences of decreasing (increasing) the period of a superlattice.

Superlattice period	*thinner*	*thicker*
Miniband position	increased	decreased
HH wavefunction overlap	increased	decreased
Effect of interface roughness	increased	decreased
Effect of Sb gradient at the interface	increased	decreased
Growth times	increased	decreased

Table 5.1.

5.2 nBn device considerations

The next step in designing a sample is to choose appropriate thicknesses for the absorber and the contact layers. The fraction of light absorbed follows a modified positive dependence on absorber thickness based on the Beer-Lambert law (per Equation 2.32) - an arbitrarily thick absorber would increase responsivity but necessitate longer growth times. The thickness of the contact layer, on the other hand, is mostly a practical choice between contact robustness (ie. its resistance to damage when bonding and testing) and acceptable optical losses in the contact superlattice, as any radiation absorbed in it does not contribute to the photocurrent.

The primary parameter of an effective nBn barrier is its heavy hole band alignment with that of $InAs_{1-x}Sb_x$ in the superlattice, which is necessary for unimpeded flow of photocarriers across the barrier. Generally, three alloys have been used: $Al_xGa_{1-x}Sb$, $AlAs_{1-x}Sb_x$, and $Al_xGa_{1-x}As_ySb_{1-y}$. The positions of their valence bands were calculated using the same approach outlined in Section 2.1.2, then their composition was optimised to align them with the superlattice. It has been a recurring observation that the inclusion of Ga in the barrier results in the alloy creating a more stable oxide when exposed to atmosphere. Although it is unclear if the actual performance of a Ga-free barrier degrades with prolonged exposure to air, it is preferable to avoid this effect in order not to introduce additional unknown variables into a detector's performance. As such, it is recommended to use either Al$_x$Ga$_{1-x}$Sb or Al$_x$Ga$_{1-x}$As$_y$Sb$_{1-x}$. A further advantage of the latter is that it can be closely lattice-matched to GaSb once a low fraction of As is included, as it increases the barrier's critical thickness.

A study of bulk InAs$_{0.89}$Sb$_{0.11}$ nBn devices, carried out by Adam Craig from Lancaster University and Magnus Wagener from Nelson Mandela University[143], has found a pronounced decrease in dark current densities as a function of barrier thickness, the cause of which is believed to be reduced electron tunnelling via midgap states in the barrier (see Figure 5.4). As most of the decrease appears to take place between 20 and 80 nm, most barriers in this work are grown with thicknesses in the range 50 to 100 nm.

Device absorbers are customarily n-doped at $\sim 6 \times 10^{16}$ cm^{-3} carrier concentration; an attempt to increase doping in a MWIR device to $\sim 5 \times 10^{17}$ cm^{-3} in comparison to other MWIR samples led to a significant decrease in responsivity associated with lowered carrier diffusion lengths, which would decrease the total effective volume of the absorber (see Sections 6.2 and 7.2.1). However the top contact superlattice layers, which are no more than 300 nm and do not contribute to the photocurrent, are routinely doped at $\sim 5 \times 10^{17}$ cm^{-3}.

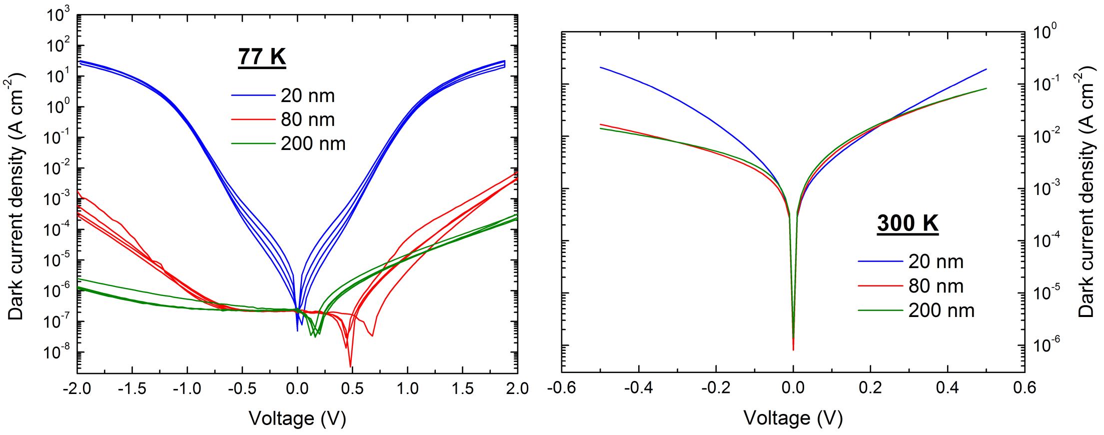

FIGURE 5.4: A comparison of dark current densities of three bulk InAs$_{0.89}$Sb$_{0.11}$ nBn devices with varied barrier thicknesses at 77 K (left) and 300 K (right). Credit to Adam Craig from Lancaster University.

5.3 Molecular beam epitaxy growth recipe

For wafer preparation steps including outgassing and and oxide desorption stages refer to Section 4.1. These are followed by 1 ML s^{-1} growth of 250-500 nm of a buffer layer of the same binary as the substrate (at substrate temperatures of 500°C for GaSb and 565°C for GaAs), which isolates any remaining substrate surface contaminants from the following epilayers. Next, if the sample is being grown on native GaSb, then the substrate is simply cooled down to superlattice growth temperature (see below) under Sb flux. However, if the subsequent layer is meant to be a buffer layer, then GaAs growth is followed by a 10 second As flux interrupt, leaving the surface Ga-terminated. The Sb valve is then fully opened and the substrate is cooled to the buffer layer growth temperature (500°C for both GaSb and AlSb), which is then grown at $\sim$1 ML s^{-1}. The substrate is then again cooled down under Sb flux to the superlattice growth temperature.

The superlattice layers are grown at $\sim$1 ML s^{-1}, which is an acceptable compromise between growth duration and crystal quality, as it is slow enough to enable each layer to self-assemble before deposition of the next one begins in the so-called Frank-van der Merwe growth, while maintaining feasible operation times. The growth rate ratio of group III (In) to group V (As/Sb) elements is kept in the range 1:1.6 to 1:1.8 as recommended by QinetiQ[144]. Optimal InAs/$InAs_{1-x}Sb_x$ substrate growth temperatures were investigated by Liu et al.[145], who studied integrated PL linewidths of a series of LWIR samples, and found an optimal high-Sb growth temperature in the range 400-410°C. It is also known that Sb and As incorporation rates are negatively correlated with substrate temperature via the temperature dependence of their sticking coefficients[145,146]. Because of these two factors, MWIR samples in this work are grown at higher substrate temperatures of 435-450°C. Finally, interface roughness is minimised by introducing growth interrupts in the form of group V soaks between InAs and $InAs_{1-x}Sb_x$ growth steps. In an effort to eliminate Sb surface segregation, Stone[147] built on the work of Kaspi et al[148] and Pillai et al[149] to optimise As and Sb predeposition times by studying their effect on the full-width-at-half-maximum (FWHM) values of InAs/$InAs_{1-x}Sb_x$ MQW XRD spectra. Based on this work, a 3 second As/Sb soak step is incorporated into the recipe as a preclude to InAs$_{1-x}$Sb$_x$ growth, which is then followed by a 10 s As exposure in preparation for the InAs layer. If the sample is a device, then dopant flux is provided by a heated GaTe source at ~215°C for the low-doped absorber, and at 225°C for the high-doped top contact superlattice.

The barrier layer was originally grown at substrate temperatures approaching optimal GaSb growth values (505°C), however there have been concerns over preserving the crystalline quality of the superlattice absorber below as it is being heated beyond its optimal growth temperature. As such, earlier nBn device barriers in this work were grown at ~470°C, while the later ones had barriers grown at the temperature of the absorber layer preceding them (as discussed in Section 5.4). None of the barriers are intentionally doped.

Finally, it must be pointed out that the principles outlined above apply to the samples grown using the Veeco GENxplore MBE reactor. One sample discussed in this work, the dual-colour QA504, however, was manufactured in the older VG V80-H system, using an earlier iteration of recipes. While the wafer conditioning and buffer layer growth proceeded in the same manner, the superlattice growth substrate temperature was kept constant at 425°C; also, the recommended III-V growth ratio was not observed. Finally, no As/Sb soak was incorporated before the InAs$_{1-x}$Sb$_x$ growth stage. The dopant density was 4×10^{16} cm^{-3}.

5.4 Characterisation: X-ray Diffraction and Transmission Electron Microscopy

5.4.1 Sb incorporation

To ensure that electrical and optical characterisation of samples can be related to their structure, the average variation of Sb incorporation across a wafer was measured for several samples. The results can be seen in Table 5.2. No dependence on distance from the centre of the wafer was observed, indicating that the substrate temperature gradient occurring at wafer edges has a limited range. The more likely explanation is the uneven relaxation of the buffer layers preceding the superlattice on samples grown on the lattice-mismatched GaAs (see Section 5.4.2), seeing that the two samples grown on native GaSb (XV0576 and XV0552) show low standard deviations of ±0.1%.

TABLE 5.2: Mean Sb fractions and their standard deviations for different samples, taken by obtaining the XRD spectra at 3 or 4 points on each wafer.

Sample	**XV0154**	**XV0160**	**XV0159**	**XV0547**	**XV0234**	**XV0552**	**XV0576**
Substrate/buffer	GaAs	GaAs	GaAs	GaAs	GaAs	GaSb	GaSb
Buffer	GaSb	GaSb	GaSb	GaSb	GaSb	-	-
Mean x_{Sb} *(%)*	17.6	17.8	17.4	25.7	37.7	30.9	16.1
Std. dev. x_{Sb} *(%)*	0.3	0.1	0.1	0.7	0.4	0.1	0.1

5.4.2 Buffer layer relaxation

The relaxation of an epitaxial buffer layer varies as a function of its thickness[150], which in turn affects the lattice constant that the following superlattice is strained on. To support the superlattice XRD fittings in this work, a series of GaSb and AlSb buffer layer samples with varying thicknesses were fabricated using the same growth conditions as those in full sample recipes. The resultant (004) $\omega - 2\theta$ scans were used to simulate the appropriate relaxations in the Bede PeakSplit software, whose input parameters are the substrate and epilayer materials, diffraction planes of the scan, and the expected percent relaxation, which is defined as

$$\text{Relaxation} = \frac{a_{\parallel} - a_{sub}}{a_{relaxed} - a_{sub}} \times 100\% \tag{5.2}$$

where a_{sub} is the substrate lattice constant, $a_{\parallel}$ is the epilayer lattice constant parallel to the substrate plane, and the relaxed lattice parameter is

$$a_{relaxed} = \frac{-(a_{\perp}(\nu - 1) - 2\nu a_{\parallel})}{1 + \nu} \tag{5.3}$$

where ν is the Poisson ratio of the epilayer and the epilayer perpendicular lattice constant $a_{\perp}$ is defined as

$$a_{\perp} = \left(\frac{sin(\Theta_{sub})}{sin(\Theta_{sub} + \Delta\omega)} - 1 \right) \times a_{sub} + a_{sub} \tag{5.4}$$

where Θ_{sub} is the Bragg angle of the substrate. Equations 5.2 and 5.3 are solved simultaneously by the software for $a_{||}$ and $a_{relaxed}$. The output parameter of interest here is the difference between the substrate and epilayer Bragg angles $\Delta\omega$, because it can be compared to the experimentally obtained position of the epilayer peak with respect to that of the substrate.

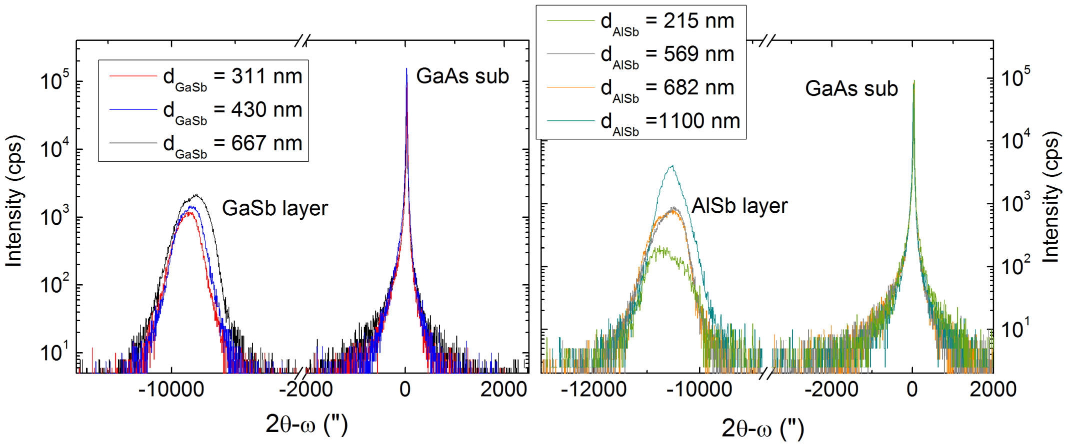

FIGURE 5.5: Symmetric coupled XRD scans of varying-thickness GaSb (left) and AlSb (right) buffer layers, all grown on GaAs substrates. The very low peak intensity of the thinnest AlSb buffer is due to gradual formation of an oxide on the surface of the AlSb samples.

For each buffer layer sample, a coupled symmetric scan was performed at four points on the wafer. The resultant epilayer peak positions (see Figure 5.5 for scans of the GaSb and AlSb wafer centres) were then fitted to the Gaussian function if the sample was under 500 nm in thickness, and estimated from raw data for samples above 500 nm. The reason for the latter is the appearance of a secondary shoulder on the thicker samples, which Reyner et al[150] attributes to interaction of the asymmetric Kα_2 emission line of the copper source with the crystal, due to insufficient filtering of this line by the beam conditioner. This makes a standard Gaussian fit unsuitable. Once a value for the substrate-epilayer peak separation is known, a Bede PeakSplit simulation is iterated until the corresponding percent relaxation is found. These mean values and their standard deviations can be seen in Figure 5.6.

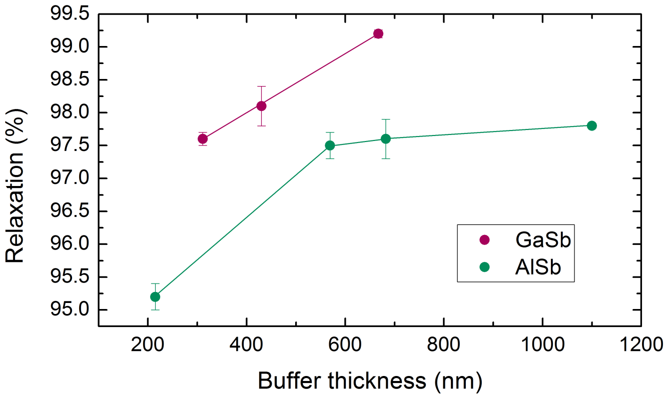

FIGURE 5.6: Relaxation of different buffer epilayers grown on GaAs substrates as a function of buffer thickness.

5.4.3 InAs/InAs$_{1-x}$Sb$_x$ nBn growth on native GaSb

This section details structural characterisation of nBn devices on GaSb substrates only.

X-ray diffraction

A number of nBn devices were grown on GaSb substrates, which provide the optimal strain-balancing environment for an InAs/InAs$_{1-x}$Sb$_x$ system. $\omega - 2\theta$ scans of MWIR samples XV0161, XV0576 and XV650 can be seen in Figure 5.7. Sample XV0161 shows sharp, well-defined superlattice peaks with no evidence of splitting which (if present) could point to either partial relaxation of the absorber layer, or relaxation of the top contact superlattice. The barrier of this sample is 53 nm of AlAs$_{0.12}$Sb$_{0.88}$, grown 'hot' at 470°C substrate temperature, compared to the SLS growth temperature of 432°C.

Sample XV0576, grown to be lattice-matched at a lower $x_{Sb} = 0.16$, can be seen in Figure 5.7. The barrier, Al$_{0.90}$Ga$_{0.10}$As$_{0.06}$Sb$_{0.94}$, is grown 'cold' at the superlattice growth temperature of 427°C and to 110 nm thickness. Valence band alignment with the superlattice was predicted at barrier Sb fraction of 0.91, so the growth of this barrier

TABLE 5.3: Barrier critical thicknesses at room and growth temperatures, calculated using the Matthew and Blakeslee model.

	Barrier h_c (nm)		
Sample	$d_{barrier}$	T_{300K}	T_{growth}
XV0161	46	47	28
XV0576	110	132	7052
XV0650	110	132	7052
XJ0292	51	34	47
XV0552	81	18	24

proceeded with the Sb valve fully opened and the As valve set to the lowest measurable position; this resulted in $x_{As} = 0.06$ and a small lattice mismatch with the GaSb substrate that varies between 0.13 and 0.2% at 300 and 77 K respectively, minimising thermally induced stresses on the epilayers as the sample undergoes temperature cycles due to testing. The flat inter-peak regions at intensities $\sim 10^2$ cps are likely due to the fact that this particular scan was acquired at the edge of the sample, where substrate-to-holder temperature gradients are more pronounced, and are not present in XRD scans taken near and in the middle of the wafer. There is evidence of very weak peak splitting, where a secondary superlattice with a period larger by about 2 Å can be fitted near the primary peaks, however characterising this peak set accurately would require scan resolution not achieved for this sample set (much more pronounced peak splitting is observed for LWIR samples, and discussed below).

One way to enhance light absorption of a detector is to simply increase the absorber thickness. An InAs/InAs$_{0.842}$Sb$_{0.158}$ sample XV0650 was grown with a 8.7 μm absorber thickness and an Al$_{0.90}$Ga$_{0.10}$As$_{0.06}$Sb$_{0.94}$ barrier, and the resultant XRD peaks can be seen in Figure 5.7. Although no quantitative comparison can be made between the FWHM values of this sample and XV0576 due to their dependence on instrument parameters, it can be seen that doubling the absorber thickness still results in sharp, well-defined superlattice peaks.

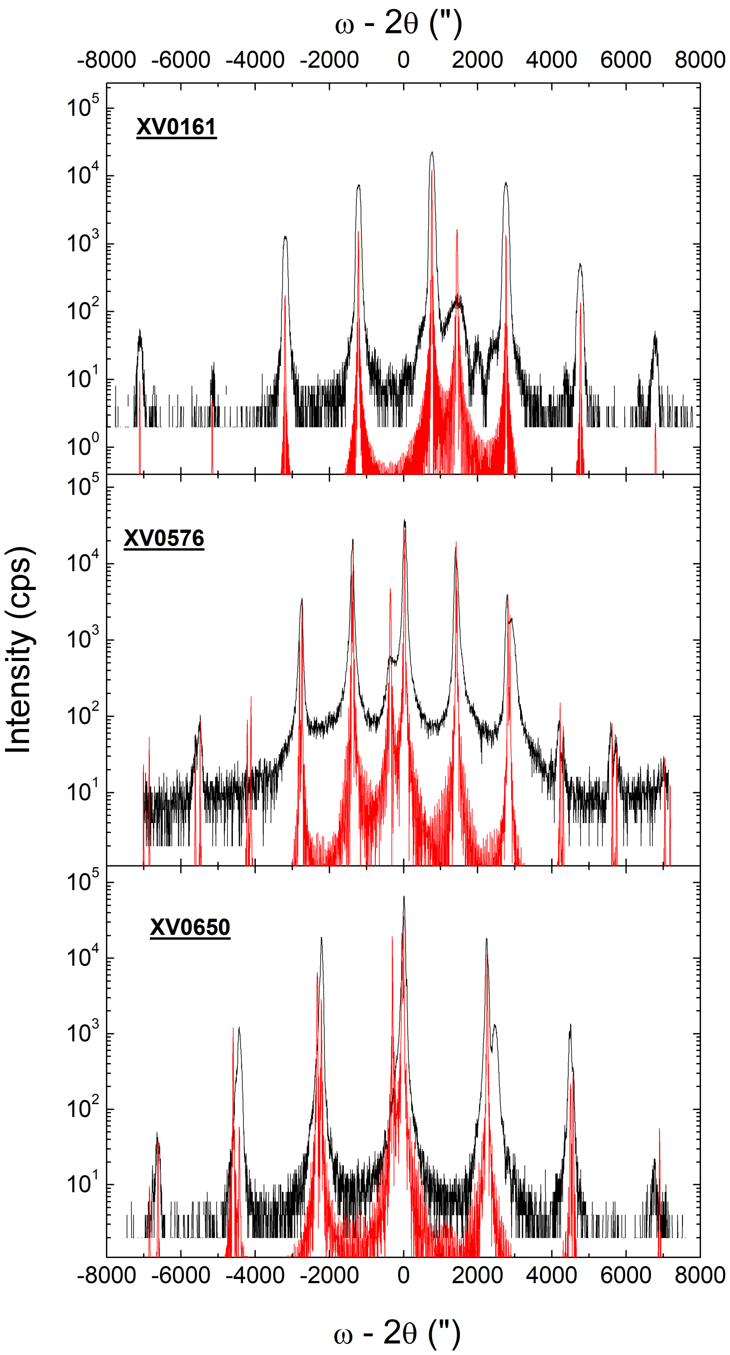

FIGURE 5.7: .

Coupled XRD scans of MWIR samples grown on native GaSb substrates (black), and their modelled structures (red).

Closer inspection, however, reveals the same weak peak splitting ($\sim$ 2 Å difference in d_{SLS}) as the one found in sample XV0576. Given the similarity of the two structures, including a very good lattice matching of this barrier to the substrate, a potential explanation could lie in comparing the critical thickness of the barriers $h_c = 132$ nm at room temperature to the actual grown thickness of 110 nm - it is possible that the real thickness is close enough to h_c to cause partial relaxation of the barrier.

Figure 5.8 shows an XRD spectrum of the $x_{Sb} = 0.40$ sample XJ0292, with its $Al_{0.58}Ga_{0.42}Sb$ barrier grown 'hot' (at 458°C, compared to 393°C superlattice growth temperature) to a thickness of 51 nm.

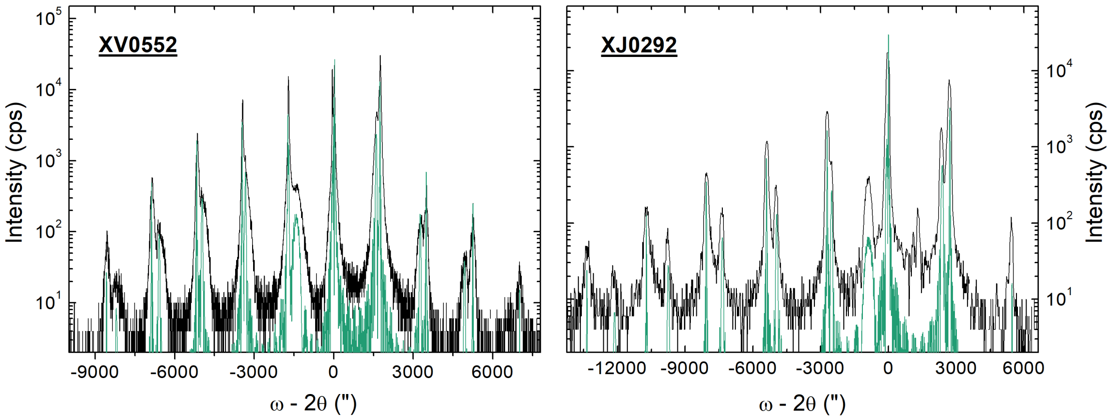

FIGURE 5.8: Coupled XRD scans of the LWIR samples grown on native GaSb substrates (black), and their modelled structures (teal).

Compared to the MWIR samples discussed above, this structure shows a set of strongly split secondary peaks with a spacing corresponding to a larger period than the primary superlattice. The same effect can be observed in sample XV0552 ($x_{Sb} = 0.31$; this fraction refers to the primary set of peaks), with a 'cold' barrier composed of $Al_{0.95}Ga_{0.05}Sb$. Fitting parameters and substrate growth temperatures can be seen in Table 5.4; for barrier critical thicknesses, refer to Table 5.3. There appears to be no correlation between superlattice peak splitting and the substrate temperature during barrier growth: sample XV0161, with its 'hot' barrier, shows no splitting (although this could be due to the X-ray scan resolution being too low to resolve the kind of faint splitting seen in the other two MWIR samples), while the 'cold' XV0552 does. Together with the sharp peaks of XV0161 this also indicates that temporarily raising the temperature of the absorber superlattice during barrier growth on top does not necessarily compromise the absorber's crystal quality. In addition, no correlation was observed between splitting and barrier growth rates, which varied between 0.5 and 1.0 ML s^{-1}. The answer, instead, appears to lie in the proximity of $d_{barrier}$ to h_c: the strongly split LWIR samples XJ0292 and XV0552 had their barriers grown to thicknesses well beyond the room temperature value of h_c, a situation that would only exacerbate as the samples are cooled to the operational temperature of 77 K due to their barrier lattice mismatch rising with decreasing temperature (see Figure 5.9); in contrast, the MWIR sample barriers all show smaller lattice mismatch with the GaSb substrate below $T \sim 480°$C and in the case of XV0161, the mismatch continues to decrease with T. As such, the priority in designing a suitable nBn barrier from a structural point of view is to grow it at thicknesses lower than h_c at all T, ie. a barrier should be designed such that its plot in Figure 5.9 is flat or decreasing with respect to the T axis. In order to complete the picture of epilayer interaction in these nBn devices, however, asymmetric rocking curve scans would be necessary in order to obtain $a_\parallel$ values of the layers and hence quantify the relaxation of each component of the nBn structure.

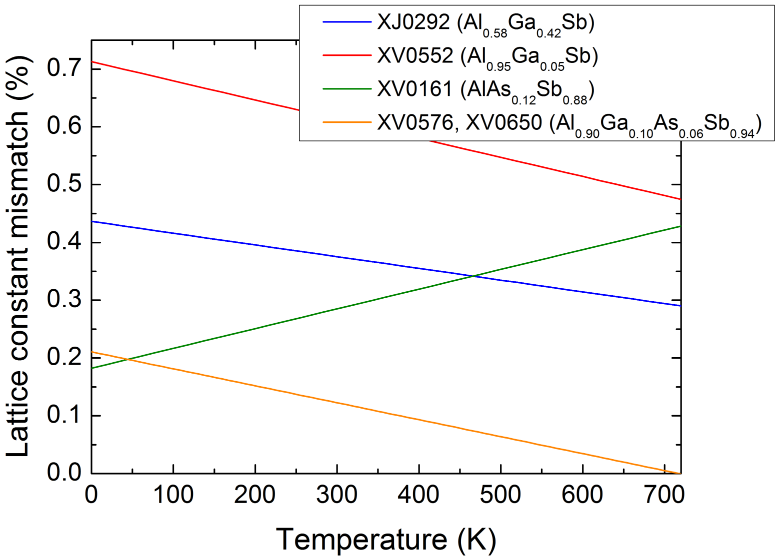

FIGURE 5.9: Lattice constant mismatch of the nBn device barriers grown on GaSb substrates as a function of temperature.

TABLE 5.4: Summary of the fitting parameters used to characterise samples grown on native GaSb substrates, fitted on the condition of no relaxation, as well as superlattice and barrier growth temperatures. "Primary SLS" refers to the main set of superlattice peaks in the XRD spectrum, and "Secondary SLS" refers to any split peaks, if present.

Sample		**XV0161**	**XV0576**	**XV0650**	**XJ0292**	**XV0552**
Primary SLS	d_{InAs} (nm)	4.60	5.71	3.63	5.21	7.42
	$d_{InAs_{1-x}Sb_x}$ (nm)	4.65	7.27	4.63	1.57	3.19
	x_{Sb}	0.178	0.16	0.158	0.4	0.31
Secondary SLS	d_{InAs} (nm)	-	5.83	3.53	5.78	7.8
	$d_{InAs_{1-x}Sb_x}$ (nm)	-	7.43	4.51	1.74	3.36
	x_{Sb}	-	0.161	0.21	0.42	0.32
$d_{absorber}$ (μm)		4.4	4.3	8.7	3.3	4.1
T_{SLS} (°C)		432	427	427	393	410
Barrier		$AlAs_{0.12}Sb_{0.88}$	$Al_{0.90}Ga_{0.10}As_{0.0.06}Sb_{0.94}$	$Al_{0.90}Ga_{0.10}As_{0.06}Sb_{0.94}$	$Al_{0.58}Ga_{0.42}Sb$	$Al_{0.95}Ga_{0.05}Sb$
$d_{barrier}$ (nm)		46	110	110	51	81
$T_{barrier}$ (°C)		470	427	427	458	410

Dual-colour nBn detector on GaSb

A simple dual-colour nBn detector can be devised by substituting an absorber layer designed for lower wavelengths in place of the contact layer of the device. Thanks to this stacked architecture no filters or mirror arrangements are needed to separate incident light into the relevant absorption bands, as the MWIR absorption layer is transparent to longer wavelengths. Extraction of carriers from the top absorber takes place at positive voltage values.

A dual-colour InAs/$InAs_{1-x}Sb_x$ nBn device (QA504) was grown on the VG V80-H system with a target $x_{Sb} = 0.36$ in the LWIR absorber and a target $x_{Sb} = 0.28$ in the MWIR one. The structure was n-doped at 4.1×10^{16} cm^{-3}. The XRD spectrum can be seen in Figure 5.10 and the full summary of the structure in Table 5.5. Unlike single-bandwidth samples described earlier, this structure incorporates an $Al_xGa_{1-x}Sb$ barrier with a stepped composition designed to minimise any valence band offsets. This is achieved in seven growth stages in which the gallium source temperature is kept constant while T_{Al} is increased in 10°C steps, with accompanying increases in T_{sub} and Sb valve position to ensure optimal crystal quality and sufficient Sb flux on the surface. Because the sticking coefficient of both Al and Ga is unity, a weighted average aluminium fraction can be calculated as 0.49; this is in good agreement with the XRD barrier peak identified at -890" (see Figure 5.10) and fitted with $x_{Al} = 0.52$ at full strain. However, the position of the 0th peak of the LWIR absorber is appreciably displaced from the substrate by about 170", pointing to presence of relaxation in the layer. In addition, a third set of peaks with a very high Sb content and a periodicity closely matching that of the LWIR superlattice can be identified. Considering that the superlattice was designed to be strain-balanced and that its absorber is relatively thin (∼900 nm), a likely explanation for the relaxation lies in the substrate temperature at the time of growth which, at 425°C, is unoptimised for the target $x_{Sb} = 0.36$ as discussed in Section 5.3, or Sb segregation to the growth surface. Another explanation may lie in the uncharacteristically large growth rate ratio of group V to III (2.8 ML/s and 1 ML/s) used at this stage of the recipe. Because of these factors, the fitting parameters proposed in Table 5.5 are an estimate based on the growth parameters and the spectral response results (see Section 6.2) rather than an accurate representation of the structure.

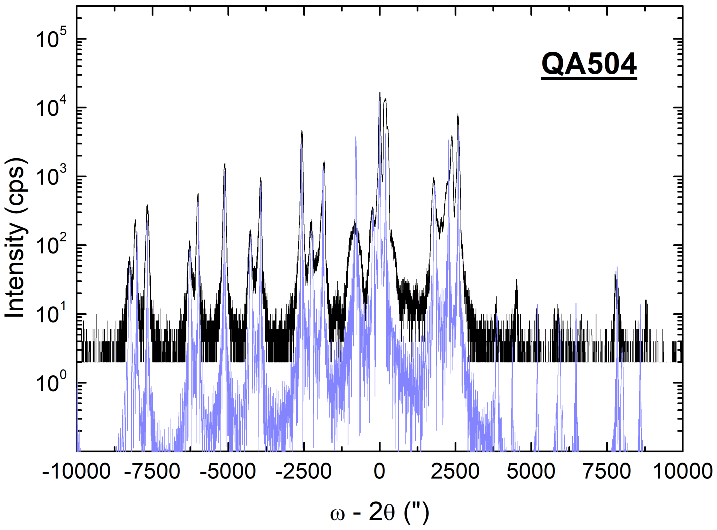

FIGURE 5.10: A coupled XRD scan of the dual colour sample QA504, grown on a GaSb substrate.

TABLE 5.5: Summary of the structural parameters of the dual-colour nBn sample QA504.

	d_{InAs} (nm)	d_{InAsSb} (nm)	x_{Sb}	d_{layer} (nm)	T_{growth} (°C)
MWIR SLS	4.78	2.35	0.275	927	425
LWIR SLS	6.85	2.03	0.35	932	425
Barrier	-	-	stepped	44	425 - 460

Transmission Electron Spectroscopy

Samples XV0161 and XJ0292 were further characterised by Richard Beanland at Warwick University using transmission electron microscopy, according to the method outlined in Section 4.2.2. A cross-sectional 2kX bright-field image of XV0161 can be seen in Figure 5.11, showing excellent crystallinity across the entire structure of the sample. A 100kX dark-field image of the barrier region can be seen in Figure 5.12. The compressed right-hand side of the image reveals a noticeable roughness of the upper barrier-superlattice interface compared to other interfaces, as well as very slight bowing of the superlattice layers. Because the critical thickness of the barrier at growth temperature is half of the actual thickness (see Table 5.3), this could have caused partial relaxation not evident in symmetric XRD scans, and subsequent defects like stacking faults. A high-contrast line terminating the barrier region (corresponding to a change in atomic number Z with respect to the layers surrounding it) can also be observed in the dark-field image, likely corresponding to unintended incorporation of Sb into the first InAs layer following the AlAsSb barrier, which is further confirmed by a spike in group V intensity immediately following barrier growth (see the HAADF data in Figure 5.13; note that the data is not resolution-limited as the measurement spot size was < 0.1 nm[151]). This could be due to either Sb segregation to the surface of the barrier, or incorporation of Sb remaining on the barrier surface following the 3 minute Sb soak before top contact growth (or a mix of both). However, the most significant feature revealed by group V intensity data is a non-abruptness of InAs/InAs$_{1-x}$Sb$_x$ interfaces that spans 2-3 nm, effectively introducing a Sb gradient across most of the well in this particular sample. Assuming Sb segregation to the surface during growth, it is possible

FIGURE 5.11: A cross-sectional 2kX bright-field transmission electron microscopic image of sample XV0161.

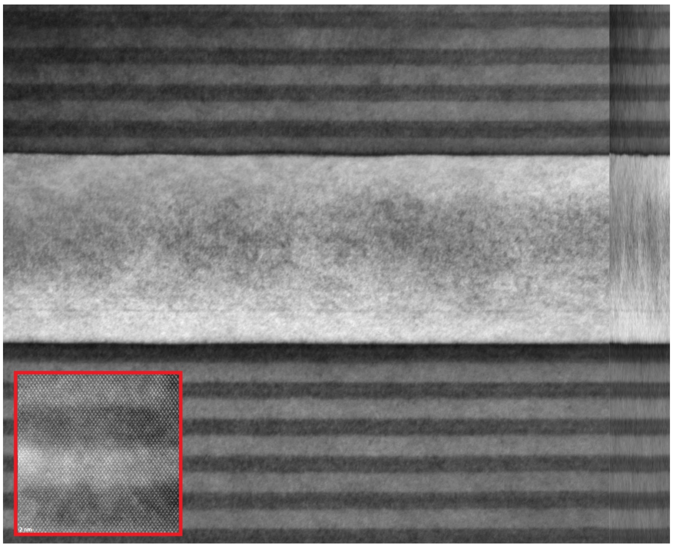

FIGURE 5.12: A cross-sectional 100kX bright-field transmission electron microscopic image of sample XV0161, showing the barrier region and the absorber and top contact superlattices. Inset: a magnification of several top contact superlattice layers.

to employ the Muraki model[152] to characterise the Sb and As gradients across the SLS interfaces. The elemental fraction x_n as a function of monolayer number n for a well with N monolayers can be calculated using

$$
\begin{aligned}
x_n &= x_0(1-R^n) \quad \text{for} \quad 1 \le n \le N \quad \text{inside the well} \\
x_n &= x_0(1-R^n)R^{n-N} \quad \text{for} \quad N \le n \quad \text{inside the barrier}
\end{aligned}
\tag{5.5}
$$

Here x_0 is the intended fraction, and R is the segregation probability $R = \exp(-d/\lambda)$ where d is half the lattice constant of the segregated-to layer, and λ is the so-called segregation length - the distance it takes for the element to decay by $1/e$. This last quantity can be obtained from the gradients of group V intensity peaks as demonstrated in the Figure 5.13 inset. The first $InAs_{1-x}Sb_x$ peak was excluded from calculations as it is the most likely one to be affected by the memory of the Sb barrier soak. The fits from the remaining peaks were averaged to values of $\lambda_{As} = 0.90 \pm 0.07$ nm and $\lambda_{Sb} = 0.97 \pm 0.10$ nm; in addition to this, human error due to noise in the gradient data was estimated to be ± 0.08 nm. Due to these two factors it is more reasonable to say that both segregation lengths are the same within their uncertainties.

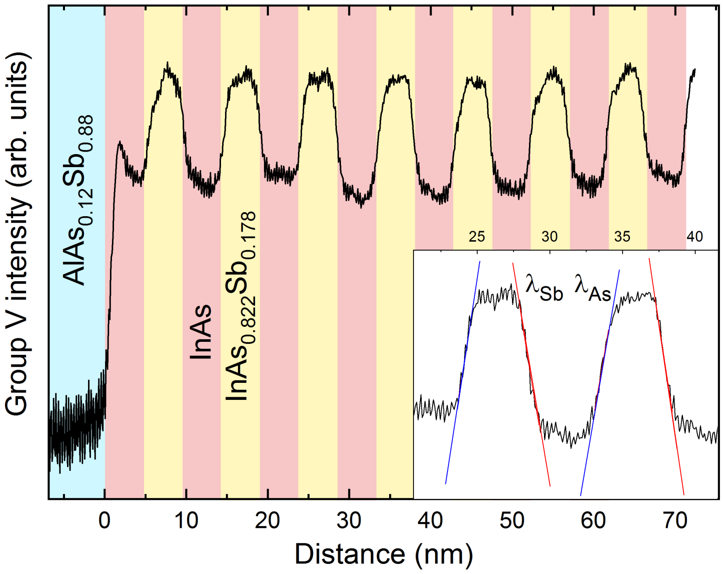

FIGURE 5.13: Group V intensity extracted from HAADF transmission electron microscopy data of sample XV0161 as a function of distance from the top of the barrier layer. An attempt was made to match the layer thicknesses extracted from XRD fits to the intensity peaks (coloured segments). Inset: Extraction of segregation length from the peak gradients.

This becomes more evident when segregation probability R is calculated for each gradient and then averaged, giving $R_{Sb} = 0.72 \pm 0.02$ and $R_{As} = 0.73 \pm 0.03$. Inserting these results into Equations 5.5 gives the equivalent x_{Sb} value across the two superlattice interfaces (Figure 5.14). According to these results, the Sb fraction does not reach the intended value for 2.0-3.0 nm of the layer thickness, which places practical limits on the minimum superlattice layer thickness.

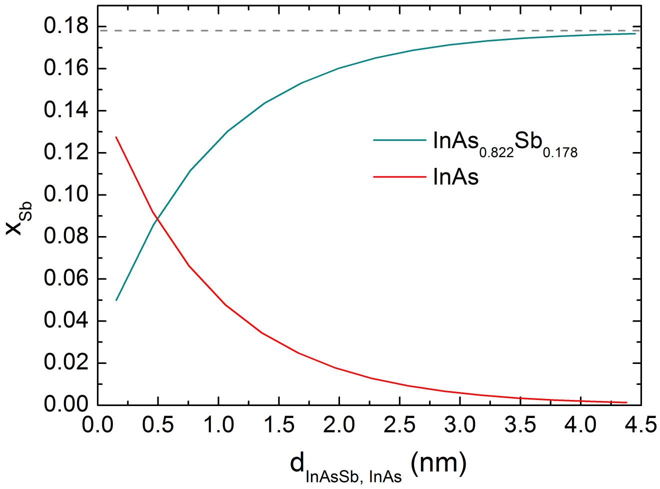

FIGURE 5.14: The gradient in Sb fraction across the $InAs_{1-x}Sb_x$ and InAs layers in sample XV0161, converted from group V intensity data using the Muraki model.

Elemental segregation during growth is a two-dimensional process that occurs on surfaces only rather than inside bulk[152,153], therefore it is reasonable to expect λ to be the same for superlattices of different periods so long as they are grown with the same deposition rate. Hence, the above analysis and the magnitude of the graded interface region is expected to apply to all samples discussed in this work.

A 3kX dark-field image of the high-Sb sample XJ0292 can be seen in Figure 5.15. As in the case of sample XV0161, no defects are evident in the entire cross-section of the device. However, an inspection of a 100kX dark-field image of the barrier region reveals a thicker period of the top contact superlattice when compared to the absorber one. A simple demonstration of this can be seen in Figure 5.16, where a section of the image containing the absorber superlattice is pasted onto the top contact SLS such that the bottom $InAs_{1-x}Sb_x$ layers align, then the superlattice periods are counted for both. It can be seen that for each 9 periods of the top contact SLS there are 10 periods of the absorber one.

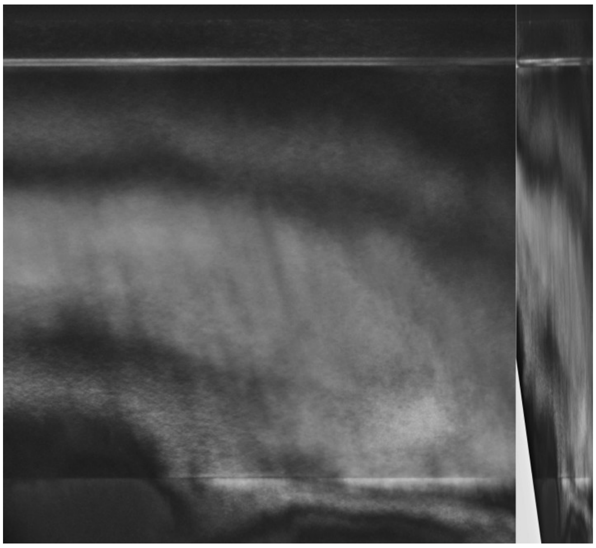

FIGURE 5.15: A cross-sectional 3kX dark-field TEM image of the high-Sb sample XJ0292 on GaSb.

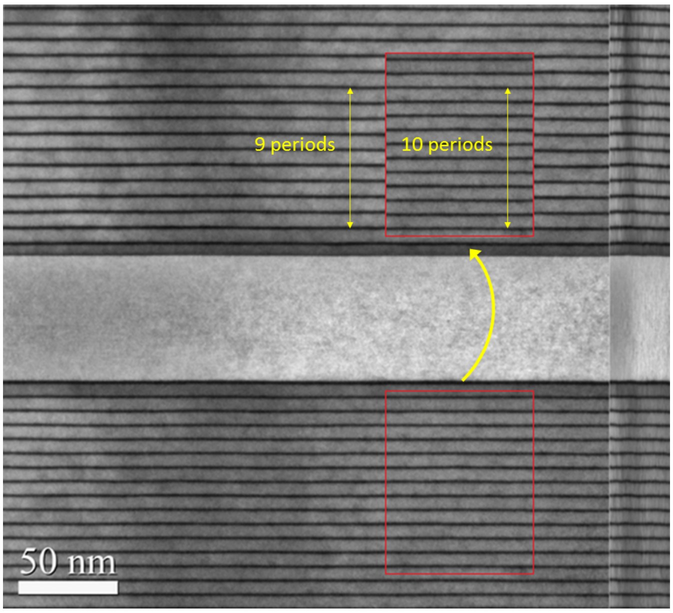

FIGURE 5.16: A cross-sectional 100kX dark-field image of the region around the XJ0292 barrier. A simple comparison of the SLS periods was carried out: a section of the bottom superlattice is pasted onto the top superlattice, and the periods counted.

This aligns closely with the sample's split peak XRD results (see Figure 5.8 and Table 5.4): the ratio of d_{InAs} and d_{InAsSb} in the primary SLS to those in the secondary SLS is 0.9 for both, confirming the origin of the splitting. Its origin does not appear to be related to the barrier design or growth: $Al_{0.85}Ga_{0.42}Sb$ is similarly well lattice-matched to the $AlAs_{0.12}Sb_{0.88}$ barrier in Sample XV0161 (see Figure 5.9); in addition, unlike the latter, the XJ0292 barrier h_c at growth temperature is very close to the actual barrier thickness (see Table 5.3). Finally, the unstrained $Al_{0.85}Ga_{0.42}Sb$ lattice constant is 6.12 Å at 300 K and 6.14 Å at growth temperature; therefore, if the barrier relaxed, the fully strained $a_{\perp}$ of the top contact superlattice would be smaller than that of the absorber superlattice, resulting in a smaller period. No section of the structure shows dislocations or defects indicative of relaxation that could force growth on a different lattice constant. Hence, a tentative explanation could be changing growth conditions: for example, if the indium cell temperature drifted during the barrier growth stage (an increase of 10% in growth rate would require a temperature rise of $\sim$ 5°C), perhaps due to temperature transients that could result due to an extended period of the indium shutter being closed while barrier growth progresses.

5.4.4 InAs/$InAs_{1-x}Sb_x$ growth on lattice-mismatched GaAs

This Section details the structural analysis of samples grown on GaAs using GaSb and AlSb buffer layers.

5.4.5 Growth on a GaSb buffer layer

The sample structures grown on GaAs substrates with buffer layers were characterised using the same XRD techniques as those in Section 5.4.3. Figure 5.17 shows the coupled symmetric scans of the MWIR samples XV0154, 0159 and 0160. These undoped epilayer samples were all grown on 325 nm of GaSb buffer layer and with the same target $x_{Sb} = 0.18$, as well as the same d_{InAs} to d_{InAsSb} ratio of 1:1; however, the actual layer thicknesses were varied in order to study the effect of superlattice layer thicknesses on their bandgap values. As a result, sample XV0154 is the thinnest, XV0160 has a superlattice period 2.2 times that of XV0154, and XV0159 has 3.3 times the period (full fitting parameters can be seen in Table 5.6).

TABLE 5.6: Summary of the fitting parameters used to characterise epilayer samples grown on GaSb buffer layers on GaAs substrates, fitted on the condition of no relaxation, as well as the superlattice growth temperatures.

Sample	**XV0154**	**XV0160**	**XV0159**	**XV0547**	**XV0234**
d_{InAs} (nm)	2.10	4.62	6.87	7.05	5.20
d_{InAsSb} (nm)	2.14	4.74	7.03	3.09	1.56
x_{Sb}	0.176	0.174	0.178	0.257	0.377
$d_{absorber}$ (μm)	0.70	0.78	0.76	0.74	0.74
T_{SLS} (°C)	424	424	424	410	413

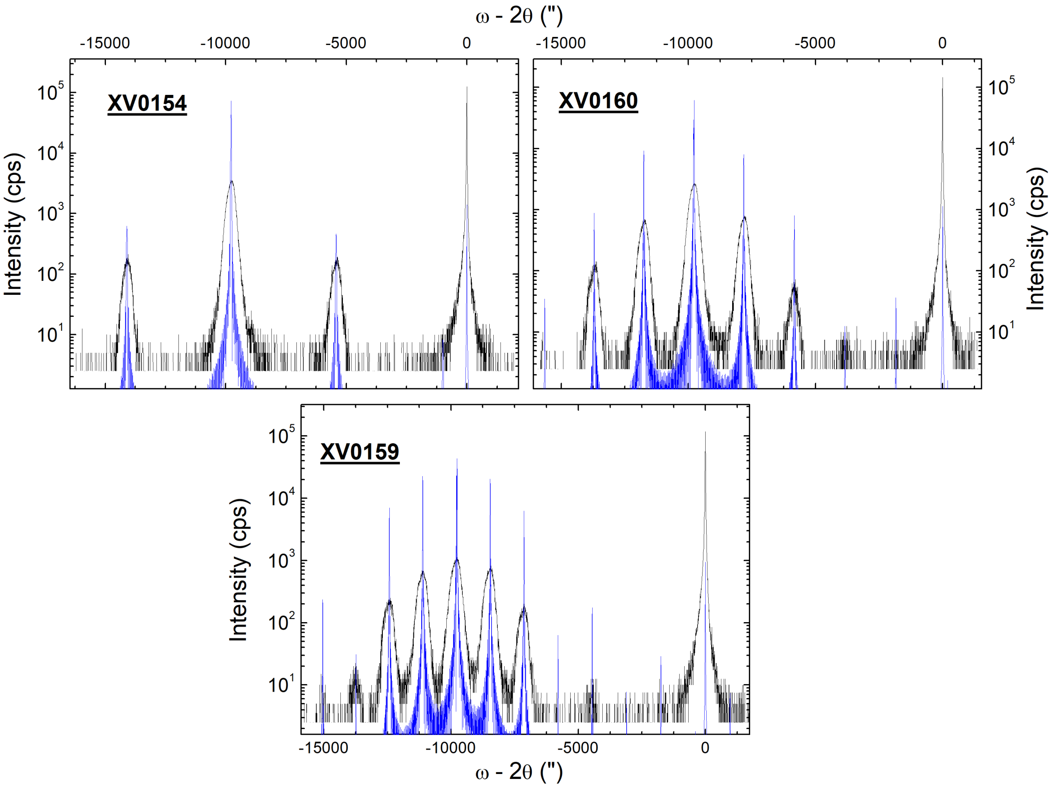

FIGURE 5.17: Coupled XRD scans of MWIR samples grown on GaAs substrates and GaSb buffer layers (black), and their modelled structures (blue).

This is evident from the spacing of the superlattice peaks in Figure 5.17 which decreases with increasing period thickness. The signal from the GaSb buffer cannot be discerned from the broad 0th superlattice peak, however based on the GaSb buffer study presented in Section 5.4.2, a 325 nm epilayer of GaSb is 97.6% relaxed and is located at -9773" with respect to the GaAs substrate. By inspection, the 0th superlattice peaks of these three samples lie in the range -9755 to -9765" with respect to the GaAs peak, which suggests that the relaxation of these layers is extremely low.

For completeness, Figure 5.18 also shows two examples of XRD spectra for high-Sb samples XV0547 ($x_{Sb} = 0.257$) and XV0234 ($x_{Sb} = 0.377$). Although no numerical analysis of the FWHM values was performed, it is clear that all samples grown on buffer layers have a degraded crystal quality when compared to the same structures on GaSb, most likely caused by the increased density of misfit dislocations (which tend to originate at the interface of the substrate and the highly lattice-mismatched epitaxial layer[154] and the local strain resulting from their presence).

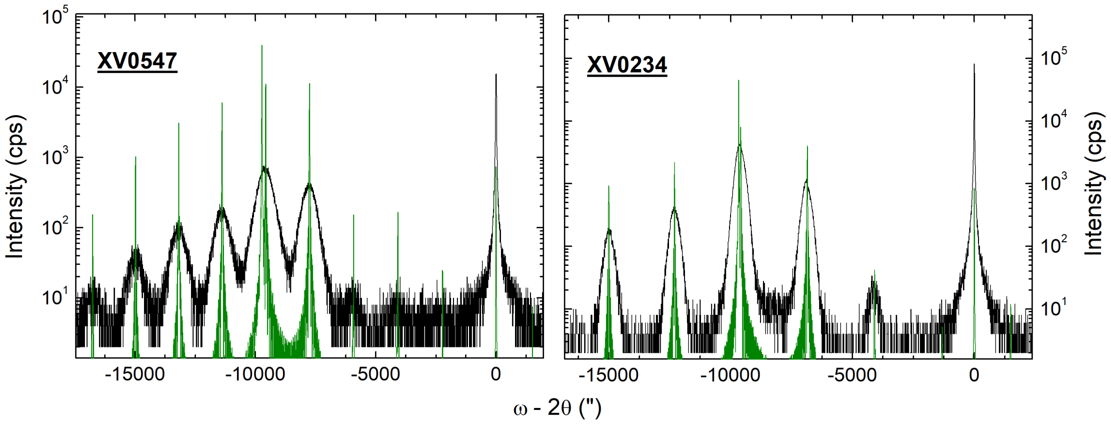

FIGURE 5.18: Coupled XRD scans of LWIR samples grown on native GaSb substrates (black), and their modelled structures (green).

5.4.6 Growth on an AlSb buffer layer

As demonstrated in Figure 5.3 in Section 5.1, it is possible to strain-balance a high-Sb ($\sim$0.35) superlattice at approximately 1:1 monolayer ratio when the substrate lattice constant is a_{AlSb}. This is in contrast to a_{GaSb}, which beyond $x_{Sb} \sim 0.18$ requires increasingly thicker d_{InAs} to strain-balance the SLS cell. In order to test the feasibility of growing an nBn device on an AlSb buffer, a test device was grown at 1:1 ML ratio incorporating $x_{Sb} = 0.33$.

The coupled XRD scan can be seen in Figure 5.19, demonstrating the same peak broadening associated with growth on relaxed buffer layers. The AlSb buffer was grown to a thickness of 1.1 μm, resulting in its 97.8% relaxation as outlined in Section 5.4.2. Just like in the case of SLS growth on the GaSb buffer, the 0th order superlattice peak is shifted away from the position of the buffer layer, however this time the shift is about 300" as opposed to $\sim$ 30", pointing to a more severe relaxation of the superlattice proper. This is expected, however, due to the fact that unlike the GaSb buffer samples, the XV0208 superlattice is not correctly strain-balanced at its $x_{Sb} = 0.33$, leading to partial relaxation. The full fitting parameters and relevant growth conditions can be seen in Table 5.7.

TABLE 5.7: Summary of the fitting parameters used to characterise the nBn device sample XV0208, grown on an 1.1 μm AlSb buffer layer. The superlattice and the barrier were both fitted fully strained, while the AlSb layer was fitted at 97.8% relaxation.

Sample	**XV0208**
d_{InAs} (nm)	3.99
d_{InAsSb} (nm)	4.09
x_{Sb}	0.33
$d_{absorber}$ (μm)	3.1
T_{SLS} (°C)	430
Barrier	$Al_{0.75}Ga_{0.25}Sb$
$d_{barrier}$ (nm)	54
$T_{barrier}$ (°C)	468

The effect of using a lattice-mismatched substrate for epitaxial growth of a superlattice structure can be fully appreciated in the TEM images of the same sample, seen in Figure 5.20: presence of misfit 60° threading dislocations is clear. Misfit dislocations, which relieve strain associated with growth beyond h_c, in {001} crystals nominally form in the <110> directions, however at large enough (>1%) lattice mismatch they are expected to form a much more irregular dislocation pattern near the lattice-mismatched interface due to initial island growth of the mismatched layer[154].

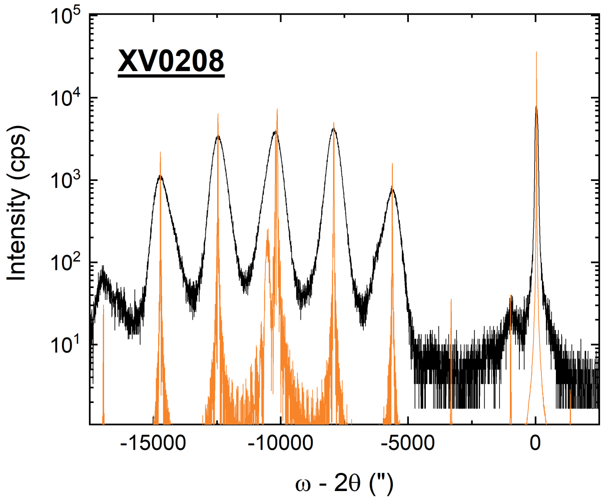

FIGURE 5.19: Coupled XRD scans of LWIR samples grown on native GaSb substrates (black), and their modelled structures (orange).

This occurrence is evident when examining the GaAs-AlSb interface in Figure 5.20 (left), which is found to be the source of most dislocations in the structure as well as have the largest density of them. In addition, due to the latent lattice mismatch between AlSb and the superlattice, the interface between the two also acts as a defect source with the more typical <110> dislocations forming.

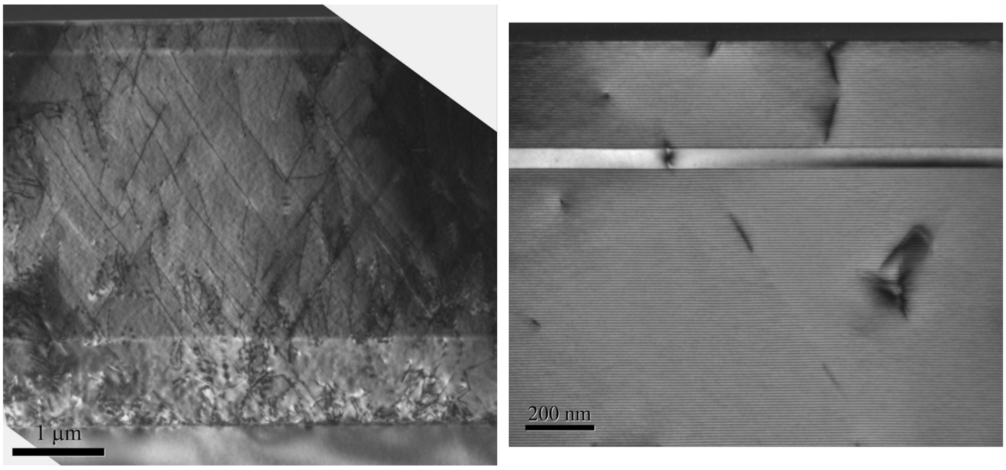

FIGURE 5.20: Dark-field transmission electron miscrocopy images of sample XV0208 with 3kX (left) and 10kX (right) magnification. Misfit dislocations are evident in the structure, especially at the buffer-substrate interface.

The magnified right-hand side image of Figure 5.20 shows the barrier region of the nBn, with a relatively lower dislocation density, likely because any residual strain between the SLS and the buffer layer would have been relieved via relaxation in the lower portion of the absorber. Nevertheless, deleterious threading dislocations (which tend to form together with misfit dislocations[155]) are still present.

5.5 Conclusions

The first part of this Section (5.1) focused on outlining the design principles of an InAs/InAs$_{1-x}$Sb$_x$ superlattice such that a strain-balanced structure with a desired fundamental bandgap E_g is achieved. In particular, the potential advantages of growth of high-Sb SLS on a_{AlSb} instead of a_{GaSb} are outlined.

In Section 5.2 the design choices for an effective InAs/InAs$_{1-x}$Sb$_x$ nBn device are presented, including barrier design, appropriate layer thicknesses, and n-doping density. All these considerations are then incorporated into a molecular beam epitaxy growth recipe in Section 5.3.

Structural characterisation of representative samples follows in Section 5.4, primarily including X-ray diffraction analysis; three nBn devices, XV0161 and XJ0292 grown on native GaSb and XV0208 grown on an AlSb buffer layer, are also analysed via transmission electron miscroscopy.

Because the epilayer SLS samples are grown on lattice-mismatched GaAs substrates with the use of AlSb or GaSb buffer layers, these buffer layers are first grown and characterised separately in order to quantify their relaxation as a function of thickness (Section 5.4.2). GaSb is found to relax 99.2% towards its native a at a thickness of 670 nm, however the AlSb buffer reaches a plateau of $\sim$ 97.5% at 570 nm that continues up to 1.1 μm. In addition, non-uniformity of x_{Sb} across a 1/4 wafer is quantified and shown to be negligible for samples grown on GaSb wafers, however buffer-grown samples demonstrate a variation of up to 0.7%, possibly due to spatially uneven relaxation of the buffer itself (Section 5.4.1).

Next, in Section 5.4.3 nBn devices grown on native GaSb are characterised. The coupled XRD scans show well-defined, narrow superlattice peaks pointing to very good crystallinity and strain balance. High resolution scans, however, reveal 'split' superlattice peaks pointing to presence of slightly structurally different superlattices. The possible explanations for this are explored; it is found that that the samples with the best XRD characteristics (XV0650 and XV0576) have barrier thicknesses under h_c at all temperatures. A dual-colour nBn device on GaSb with a stepped-composition barrier is also demonstrated, however its heavily split XRD spectrum suggests that pseudomorphic growth was not achieved.

In the following Section 5.4.3, one MWIR and one LWIR nBn device grown on GaSb are characterised using transmission electron miscroscopy. The samples are shown to be entirely discloation-free, supporting the XRD results. More significantly, group V intensity as a function of thickness was characterised for sample XV0161, revealing a non-negligible Sb gradient across the SLS interfaces; the Muraki model[152] was then employed to find a segregation length of $\lambda_{Sb} \sim 0.95$ nm.

A LWIR sample XJ0292 was also characterised via TEM, showing similarly dislocation-free structure. However, a comparison of the absorber to contact superlattice periods showed the latter to be about 11% thicker - this potentially explains the origin of the secondary XRD SLS peaks as their period is larger by the same amount.

In Section 5.4.4, all samples grown on buffer layers exhibit peak broadening. For epilayers grown on GaSb buffers, the displacement of the 0th order SLS peak from the GaSb buffer peak is negligible, indicating little to no relaxation. The nBn device XV0208 grown on AlSb, however, shows a peak displacement of about 300". Degraded crystal quality is confirmed in TEM images which show an array of misfit and threading dislocations, concentrated mostly around the two AlSb interfaces.

5.5.1 Future work

In the future, the simplest way of improving the understanding of these structures would be to implement asymmetric rocking curve scans using the Bede QC200 XRD system. This would give access to the $a_{\parallel}$ values of the samples, which together with $a_{\perp}$ could be used to quantify layer relaxation. In order to further improve crystal quality of the superlattices, substrate growth temperatures could be further optimised. Minimising dislocation density in buffer layer samples is unlikely (and impractical) to be achieved by simply thickening the buffer layer; instead, SLS dislocation filters promise a more practical approach[156]. This is particularly pertinent to growth based around the AlSb lattice constant: a well-designed dislocation filter, rather than a simple buffer, appears to be the necessary next step to achieving functional devices. Finally, barrier quality could be improved by ensuring $d_{barrier} < h_c$ at all relevant temperatures, and that $a_{barrier}$ is as closely lattice-matched to the substrate as possible within the nBn design parameters.

Chapter 6

II. Results and discussion: Optical Properties

Three optical properties of the samples were measured in order to characterise the wavelength response and bandgap behaviour of InAs/InAs$_{1-x}$Sb$_x$ superlattices. Temperature dependent absorption coefficients of the undoped InAs/InA$_{1-x}$Sb$_x$ superlattices were calculated from transmission measurements performed on a Fourier Transform Infrared spectrometer, and the temperature dependence of the fundamental bandgaps $E_g(T)$ was then extracted; this is outlined in Section 6.1.1. Spectral response of the nBn devices, and the extracted $E_g(T)$ are presented in Section 6.2. Finally, three MWIR epilayer samples were characterised at 4 K using photoluminescence (Section 6.3). The resultant $E_g(T)$ datasets are then modelled with the use of the single-oscillator temperature dependence model described in Section 2.1.2 and the calculated parameters are related to the more commonly used Varshni model in Section 6.4. Finally, the Kronig-Penney model (Section 2.1.2) is combined with the $E_g(T)$ data to calculate the band structure, band positions and band offsets of the undoped epilayer samples in Section 6.5.

6.1 Fourier Transform Infrared Spectrometry

This Section details transmission measurements performed on undoped superlattice epilayers, and the resultant fundamental bandgap $E_g(T)$ temperature dependencies.

6.1.1 Transmission

Transmission spectra for various samples at different temperatures were obtained using the Vertex 70 Fourier Transform IR spectrometer (see Section 4.3 for the method). The measurements were taken either at room temperature by mounting the samples on a magnetic plate, or by installing the specimen in an LN_2-cooled cryostat and obtaining a set of temperature-dependent spectra. Because the inclusion of the cryostat introduces significant additional factors into the measurement, this Section as well as 6.1.2 are divided into two parts based on each method.

Transmission at 300 K

Figure 6.1 shows example transmission spectra obtained from Samples XV0160, XV0545 and XV0443. Atmospheric absorption bands can be observed at several points, including H_2O in the atmospheric window (roughly 5 to 8 μm) and a CO_2 peak at $\sim$14.5 μm. It is prudent to note that a mid-infrared source FTIR equipped with a KBr beamsplitter is unsuitable to analyse spectra beyond $\sim$ 17 μm, due to severely decreased intensity of the blackbody source and poor efficiency of the KBr beamsplitter at these wavelengths[137].

The majority of radiation not transmitted can be attributed to thickness-independent Fresnel reflection in the GaAs substrate, described by Equation 2.33 where the extinction coefficient k_{GaAs} is 0 for the entire range under consideration (see Figure 6.3).

However, when the thickness of a layer begins approaching light wavelengths in free space, Fabry-Perot fringes can form due to constructive and destructive light interference. Therefore, in order to aid their identification in the experimental spectra a model designed by Steven J. Byrnes[157] is used, which implements a series of classical equations using a transfer matrix method to calculate propagation characteristics across a stack of variable-thickness layers. The relevant input is the layer thicknesses, the coherence characteristics of each layer (an incoherent layer is thick and non-uniform enough to average out the Fabry-Perot fringes - in this case, only the substrate), and

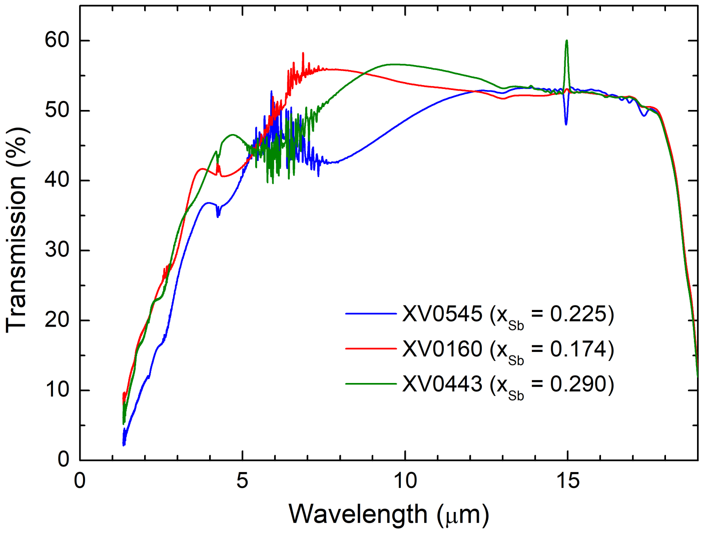

FIGURE 6.1: Example transmission spectra obtained at room temperature using an FTIR.

heavy hole well and barrier thicknesses in the superlattice. Refractive index as a function of wavelength data was collated from a number of sources[54], including the imaginary extinction coefficient k for GaAs, InAs and GaSb, which however decay to 0 at comparatively short wavelengths and play no further role in the analysis of fundamental SLS bandgaps. The refractive index of a ternary is a function of the material's composition; therefore, n_{InAsSb} at x_{Sb}=0.20, 0.25, 0.30 and 0.35 were interpolated from data found in Paskov et al[55]. The real effective refractive index of the superlattice is calculated using Equation 2.35[53]. Although IR beam divergence is likely to be present in all the measurements, only light at normal incidence is modelled. A resultant output from the calculation can be seen in Figure 6.2 overlaid with the experimental spectrum of the two samples XV0160 and XV0443. For both samples, slight offset is observed with respect to the experimental peaks, likely due to the difference between the real and modelled x_{Sb} values and other simplifications. The real peaks are also broader, most likely owing to the non-ideality of the superlattice interfaces as discussed in Section 5.4.3, causing the thin films to be only partially coherent. For the MWIR sample XV0160, assuming that the fundamental absorption edge begins around 6.5 μm (as derived later in Section 6.5), two useful observations can be made. First, apparent absorption at wavelengths beyond 7 μm can be at least partially attributed to free carrier absorption[52,158] and possibly deep state absorption[159]; second, the characteristic 'knee' at ∼ 3.5 μm, is more likely to be due to a higher-band transition rather than a reflection artifact, because none of the layers in the structure have thicknesses conducive to multiple reflection. The latter observation can also be made for sample XV0443. All other fringes at shorter wavelengths appear to be attenuated by the absorptive and non-ideal properties of the superlattices.

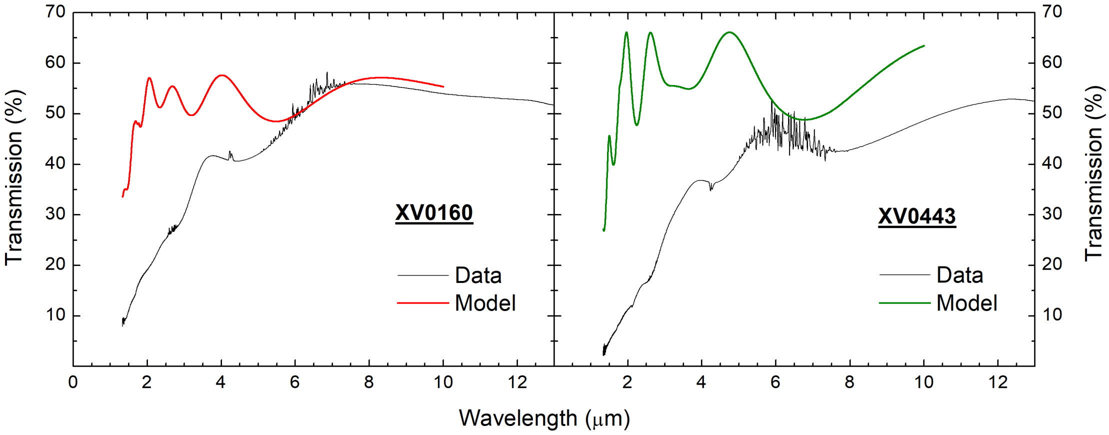

FIGURE 6.2: Comparison between the transmission data and its modelled curve for the samples XV0160 and XV0443. Absorption due to the superlattice is not included in the model, causing the rising offset between the two curves.

In order to extract the absorption coefficients of the superlattices (see Section 6.1.2), the sample spectra need to be normalised with respect to the non-superlattice layers. All the samples in this work are normalised to the spectra of semi-insulated GaAs substrates, rather than to GaSb buffer layers grown on GaAs. The reason is evident from Figure 6.3: the presence of a thin layer of GaSb introduces reflection artifacts not present in the superlattice samples since the GaSb buffer layer in the latter does not form an interface with air. As GaSb is not expected to contribute to absorption at wavelengths of interest here, it is excluded from normalisation. The increased transmission feature of GaAs at ∼ 1.5 μm is not due to specimen reflection and disappears in GaAs spectra taken in the cryostat, pointing to its origin in the apparatus.

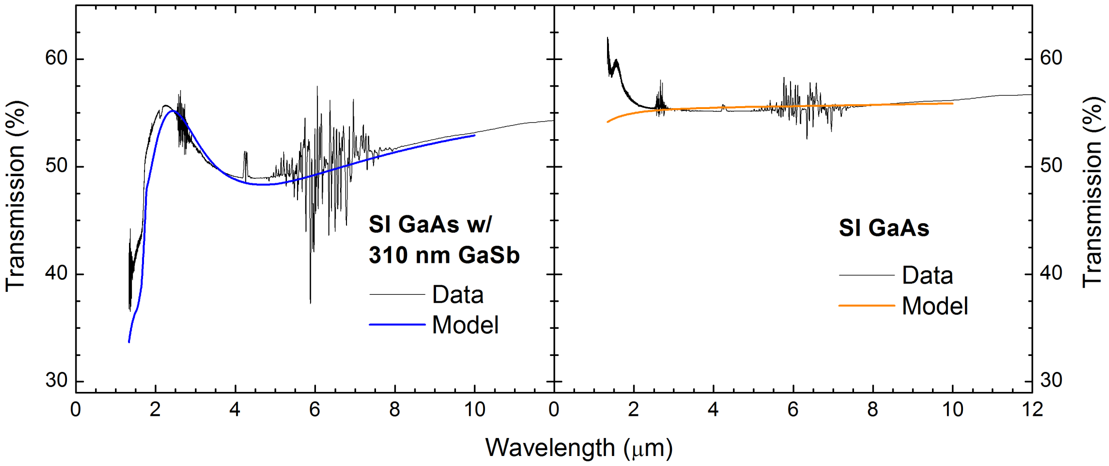

FIGURE 6.3: Left: 300 K transmission spectrum of a 310 nm GaSb buffer layer grown on a semi-insulated GaAs substrate. Right: the spectrum of a SI GaAs substrate only.

Transmission below 300 K

The transmission lineshape of a specimen is susceptible to variations in experimental conditions, and so care needs to be taken when introducing additional instruments into the measurement and analysing the resultant spectra. The inclusion of a cryostat mount in the beam path has several potential effects on either the magnitude or shape of the spectrum, which can be due to additional reflection paths, unaccounted for absorptive layers, or potentially inconsistent sample placement in the beam. The additional reflective/absorptive components are the ZnSe transmission windows (with no AR coating), the polished copper sample holder (chosen for its thermal conductivity), the acrylic sample plate, and the vacuum-grade aluminium foil used to shield the chamber from any outgassing of thermal grease (discussed below). The reflectivity of copper is a constant near-100% in the optical range under consideration[160], while the transmission of uncoated ZnSe is a constant 70%. However, transmission of acrylic in the infrared region is wavelength-dependent[161] and potentially entirely opaque. Therefore, if the alignment of the sample plate with respect to the window is inadvertently changed between the reference and the sample measurements, it could lead to a modulation of the total amount of IR light reflected and cause a baseline error in the transmission data. Additionally, the holder and sample assembly take a non-negligible amount of time to thermally settle at a desired temperature and as such, in order to ensure good thermal contact of the copper sample holder with the cryostat, the holder components are coated with cryogenic vacuum grease; this, however, appeared to occasionally introduce thin films of grease on the windows and the sample the first time the grease was introduced into vacuum, possibly through outgassing of trapped air. This was subsequently eliminated by wrapping the greased area with aluminium foil. In order to identify instrumental artifacts, a series of measurements without sample proper were taken. Figure 6.4a) shows reflective fringes resulting from the ZnSe transmission windows (red), the copper and perspex sample holder (black), and the Al foil (blue). The modulation of the spectrum by the foil is unexpected and is more likely due to the fact that the foil obscures some of the reflective copper plate when included. All the reflection fringes can be eliminated from the spectra by very carefully handling the cryostat between taking the reference measurement and installing the sample, so the alignment of all components remains unchanged. Similarly, it is preferable to take all relevant measurements as closely to each other in time as possible.

The wavenumber axis can be affected primarily by two factors: the position of the sample in the beam, and the size of the sample aperture. This is because in a real FTIR system, the beam of light entering the interferometer is never perfectly collimated since this would require an ideal point source. This results in the presence of divergent light rays with an apparent wavelength shorter than the rays in the centre of the beam. In the optimal factory-supplied configuration (used for the measurements in Section 6.1.1), the sample surface is located in the centre of and perpendicular to the beam focus as seen in Figure 4.5, which minimises any influence of beam divergence. The custom-made cryostat sample holder, however, introduces an offset of about 1 cm from the beam image plane, and also has a rotational axis. Therefore, it is necessary to ensure that the holder position is preserved exactly the same when handling the cryostat between the reference and sample measurements, because an off-centre sample placement (as well as planar misalignment with the beam) can introduce shifts in the wavenumber axis[137].

In addition to transmission artifacts of cryostat components, the effect of placing a 4 mm aperture at the sample beam focus was also measured. This was done by obtaining the 300 K spectrum of a polystyrene optical filter at 4 cm^{-1} resolution with and without the aperture present (Figure 6.4 b)). The instrument aperture was set to 6 mm, which is standard for all measurements in this work. As expected, no measurable wavenumber shift occurs due to the presence of an extra aperture.

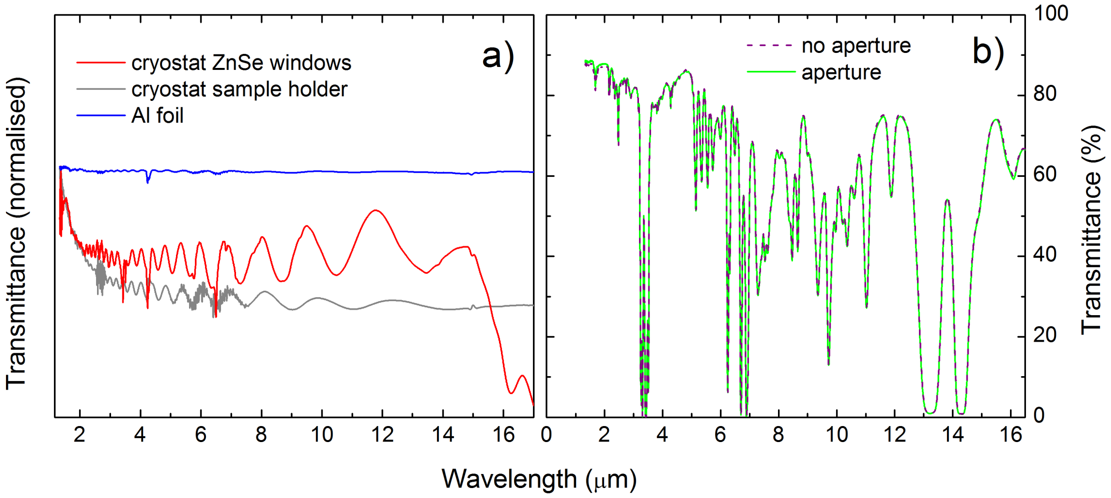

FIGURE 6.4: Left: the normalised transmission spectra of various cryostat components, showing their reflective fringes. Right: The spectra of the polystyrene optical filter with and without the 4 mm aperture installed inside the sample compartment, showing no wavenumber shift due to the presence of the aperture.

Due to the number of measurements required to obtain a single absorption coefficient spectrum (ie. background measurement for the substrate followed by the substrate measurement, followed by the same sequence for the sample proper) it is necessary to be able to differentiate baseline errors incurred by measurement or contaminated sample surface, and genuine absorption features near the bandgap. The latter includes the following processes, in order of magnitude: free carrier absorption below the bandgap[52], doping and shallow impurity states (which combine into the Urbach absorption tail, discussed in detail in Sections 2.1.3 and 6.1.2); heavily localised deep states[159]; and near-bandgap exciton states decaying into a constant α offset[20]. The latter two are not expected to exceed $\sim 10^1$ cm^{-1} in magnitude and thus cannot be resolved in the transmission data in this work. Free carrier absorption manifests itself as an (often monotonically increasing with wavelength) absorption feature located several tens of meV below the optical bandgap, and can be discarded from analysis. In contrast to these intrinsic mechanisms however, which can be either discounted due to their irresolvably small α value (deep state and exciton transitions) or easily identified (free carrier absorption), instrumental baseline errors can be non-negligible and vary from measurement to measurement. These have been identified to arise almost exclusively from the inclusion of the cryostat and its in-house built sample holder in the apparatus. First, it has implications for the geometry of the beam path. Unlike the supplied Bruker holder for room-temperature measurements, the custom holder has a rotational axis, and so the perpendicularity of the beam path and the holder aperture needs to be judged by eye every time the holder is installed. In addition, the holder aperture is displaced from the beam focus. The combined effect of these two factors on detected beam intensity can be qualitatively appreciated in Figure 6.5: the rotation of the sample away from perpendicular alignment with the beam path will cause a lateral shift in the beam, which will subsequently fail to focus on the detector; similarly the displacement of the sample towards the IR source and away from the beam focus shifts the focus towards the mirror. In both cases transmission of the sample would be underestimated due to signal loss.

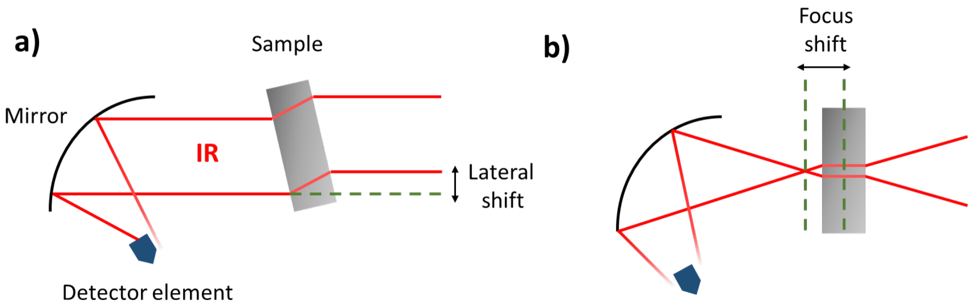

FIGURE 6.5: Effects of sample misalignment in the FTIR optical beam path. a) Sample rotation causes a lateral shift in the transmitted beam path with respect to the mirror, and effectively the detector element. b) A visual approximation of two separate factors: non-negligible sample thickness, and sample placement in front of the beam focus. In both cases the beam focus is translated forwards. Figures adapted from Bruker Application Note[162].

In a related scenario, some conditions can change between the reference and sample measurement taken on the day. For example, thermal grease (despite being vacuum-graded) has been observed to evaporate at an unknown rate (probably due to expansion of trapped air pockets) and form a layer on the ZnSe windows and the sample; this however was addressed with the introduction of covering Al foil.

6.1.2 Analysis of absorption coefficients

Magnitudes and features at 300 K

By normalising the transmission spectrum of a non-device sample to that of semi-insulating (SI) GaAs it is possible to derive the absorption coefficient spectrum of the superlattice. This is done by solving Equation 2.32 (which takes into account mutliple reflections in thin films[52]) numerically. In this context, the superlattice transmission is defined to be $^{I}/_{I_0}$, where I is the spectral data of the sample, and I_0 that of SI GaAs obtained at the same temperature. Reflectivity R_s is calculated with the use of Equation 2.33; and even though the extinction coefficient k_{SLS} is unknown, it can be realised that $(1 \pm n_{SLS})^2 \gg k_{SLS}^2$ when the absorption coefficient α is of the order of $\sim 10^3$ cm^{-1} and below, which is true for the parts of the spectrum that are of interest. As such, k_{SLS} can be taken to be 0.

Three typical examples of absorption coefficient spectra taken at 300 K can be seen in Figure 6.6 a). The dependence of the position of the absorption edge on x$_{Sb}$ is evident, and will be discussed in detail in Section 6.5. It is worthwhile to further analyse the α spectra in this work in comparison to other prominent detector structures operating in the IR region: bulk HgCdTe and InAs/GaSb type-II superlattices; as well as related low-bandgap alloys InSb and InAs$_{1-x}$Sb$_x$ (all of which are direct bandgap systems[8,16,30,49,77]).

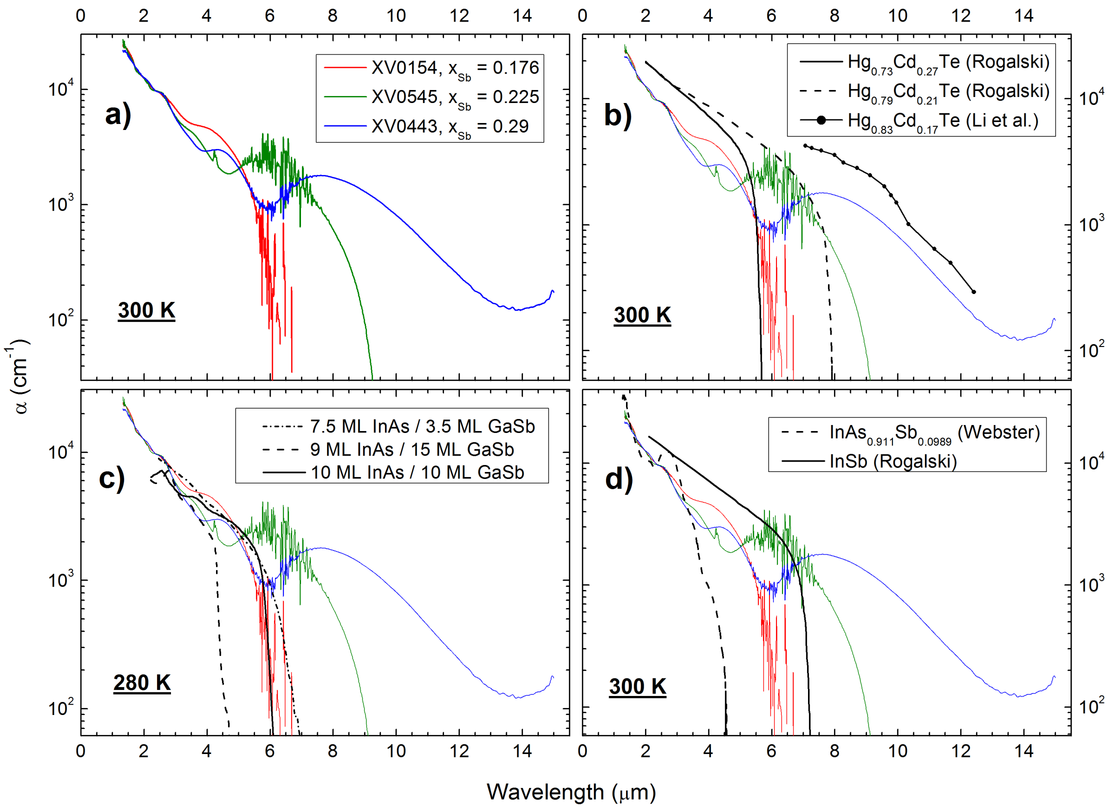

FIGURE 6.6: Absorption coefficient spectra of three samples (colour), obtained at 300 K, and literature comparisons (black). a) The data from this work. b) Bulk $Hg_{1-x}Cd_xTe$ epilayers with different compositions[7,76]. c) InAs/GaSb T2SL grown on GaSb substrates with varied superlattice periods[163]. d) Undoped bulk InSb and $InAs_{0.911}Sb_{0.089}$[5,42].

Typical α spectra for these systems can be seen in Figure 6.6, overlaid in black over the InAs/$InAs_{1-x}Sb_x$ data from this work. 6.6 b) shows the room-temperature spectrum of a number of undoped bulk $Hg_{1-x}Cd_xTe$ thin films (two MWIR[5] and one LWIR[76]). 6.6 c) shows three InAs/GaSb T2SL spectra (taken at 280 K) grown on GaSb with varied superlattice periods[163]. And finally, 6.6 d) shows the two bulk III-V materials: the absorption curve of bulk InSb[5] as well as $InAs_{0.911}Sb_{0.086}$[42], each with a cut-off in the MWIR region. It becomes immediately apparent that the magnitude of the absorption coefficients of the InAs/$InAs_{1-x}Sb_x$ epilayers is very comparable in magnitude and behaviour to that of the other materials: the onset of fundamental transition of these superlattices occurs near $\alpha \sim 10^3$ cm^{-1} and rises to a magnitude of 10^4 cm^{-1} across the infrared range of photon energies. Interestingly, the long-wavelength

$Hg_{0.83}Cd_{0.17}Te$ sample shows a gradient of fundamental absorption that is very similar to that of sample XV0443, although the bulk nature of the conduction band ensures a monotonic increase of α while the XV0443 absorption demonstrates the more step-like nature of superlattices. Also, as a direct consequence of the miniband superlattice band structure, Tian et al[163] find the form of $\alpha_{InAs/GaSb}$ to vary in response to the thickness of the GaSb barrier in three InAs/GaSb samples (see Figure 6.6 c)), an effect also observed in the InAs/$InAs_{1-x}Sb_x$ epilayers and further discussed in Section 6.5.

Extraction of the fundamental bandgap E_g

Figure 6.7 shows the absorption coefficient of sample XV0545 obtained at 300 K and normalised to a SI-GaAs substrate.

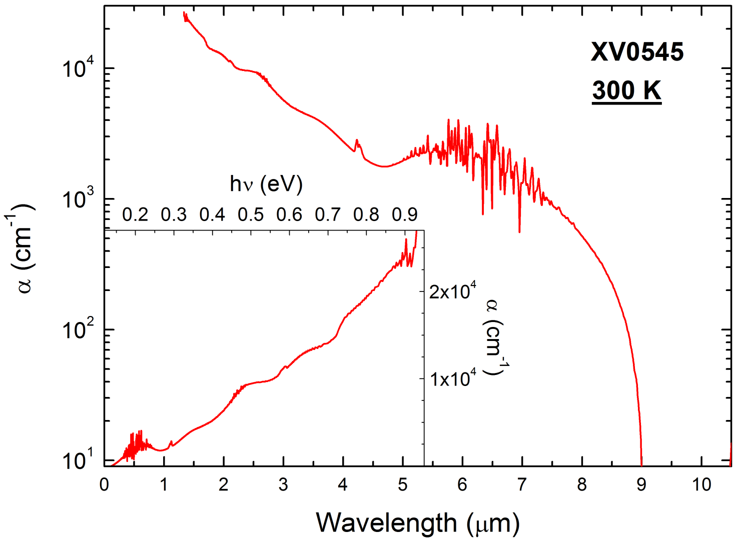

FIGURE 6.7: The absorption coefficient α spectrum of the sample XV0545, obtained at room temperature. The inset shows the same data plotted on a linear scale as a function of photon energy.

A sharp onset of absorption can be observed at $\sim 9\mu$m which eventually becomes shallower. This behaviour is characteristic of quantised energy minibands and steps in the density of states; the decreasing gradient of the onset would be indicative of a decaying wavefunction overlap[42]. However, the features such as the valley at $\sim 4.7\mu$m could be a reflection artifact as Equation 2.32, which aims to account for multiple internal reflections, assumes an air-sample-air interface, whereas the real sample is a structure with two additional internal interfaces due to the presence of the buffer layer, and which could introduce second-order reflection effects.

In order to analyse the bandgap region of the absorption, an attempt is made to identify the so-called Urbach tail of absorption due to sub-bandgap states (see Section 2.1.3). In the Urbach region, α_U assumes an exponential form which manifests itself as a straight line on a semi-log plot of $\alpha(h\nu)$, and which can be seen in Figure 6.8.

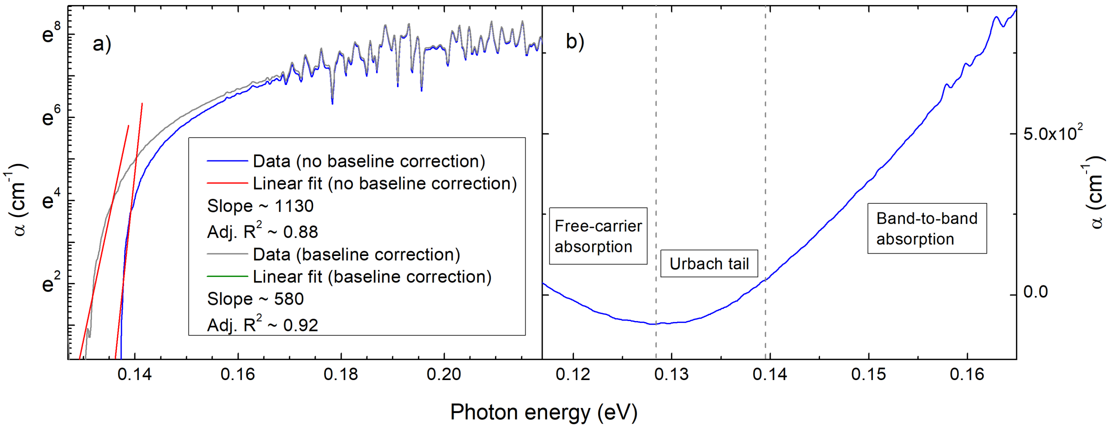

FIGURE 6.8: An attempt at identifying the Urbach tail of states in the absorption spectrum of the sample XV0545: a) The linear fits of original (blue) and baseline-corrected (grey) data have adjusted R^2 values of about 0.9 and slopes of $\sim 580 - 1130$, indicating an extremely low value of E_U; b) a visual inspection of the α spectrum indicates that the Urbach tail terminates at ~ 0.140 eV.

The characteristic energy width of the tail E_U, which can be understood as the representation of structural and thermal disorder in the material[46], is then equal to $(\mathrm{d}ln(\alpha_U)/\mathrm{d}h\nu)^{-1}$. However, when this analysis is applied to the absorption onset region of the spectrum data, the quality of the linear fit represented by the adjusted R^2 value is below only about 0.90, with an extremely low E_U value of just under 1 meV. Upon first inspection, this could be due to a baseline error in the original spectrum resulting in part of the tail falling under 0 cm^{-1}, which would exclude it from logarithmic analysis. However, the application of a baseline correction to this data, which results in an E_U value of only $\sim$ 1.7 meV, does not appreciably improve the quality of the fit ($R^2 \sim 0.92$ as opposed to 0.88). Several other explanations are possible. First, E_U inherently increases with doping[51]; however, the sample under consideration has no intentionally introduced dopants beyond background contamination of the MBE growth chamber. In addition, this particular sample is well strain-balanced, which would minimise any parameters related to structural disorder. However, a study performed by Bansal et al[52] on high quality undoped $InAs_{1-x}Sb_x$ crystals ($x_{Sb} \leq 0.05$) finds the E_U value at 300 K to be $\sim$ 40 meV, which the authors establish to be due to fundamental alloying-induced disorder (similarly, the lowest observed Urbach parameter of highly crystalline undoped GaAs at room temperature has been reported as ~7 meV[46]); and because samples like XV0545 are more complex structures grown on mismatched substrates which is known to cause dislocations (as per Section 5.4.4), its E_U would be expected to be higher. As such, it is possible that at least part of the true Urbach tail is obscured due to a baseline offset in α introduced when normalising the sample spectrum to that of GaAs, a proposition supported by observing a region of negative value of $\alpha(h\nu)$ near 0.130 eV in Figure 6.8 b), and by inspecting the region just beyond 0.130 eV, which demonstrates a weakly exponential behaviour. Although E_U cannot be calculated reliably, in both graphs presented in Figure 6.8 the exponential region appears to terminate near $h\nu = 0.140$ eV, falling in the α range below 100 cm^{-1} which is of the same order of magnitude as the one in the study by Bansal et al[52]. Therefore, on the assumption that this analysis is sufficient, $h\nu = 0.140$ eV is chosen as the cross-over energy between Urbach and band-to-band absorption.

It is informative to plot α as a function of photon energy $h\nu$, in line with Equations in 2.36 for direct and indirect bandgap materials. The inset of Figure 6.7 shows the result for XV0545 plotted on a linear Y-axis, which, qualitatively, follows the same form as the $\alpha_g(h\nu)$ function (see Equation 2.32). To better appreciate this observation, and to consider the fact that Equation 2.32 is defined for energies near the bandgap only, α_g^2 and $\alpha_g^{1/2}$ are plotted as functions of $h\nu$ in Figure 6.9.

By the mathematical definition of α_g, a direct-bandgap material will result in a single straight line in the α_g^2 plot. In an attempt to identify E_g, the first section of the α_g^2

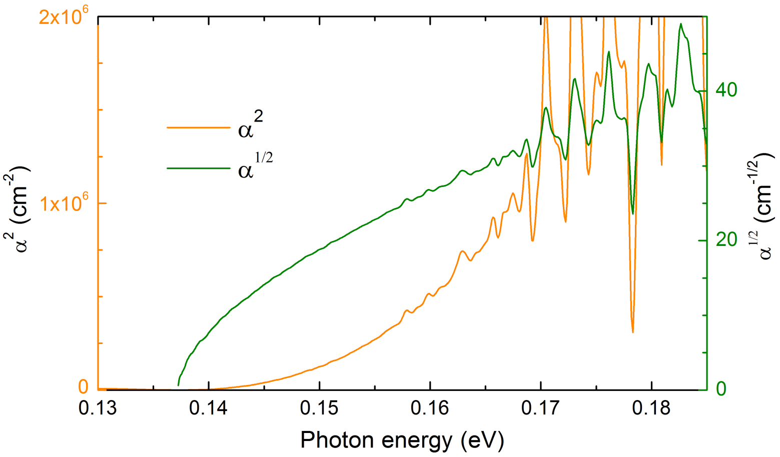

FIGURE 6.9: $\alpha_g^{1/2}$ and α_g^2 of the sample XV0545 in the vicinity of the bandgap, plotted as a function of photon energy.

spectrum above the Urbach tail but below the atmospheric absorption window that demonstrates linear behaviour is fitted to a straight line in Figure 6.9. Although the linearity of the fit is not immediately obvious due to stray bands of atmospheric absorption, the adjusted R^2 value of the fit is 0.97, while the linear region itself is expected to extend into the atmospheric window as well. Using this method, the fundamental bandgap E_g is found to be 0.148 eV.

Unlike the direct bandgap spectrum, the case of an indirect bandgap is less straightforward due to the presence of two transitions instead of one: $E_g \pm E_{ph}$, corresponding to both phonon emission and absorption. As such, the $\alpha^{1/2}(h\nu)$ plot is actually expected to contain two straight-line regions near the optical bandgap, corresponding to the two processes[57,164], and because the energy of the assisting phonon can only be $\pm E_{ph}$, the value of E_g would then be located equidistant between the x-intercepts of the two fits. Importantly, the phonon emission process ($E_g + E_{ph}$) is expected to dominate near-bandgap absorption due to its increased probability, resulting in a specific form of $\alpha^{1/2}$ that can be seen in the inset of Figure 6.10[57]. It can be appreciated in the same Figure (bottom) that this behaviour is not reproduced in the $\alpha^{1/2}$ data for XV0545. A single linear region between 0.148 eV and the atmospheric window is discernible; this would be interpreted to correspond to the higher-energy phonon emission process, while the low-α_g absorption appears to be obscured by the same measurement artifact that causes the abnormally steep Urbach tail. As such, $E_g + E_{ph} = 0.126$ eV with the true indirect bandgap located below that.

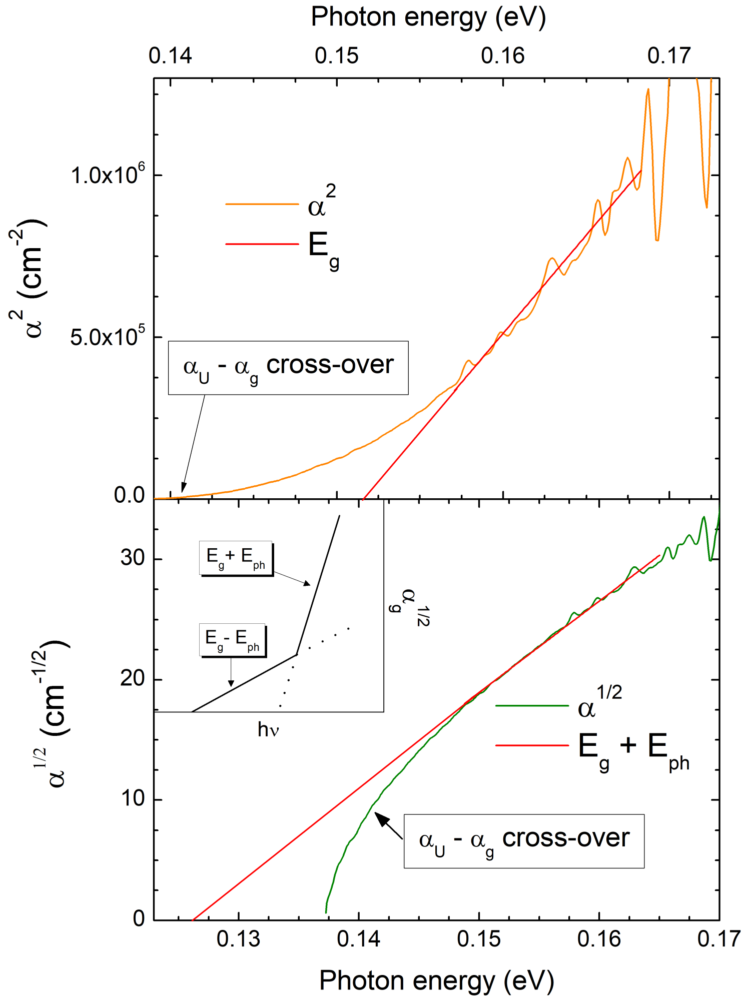

FIGURE 6.10: The two linear fits of α_g^2 (top) and $\alpha^{1/2}$ (bottom) of sample XV0545 in the region of the bandgap. The Urbach tail is taken to terminate near 0.140 eV. Only one linear fit is possible for $\alpha_g^{1/2}$, which is thought to correspond to the phonon emission transition. The inset shows the expected behaviour of $\alpha^{1/2}$.

This analysis was applied to a number of sample spectra with different x_{Sb} and superlattice structures, taken at room temperature without the use of a cryostat. The location of the first straight-line absorption feature was consistently found to occur in the $1 - 4 \times 10^3$ cm^{-1} range of the absorption spectrum, which is in agreement with values found for InAs/InAs$_{1-x}$Sb$_x$ superlattices[165] and other similar structures as noted in the preceding Section. Unlike the near-bandgap spectrum of sample XV0545, some

$\alpha^{1/2}$ curves demonstrate behaviour consistent with that shown in the inset of Figure 6.10 allowing for tentative fits of low-α phonon absorption ($E_g - E_{ph}$) transitions. An example of such behaviour can be seen in Figure 6.11 for sample XV0443, where an additional weak transition is fitted right above the Urbach tail.

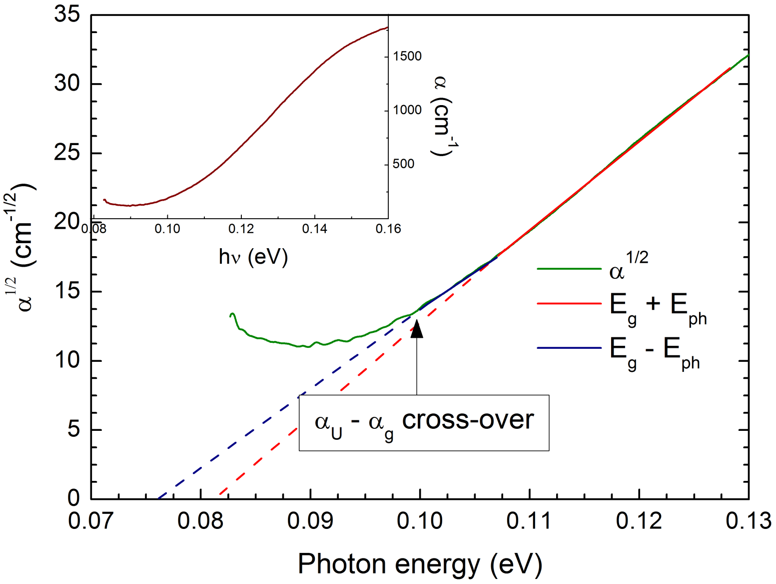

FIGURE 6.11: The two linear fits of $\alpha^{1/2}$ of sample XV0443 in the region of the bandgap. $E_g + E_{ph}$ (phonon emission) is the dominant absorption mechanism in indirect semiconductors. The lower-energy phonon absorption process is denoted $E_g - E_{ph}$.

However, because the boundary between this transition and the sub-bandgap tail is not clearly defined, and the subsequent uncertainty in the fit gradient, the obtained phonon absorption transition values (if any) are not as robust as those of phonon emission and direct bandgap ones. The full results are gathered in Table 6.1.

The bandgap-narrowing effect of Sb incorporation is evident across all samples; the variability of E_g for equal-Sb samples XV0160, 0154 and 0159 is explained by miniband shifts arising due to varied barrier and well thicknesses (see Section 6.5). The indirect transition values are always lower than the direct bandgap ones, albeit by an inconsistent offset (in strictly analytical terms, the $\alpha^{1/2}$ analysis is much more sensitive to x-axis shifts caused by baseline errors than α^2, yielding less reliable fits). In order to further investigate the direct/indirect nature of the fundamental transition

TABLE 6.1: Fitting of the various near-band edge transitions to room-temperature absorption coefficients α of different samples, exploring both possibilities of the structures being either indirect ($\alpha^{1/2}$) or direct α^2 materials. ($\alpha^{1/2}$) corresponds to near-band edge fits of phonon (-) absorption and emission (+) transitions.

			$\alpha^{1/2}$		α^2
Sample	x_{Sb}	*Urbach edge (meV)*	$E_g + E_{ph}$ *(meV)*	$E_g - E_{ph}$ *(meV)*	E_g *(meV)*
XV0160	0.174	190	151		196
XV0159	0.178	181	164		185
XV0154	0.176	211	187		220
XV0440	0.30	108	57	35	114
XV0443	0.29	101	80	68	117
XV0446	0.275	108	76	63	115
XV0448	0.29	120	119	115	136
XV0545	0.225	140	129		151
XV0234	0.37	134	76	65	138
XV0558	0.235	141	105	85	162
XV0232	0.31	130	129		149
XV0560	0.26	160	116	88	165
XV0235	0.41		19		78

in the InAs/InAs$_{1-x}$Sb$_x$ system, a supporting result can be derived from an α spectrum by calculating its first derivative and identifying the peak corresponding to the maximum change in fundamental absorption (or the maximum change in the joint density of states). Typical results, which can be seen in Figure 6.12 for selected samples, are consistently much closer to the bandgap values obtained using the α^2 fitting method, rather than the $\alpha^{1/2}$ fits, which strongly suggests that the band structure of the InAs/InAs$_{1-x}$Sb$_x$ system is direct. As such, α^2 results only are used for further analysis.

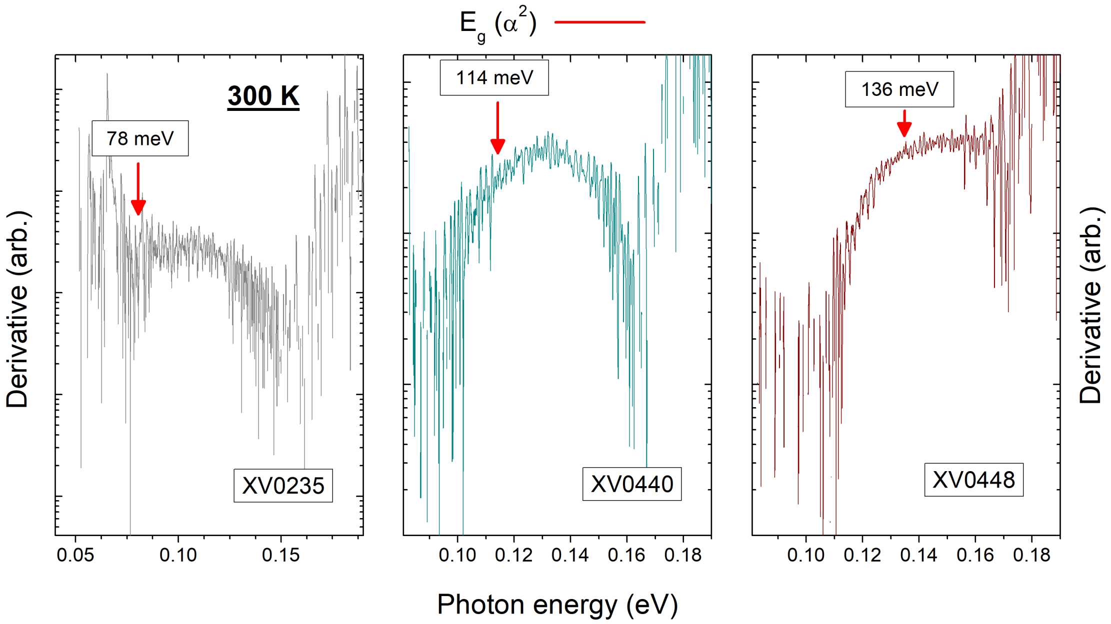

FIGURE 6.12: First derivatives of $\alpha(h\nu)$ of samples XV0235, XV0440 and XV0448 in the vicinity of the fundamental band-to-band transition. $E_g(\alpha^2)$ refers to the bandgaps derived from the absorption coefficients.

Temperature-dependent bandgaps $E_g(T)$

The investigation of InAs/InAs$_{1-x}$Sb$_x$ absorption coefficients was extended to cryogenic temperatures by installing the samples in an OptistatDNV2 cryostat, which was then mounted in a custom holder in the optical path of the FTIR beam (for the full description of the procedure see Section 4.3). The implications of this change in experimental conditions for the resultant data are explored in detail in Section 6.1.1, however the extraction of bandgap values proceeds in the same manner as in Section 6.1.2 A typical evolution of the temperature-dependent α spectrum (sample XV0232) can be seen in Figure 6.13.

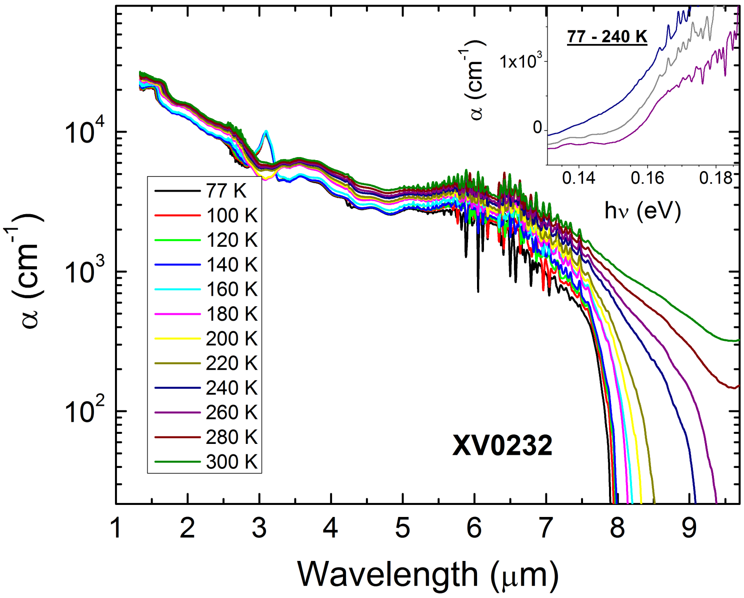

FIGURE 6.13: Temperature-dependent absorption coefficient of sample XV0232.

A relative increase of the α values with respect to the 77 K curve is observed for all samples as higher bands are filled with carriers at lower energies due to temperature-induced bandgap narrowing, and the steepness of the absorption onset above the bandgap decreases with the shift to higher wavelengths due to the $\alpha_g \propto \lambda^{-1/2}$ dependence on the latter (as per Equation 2.36). Importantly, a plot of $\alpha(h\nu)$ near the bandgap for three temperatures (77, 160 and 240 K as seen in the Figure 6.13) shows no temperature dependence of the absorption gradient characteristic of an indirect semiconductor as outlined in Figure 6.6, further supporting the proposition of a direct fundamental bandgap transition in InAs/InAs$_{1-x}$Sb$_x$. Although the instrumental factors discussed in Section 6.1.1 leave some reflection artifacts in the curves (as can be seen at shorter wavelengths in Figure 6.13) and the multi-step normalisation procedure introduces baseline offsets below 10^3 cm^{-1} in some spectra, it should be noted that due to the mathematical form of α^2 the straight-line fits are largely resistant to systematic errors and generally did not

TABLE 6.2: Comparison of fundamental bandgaps obtained at 300 K with and without the cryostat in place. The differences arise due to instrumental factors introduced by the inclusion of a cryostat in the measurement.

	Bandgap at 300 K (no cryostat) (meV)	*Bandgap at 300 K (cryostat) (meV)*
XV0154	220	223
XV0159	185	176
XV0160	196	188
XV0545	149	140
XV0232	149	152
XV0440	114	112

require baseline corrections, which can be confirmed by examining the 300 K bandgaps taken with and without the cryostat in place. The differences between the two measurements, which can be seen in Table 6.2 for a number of samples, allow to estimate the uncertainty when fitting the temperature-dependent spectra, and which is calculated to be ±6 meV using a simple average.

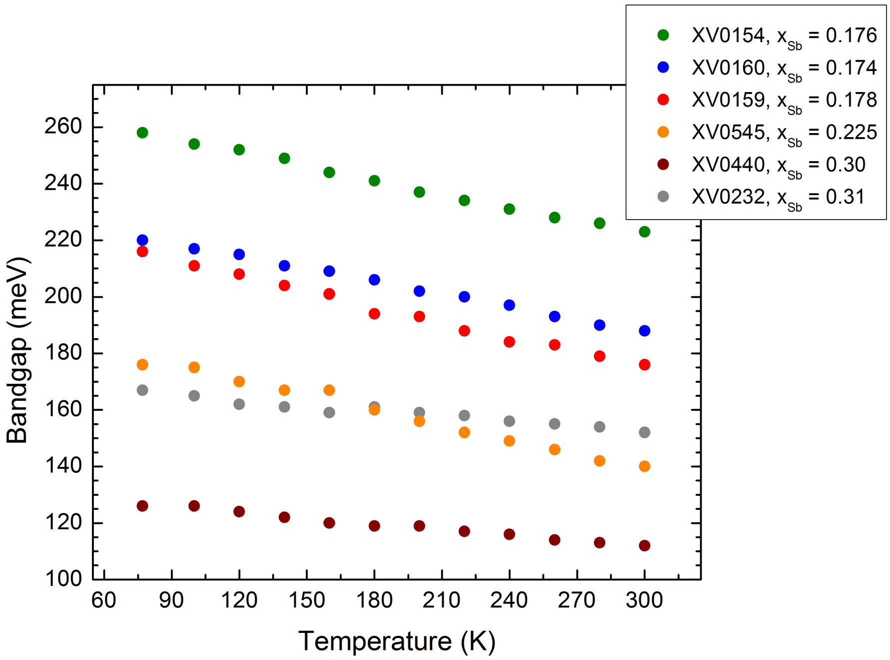

FIGURE 6.14: Temperature dependence of the bandgaps of a range of epilayer samples, derived from their absorption coefficients.

The final temperature dependencies of a range of samples with $x_{Sb} = 0.174 - 0.31$ can be seen in Figure 6.14. All samples undergo a narrowing of the bandgap as expected of the III-V materials in the high-temperature regime. The total reduction in bandgap varies in the range 15-35 meV is more shallow for higher-Sb samples, which could have implications for the operational range of LWIR devices based on these structures. For the full analysis of temperature dependence of these superlattice in context of the Einstein single-oscillator model see Section 6.4.

6.2 Spectral response

Temperature-dependent spectral response (SR) measurements were carried out on a number of nBn samples using the methods outlined in Section 4.6.1. The samples characterised were often designed so that their Sb fraction and SLS periodicity match a transmission sample so that their optical characteristics can be compared. Because the raw spectrum data has no reference channel (unlike transmission measurements), the obtained spectra were customarily normalised to a theoretical blackbody curve calculated at 1320 K, the temperature of the FTIR MWIR source. The resultant temperature-dependent spectra for the MWIR samples XV0161, XV0576 and XV0650 can be seen in Figure 6.15 (see Table 5.4 for their structures). For each sample the temperature varies from 77 K in 20 K steps up to the temperature at which the signal-to-noise ratio becomes too small to be produce a useful spectrum; all three samples exhibit measurable signal response up to 280 K. Although the $x_{Sb} = 0.178$ sample (XV0161) has the longest fundamental cut-off wavelength of the three MWIR samples (corresponding to the smallest fundamental bandgap of the three samples; see Section 6.4 for the extracted bandgap values), the absorption edges have different gradients and so their 50% cut-off wavelengths $\lambda_{50\%}$ (the wavelength at which the response intensity falls by half) and maximum response SR_{max} don't follow a simple x_{Sb} dependence.

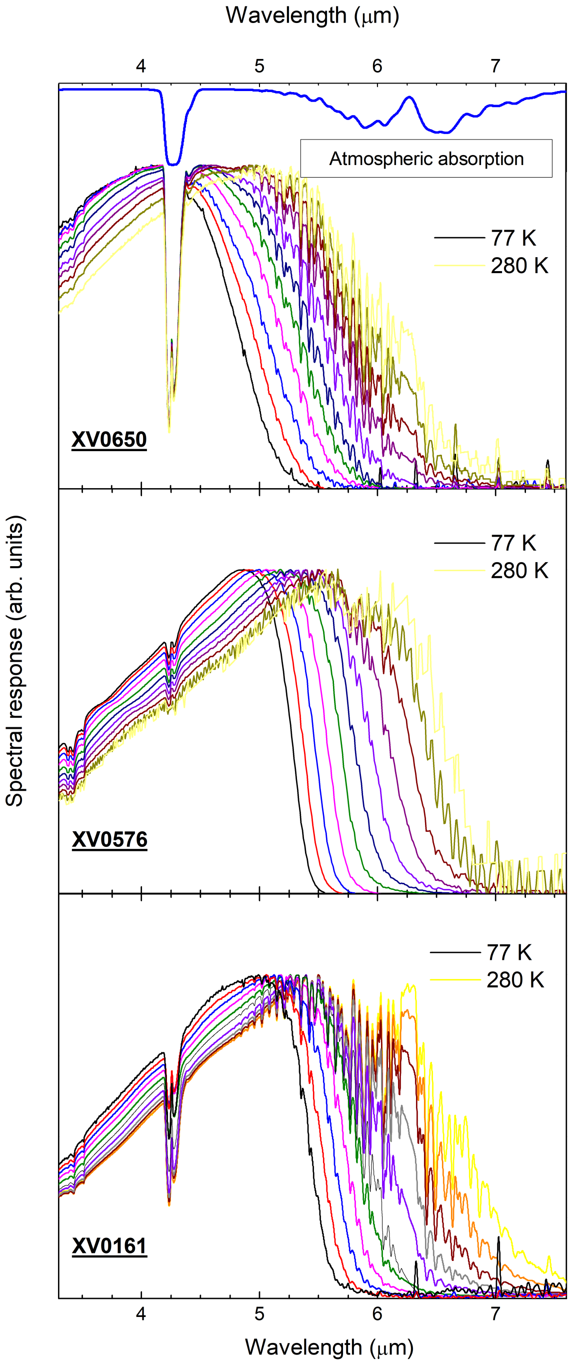

FIGURE 6.15: Normalised temperature-dependent spectral response curves of three MWIR samples. Each curve corresponds to a 20 K increase in temperature from the previous measurement. Atmospheric absorption (not to scale), which causes a partial decrease in response near high-T peaks, is shown for reference.

This effect can be appreciated in Figure 6.16, which shows normalised spectral responses of the three samples at 160 K. Here, the approximate SR$_{max}$ positions are extracted by estimating their values from the graph. Because all three spectra have atmospheric absorption features that obscure the true position of SR$_{max}$, an uncertainty for each is also estimated (see Table 6.3 for the results). $\lambda_{50\%}$ values are obtained by linearly fitting the absorption edge before the Urbach tail and finding the value of the fit at 50% spectral response.

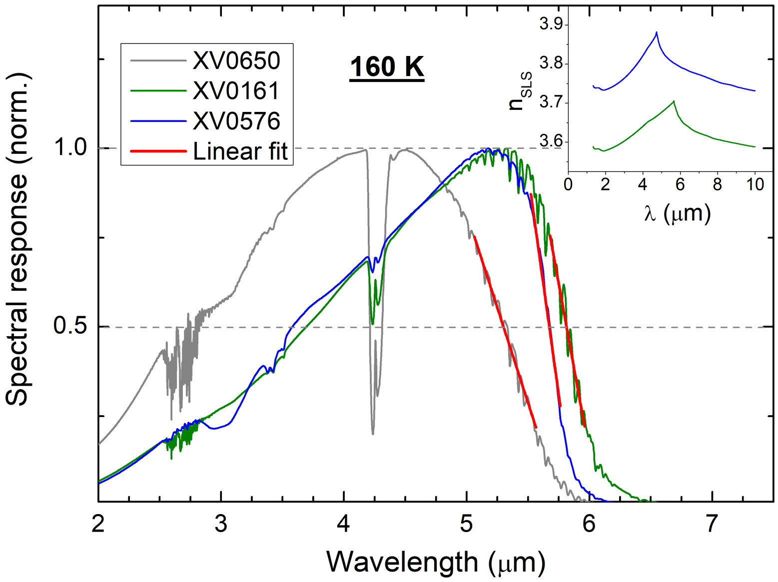

FIGURE 6.16: Normalised spectral response curves of three MWIR samples at 160 K. The grey dotted lines are included to help identify maximum and 50% response for each. Inset: calculated refractive indices of samples 0161 (green) and 0576 (blue).

Sample XV0650 shows the weakest onset of fundamental absorption of the three. This is likely due to the intentional increase in n-doping of the absorption layer compared to all the other nBn devices in this work (5×10^{17} cm^{-3} as opposed to 6×10^{16} cm^{-3}), which is believed to have caused a reduction in the effective absorbing volume via a shortened minority carrier diffusion length (the mean distance a carrier will diffuse from its point of creation before it recombines), and was also observed to severely affect the sample's responsivity (see Section 7.2.1). The other two samples, however, have the same target doping levels and absorber thicknesses despite demonstrating

TABLE 6.3: The 50% cut-off wavelengths $\lambda_{50\%}$ and the maximum spectral responses SR$_{max}$ of MWIR samples.

Sample	**XV0161**	**XV0650**	**XV0576**
$\lambda_{50\%}$ (μm)	5.81	5.29	5.67
SR_{max} (μm)	5.29 ± 0.03	4.34 ± 0.16	5.20 ± 0.02

different gradients. Therefore, in terms of fundamental transition processes, a tentative explanation for this difference could be provided in the context of oscillator strength S of the transition between the conduction and the first heavy hole bands. This quantity is fundamentally defined as proportional to the quantum probability of transition between two energy levels[166], and can be redefined such that[165]

$$S \propto n_{SLS}\left(\frac{\alpha_0}{\rho_0}\right) \tag{6.1}$$

where n_{SLS} is the refractive index of the superlattice, α_0 is the absorption coefficient of the ground-state transition, and ρ_0 is the ground-state optical joint density of states. Using Equation 2.35 to find n_{SLS} as a function of wavelength yields an S value for XV0576 that is approximately 0.2 higher near the absorption edge than that of XV0161 (see Figure 6.16 inset), which could provide the explanation; however it is worth noting that Webster et al[165] use spectroscopic ellipsometry to find n_{SLS} to be approximately 3.6 for a series of InAs/InAs$_{1-x}$Sb$_x$ SLS samples regardless of their structure. An alternative explanation is offered by the fact that the ground-state joint optical density of states varies as $\rho_0 \propto d^{-3}$, where d is the superlattice period[165]. This means that S increases proportionally to d^3 (Equation 6.1), which would increase S for XV0576 as expected. On the other hand, this difference in absorption gradient could have a purely growth-related explanation: for example, a minor decrease in real MBE dopant growth rates over time could be a structural explanation for the small difference in absorption onset, as the sample XV0576 was grown a year later than XV0161.

Figure 6.17 shows the spectral response of two LWIR nBn samples. Sample XV0548 has $x_{Sb} = 0.30$ while for XV0552 it is 0.31, and their $\lambda_{50\%}$ are 8.7 to ~11.1 μm for the former, and 8.5 to ~10.7 μm for the latter. Uncharacteristically, maximum response shows very weak temperature dependence. This unusual behaviour of SR$_{max}$, combined with an uncharacteristic 'shoulder' emerging at higher temperatures, could point to non-neglibile O_3 absorption which falls almost exactly where the shift in SR$_{max}$ would be expected to occur (compare Figure 1.2). The anomalous 100 K curve of sample XV0552 could have been caused by insufficient delay between measurements after warming the cryostat to the set temperature, and the sample not settling thermally. The reason for the abnormally small Urbach tail is unclear, however, and could be another measurement artifact.

The gradient of the absorption edge at 77 K for both samples was fitted, and found to be marginally larger for sample XV0552 (by 6%). Although this could potentially be attributed to the different factors affecting oscillator strength as discussed above, this difference is small enough that it could be a random rather than a real effect.

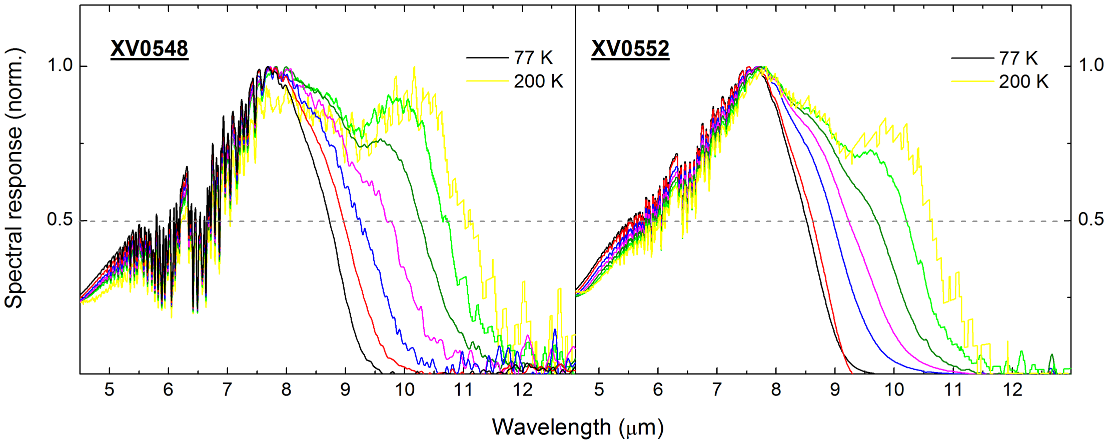

FIGURE 6.17: Normalised temperature-dependent spectral response curves of two LWIR samples. Each curve corresponds to a 20 K increase in temperature from the previous measurement.

The spectral response of the dual-colour sample QA504 was measured at -0.2 V for the LWIR absorber, and at +0.1 V for the top MWIR absorber. Both spectra can be seen in Figure 6.18. The $\lambda_{50\%}$ values for the two spectra at 77 K are, respectively, 8.54 μm and 6.03 μm. Predictably, the onset of absorption is stronger in the MWIR layer (by ~ 20%)

due to its strength increasing with the size of the optical bandgap.

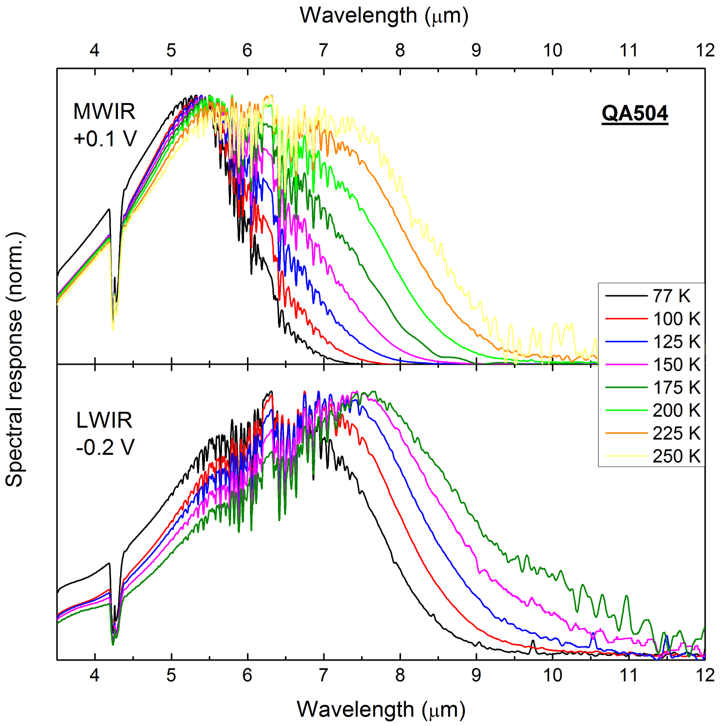

FIGURE 6.18: Normalised spectral response of the MWIR and LWIR absorbers of the dual-colour sample QA504.

In contrast to all the other nBn devices in this Section, the LWIR sample XV0208 was grown on the lattice-mismatched GaAs substrate using a ∼1 μm AlSb buffer layer as a virtual substrate (see Section 5.4.6 for its structural characteristics). The spectral response of the device can be seen in Figure 6.19. The apparent lack of temperature dependence of maximum response is even more pronounced than for the LWIR samples XV0548 and XV0552; instead, the expected response to temperature occurs in a weak 'shoulder' feature beyond ∼ 8 μm. It is not clear what type of transition, if any, could be responsible for this behaviour; given that XV0208 is the only nBn device discussed here that is not strain-balanced according to the design rules in Section 5.1, it is possible that partial relaxation or another source of non-homogeneity in the crystal provides the dominant transition mechanism. Otherwise, in strictly instrumental terms, it is possible that the ZnSe window of the cryostat was contaminated at the time of the measurement, obscuring part of the LWIR spectrum.

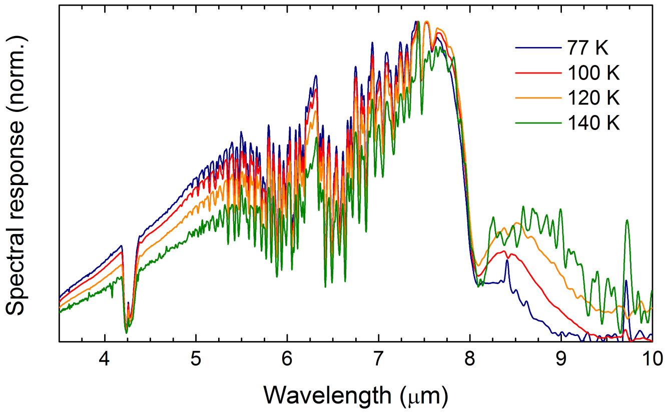

FIGURE 6.19: Spectral response of the XV0208 nBn device grown on an AlSb buffer layer.

An interesting, if qualitative, feature of temperature dependence of spectral response can be observed when the spectra are normalised to pre-amplifier gain. The relative magnitude of signal response to infrared light plotted on the y-axis can then be compared for different temperatures, and to estimate the temperature range within which maximum response occurs. The results for samples XV0576 and XV0552 can be seen in Figure 6.20 (it must be noted that these curves were not normalised to the blackbody spectrum, hence lineshapes being different to those presented earlier in the section). For the MWIR sample, the recorded signal peaks at 140 K and falls below it, which implies that the true maximum signal response lies in the 120 - 160 K range. For the LWIR sample, the range is 100 - 140 K.

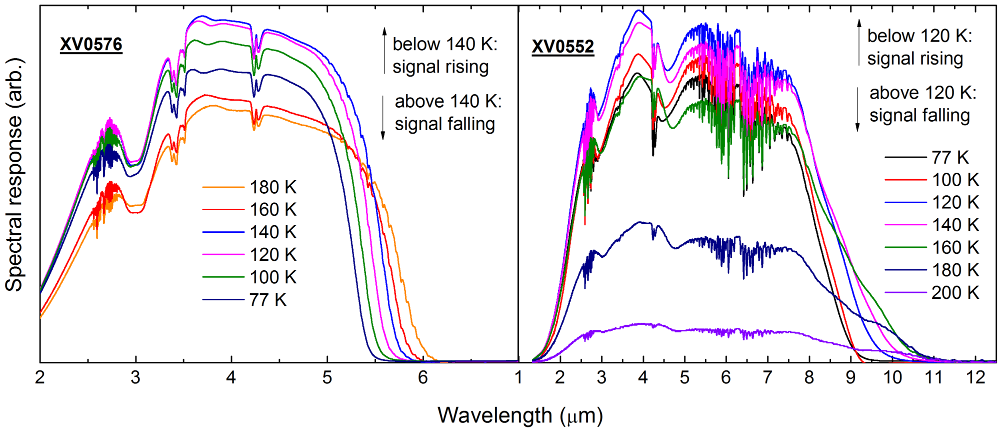

FIGURE 6.20: Spectral response of the MWIR XV0576 sample (left) and the LWIR XV0548 sample (right) normalised to pre-amplifier gain.

This effect could be due to two competing factors: initially, as the temperature decreases from 300 K, the lieftime of minority carriers steadily increases resulting in carrier collection from a larger volume and hence, a stronger signal. On the other hand, the subsequent signal fall at the lowest temperatures could be explained by carriers not having enough thermal energy to overcome minor potential barriers in the structure, and so not being collected anymore.

Extraction of bandgap values

Although spectral response data presented in Section 6.2 carries no numerical information about responsivity of the devices, their functional form is directly related to responsivity and hence directly proportional to quantum efficiency (as per Equation 2.42). Quantum efficiency is, in turn, directly proportional to the absorption coefficient given sufficient absorber thickness and diffusion length[167,168], which subsequently enables bandgap analysis analogous to that employed in Section 6.1.2 to be carried out on absorption edges of spectral response curves. This provides a valuable reference frame for bandgap results derived from $\alpha(h\nu)$ spectra, as spectral response does not require reference measurements or correction for reflection artifacts.

The absorption edge analysis for the spectral responses proceeded in the same way as for the $\alpha(h\nu)$ spectra: first, the Urbach region was visually identified in the linearly plotted data, then the absorption region demonstrating linear behaviour on a $\mathrm{SR}^2(h\nu)$ plot was fitted and the x-intercept identified. The process is reiterated in Figure 6.21 for sample XV0576 at temperatures equal to 77, 140 and 200 K. For all samples, the good signal-to-noise ratios permitted the fitting of bandgaps for most temperatures presented in Section 6.2.

Once again, the bandgap positions are confirmed qualitatively by examining first derivatives of the spectra; examples can be seen in Figure 6.22. Just as in the case of the first derivatives of $\alpha(h\nu)$, the $E_g(SR^2)$ bandgaps are compared to the first derivative peak positions, and found to be close.

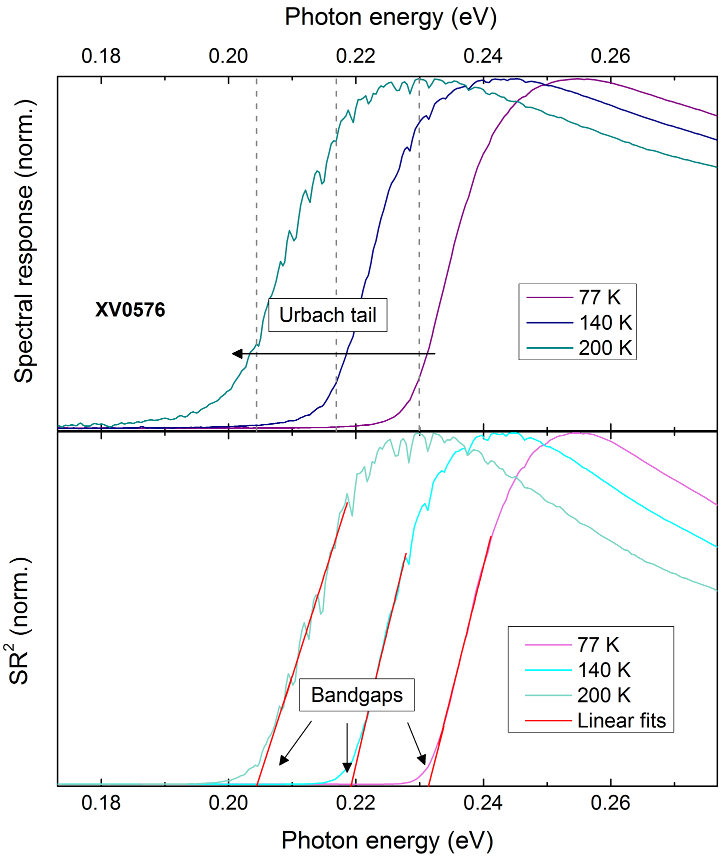

FIGURE 6.21: Bandgap extraction from the spectral response data of sample XV0576. Top: identification of the exponential Urbach region. Bottom: linear fits of the absorption edge extrapolated to the x-axis result in the fundamental direct bandgap E_g.

The full bandgap temperature dependence for the GaSb nBn devices considered in Section 6.2 can be seen in Figure 6.23. Because of thermally generated carriers the signal-to-noise ratio degrades faster in lower-bandgap systems, so some higher-temperature spectra were discarded from the analysis. Just as in the case of the results derived from $\alpha(h\nu)$ spectra (Figure 6.14) the narrowing of the bandgaps due to both increased Sb content and increasing temperature is evident, however unlike the temperature dependencies derived from epilayers there appears to be no dependence of the gradient on x_{Sb}. The full quantitative analysis of these results is presented in Section 6.4.

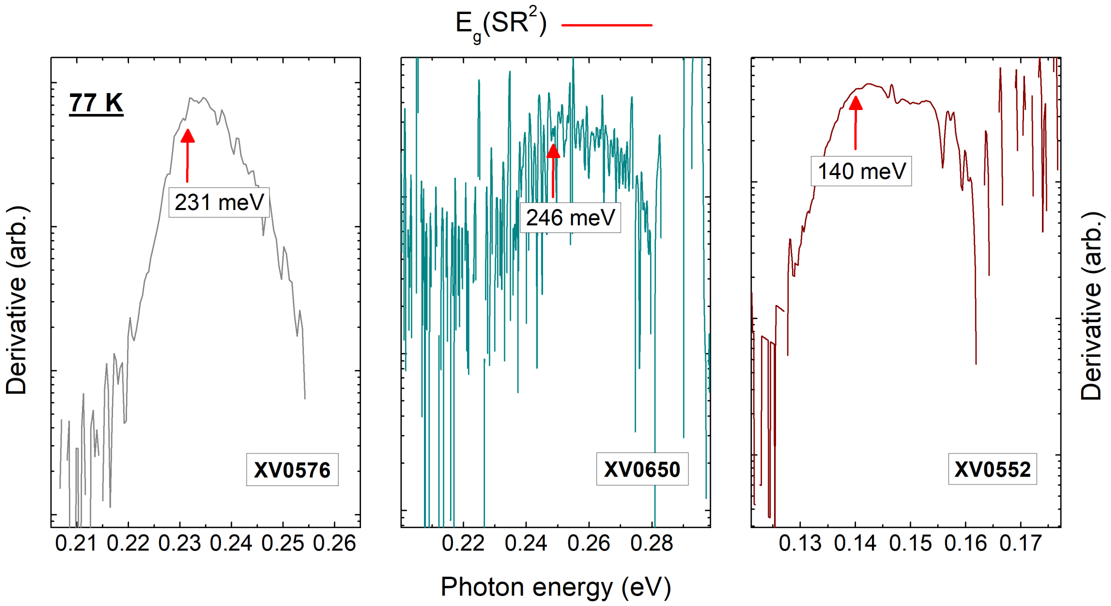

FIGURE 6.22: First derivatives of the spectral responses of samples XV0576, XV0552 and XV0161 corresponding to the band-to-band absorption onset. $E_g(SR^2)$ refers to the bandgaps derived from the spectral response curves.

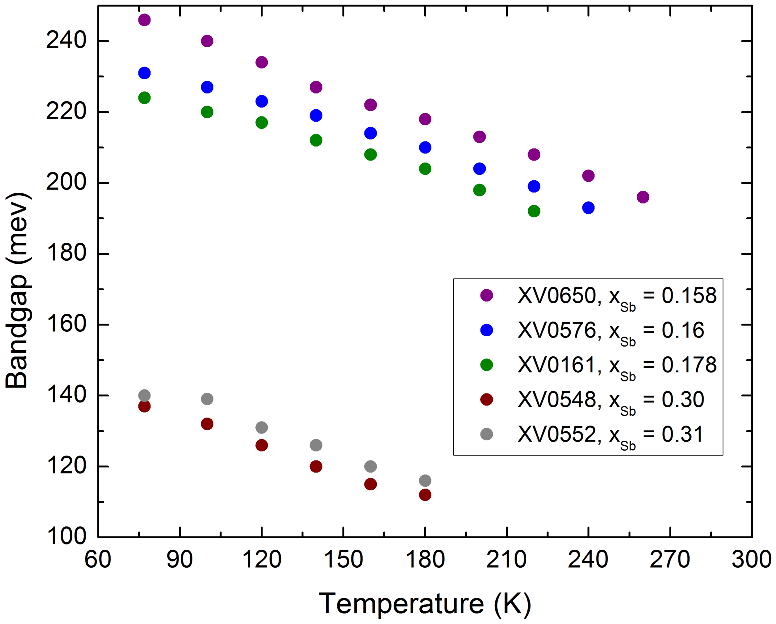

FIGURE 6.23: Temperature dependence of the bandgaps of a range of nBn devices, derived from their spectral response curves.

6.3 Photoluminescence

In order to ascertain the band-to-band transition value of the samples XV0154, XV0159 and XV0160 close enough to 0 K to pin the zero-point bandgap parameter E_0 of the single-oscillator model (see Equation 6.2 in Section 6.4), their photoluminescence (PL) spectra were acquired at 4 K by mounting each sample in a He-cooled cryostat prior to the measurement. As mentioned in Section 4.4, the 4 K bandgaps were assessed via a power dependence measurement: a NIR (785 nm) laser with 2.55 W cm^{-2} power density was impacted on a sample, the intensity of which was subsequently modulated with the use of optical filters between 50% and 0.4%. This approach exploits the effect of band filling of the sub-bandgap tail of states: an increase in peak position at low pump power points to this low-density tail of states being filled with carriers, eventually turning into a plateau at the onset of band-to-band transitions, which are characterised by a much larger density of states. The normalised spectra for the three samples are summarised in Figure 6.24; the pumping power was decreased in steps until the peaks could no longer be reliably identified.

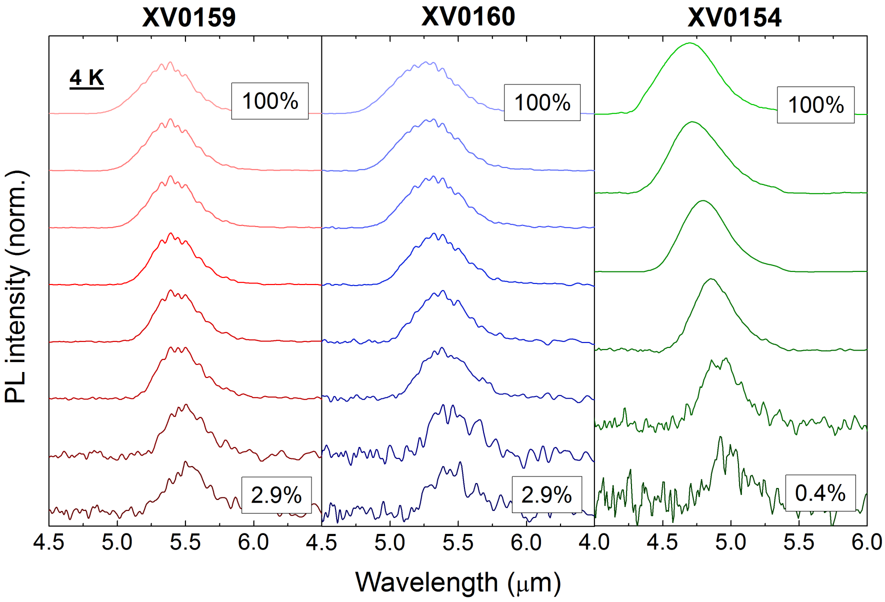

FIGURE 6.24: Power-dependent photoluminescence measurements of samples XV0154, XV0159 and XV0160 at 4 K. Here, the optical filter values were varied between 100% (no filter) and 0.4% of the laser pump power 2.55 W cm^{-2}.

XV0154 was the only sample characterised with the MWIR detector InSb, while the other two had spectra obtained with LWIR CMT detectors; this explains the stronger signal of XV0154.

The characteristic behaviour of the superlattices in response to varied pump power is plotted in Figure 6.25, where solid symbols represent peak position maxima (each peak position was characterised with a Gaussian fit). There is a pronounced decreasing trend in peak position at filter values below 20%, with asymptotic-like behaviour for sample XV0154 at $< 1\%$. This kind of saturation curve indicates that the sub-bandgap tail of states is not fully filled up to a certain pump power, and only once the band-to-band electron-hole recombination process begins (characterised by a much larger density of states), the pump power-dependence of the peak position declines[39]. As such, only the peak positions at 33% and above are considered in the 4 K bandgap extraction.

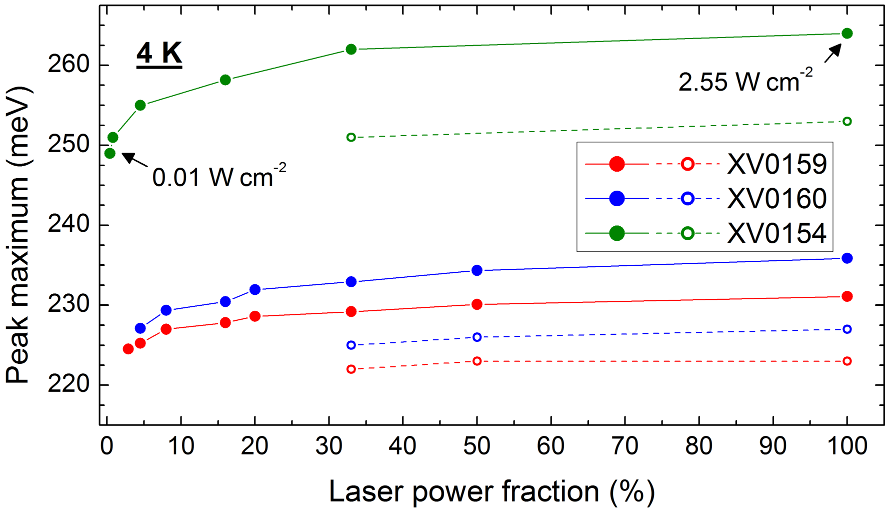

FIGURE 6.25: 4 K Gaussian fit photoluminescence peak positions of samples XV0159, XV0160 and XV0154 as functions of laser pump power. The solid lines and symbols represent the maximum peak positions of the Gaussian fits, and the dashed lines and hollow symbols represent their first derivative maxima.

The procedure follows the same first derivative method outlined in Sections 6.1.2 and 6.2: first, Gaussian curves are fitted to each spectrum (see Figure 6.26 for the fits at 33% filter value), then derivatives are taken and their maxima identified (Figure 6.26 inset). These first derivative maxima for each pump power are also included in Figure

6.25 as hollow symbols. Both XV0154 and XV0160 increase by 1 meV for each analysed pump power, with an average value of 252 and 226 meV respectively; XV0159, meanwhile, increases by 1 meV between 33 and 50% then stabilises at the peak value of 223 meV. XV0154 also undergoes the most downwards shift between the peak and derivative positions; this could be due to the broadness of the PL peak itself, which would shift the position of maximum gradient away from the peak and which could be due to the region of Sb composition gradient in the ternary layer. As discussed in Section 5.4.3, this composition gradient at the InAs/InAs$_{1-x}$Sb$_x$ interface has a non-negligible thickness of about 2 nm, and therefore its bending of the band structure (normally assumed to consist of perfectly sharp wells) would cause the most broadening in the photoluminescence peak of the thinnest superlattice.

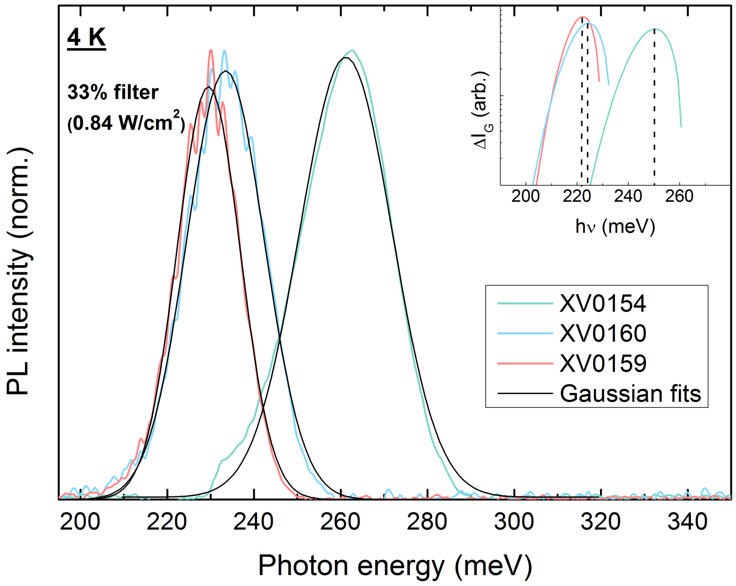

FIGURE 6.26: Gaussian fits of the photoluminescence peaks of samples XV0159, XV0154 and XV0160, obtained at 4 K and with the use of a 33% optical filter mounted over a 2.55 W cm^{-2} power density NIR laser. Inset: First derivatives of the Gaussian fit curves with their maxima marked in black dashed lines.

6.4 Temperature dependence of the InAs/InAs$_{1-x}$Sb$_x$ bandgap

6.4.1 Temperature dependence of undoped epilayers

As briefly explained in Section 2.1.2, the most commonly used fit of the III-V temperature dependence, the empirical Varshni model, has been reported to mischaracterise the very low-temperature behaviour of the bandgaps (where its quadratic form is most pronounced). An alternative semi-empirical model which incorporates phonon-electron interaction as well as lattice expansion effects on bandgap narrowing is the Einstein oscillator model, the most simple version of which, the single-oscillator model[46], has been found to accurately describe InAs, InSb as well as InAs$_{0.911}$Sb$_{0.089}$ temperature behaviour[39]. The equation takes the form

$$E_g(T) = E_0 - S_g k \left(\frac{T_E}{exp(T_E/T) - 1} \right) \tag{6.2}$$

where $kT_E = h\omega_{ph}$ is the lattice energy associated with the effective phonon frequency, S_g is a coupling scale factor of the high-temperature region, and the denominator of the bracketed term is the phonon occupation number (the average number of phonons of energy $h\omega_{ph}$ at temperature T). The significance of the characteristic T_E of a material is that $\frac{1}{2}T_E$ denotes the boundary between the low and high-temperature regimes of its temperature dependence; also, it has been shown[46,169] that $T_D \approx {}^3/_4 T_E$ where T_D is the Debye temperature. The 0 K bandgap E_0, here defined for a highly crystalline material, includes the bandgap narrowing contribution due to zero-point motion which is equal to $\frac{1}{2}S_g kT_E$. The significance of each parameter is briefly presented in Figure 6.27 using InAs and InSb fits as derived by Webster et al[39].

Figure 6.28 collates experimental bandgap values derived from photoluminescence (diamonds, $E_g(PL)$) and absorption coefficient (circles, $E_g(\alpha)$) spectra for the three period-varied MWIR samples XV0154, XV0160 and XV0159 (discussed eg. in Section 6.3). The $E_g(\alpha)$ data shows pronounced linear behaviour down to lowest-measured $T = 77$ K, placing an upper limit on T_E of about 150 K; in addition, due to the functional form of Equation 6.2, E_0 also cannot be lower than $E_g(77K)$.

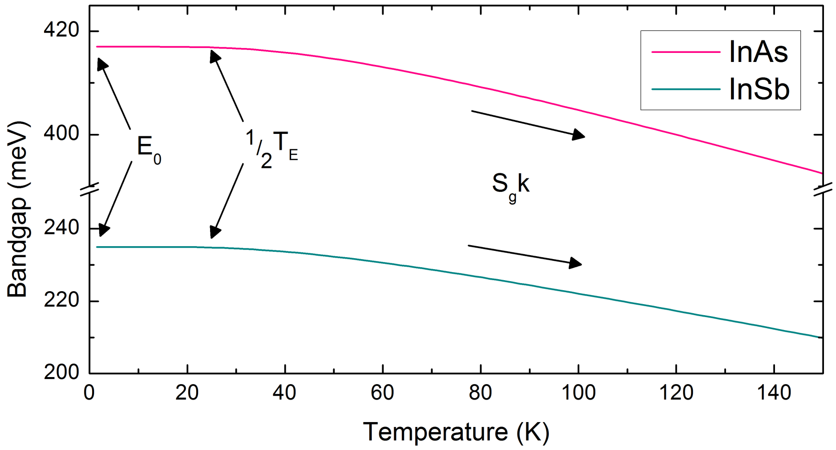

FIGURE 6.27: Bandgap temperature dependence of InAs and InSb based on the Einstein single-oscillator model. The significance of each parameter is denoted on the graph. Fit parameters from Webster et al[39].

The 4 K $E_g(PL)$ data points of samples XV0159 and XV0160 derived in Section 6.3 are used to pinpoint the value of E_0, however the XV0154 result, at 253 meV, appears to be severely underestimated when compared with the $E_g(\alpha)$ data. The first derivative method identifies the strongest change in the joint optical density of states, which usually corresponds to the onset of a band-to-band transition. It is possible, however, that due to a large number of dislocations the sub-bandgap density of states (the Urbach tail) is large enough to dominate over the first interband transition. Sample XV0154 is likely to have more defect-induced states than the other two because its superlattice period is the smallest, so that the $\sim$ 2 nm interface roughness (derived in Section 5.4.3) would span across the entire superlattice cell. As such, because the PL result for XV0154 does not appear likely to represent the fundamental band-to-band transition, it is excluded from temperature fit.

The temperature dependence fits for samples XV0159 and XV0160 were deducted as follows: first, the gradient of the high-temperature region is estimated using simple linear fits. The E_0 parameter is pinned at the $E_g(PL)$ value and the Einstein temperature T_E is decreased incrementally from 150 K until the best agreement with E_0 and $S_g k$ is achieved.

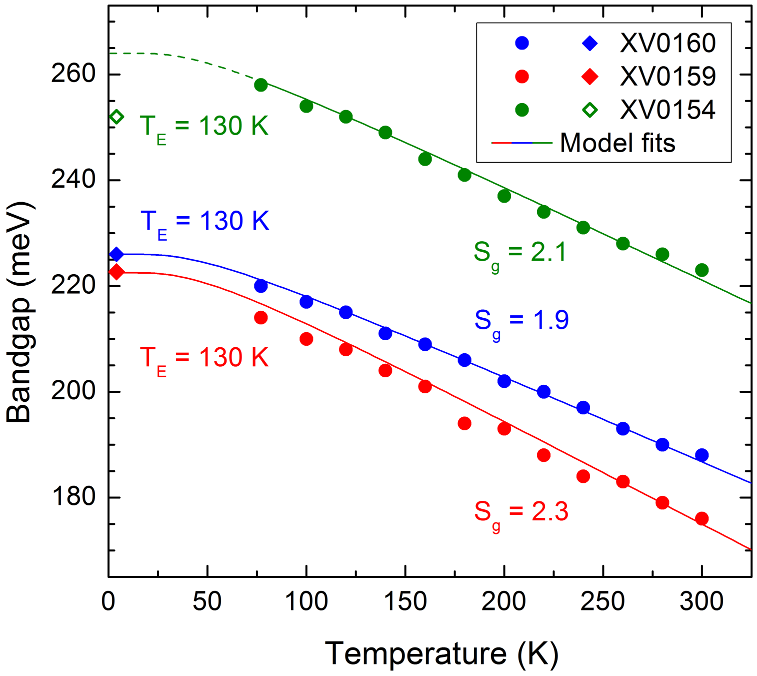

FIGURE 6.28: Bandgap temperature dependence of samples XV0154, XV0159 and XV0160. Experimental data points were extracted from photoluminescence (diamonds) and absorption coefficient spectra (circles). Continuous coloured lines represent model fits. For sample XV0154, the sub-77 K region is a tentative fit based on the results for the other two.

For XV0154, E_0 is provisionally set 8 meV above the 77 K value (which is the case for the other two samples), however because predicting T_E is not trivial without knowing the corresponding Debye temperature of the material, the choice of this parameter (and hence the expected low-temperature behaviour, marked in green dashed lines on Figure 6.28) is tentative at best. The fit parameters are presented in Figure 6.28 as labels of each sample dataset, as well as listed in Table 6.4.

Recalculated Varshni parameters (see Equation 2.28) are also included to allow more convenient comparisons with other materials, according the following relations[42]: $\alpha = S_g k$ and $\beta = {}^1\!/\!_2 T_E$. The term ${}^1\!/\!_2 S_g k T_E$ is equivalent to the product $\alpha\beta$ in the Varshi model and represents the 0 K bandgap reduction due to zero-point lattice motion. The three samples show slight variation in the gradient parameter of the linear region S_g; however, rather than a physical phenomenon, it is more likely explained by the very high sensitivity of T_E to the value of E_0: for example, if $E_0(XV0159)$ was just 3 meV

TABLE 6.4: Single oscillator fit parameters for samples XV0154, XV0160 and XV0159 as seen in Figure 6.28, and the recalculated Varshni model parameters (here $\alpha = S_g k$ and $\beta = 1/2T_E$). Literature data denoted * is from[39], ** is from[40].

	Single-oscillator model			Varshni model	
	S_g (eV K^{-1})	T_E (K)	$1/2 S_g k T_E$ (eV)	α ($\times 10^{-4}$eV K^{-1})	β (K)
XV0154	2.1	130	12	1.81	65
XV0159	2.3	130	13	1.98	65
XV0160	1.9	130	11	1.64	65
$^*InAs$	3.2	145	-	2.76	93
$^*InSb$	3.13	133	-	3.2	170
$^*InAs_{0.911}Sb_{0.089}$	2.85	230.8	28.3	3.59	115.4
$^{**}InAs/InAs_{0.63}Sb_{0.37}$	-	-	-	2.42	106
$^{**}InAs/InAs_{0.72}Sb_{0.28}$	-	-	-	1.67	95.8
$^{**}InAs/InAs_{0.78}Sb_{0.22}$	-	-	-	2.75	139

lower, all three sets of data could be fitted with the same value of $T_E = 120$ K and $S_g = 1.9$. Given the difficulty of establishing $E_g(PL)$ to such precision, it is plausible that these parameters actually agree with each other within the uncertainties of the photoluminescence measurements.

Upon examining other data from literature it becomes evident that superlattice structures show far less pronounced bandgap temperature dependence (represented by the S_g (Einstein) and α (Varshni) parameters) than the constituent bulk materials InAs and InSb, as well as As-rich bulk $InAs_{1-x}Sb_x$. The Varshni parameters reported for a series of $InAs/InAs_{1-x}Sb_x$ structures in Ref[40] demonstrate more comparable but still more pronounced bandgap reduction behaviour than samples presented here, although this could potentially be explained by differences in growth mode and conditions as well as lattice-matching methods, rather than x_{Sb} or superlattice period dependence. The samples also show the lowest T_E values in the dataset (even when we consider the upper limit placed on T_E by the lack of curvature in $E_g(\alpha)$, which is ~ 150 K). This indicates that even though the superlattices have weak bandgap response to increasing temperature, this response arises at lower temperatures than other structures/materials (ie. the thermal energy reaches minimum phonon energy sooner). It is worth noting, however, that this is advantageous for the design of superlattices for infrared detectors as linear response down to $T = 77$ K (the temperature of liquid nitrogen, which is commonly used as an IR detector coolant) helps in predicting the spectral range of the detector, while weak temperature dependence allows for larger ranges of operational temperature while minimising the detector's spectral response shift. Importantly, this behaviour is replicated for samples with higher x_{Sb} as presented in Figure 6.29.

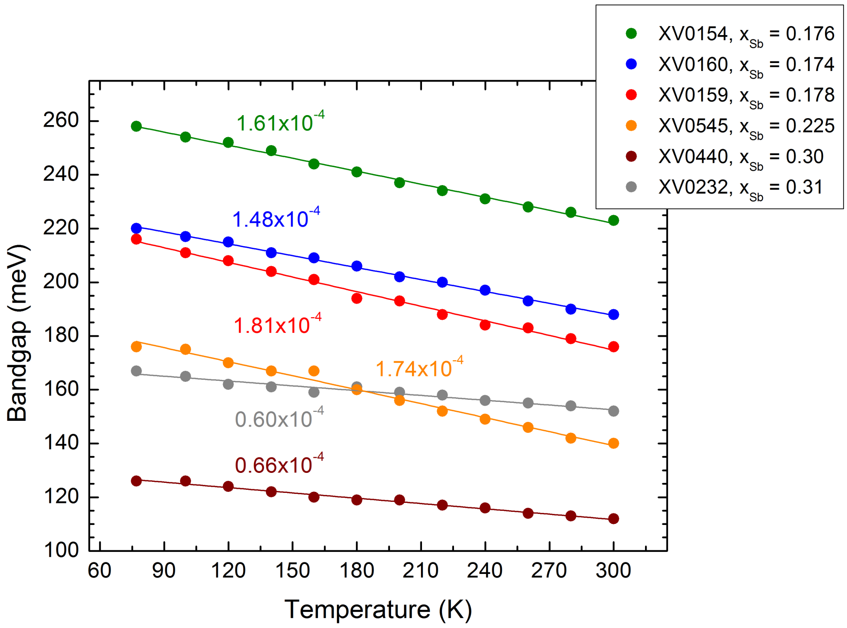

FIGURE 6.29: Bandgap temperature dependence of a number of undoped epilayer samples with different superlattice periods and x_{Sb}. The coloured labels represent the linear gradient of the fits in units of eV K^{-1}.

Because the remaining three samples (XV0545, XV0440 and XV0232) do not have $T < 77$ K data, only the high-T region can be fitted. Simple linear fits can be used as a reasonable estimate: this can be demonstrated on samples XV0154, XV0159 and XV0160 by comparing absolute linear fit gradients (included as colour-coded labels in units of eV K^{-1} on Figure 6.29) of their high-T regions with the $S_g k$ (and α) parameters of the model fits in Table 6.4. It becomes immediately apparent that a linear fit overestimates the gradient by about 9-12% compared to the full model, which is due to the fact that the 'linear' term of the single oscillator expression actually retains slight curvature even beyond $1/2T_E$. Nevertheless, it enables comparisons between the samples, including the observation that while sample XV0545 shows a gradient consistent with the lower x_{Sb} superlattices XV0160, XV0154 and XV0159, the two high-Sb samples XV0440 and XV0232 demonstrate an even less pronounced temperature dependence, with bandgaps reducing by less than 15 meV from LN_2 to room temperature. All datasets retain linearity down to 77 K.

6.4.2 Temperature dependence of nBn devices

Temperature dependence of the nBn devices was extracted using the approach outlined in Section 6.2. Just as in the case of the high-T $E_g(\alpha)$ datasets of the undoped epilayers discussed in Section 6.4.1, the raw data derived from spectral response ($E_g(SR)$) and presented in Figure 6.23 shows strong linearity down to 77 K, making linear fitting an acceptable method of estimating S_g (α in the Varshni model). The resultant absolute gradients (units of eV K^{-1}) are fitted in Figure 6.30.

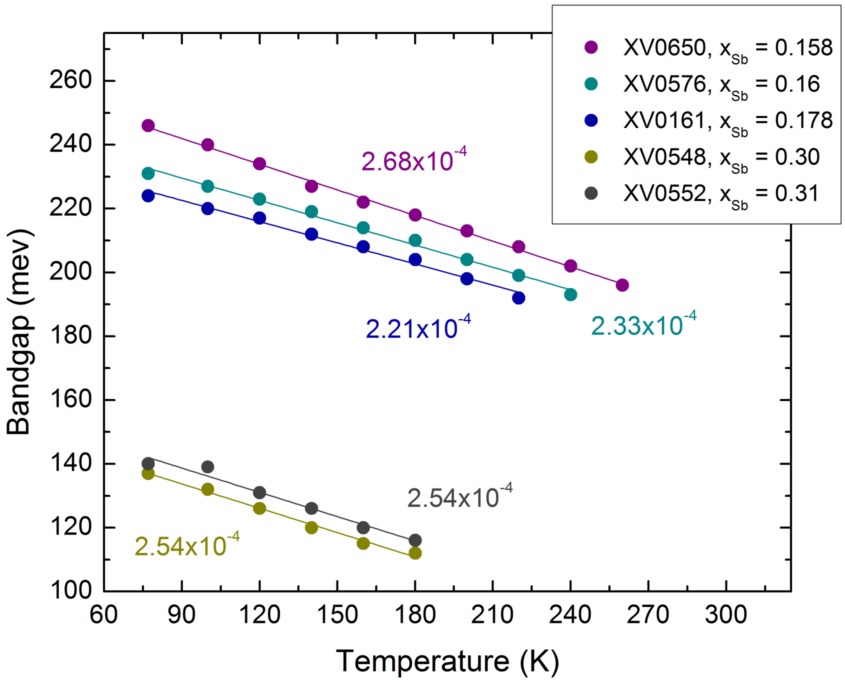

FIGURE 6.30: Bandgap temperature dependence of a number of doped nBn device samples with different superlattice periods and x_{Sb}. The coloured labels represent the linear gradient of the fits in units of eV K^{-1}.

Two observations can be readily made: first, the bandgap decrease of the devices is more pronounced than that of epilayers, and second, it is more consistent: the high-Sb devices show no decline in temperature dependence compared to the other samples, which is helpful in predicting the optical behaviour during photodetector design process. The distinction between the epilayers and the devices is visually presented in Figure 6.31.

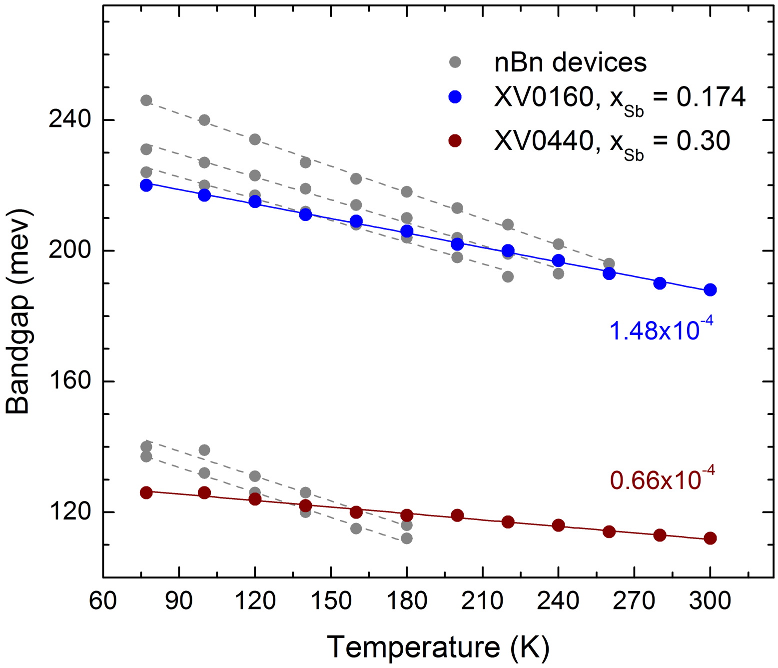

FIGURE 6.31: Comparison of the temperature dependence of epilayers and nBn devices. The grey curves correspond to the nBn temperature dependencies in Figure 6.30. Samples XV0160 and XV0440 are undoped epilayers.

Once again, there is no obvious pattern in x_{Sb} or superlattice period that could explain the discrepancies: the device XV0161 was designed to implement the same superlattice present in XV0160, while the epilayer XV0440 has a comparable period to the two LWIR nBn devices XV0552 and XV0548. Increased carrier concentration is known to contribute to bandgap narrowing due to the electrostatic interaction of electrons and holes[170], however for this explanation to work, carrier concentration in the nBn devices would have to increase with temperature (intrinsic carrier concentration does have a

TABLE 6.5: Linear fit gradients of the nBn devices recalculated as the Varshni α parameters. The three reference device results were obtained by Klein et al[173], and the two consecutive values refer to either spectral response or absorption measurement types.

	m ($\times10^{-4}$ eV K^{-1})	α ($\times10^{-4}$ eV K^{-1})
XV0650	2.68	2.44 ± 0.24
XV00576	2.33	2.12 ± 0.21
XV0161	2.21	2.01 ± 0.20
XV0548	2.54	2.31 ± 0.23
XV0552	2.54	2.31 ± 0.23
MWIR bulk InAsSb nBn	-	3.8
MWIR InAs/GaSb SLS pin	-	3.0, 3.1
LWIR InAs/GaSb nBn	-	2.5, 2.8

temperature dependence - however, there is no reason to believe that this would behave differently in the epilayers and the nBn devices). Two additional sources of carriers in the nBn's are dopants and dark current density, the first of which are expected to be fully ionised at all temperatures under consideration[171], while the dark current densities, even though temperature-dependent, would be far too small compared to the carrier concentration required for measurable bandgap reduction. Phonon-electron interaction is a major contributor to temperature-induced bandgap shrinkage[172]; however, analysis of phonon dispersion relations is beyond the scope of this work. The reason for the different temperature dependencies remains unclear.

It was found in Section 6.4.1 that the linear temperature fits overestimate the S_g parameter of the single oscillator model (and by association α in the Varshni model) by about 10%. Because this offset arises due to the functional form of the single oscillator equation, not the physical features of the system, and to enable comparison with other materials, the $\alpha = S_g k$ parameter of the nBn devices is estimated to be $0.91 \times m \pm 10\%$ where m is the linear gradient of the nBn temperature dependence in Figure 6.30. A comparison is drawn with several devices studied in Klein et al[173] in Table 6.5: bulk $InAs_{0.9}Sb_{0.1}$ nBn with an undoped barrier, a MWIR InAs/GaSb SLS pin, and a LWIR InAs/GaSb SLS nBn.

The multiple values for the reference devices are due to different measurement types yielding different results. It can once again be observed that the bandgap reduction due to temperature is less pronounced in the samples presented in this work than in comparable structures. The latter two literature structures in Table 6.5 were characterised using both absorption and spectral response measurements; therefore the differences are unlikely to be due to method, and can be said to be a real feature of these superlattices.

6.5 Band structure modelling of InAs/InAs$_{1-x}$Sb$_x$

As an aid in fine-tuning the optical properties of InAs/InAs$_{1-x}$Sb$_x$-based nBn devices, a model of carrier dispersion was designed based on the Kronig-Penney model of a particle tunnelling through a succession of perfectly square finite potential barriers with sharply defined interfaces. In this simplified approach, coupling effects between the electron and hole bands are ignored, and the model is most effective at describing dispersion relations near the $\Gamma = 0$ point of the Brillouin zone.

The contribution of strain to the band shift (as well as splitting of degenerate valence bands) of the superlattice is represented in the model as hydrostatic and shear strain arising at InAs/InAs$_{1-x}$Sb$_x$ heterojunction; Sections 2.1.1 and 2.1.2 present the underlying calculations in full detail. The energetic height of the potential barrier experienced by a carrier must be known before carrier minibands are calculated, and are obtained via Equations 2.26 and 2.27, here repeated for completeness:

$$\begin{aligned} E_v &= \underbrace{E_{v,av} + \frac{\Delta_0}{3}}_{\text{unstrained}} + \Delta E^{hy}_{v,av} + max(\Delta E^{sh}_{hh}, \Delta E^{sh}_{lh}) \\ E_c &= \underbrace{E_{v,av} + \frac{\Delta_0}{3} + E_g(T)}_{\text{unstrained}} + \Delta E^{hy}_c \end{aligned} \tag{6.3}$$

The terms superscripted with ^{hy} and ^{sh} are strain-induced band shifts derived fully in Section 2.1.2, while the spin-orbit splitting term Δ_0 is taken from Vurgaftman et al[28] (for the full list of model parameters see Table 6.6). The bandgaps $E_g(T)$ of InAs and InSb at a given T are calculated using the single-oscillator model of temperature dependence discussed in Sections 2.1.2 and 6.4.1; the bandgap of $\mathrm{InAs}_{1-x}\mathrm{Sb}_x$, in turn, is interpolated with the use of the temperature-dependent double-oscillator model of bandgap bowing outlined in Section 2.1.2. The effective electron and heavy hole masses are calculated using Equations 2.12, 2.13 and 2.14. With the exception of the $\mathrm{InAs}_{1-x}\mathrm{Sb}_x$, all the valence band positions in the model follow the approach and values summarised in Vurgaftman et al[28], and normalised with respect to the InSb valence band. As a result, the only free parameter of the model is the valence band position of $\mathrm{InAs}_{1-x}\mathrm{Sb}_x$, which is varied to match the bandgap values derived experimentally in 6.1.2 and 6.2. Figure 6.32 visualises all the parameters that will be discussed in the rest of the chapter; the green arrow denotes the fitting parameter valence band position of $\mathrm{InAs}_{1-x}\mathrm{Sb}_x$, while the output parameters are highlighted by blue arrows (note that VBP_{InAsSb} and $E_{v,InAsSb}$ are equivalent).

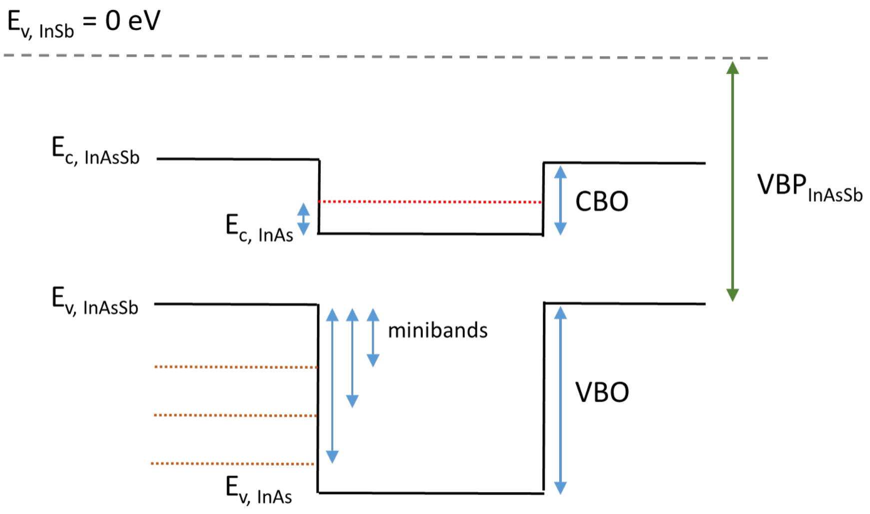

FIGURE 6.32: Parameters of the band structure of the type-IIb $\mathrm{InAs}/\mathrm{InAs}_{1-x}\mathrm{Sb}_x$ superlattice as defined in the model. The green arrow signifies the fitting parameter, and the blue arrows denote the resultant model parameters.

TABLE 6.6: Material parameters used in modelling InAs/InAs$_{1-x}$Sb$_x$ superlattices.

	InAs	*InSb*	$InAs_{1-x}Sb_x$
a (Å)	see Eq. 2.5	see Eq. 2.5	-
E$_{v,av}$ (eV)	-0.59	0	-
c$_{11}$	0.8329	0.6847	-
c$_{12}$	0.4526	0.3735	-
Δ_0 (eV)	0.39	0.81	-
a$_v$ (eV)	1	0.36	-
b (eV)	-1.8	-2	-
a$_c$ (eV)	-5.08	-6.94	-
Spin-orbit bowing (eV)	-	-	1.2
b$_0$ (eV)	-	-	0.938
S$_1$	-	-	22.98
S$_2$	-	-	18.8
T$_1$ (K)	-	-	115.8
T$_2$ (K)	-	-	275.6
S$_0$	3.2	3.13	-
T$_E$ (K)	145	133	-

When designing the band structure of an nBn device, a correct valence band alignment of the barrier with the superlattice is crucial for high quantum efficiency. The parameters used in modelling the barrier alloys are presented in Table 6.7. Note that the barriers incorporated into the devices are never binaries, so their parameters are interpolated from their binary values using the standard Vegard's law approach (see Section 2.1.1).

The quasi-confining nature of a superlattice results in quantisation of allowed energy levels similar to the quantum well structure in its dependence on well depth and thickness; however due to the barrier thickness being sufficiently small to allow carrier tunnelling, these energy levels broaden into bands of allowed $E(k)$ states. Fine-tuning of the optical properties of superlattice-based detectors requires understanding of how the superlattice period shifts the total bandgap of the structure. This is demonstrated

TABLE 6.7: Material parameters used in modelling the nBn barrier alloys.

	GaSb	*AlSb*	*AlGaSb*	*AlAs*	*GaAs*	*AlAsSb*
a (Å)	Eq. A.8	Eq. A.8	-	Eq. A.8	Eq. A.8	-
$E_{v,av}$ (eV)	-0.03	-0.41	-	-1.33	-0.8	-
c_{11}	0.8842	0.8769	-	1.25	1.221	-
c_{12}	0.4026	0.4341	-	0.534	0.566	-
Δ_0 (eV)	0.76	0.676	-	0.28	0.341	-
a_v (eV)	0.8	1.4	-	2.47	1.16	-
b (eV)	-2	-1.35	-	-2.3	-2	-
SO bowing (eV)	-	-	0.3	-	-	0.15

TABLE 6.8: Structures of samples XV0154, XV0159 and XV0160. All were grown on SI GaAs substrates and 325 nm of a GaSb buffer layer.

	XV0154	*XV0160*	*XV0159*
x_{Sb}	0.176	0.174	0.178
$d_{absorber}$ (nm)	710	780	750
d_{InAs} (nm)	2.10	4.66	6.86
d_{InAsSb} (nm)	2.16	4.79	7.04
Period multiplier	×1.0	×2.2	×3.3

on three samples XV0160, XV0154 and XV0159, grown on SI-GaAs substrates and 325 nm of GaSb buffer layer, implementing a superlattice structure that is identical aside from a varied period multiplier; the effective bandgap shift due to period change was already demonstrated in practice in Section 6.4.1. The structures of each are repeated in Table 6.8.

The structures are simulated at 300 K, and compared to the room-temperature $E_g(\alpha)$ as well as their full absorption coefficient curves. The $InAs_{1-x}Sb_x$ valence band position $VBP_{InAsSb} = -0.390$ eV with respect to $VBP_{InSb} = 0$ eV gives the best agreement with data for all three samples, and figures 6.33, 6.34 and 6.35 show these combined results. The top graph represents the colour-coded absorption coefficient $\alpha(300K)$; the grey curve is the corresponding first derivative plotted on a semi-log scale to enhance the relevant features, and the top labels represent the calculated miniband transitions, where e1 is the only electron miniband and hh1-4 represent the successively higher heavy hole minibands. The $E(k)$ dispersion relation (normalised to the superlattice period) is plotted in the bottom left graph: the red-shaded region represents the electron well in the superlattice and the orange-shaded region corresponds to the valence band heavy hole well, both bounded by continuum. Finally, the bottom right graph represents the position of the minibands at $\Gamma = 0$ (with the exception of e1 of XV0154, whose e1 band appears to be indirect) as a function of distance d in the superlattice cell, where $d = 0$ denotes the start of the InAs barrier layer. For clarity, all the $E(k)$ and band diagrams are normalised to the bottom of the heterojunction conduction band.

None of the samples presented in this work possess more than one electron miniband, which is due to the weakly electron-confining nature of the type IIb InAs/InAs$_{1-x}$Sb$_x$ superlattices (as discussed in Section 2.1.2), as well as superlattice periods that are generally smaller than those discussed in literature. On the flip side, the strongly confining heavy hole wells in InAs$_{1-x}$Sb$_x$ result in generally flat heavy hole bands whose number increases with increasing well thickness, while the width reduces due to weakening interactions between wells. The strained valence band offset VBO and the strained conduction band offset CBO are both found to be the same for all three samples: $VBO = 202$ meV and $CBO = 83$ meV, which is in line with the expectation of a weakly confining type-IIb band structure.

In an attempt to identify the corresponding absorption onsets, the calculated carrier transitions E_m are overlaid on the absorption coefficients and their first derivatives as dashed vertical lines in Figures 6.33, 6.34 and 6.35. The samples show good qualitative agreement with the first derivative peaks. The identified transition values correspond to the shortest energetic distance between the two electron and hole minibands, ie. their absorption onsets - it is at these energies that the electron-hole wavefunction overlap for the given transition is the strongest, and which will gradually diminish with increasing photon energy until it reaches the top of the miniband.

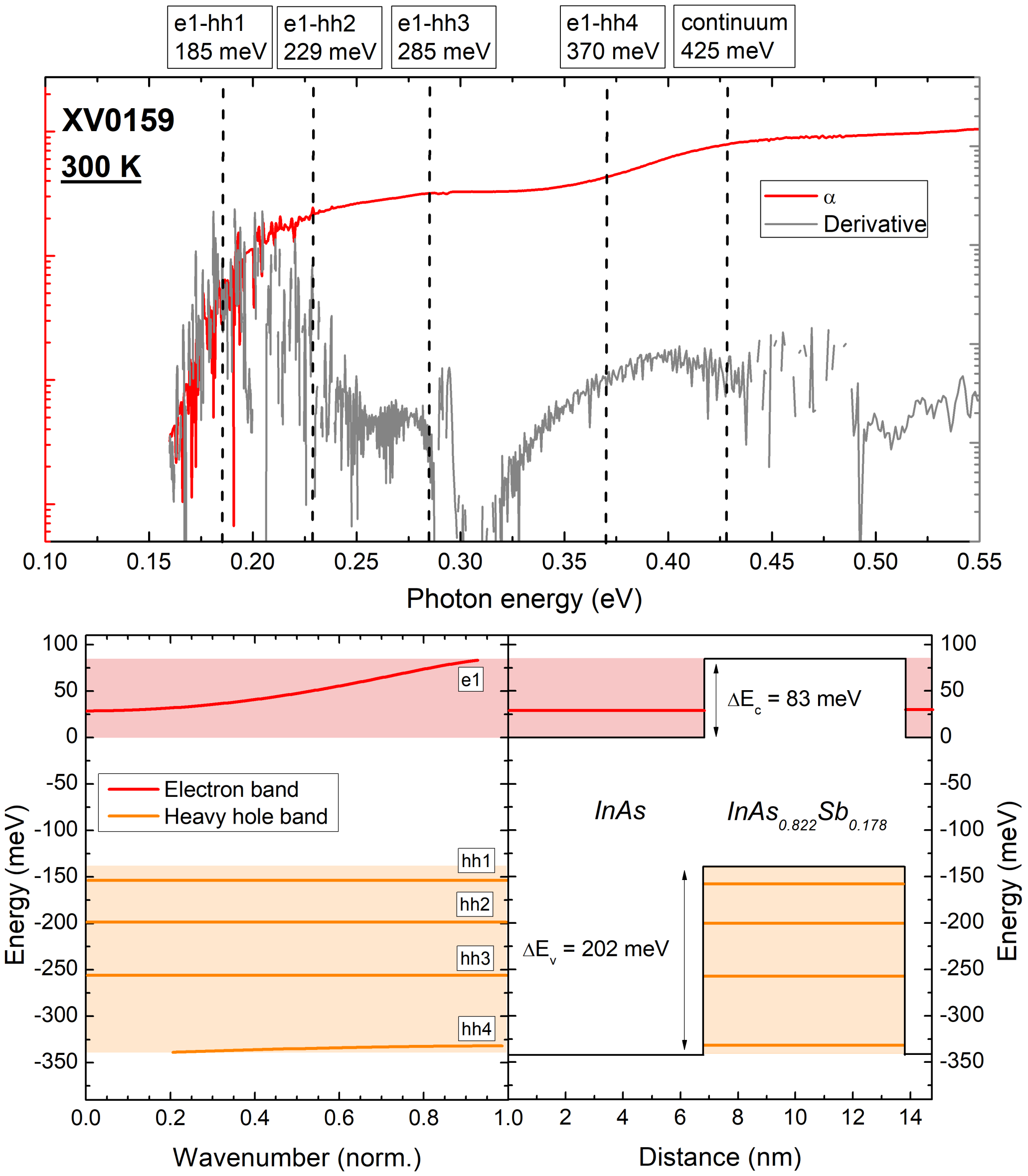

FIGURE 6.33: Top: the colour-coded absorption coefficient $\alpha(300K)$ (its derivative in grey) of sample XV0159 with identified miniband transitions marked in dashed lines. Bottom left: the calculated carrier dispersion relation $E(k)$, with shaded areas corresponding to superlattice well/barrier regions. Different minibands are labelled e and hh. Bottom right: the band diagram arising from the dispersion relation, with the $\Gamma = 0$ miniband values included.

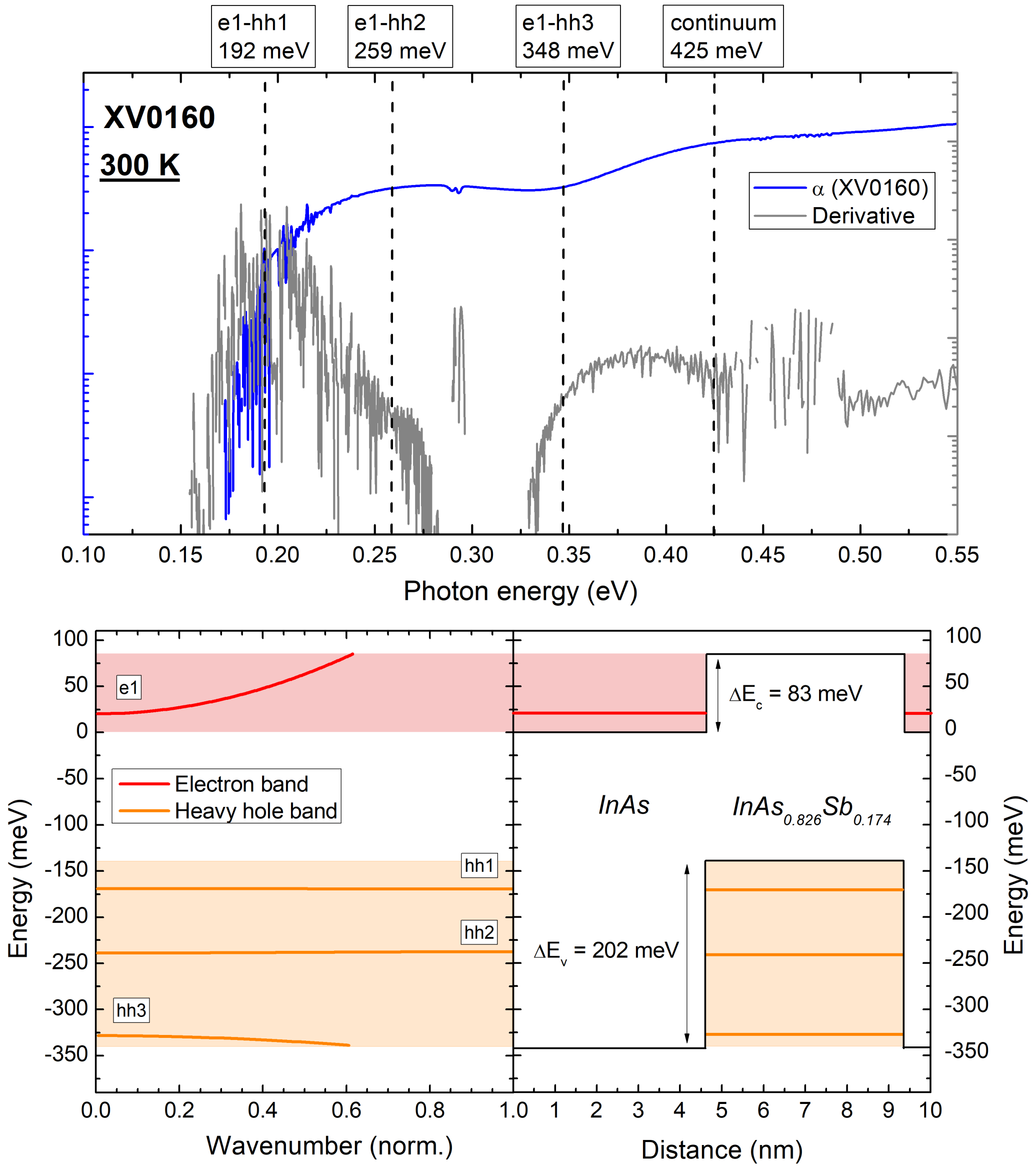

FIGURE 6.34: Top: the colour-coded absorption coefficient $\alpha(300K)$ (its derivative in grey) of sample XV0160 with identified miniband transitions marked in dashed lines. Bottom left: the calculated carrier dispersion relation $E(k)$, with shaded areas corresponding to superlattice well/barrier regions. Different minibands are labelled e and hh. Bottom right: the band diagram arising from the dispersion relation, with the $\Gamma = 0$ miniband values included.

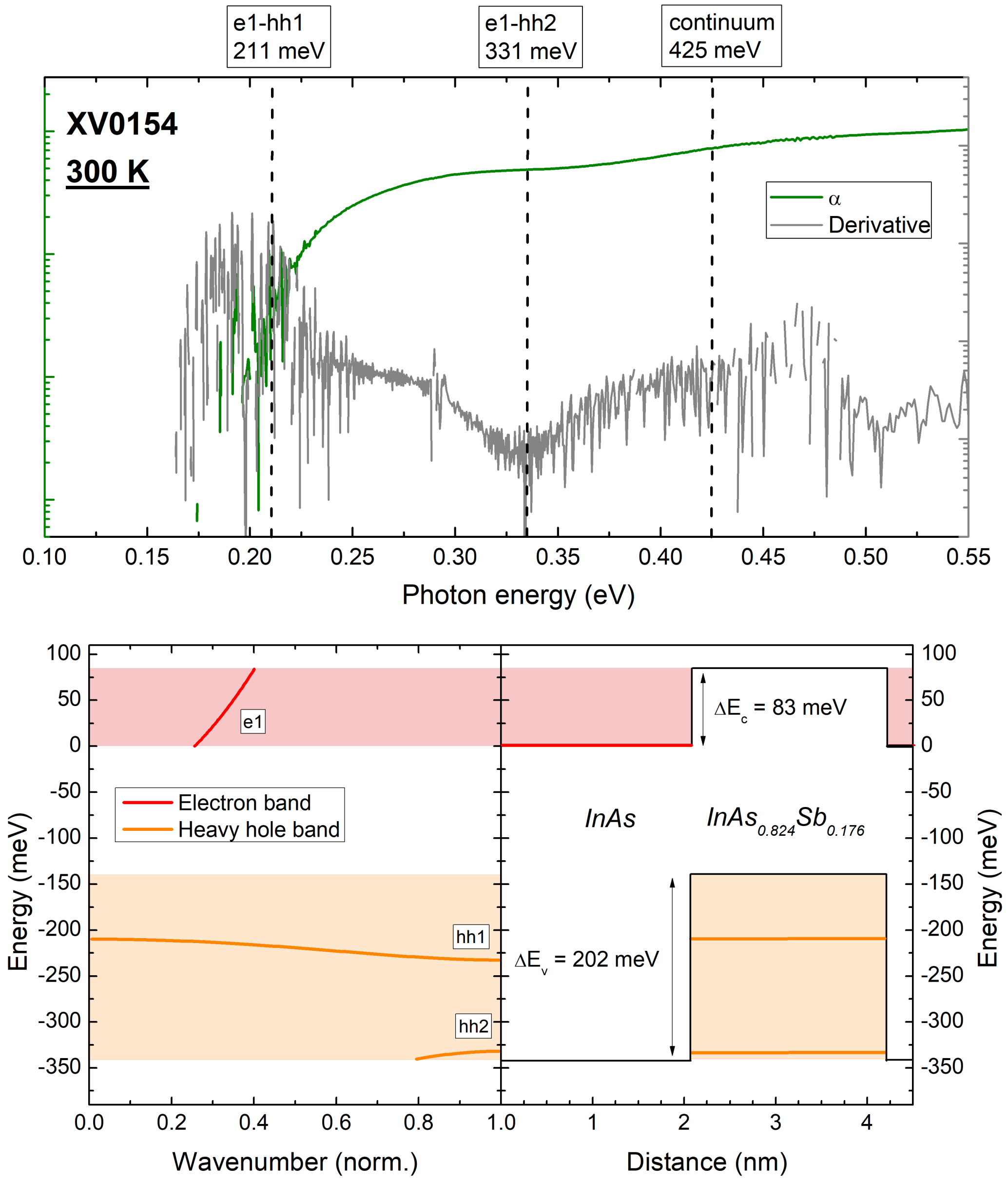

FIGURE 6.35: Top: the colour-coded absorption coefficient $\alpha(300K)$ (its derivative in grey) of sample XV0154 with identified miniband transitions marked in dashed lines. Bottom left: the calculated carrier dispersion relation $E(k)$, with shaded areas corresponding to superlattice well/barrier regions. Different minibands are labelled e and hh. Bottom right: the band diagram arising from the dispersion relation, with the $\Gamma = 0$ miniband values included.

The above approach was applied to all bandgap data derived in Section 6.1.2 at temperatures 300 K, 160 K and 77 K, in order to identify the InAs$_{1-x}$Sb$_x$ valence band position (VBP_{InAsSb}), InAs/InAs$_{1-x}$Sb$_x$ valence band offsets (VBO), conduction band offsets (CBO) and miniband positions with respect to the bottom of their wells. The unstrained VBP_{InAsSb}, the fitting parameter of the model, was derived by iteration for each sample and is plotted as a function of x_{Sb} in Figure 6.36 for each of the three temperatures. Any data points that are aligned vertically (ie. have the same x_{Sb} value) correspond to the data from the same sample.

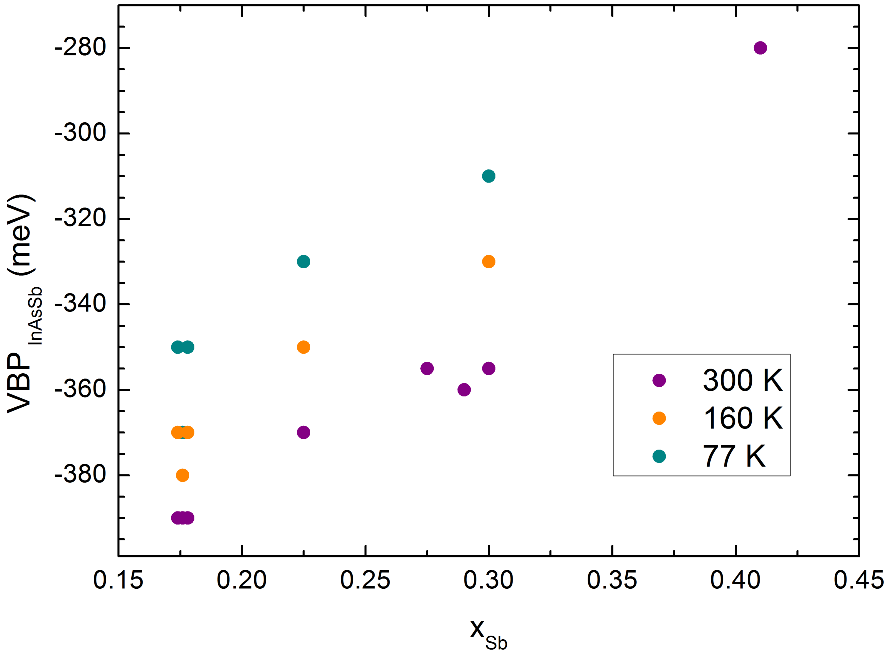

FIGURE 6.36: Unstrained valence band position of InAs$_{1-x}$Sb$_x$ as a function of x_{Sb}, derived at three temperatures from the $E_g(\alpha)$ data. The position of the band is defined with respect to $E_{v,InSb} = 0$ meV.

As expected, VBP_{InAsSb} tends towards $VBP_{InSb} = 0$ meV with increasing x_{Sb}, simultaneously raising the confining potential of the InAsSb superlattice wells (see Figure 6.37). It can be seen that in this formulation of the band structure model, the valence band position of InAs$_{1-x}$Sb$_x$ at a given Sb fraction has a linear dependence on temperature corresponding to a downwards shift of about 20 meV between 300 and 77 K (note that no cryogenic data was available for sample XV0235 at $x_Sb = 0.41$).

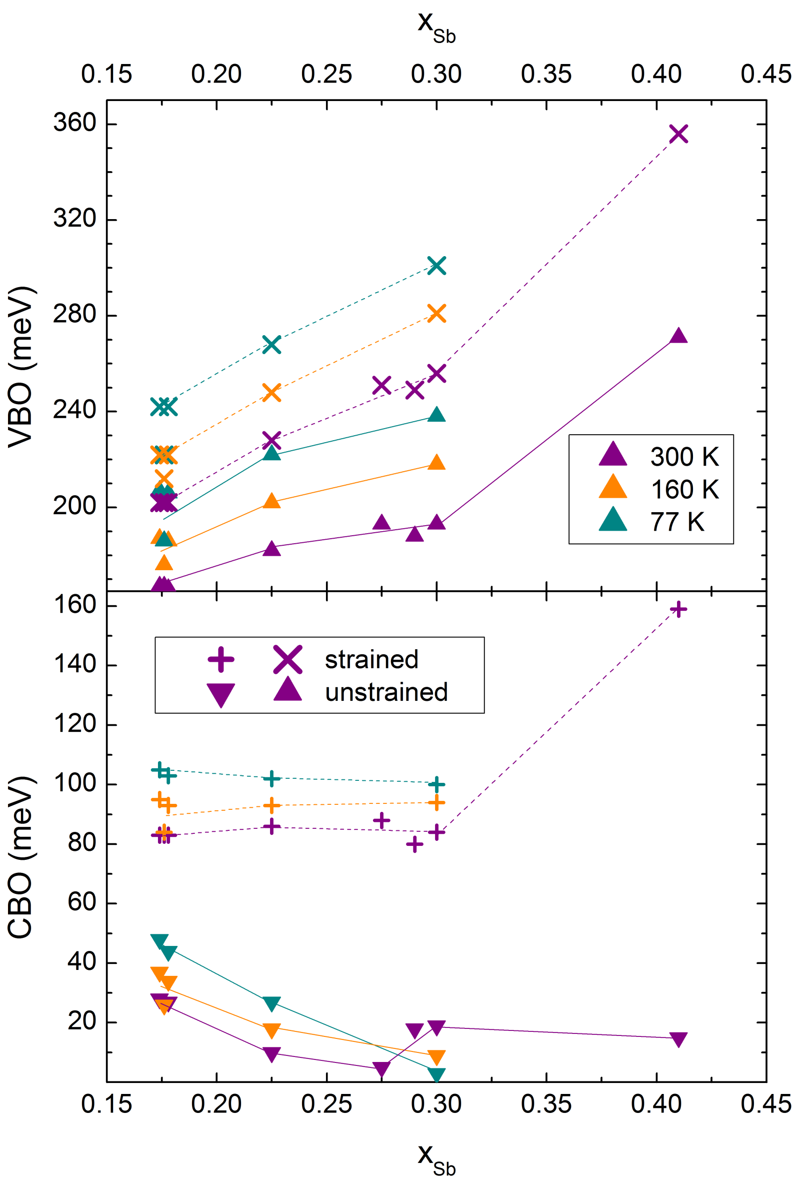

FIGURE 6.37: Top: valence band offset of InAs/InAs$_{1-x}$Sb$_x$ as a function of x_{Sb}. Bottom: the corresponding conduction band offsets. The crosses/triangles on both represent the strained/unstrained offsets respectively, and lines are included as a visual guide.

Figure 6.37 shows the resultant valence (top) and conduction (bottom graph) band offsets that arise when the band structure is calculated using the VBP_{InAsSb} values from Figure 6.36 (note that the two graphs have different y-scale ranges, corresponding to significantly larger VBO values compared to CBO).

The InAs/InAs$_{1-x}$Sb$_x$ valence band offset, or VBO, is parameter crucial for detector design which dominates the value of the fundamental bandgap experienced by heavy holes (whereas the miniband position is only the secondary contribution - unlike the InAs/GaSb superlattice). The values are colour-coded for measurement temperature the same way as in Figure 6.36; the crosses on both graphs represent the strained (due to epitaxial growth on a substrate) band positions that are actually present in the sample band structure. Simply subtracting the known contribution of hydrostatic and shear strain (as per Equations 6.3) results in the unstrained (substrate-independent) valence band offsets:

$$VBO = |E_{v,InAs} + \frac{\Delta_{0,InAs}}{3} - E_{v,InAsSb} - \frac{\Delta_{0,InAsSb}}{3}| \tag{6.4}$$

which are visualised in both graphs of Figure 6.37 as triangles. Due to the direct correspondence to VBP_{InAsSb}, the VBO values show the same (albeit negative) linear temperature dependence, with a decrease of about 45 meV as temperature rises from 77 to 300 K. As stated before, VBO increases with x_{Sb}, yielding stronger heavy hole confinement and narrower bandgaps. The conduction band position CBO, which has little effect on the absorption properties of weakly confining type-IIb superlattices, shows very little x_{Sb} dependence.

When the shear and hydrostatic strain contributions (the former of which is found to be dominant in all samples) are excluded from the band position calculations, the offsets of both bands shift appreciably downwards; the CBOs, which are strongly affected by shear strain, lose most of their value in line with the broadly accepted weak type-IIb alignment of the InAs/InAs$_{1-x}$Sb$_x$ superlattice.

A miniband position is defined as the energetic distance of the carrier miniband in a superlattice from the bottom of the respective bulk conduction/valence band position, as can be appreciated in the Figures 6.35, 6.33 and 6.34 band diagrams. It is found that the miniband position (and thus it contribution to bandgap widening) is far more sensitive to the thickness of the superlattice period d_{SLS} than the band offsets (and thus confinement potentials); indeed there is no correlation between the depth of the potential well and the carrier energy levels (as one would naively expect from a quantum well approximation of the superlattice); and even if a weak correlation is hidden in the data, it would be overridden by other dominant factors which arise due to the fact that multiple structural parameters are varied between the samples. Instead, it is possible to observe a clear dependence of the *sum* of the e1 and hh1 minibands on the total superlattice period, in a manner analogous to the bandgap control method in InAs/GaSb superlattices; this is important for the fine-tuning of the superlattice bandgap (as demonstrated earlier in the chapter on samples XV0160, XV0159 and XV0154) for their use in detectors. The plot of the miniband sum as a function of the total superlattice period can be seen in Figure 6.38. The decrease is most pronounced on the short end of the d_{SLS} range, with the larger d_{SLS} values assuming a more shallow slope.

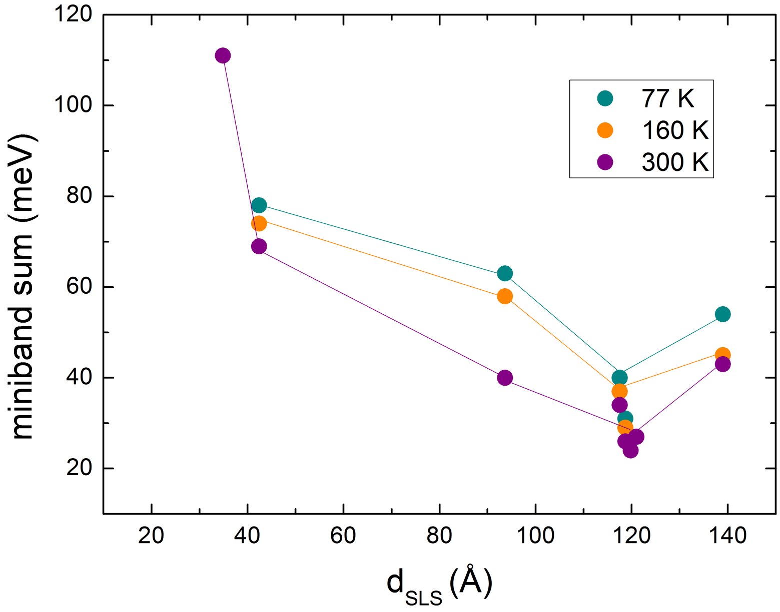

FIGURE 6.38: The sum of the e1 and the hh1 miniband positions as a function of superlattice period for a range of samples and temperatures. The lines are a visual guide only.

As can be seen, bandgap control in InAs/InAs$_{1-x}$Sb$_x$ superlattices can be achieved by two methods: variation of x_Sb (and therefore the valence band offset) and variation of the superlattice period d_{SLS}. In the most general terms, the advantages and disadvantages of thinner/thicker superlattices are already presented in Table 5.1 in Section 5.1.

Additional caveats arise with the use of the MBE growth method due to the fact that the group V (As/Sb) incorporation into an alloy cannot be easily predicted as a result of their temperature-dependent (and always less than 1) sticking coefficients (as discussed in Section 4.1). It is generally found that the growth-to-growth variation around the target x_{Sb} can be 0.01-0.02. Moreover, Sb variation of up to ±0.07 has been measured across wafers due to slight substrate temperature gradient present during growth (see Section 5.4.1). In contrast, superlattice period control is achieved via temperature variation of a single group III element (In) with a temperature-independent sticking coefficient of 1, resulting in good parameter uniformity and an error of no more than 1% of the total d_{SLS}. It can be shown that the error on layer thickness has an appreciably less deleterious effect on the reproducibility of the bandgap than the Sb variation, by modelling samples XV0160 (MWIR) and XV0440 (LWIR) with 1% variation of d_{SLS}, and $x_{Sb} \pm 0.01$. For sample XV0160, the uncertainty on the period is less than 1 Å, which results in a bandgap shift of less than 1 meV; meanwhile the x_{Sb} shift results in a bandgap change of ±6 meV, corresponding to an effective cut-off wavelength range of 6.13-6.52 μm in the detector. Since the detected wavelength has a reciprocal dependence on energy of the bandgap, the optical properties of a LWIR superlattice are increasingly more sensitive to Sb incorporation variations during growth than the MWIR ones. This is evident from modelling the changes in XV0440: once again the 1% error in d_{SLS} results in a less than 1 meV shift, whereas the ±6 meV bandgap range resultant from a ±0.01 Sb drift gives rise to an effective 10.7-11.7 μm cut-off wavelength range in the final detector. It is therefore possible to make the argument in favour of utilising d_{SLS} as a control parameter for the bandgap, especially in long-wavelength superlattices: the larger the fraction of the bandgap that arises from the miniband size rather than VBP_{InAsSb}, the smaller its overall error. On the other hand, however, smaller d_{SLS} will result in a lowered optical ground state density of states as per Equation 6.1; in the end, the final form of the optimised structure will depend on the priorities and the manufacturing methods of the user.

6.5.1 Conclusions

This Section summarised the optical properties of this work's samples: transmission, absorption coefficients and photoluminescence of undoped InAs/InAs$_{1-x}$Sb$_x$ superlattices, and the spectral response of the nBn devices. Fundamental optical bandgaps E_g are identified, and later compared to theoretical values derived using the Kronig-Penney model.

Section 6.1 focuses on the results derived from Fourier Transform Infrared spectrometry: absorption coefficients α (Section 6.1.1) and spectral response SR (Section 6.2). First, in Section 6.1.1, transmission spectra of the undoped epilayer samples are presented, followed by an outline of how they are used to calculate absorption coefficients.

These absorption coefficients α are presented in Section 6.1.2. 300 K absorption coefficients of three representative samples with $\lambda_{cut-off} \sim 6$, 9 and 13 μm were then compared to literature values of other materials, bulk and SLS, commonly used in IR detectors (including HgCdTe), and were found to have comparable values. This is a particularly useful observation in the light of the expectation that the InAs/InAs$_{1-x}$Sb$_x$ SLS system would have impeded absorption compared to other materials (as discussed in Section 3.4.2). Next, the procedure of extracting the fundamental bandgap E_g from $\alpha(h\nu)$ is outlined; E_g values are found for a series of samples at 300 K, showing a consistent dependence on x_{Sb}. This analysis is then extended to temperature-dependent absorption coefficients, and $E_g(T)$ is obtained.

Extraction of $E_g(300K)$ initially proceeded under two scenarios: that the system has a direct ($\alpha \propto (h\nu)^{1/2}$) and indirect bandgap ($\alpha \propto (h\nu)^2$). However, the first-derivative method (Figures 6.12 and 6.22), better overall robustness of the direct-bandgap results (Table 6.1), lack of temperature dependence in the $\alpha(T)$ gradients (Figure 6.13 inset), and better agreement of α- and SR-derived data strongly favoured the direct-bandgap scenario, and so all subsequent analysis was carried out under this assumption.

The other FTIR-derived measurement presented was temperature-dependent spectral response of the nBn devices (Section 6.2). Analysis of $SR(160K)$ of three similar MWIR devices shows that XV0576 has the sharpest absorption onset, likely due to an appropriate combination of doping density and superlattice period. Sample XV0650 appears adversely impacted by the ten-fold increase in n-doping compared to the other two samples. $SR(T)$ of two LWIR samples is also presented, with $\lambda_{50\%}$ varying between 9 at 77 K and 11.5μm at 200 K. The dual-colour QA504 device is shown to operate as expected, despite the likeliness that the layers in the sample are at least partially relaxed. XV0208, grown on an AlSb buffer, shows atypical features near $\lambda_{cut-off}$, suggesting that absorption features are dominated by transitions other than direct band-to-band. Instrumental factors are also possible. Further, $E_g(T)$ of the GaSb-grown nBn devices were extracted using $SR^2(h\nu)$ linear fits.

Three MWIR undoped epilayer samples were characterised at 4 K using power-dependent photoluminescence measurements in Section 6.3. The resultant peaks were fitted with Gaussian fits and analysed using the first-derivative method, which identifies the point of strongest change in absorption, was then applied.

In Section 6.4, all the $E_g(T)$ data derived in previous Sections is collated and analysed using the single-oscillator model outlined in Section 2.1.2. The full temperature fits of the $E_g(T)$ datasets are presented for samples XV0154, XV0159 and XV0160; the samples were designed to have the same x_{Sb} but different d_{SLS}, which results in clear bandgap differences at all temperatures. The single-oscillator fitting parameters are then recalculated into the Varshni model parameters and compared to literature results for comparable bulk materials, as well as other InAs/InAs$_{1-x}$Sb$_x$ superlattices. In all cases, temperature response of the bandgaps calculated here is found to be less pronounced than the literature values. Einstein temperature T_E is also found to be less than in literature. The nBn devices are found to be more temperature-dependent than the undoped superlattices, however their comparison with literature nBn values follows the same pattern.

In the final Section of the Chapter (6.5), the Kronig-Penney model is used to model in detail the band structure of InAs/InAs$_{0.825}$Sb$_{0.175}$ samples XV0154, XV0159 and XV0160, and the miniband differences arising from their varied d_{SLS}. The model is then applied to other undoped epilayer samples with $E_g(T)$ datasets in order to derive the InAs$_{1-x}$Sb$_x$ valence band position VBP_{InAsSb} with respect to $VBP_{InSb} = 0$ eV, which is a standard reference point for VPB of III-V semiconductors. Strain-free valence and conduction band offsets (VBO and CBO) are also calculated as a function of x_{sb}, demonstrating the type-IIb nature of the InAs/InAs$_{1-x}$Sb$_x$ superlattice.

6.5.2 Future work

In terms of methodology, the cryogenic FTIR transmission measurement can be refined: the sample holder could be redesigned such that it has no rotational axis and is located at the beam focus, which would minimise baseline errors. Although an in-house designed nitrogen purging system for the FTIR is in place, its use has not been optimised. Time-resolved photoluminescence spectra could also be commissioned in order to better differentiate between different types of carrier transitions in the superlattices.

The absorption coefficient α can be improved by increasing the ratio of the heavy hole well thickness d_{InAsSb} to d_{SLS}[119]; for LWIR applications, this would require the optimisation of strain-balanced growth on the AlSb constant as discussed in Section 5.5.

The modelling capabilities could be extended by incorporating the option to calculate the associated densities of states, and e1-hh1 wavefunction overlaps.

Chapter 7

III. Results and discussion: Device Performance

In addition to spectral response obtained on a Fourier Transform Infrared spectrometer (Section 6.2), the properties of a series of nBn devices were characterised using a cryogenic probe station (see Section 4.6.3 for the method) and a blackbody apparatus (Section 4.6.2). The first measurement provided the dark current response to bias (IV characteristics), outlined in Section 7.1.1, yielding dark current density J_d for each device. In Section 7.1.2 this data is further processed into voltage-dependent Arrhenius plots which provide information about activation energy E_a and the valence band offset at the barrier interface. The blackbody measurement is used in combination with bandpass filters to obtain the responsivity R of an nBn within a certain wavelength range (Section 7.4), which is then recalculated into quantum efficiency QE in Section 7.2.2. Finally, the R and J_d data is combined into specific detectivity D^* in Section 7.3.

7.1 IV characteristics

7.1.1 Dark current density J_d

Dark (leakage) current - the current flow in the device arising in response to factors other than the generation of photocarriers - is measured for a number of samples using the method outlined in Section 4.6.3 and analysed with reference to the current mechanisms discussed in Section 2.2.2. In order to ensure the reliability and repeatability of the data, three devices for each sample were chosen with diameters $d_{dev} = 800, 400$ and 200 μm at the beginning of the measurement, then re-measured between 77 and 300 K at temperature intervals of 20 K; these temperature-dependent current densities are plotted as an absolute function of device bias (ie. so-called JVT plots) for six samples in Figure 7.1. The relevant structural information for each sample is included on graph (the full details can be seen in Appendix B); it is important to note that the dual-colour QA504 sample is structured such that the bottom superlattice acts as the LWIR absorber, while the top superlattice, customarily designed as the optically inactive contact layer, assumes the role of the MWIR layer. Therefore the positive bias region represents the dark current in the MWIR layer.

Sample XV0161 demonstrates a significant overall decrease of current between 300 and 77 K, indicating a large value of activation energy E_a (discussed in detail in the following Section 7.1.2), as well as the lowest J_d values of all the samples (the noisy 77 and 100 K curves correspond to the noise floor of the multimeter). At low temperatures two distinct types of behaviour are in evidence: voltage dependence at lower bias and current saturation at voltages above -0.35 V in magnitude. The former likely arises due to carrier tunnelling across the non-negligible valence band offset at the barrier interface, which proceeds until the potential barrier is overcome at higher bias and the current starts tending towards diffusion-limited behaviour. As temperature rises, thermal energy supplied to the carriers increasingly contributes to overcoming the barrier, indicated by decreasing voltage dependence. The presence of a valence band offset in Sample XV0161 is indeed further confirmed in the voltage dependence of activation energy E_a, at outlined in Section 7.1.2, and is the likely reason for the low overall J_d of XV0161.

The instance of a misaligned barrier contributing to a deceptively low dark current is thought to explain the elevated J_d of XV0576: a strain-balanced device grown on native

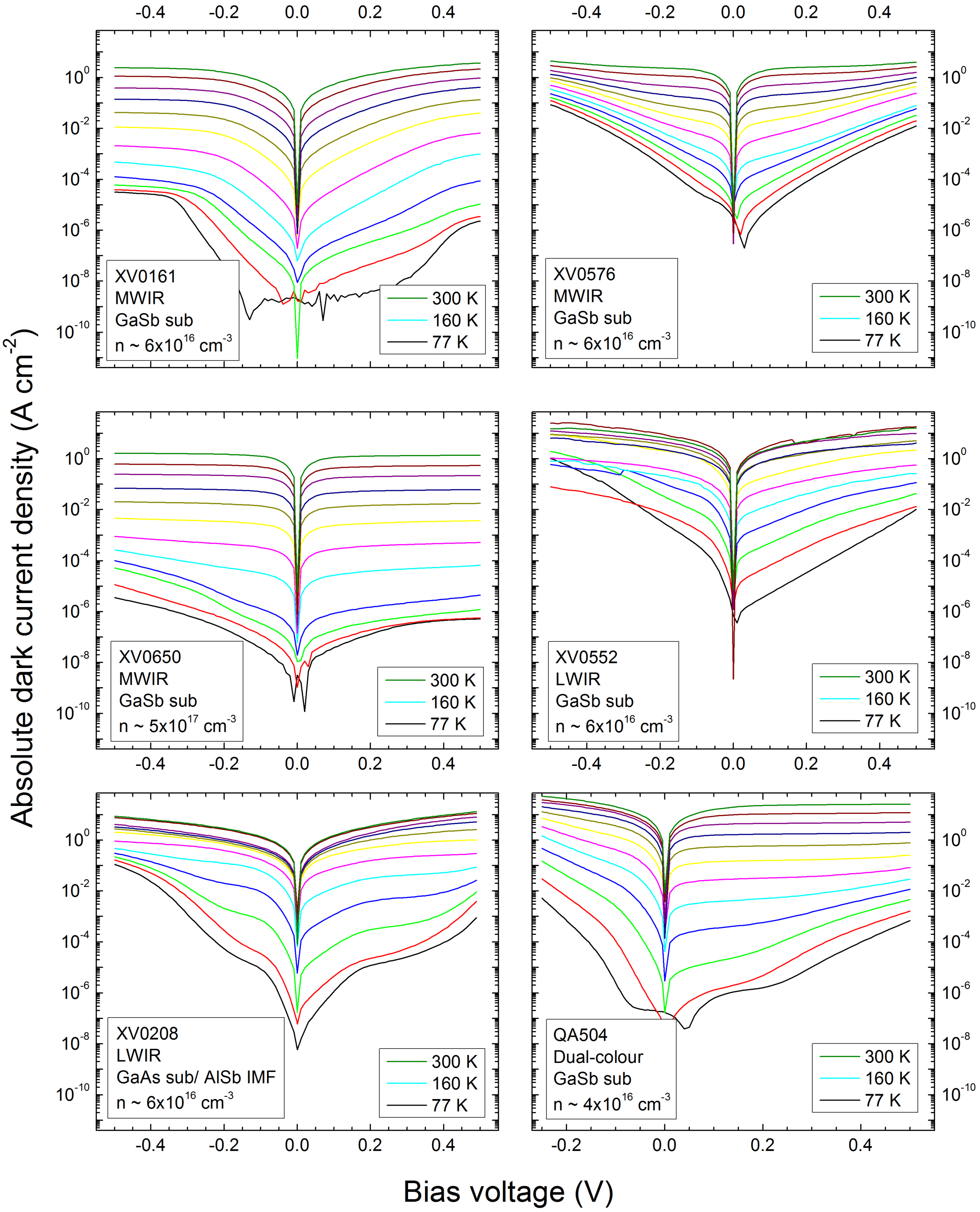

FIGURE 7.1: Temperature-dependent absolute dark current densities as functions of device bias, measured between 77 and 300 K with increments of 20 K. All results are for d_{dev} = 400 μm, aside from QA504, which is for d_{dev} = 200 μm.

GaSb with a well-aligned (see Section 5.4.3), lattice-matched 110 nm barrier nevertheless shows poor dark currents when compared to both the rest of the sample set as well as other comparable technologies (eg. Rule 07 in the following Section). The device displays diffusion-limited behaviour at higher temperatures as expected, but an onset of voltage dependence can be observed as temperature decreases to $T = 77$ K. Assuming that the dark current in sample XV0161 is artificially suppressed by a valence band offset, it is possible that the low doping of the XV0576 is insufficient to suppress J_{SRH}. Another possibility is a tunnelling current mechanism somewhere in the sample (which would have a stronger than J_{SRH} voltage dependence). Because no other immediate explanation arises from the structural properties of the nBn itself, a complementary explanation can potentially be found in the growth process of the device, such as an abnormally high concentration of background impurities or the insufficient optimisation of the growth stage of the GaSb buffer layer that follows substrate deoxidisation, resulting in additional dislocations.

Sample XV0650 incorporates a superlattice and barrier structure that is very similar or identical to that of XV0576, but demonstrates J_d response much more characteristic of an ideal nBn device: a strong and sustained temperature dependence of the current as well as diffusion-limited behaviour down to 160 K. The sample is structurally different in two ways: $d_{absorber}$ is doubled to 8.7 μm, and the n-doping increased by on order of magnitude to 5×10^{17} cm^{-3}. The expected consequence of the latter is two-fold: it disables mid-bandgap traps acting as recombination centres, and reduces the effective absorber volume via decreased carrier lifetimes, preventing collection of majority carriers generated deeper in the absorber. In turn, the thicker absorber is shown to result in no additional degradation of crystal quality in the XRD scans in Section 5.4.3; also, a combined effect of reduced carrier lifetimes and increased absorber thickness could be that any extra dark current generated in the GaSb buffer layer (as discussed above) never reaches the top contact. While the J_d characteristics of this sample are thus desirable for detector performance, quantum efficiency measurements (see Section 7.2.1) show poor photocarrier extraction compared to XV0576 - for optimal detector performance, a correct balance of absorber doping and thickness will need to be achieved.

Samples XV0552 and XV0208 are LWIR devices with $x_{Sb} = 0.31$ and 0.33 respectively.

The overall increase of current magnitude due to the narrowing of the bandgap (and thus increasing the trap-assisted SRH process across it) is apparent. The lowest temperature curves have pronounced voltage dependencies that are likely a combination of absorber depletion and valence band offset tunnelling (in Section 7.1.2 both samples are shown to have non-negligibly offset valence band junctions with their barriers, which would artificially impede the dark current). The 'bunching' of the higher-T curves in the diffusion-limited regime occurs at very high currents and is a combination of suitably lower activation energies and the read-out circuit resistance becoming non-negligible. Although XV0208 was grown on an the lattice-mismatched GaAs substrate with an AlSb buffer layer rather than the native GaSb (and hence is affected by a larger dislocation density - see Section 5.4.6), it shows lower J_d which however could be due a more strongly misaligned barrier or a barrier elsewhere in the device, rather than a property of the structure.

The sixth JVT plot shows the dual-colour QA504 sample where both superlattices act as absorbers. Despite the coupled XRD scan showing strong evidence of relaxation in the entire structure, the MWIR (top) superlattice displays diffusion-limited behaviour down to 140-160 K, albeit some evidence of high-bias dependence is present. Bias dependence dominates the current in the LWIR layer up to much higher temperatures, however, likely due to a large potential barrier experienced by minority holes as they are extracted across the stepped barrier layer and into the MWIR absorber.

Comparison with Rule 07

The dominant infrared detector technology is based on bulk HgCdTe material, and is known to have the lowest dark currents in the field (see Section 3.3). In order to enable easy comparison of other IR technologies with CMT, and to provide a convenient benchmark for their performance, Tennant et al[78] have derived an empirical relationship between the dark current density of the CMT detector J_d, its cut-off wavelength $\lambda_{cut-off}$ and the detector temperature. Because J_d calculated with Rule 07 represents diffusion current due to Auger 1-generated minority carriers in an n-doped neutral absorber[79], the comparisons can be carried out independently of bias and represent a useful reference point for superlattices, whose Auger processes are meant to be suppressed. In order to plot the J_d data discussed in the preceding Section as a function of the cut-off wavelength $\lambda_{cut-off}(T)$ for each sample is taken to be $\lambda_{50\%}$ as defined in Section 6.2.

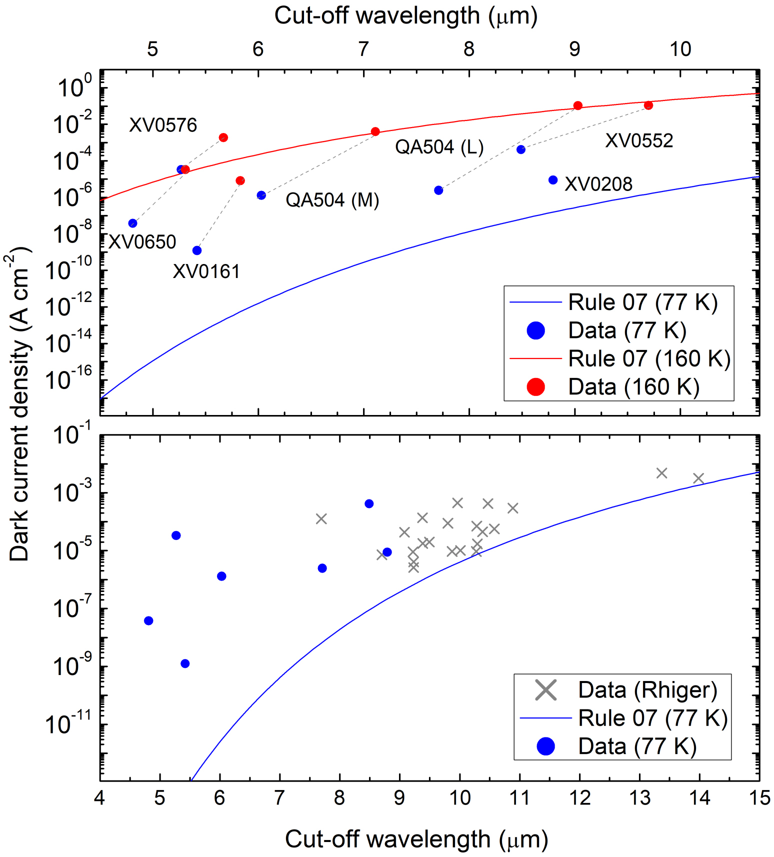

FIGURE 7.2: Comparison of dark current densities from this work with Rule 07 as functions of cut-off wavelength. The grey dashed lines join the data points for the same sample, aside from XV0208. Top: the data and Rule 07 plotted at $T = 77$ and 160 K. Bottom: Comparison of the data to other IR structures incorporating barrier architecture (collated by Rhiger[79]).

The top graph of Figure 7.2 shows the $J_d(\lambda_{cut-off})$ data plotted for two operational temperatures: 77 and 160 K, with the equivalent Rule 07 plots included. All the J_d values were extracted from bias of -0.1 V aside from Q504 MWIR, which was +0.1 V. The grey dashed lines join the data points for the same sample. It is evident that at $T = 77$ K all the samples are operating in a regime limited by tunnelling and potentially SRH, because all the J_d values lie several orders of magnitude above Rule 07; although the LWIR samples lie closer to Rule 07 than the MWIR ones, this could be a sign of compromised carrier extraction due to a barrier valence band offset. In contrast, it can be appreciated that diffusion becomes more prominent at 160 K. The bottom graph draws a wider comparison with literature LWIR devices implementing a barrier as collated by Rhiger[79] (also briefly presented in Section 3.3). The author notes that the proximity of J_d to Rule 07 increases with $\alpha_{cut-off}$ (which is also observed in this work) and speculates that this could be due to the fact $J_{SRH} \propto n_i$, whereas $J_{diff} \propto n_i^2$, where n_i is the intrinsic carrier density[64,174]; because n_i increases with $\lambda_{cut-off}$, diffusion current would come to dominate over J_{SRH} at lower temperatures.

7.1.2 Arrhenius plot and activation energies

A current-related advantage intrinsic to the nBn architecture is that the barrier layer suppresses surface majority carriers as well as bulk ones, effectively acting as a passivation layer. That this is the case for the structures discussed here is demonstrated in Figure 7.3, which features a plot of dark current density J_d at a constant temperature and voltage (noted on the graph) plotted as a function of the diameter-to-area ratio of each device. A flat line is characteristic of current densities with no significant surface current component, which is observed for all the presented structures.

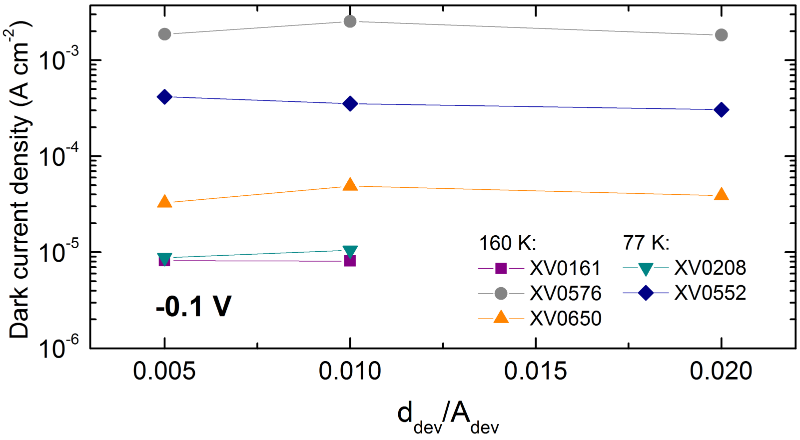

FIGURE 7.3: J_d of nBn devices at a constant temperature and voltage plotted as a function of the diameter-to-area ratio of each device. A flat line shows that there are no significant surface currents in the device.

An Arrhenius plot is the $J_d(V,T)$ of a sample at a constant V plotted as a function of $1000/T$. The usefulness of this format arises from the observation that both J_{SRH} and J_{diff} vary exponentially in response to temperature, according to the relationships outlined in Section 2.2.2:

$$\begin{aligned} J_{SRH} \propto n_i \propto T^r exp\left(\frac{-E_{tr}}{kT}\right) \\ J_{diff} \propto n_i^2 \propto T^r exp\left(\frac{-E_{diff}}{kT}\right) \end{aligned} \tag{7.1}$$

where E_{tr} is roughly equal to $1/2E_g$ and $E_{diff} \sim E_g$ at cryogenic temperatures; whereas r is a factor related to the Moss Burstein energy of the superlattice and can vary between ~ 1.5 and ~ 3[64] (see below). As such, an Arrhenius plot is a more convenient tool for identification of diffusion- and SRH-limited current regimes than simple JVT curves.

The conventional way of representing combined current in a p-n diode, $J \sim exp(-E_a/kT)$[175], is insufficient for a doping regime where the resultant Moss-Burstein (band filling) energy is non-negligible compared to kT[64]. That this is the case for the discussed superlattices can be shown by comparing the joint optical density of states to the doping levels[165]:

$$\rho_0 = \frac{2}{\pi E_1 d_{SLS}^3} \tag{7.2}$$

where E_1 is the electron bandwidth $E_1 \equiv E(\pi/d) - E(0)$[95] calculated using the model in Section 6.5, and d_{SLS} is the total superlattice period. The ratio of the doping density n_D to ρ_0 then gives an estimate of the band edge shift due to band filling, and the sample-specific results can be seen in Table 7.1. The kT values represent the nominal operational temperatures, 77 K for LWIR and 160 K for MWIR devices. It can be immediately appreciated that in none of the cases band filling is negligible; and while sample QA504 cannot be reliably modelled due to high relaxation of its layers, there is

TABLE 7.1: Optical joint densities of states of the nBn devices, and the resultant estimated Moss-Burstein (band filling) energies. kT is defined at the nominal operational temperatures for the detectors, $T = 77$ K for LWIR and $T = 160$ K for MWIR.

Sample	d_{SLS} **(cm)**	E_1 **(eV)**	ρ_0 **(eV^{-1}cm^{-3})**	**Band filling (eV)**	**kT (eV)**
XV0161	9.25×10^{-7}	0.066	1.22×10^{19}	0.005	0.0138
XV0576	13.31×10^{-7}	0.057	4.74×10^{18}	0.013	0.0138
XV0650	8.27×10^{-7}	0.08	1.41×10^{19}	0.036	0.0138
XV0552	10.61×10^{-7}	0.073	7.30×10^{18}	0.008	0.0066
XV0208	8.08×10^{-7}	0.091	1.33×10^{19}	0.005	0.0066

no reason to expect its Moss-Burstein energy to behave differently. As such, per recommendation of Klipstein et al[64] r is taken to be 1.5.

A representative activation energy E_a (which is equivalent to E_{tr} and E_{diff} from Equation 7.1 depending on the dominant current mechanism) for a given sample is calculated at -0.1 V bias, as this is a reasonable choice for operational voltage. The data is then plotted on an Arrhenius graph and the high-T regime is fitted with the $J_d \propto T^{1.5} exp(-E_a/kT)$ function, the results of which can be seen in Figure 7.4. The black lines represent the fits, the red lines are the corresponding Rule 07 curves, and the insets show the bias dependence of J_d in the range -0.01 to -0.4 V (positive for the QA504 MWIR layer). The effect of the barrier on carrier flow can be discerned in samples whose dark current is further suppressed than the ideal Auger-1 diffusion-limited scenario of Rule 07: XV0161, XV0208 and XV0552 (note that the high-T J_d of XV0208 shows anomalous behaviour more likely arising due to experimental rather than structural factors, such as not allowing enough time for it to reach thermal equilibrium, and device damage at 280 and 300 K; as such, this data is excluded from the fit). Samples XV0576 and XV0650 show diffusion-limited behaviour approaching Rule 07 at higher temperatures, with the cross-over temperatures T_0 of around 200 and 140 K respectively; meanwhile, sample XV0552 demonstrates both SRH-dominated behaviour and strong bias dependence.

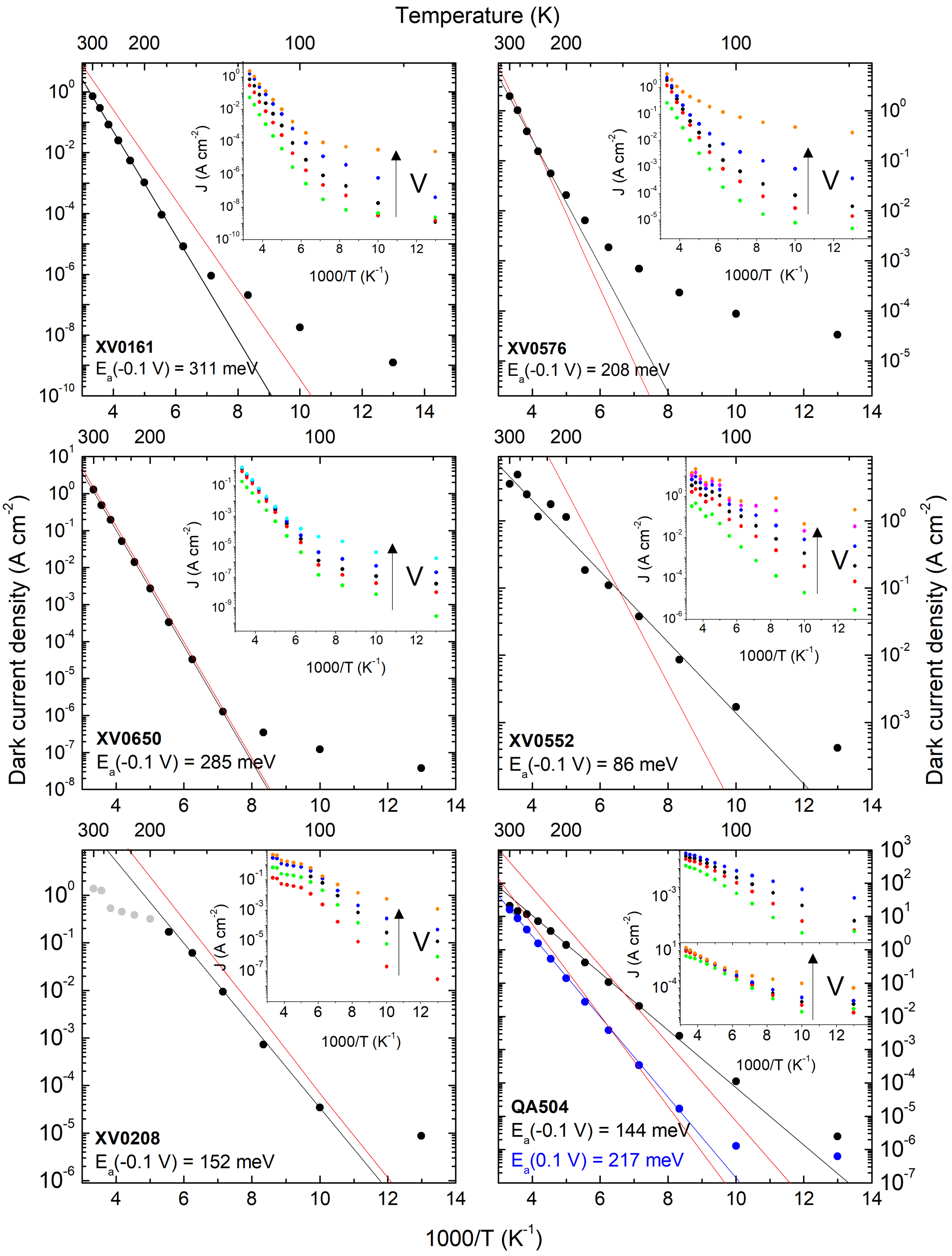

FIGURE 7.4: Arrhenius plots and J_d voltage dependencies of nBn devices. The operational bias on all the main graphs is -0.1 V (+0.1 V for the QA504 MWIR layer). The black curves are Arrhenius fits and the red curves represent Rule 07. Insets: voltage dependence of J_d in the range -0.01 to -0.4 V.

Importantly, when the low-temperature regions are fitted, only sample XV0161 shows E_a of approximately half $E_g(77K)$, equal to 97 meV; the low-T activation energy of all the other samples is much lower, and thus likely representing contribution of band-to-band tunnelling in a small depletion region present next to the barrier, or barrier tunnelling where $d_{barrier}$ is sufficiently small, rather than the SRH current.
Designing an effective nBn device is dependent on incorporation of a barrier that results in a flat valence band across the whole structure. In practice, calculating the barrier from literature parameters does not guarantee a full barrier alignment and should be complemented with observations from experimental data. Two types of measurements in this work can give insight into the barrier alignment: activation energy extracted from Arrhenius plots, and responsivity voltage dependence (Section 7.2.1). When E_a for the same device is calculated at different voltages, the presence of bias dependence at lower values points to the existence of valence band offset between the SLS and barrier. This bias dependence in presence of a valence band offset can be linked to voltage-activated carrier tunnelling across a potential barrier with a thinner (due to band bending) thickness, as seen in Figure 7.5.

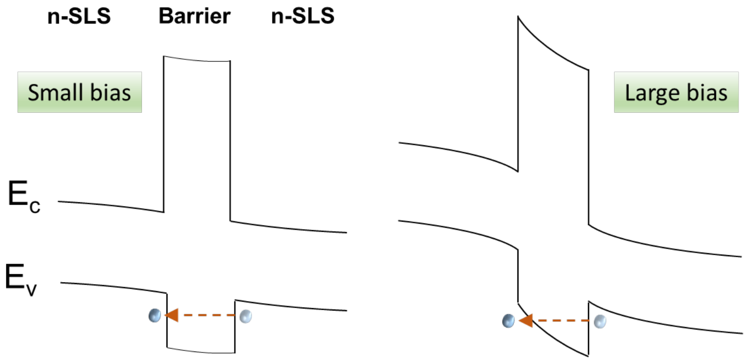

FIGURE 7.5: An nBn device with a non-zero valence band offset under negative bias. Increased bias causes enhanced carrier tunnelling.

The relationship between the high-T E_a obtained from Figure 7.4, the low-T bandgap $E_g(77K)$ (extracted from spectral response measurements as per Section 6.2) and bias V for each sample is summarised in Figure 7.6. Because J_d is considered diffusion-limited when its E_a approaches $E_g(0K)$ and SRH-limited when $E_a \sim 1/2 E_g(0K)$, the ratio

$(E_a)/(E_g(77K))$ is plotted on y-axis for easy identification (it is believed that $E_g(77K) \sim E_g(0K)$ is a reasonable approximation considering the temperature-dependent bandgap behaviour observed in 6.4). A structure is defined to have no barrier when the 'low-bias' regime, taken to fall below -0.2 V, shows no appreciable voltage dependence.

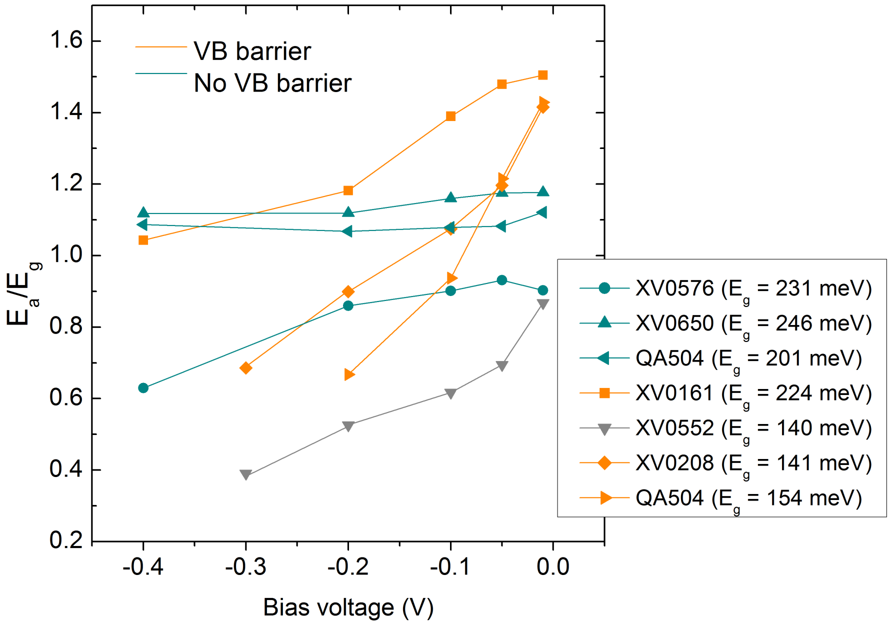

FIGURE 7.6: The ratio of activation energy E_a to the 77 K bandgap of each device as a function of bias. The blue guiding lines denote samples with no substantial valence band offset between the superlattices and the barrier, while the orange lines represent samples affected by barrier presence.

Three samples fulfill this criterion: XV0576, XV0650 and QA504 MWIR. The fact that the latter two structures also demonstrate $E_a > E_g(77K)$ (where $E_a = E_g(77K)$ is maximum theoretical value) could be a convolution of three factors. First, $E_g(77K)$ could be an underestimate of $E_g(0K)$ (in which case all the ratios would shift downwards). Second, because the r parameter in Equation 7.1 can have a value anywhere between 1.5 and 3, it is possible that it is underestimated (which would overestimate E_a and again shift all the curves downwards). The third (and least pronounced) factor is that since a variation of $x_{Sb} \pm 0.001$ is known to exist across devices grown on GaSb (see Table 5.2 in Section 5.4.4), the different devices used in JVT and spectral response measurements could potentially have slightly different bandgaps. Once these factors are accounted for it is reasonable to say that these two devices are diffusion-limited. The strong voltage dependence of the QA504 LWIR layer where there is none in the MWIR layer is easily explained by the stepped architecture of the barrier: carriers flowing out of the MWIR layer do not experience a potential barrier at any point, whereas the LWIR carriers need to overcome a number of potential steps in order to be collected. This is reflected in both the inflated low-V E_a value and the overall voltage dependence. For sample XV0552, the significance of the valence band offset is unclear; while the sample does show voltage dependence, E_a never rises above $E_g(0K)$, pointing instead to an E_a behaviour dominated by a combination of diffusion and SRH mechanisms.

7.2 Quantum efficiency

7.2.1 Responsivity

Responsivity of two MWIR and two LWIR samples was acquired using the method described in Section 4.6.2. In order to precisely quantify the optical power that reaches the sample surface, additional characterisation of the bandpass filters was carried out in order to obtain Γ, the bandpass filter transmission factor, which represents the fraction of the blackbody power modulated by the blackbody lineshape, filter transmission, and atmospheric absorption. The blackbody energy density was calculated using the emitter temperature $T_{BB} = 550°\text{C}$ and the equation

$$S_{BB} = \frac{8\pi hc^2}{\lambda^5} \frac{1}{exp\left(\frac{hc}{kT_{BB}\lambda}\right) - 1} \tag{7.3}$$

where λ is the wavelength of the emitted photon. The resultant curve, representing energy per unit volume per unit wavelength, is then normalised to the integrated area of the spectrum. The filter transmission spectra were obtained using the FTIR - it is generally recommended to obtain the filter spectrum at the same temperature as that of the actual responsivity measurement, because the bandpass range shifts a small distance (~0.05 μm) towards higher wavelengths in response to rising T. The rest of

the process of calculating Γ can be understood with the help of Figure 7.7: the transmission spectrum (which shows some reflection artifacts, discussed in Section 6.1.1) has the atmospheric absorption subtracted from it, the output of which is then multiplied by the normalised blackbody spectrum, and that is finally integrated to find the area. The LWIR bandpass filter (not shown) covers the range 8.0-10.2 μm at 77 K.
Gold is near 100% reflective in the MIR region, hence it is also important to account for any topside electrical contacts on the device. This is done based on the CAD file of the device mask and the contacts are found to reduce the effective device area by about 37%.

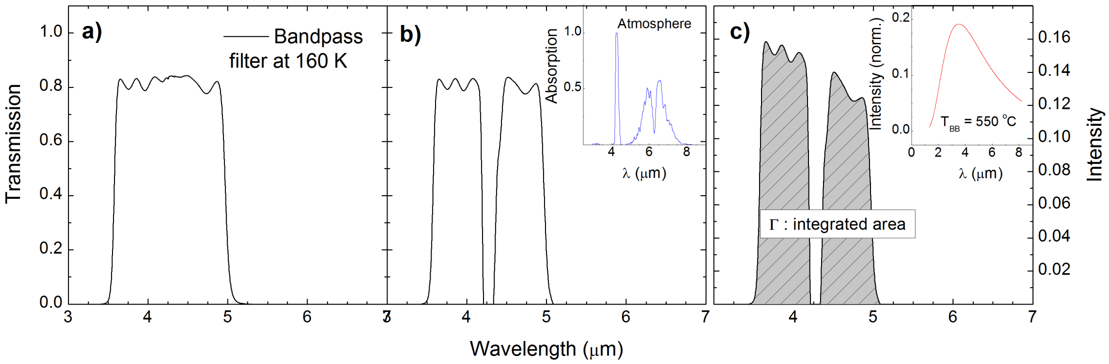

FIGURE 7.7: Calculating the filter transmission factor from transmission data of the 3.7-5.0 μm filter. a) Transmission spectrum of the filter at 160 K. b) Transmission spectrum after accounting for atmospheric absorption (see Inset). c) Multiplying b) by the normalised blackbody energy density spectrum at $T_{BB} = 550°\text{C}$ (see Inset) and integrating results in the fraction of the blackbody power output incident on the device.

Care needs to be taken to precisely align the different components of the measurement, and to isolate any reflected light and light otherwise not emitted by the blackbody element from impacting the detector. For each measurement the pre-amplifier gain (in A/V) and the corresponding lock-in signal (in V) were recorded. The lock-in signal is further converted from V_{rms} to V_{peak} by dividing the former by 0.45 as required by the SR830 signal conversion process[176]. Multiplying gain and V_{peak} yields I_{peak} with responsivity equal to

$$R = \frac{I_{peak}}{P_{BB}} \tag{7.4}$$

where P_{BB} is the incident optical power calculated using Equation 4.5. For the sample XV0576, responsivity was measured at multiple aperture diameter ($2r_a$) and aperture-device distance (d) values in order to ascertain the influence of physical parameters on the results, which can be seen in Figure 7.8.

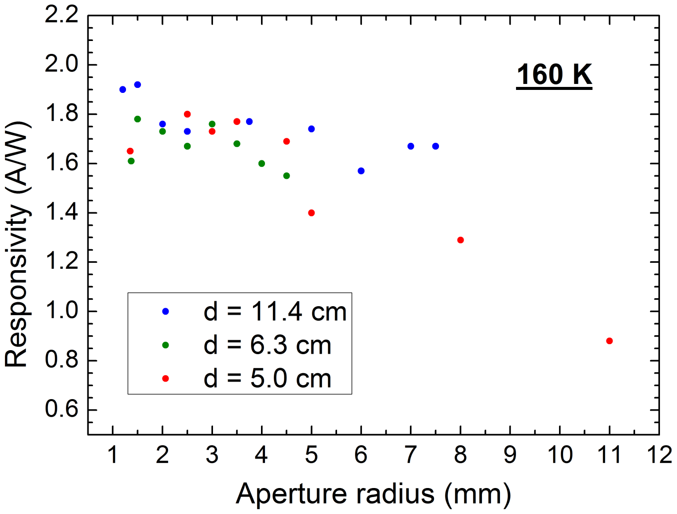

FIGURE 7.8: Responsivity of the MWIR sample XV0576 as a function of aperture diameter (x-axis) and aperture-device distance d (colour-coded).

The device diameter was 800 μm, device temperature 160 K and bias -0.1 V. No systematic dependence can be discerned on either r_a or d. The very slight decrease with increasing r_a, if real, could be attributed to an increasing amount of stray (ie. not black-body) light entering the aperture as its radius increases. This effect is evident in the two measurements taken at $r_a = 11$ and 8 mm: they were taken at a value of r_a exceeding the calculated limit imposed by the geometry of the setup and as such, they are excluded from analysis. Otherwise, the random scatter of values points to a dominance of factors such as small shifts in alignment between measurements, human error in setting aperture size, and fluctuation of the lock-in signal (although error specifically due to signal fluctuation was not quantified, the lock-in signal was generally stable for all samples, so it would be reasonable to assume that the uncertainty calculated for sample XV0576 is the same for the rest). The mean responsivity of XV0576 in this measurement is then calculated to be 1.70±0.11 A/W. This can be compared to peak responsivities of MWIR

InAs/InAs$_{1-x}$Sb$_x$ nBn detectors by Teledyne, presented in Section 3.5.1, specifically in Figure 3.9, which shows peak R of ~2.25 A/W at temperatures above 200 K. While this is an appreciably higher value, it should be noted that this peak lies at a shorter wavelength $\sim$ 4.2 μm, and is obtained using anti-reflection coating[130].

The XV0576 result is also a far higher value than 0.23±0.01 A/W found for the sample XV0650 (obtained using identical methods). As discussed in Section 6.2 regarding the gradient of absorption onset, this is most likely explained by the increased n-doping in the absorber (5×10^{17} cm^{-3} versus 6×10^{16} cm^{-3}), which would cause a severely decreased minority carrier diffusion length (and a smaller resultant absorbing volume) through increased majority electron concentration. This has clearly impeded responsivity of the device; on the other hand, limiting minority carrier diffusion length is useful in preventing cross-talk between pixels in linear or 2D arrays.

In addition to Arrhenius plots, studying the bias dependence of responsivity is another method of gauging the presence of a valence band offset between the barrier and the superlattice layers. Figure 7.9 shows the responsivity of the two MWIR samples plotted as a function of device bias.

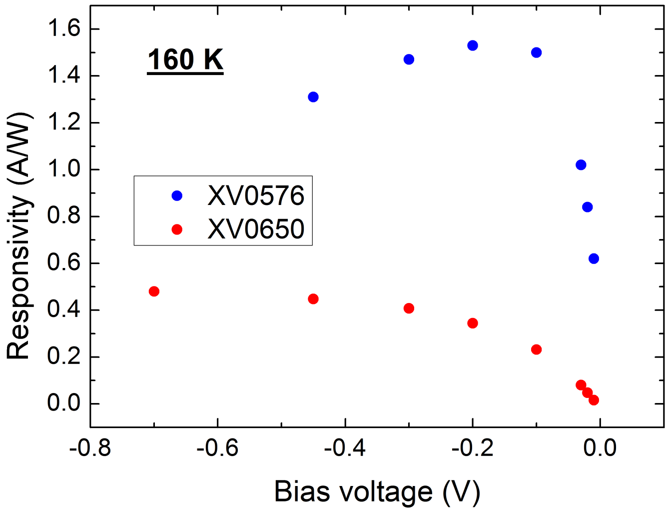

FIGURE 7.9: Bias dependence of the responsivity of samples XV0650 and XV0576.

Some presence of a valence band offset with the barrier is evident below -0.1 V (both samples have nearly the same x_{Sb} and barrier composition, as shown in Table 5.4). At higher voltages XV0650 tends towards an asymptote while XV0576 begins to decline - this is most likely symptomatic of the more strongly bias-dependent dark current flowing in XV0576 at higher V, as seen in Figure 7.1, and so causing loss of photocurrent. This is in contrast to XV0650 whose IV behaviour at 160 K is diffusion-limited and so V-independent.

Two LWIR samples, XV0548 and XV0552, were also characterised, with the results plotted in Figure 7.10. Sample XV0552, despite the poorer barrier alignment with the valence band, has its responsivity saturate at -0.1 V, the same region as sample XV0576; while the structurally compromised XV0548 barrier (due to the Al flux changing during barrier growth, causing a graded composition) is evident in the voltage dependence of XV0548. Despite the additional potential barrier, however, XV0548 shows responsivity of about two orders of magnitude larger than the other sample, indicating influence of another structural factor, such as poorer strain balancing. The overall poor reponsivity of these samples is more likely explained by the misalignment of the 8.0-10.2 μm filter bandwidth with their spectral response range rather than a more fundamental limitation of the structures, as shown in the following Section 7.2.2.

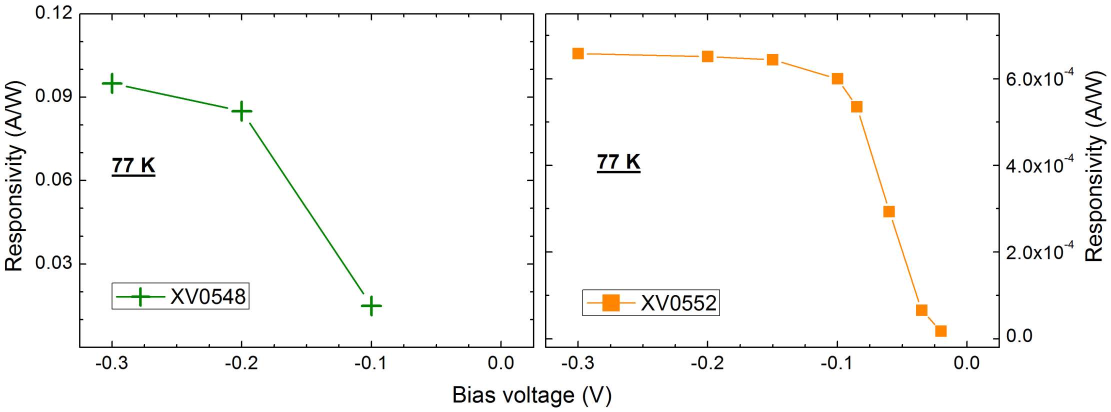

FIGURE 7.10: Bias dependence of the responsivity of samples XV0548 (left) and XV0552 (right).

TABLE 7.2: The external and internal quantum efficiencies of two MWIR and two LWIR samples. Data obtained at -0.1 V bias and 160 K (MWIR) and 77 K (LWIR).

Sample	**XV0576**	**XV0650**	**XV0548**	**XV0552**
EQE (%)	32.6±2.2	4.3±0.3	0.26±0.07	$(1.2\pm0.08)\times10^{-2}$
IQE (%)	49.7±3.4	6.6±0.5	0.35±0.09	$(1.6\pm0.01)\times10^{-2}$

7.2.2 External quantum efficiency

External quantum efficiency *EQE* is fundamentally defined as a ratio of carriers collected by the detector to incident photons of a given energy (see Equation 2.40). In order to quantify the total photon flux emitted by a blackbody within a certain wavelength interval, first the blackbody spectral radiance is defined in terms of wavelength[142]:

$$L_\lambda = \frac{2hc^2}{\lambda^5}\frac{1}{exp(^{hc}/_{\lambda kT}) - 1} \tag{7.5}$$

which denotes power emitted per unit area per solid angle per unit wavelength interval. Dividing by photon energy and integrating over photon wavelength then yields photon number per second per unit area per steradian[1]:

$$N_{ph} = \int_{\lambda_1}^{\lambda_2} \frac{L_\lambda}{hc/\lambda} d\lambda \tag{7.6}$$

To acquire photon flux incident on the device, N_{dev}, Equation 7.6 is integrated across the entire spectrum, then modulated by system throughput Θ, ZnSe window transmission and the filter transmission factor just like Equation 4.5. Multiplying N_{ph} by the fundamental charge then gives the hypothetical maximum current I_{max} at 100% QE. External quantum efficiency is then simply

$$EQE = \frac{I_{peak}}{I_{max}} \tag{7.7}$$

defined for the wavelength range of the filter used. The resultant quantum efficiencies at -0.1 V, obtained from the same data as that for responsivity, can be seen in Table 7.2.

The MWIR sample XV0576 demonstrates good quantum efficiency for a device with no anti-reflective coating or double-pass architecture, comparable with InAs/GaSb- as well as $InAs_{1-x}Sb_x$-based structures reported in Sections 3.4.2 and 3.5, and is expected to be improved further with a fine-tuned barrier composition. Sample XV0650 is obviously affected by its doping density as discussed before; moreover, the LWIR samples suffer from filter misalignment as shown in Figure 7.11.

An instrumental factor to consider is the choice of bandpass filters for these tests, whose spectral ranges do not align with the the region of maximum response of the sample (see Figure 7.11). This is particularly pronounced for the LWIR samples whose absorption edge just barely falls within the 8-10.2 μm filter range, because the modulation of the incident blackbody power by the filter transmission factor (Equation 4.5) assumes absorption across the entire bandpass range. The real quantum efficiencies are therefore likely to be higher (especially for the LWIR samples) and an optimised measurement setup would make use of custom-designed bandpass filters.

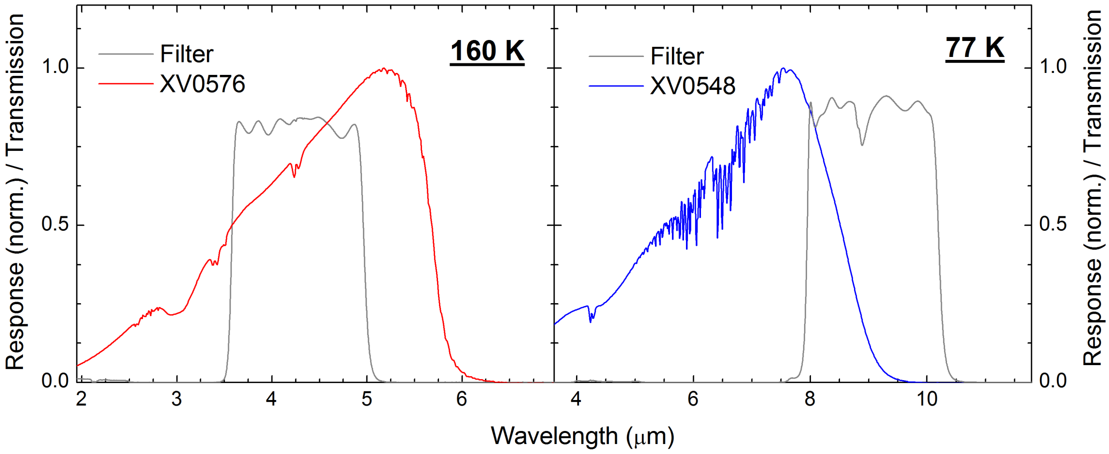

FIGURE 7.11: Spectral responses of samples XV0576 and XV0548 compared to the bandpass filter ranges used in the quantum efficiency measurements.

7.2.3 Internal quantum efficiency

Internal quantum efficiency (IQE) is defined as external QE divided by $(1 - R_s)$, where R_s is the reflection at the sample-air interface, ie. it is a ratio of generated electron-hole pairs to the number of photons entering the absorber (see Section 2.2.3). Because R_s is a function of the refractive index n_{SLS} and the extinction coefficient k_{SLS}, it is also indirectly dependent on photon wavelength λ (Equations 2.33, 2.35 and 2.34). Ideally, EQE would have been quantified as a function of λ as well (eg. by employing a monochromator), but even with a single integrated EQE value it is possible to estimate the resultant IQE. First, an effective n_{SLS} for each sample within the bandpass range can be established from the n_{SLS} spectrum in Figure 7.12 by taking a mean of the data within these limits. This yields $n_{0576} = 3.84 \pm 0.02$, $n_{0650} = 3.85 \pm 0.02$ for the MWIR samples and $n_{0548} = 3.01$, $n_{0552} = 2.82$ for the LWIR ones. Second, for the purposes of estimation, it can be realised that $(1 \pm n_{SLS})^2 \gg k_{SLS}^2$ when the absorption coefficient α_{SLS} is of the order of $\sim 10^3$ cm^{-1} and below. k_{SLS} can subsequently be ignored without any appreciable loss of accuracy. Applying the simplified Equation 2.33 and subsequently 2.41 to each sample then yields estimated internal quantum efficiency of the device and the results can be seen in Table 7.2. So far this approach ignores the losses in the top contact superlattice, as photocurrent generated in that region does not contribute to the signal and so the real IQE will be somewhat larger.

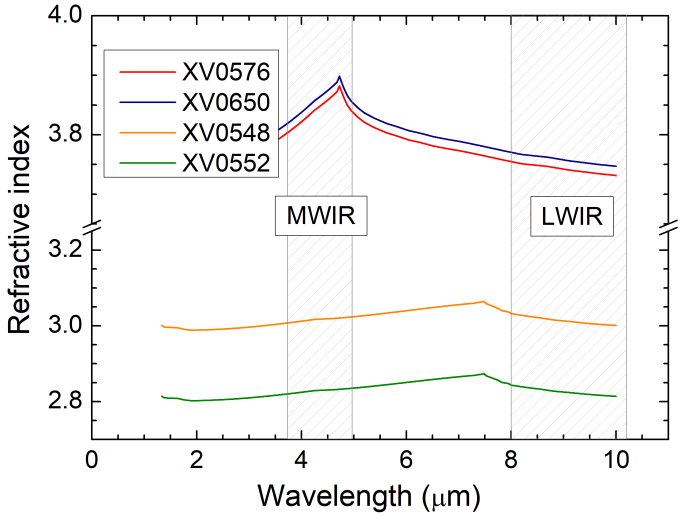

FIGURE 7.12: The calculated refractive indices of the four samples with the bandpass filter ranges overlaid in grey.

7.3 Specific detectivity

By combining the dark current data discussed in Section 7.1 and device responsivity (Section 7.2.1) it is possible to obtain the specific detectivity D^* of the samples - the reciprocal of noise-equivalent power, or the incident power necessary to lift the signal above the noise floor of the detector, per unit bandwidth and normalised to device area. Idealised noise current I_n is assumed to arise from two sources: thermal noise I_T and shot noise I_{sh}. Thermal noise is a function of the dynamic resistance of the device, $R_{dyn} = \mathrm{d}V/\mathrm{d}I$, which parametrises the response of current to a change in bias and so can be extracted from data in Section 7.1. The R_{dyn} data for the four samples discussed in Section 7.2.1 can be seen in Figure 7.13.

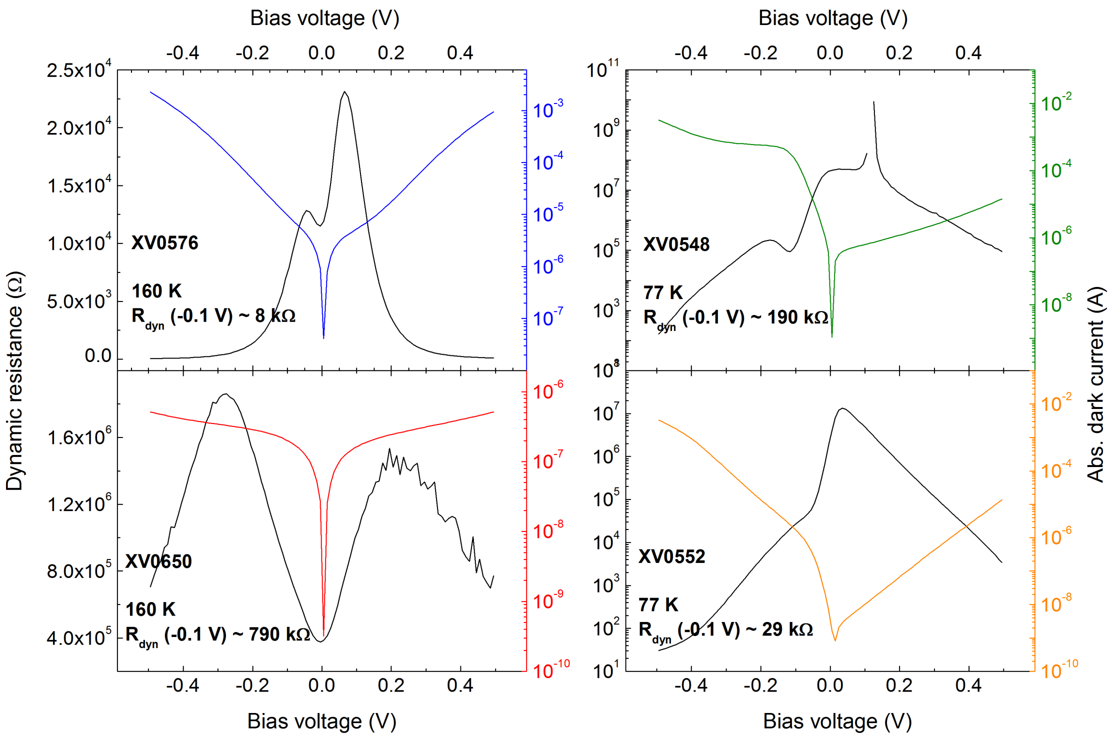

FIGURE 7.13: Dynamic resistance of two MWIR samples XV0576 and XV0650 (left column) and two LWIR samples XV0548 and XV0552 (right). The colour plots represent the corresponding absolute dark current in the device. All the devices had a diameter of 800 μm, with an effective (due to a reflective contact) diameter of ~635 μm.

Sample XV0650 (red) demonstrates some noise at higher positive bias values that is not immediately evident in the current data, and is likely due to a failing electrical contact to the sample. The gap in the data around +0.1 V for sample XV0548 (green) corresponds to a single anomalous value of negative R_{dyn}. This is because the current at this voltage undergoes a very small ($< 0.05\%$) dip in value then rises again, creating a negative and artificially small denominator for R_{dyn}; due to this, it is likely that the following spike at $R_{dyn} \sim 10^{10}\Omega$ (where the current measurement recovers its rising tendency) is also spurious.

Once R_{dyn} at the operational bias is known, the total I_n becomes straightforward to calculate as per Equation 2.45. It should be noted that because responsivity is modulated by the effective (rather than total) size of the device due to the reflective top contact (where the real device diameter was 800 μm and the 'effective' diameter was ~635 μm), I_n is also scaled by the ratio of these two areas. Δf is taken to be 1 Hz. Once these factors are accounted for, the D^* of a sample is calculated for R at each bias in Figure 7.8, and the resultant values for the three devices (excluding XV0552) can be seen in Figure 7.14.

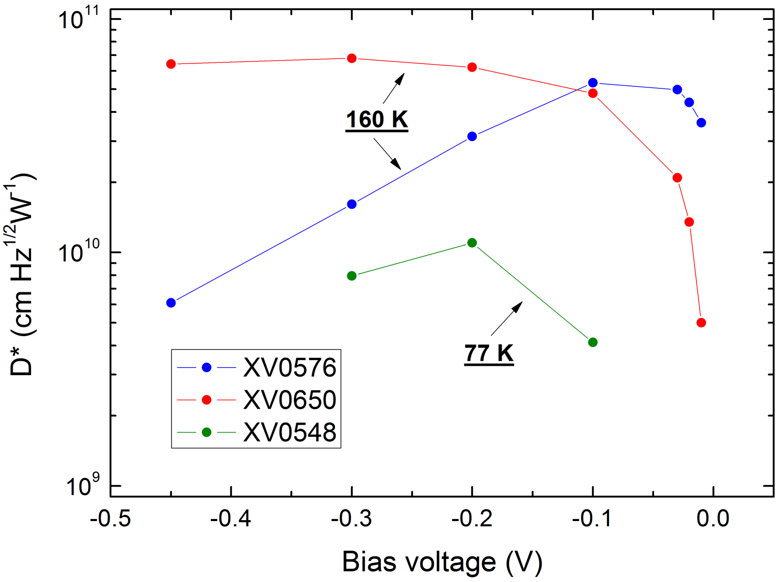

FIGURE 7.14: Specific detectivity (D^*) of the three samples XV0650, XV0576 and XV0548 as a function of bias.

Sample XV0548 shows a predictably lower result owing to its poor responsivity and (typically for LWIR) high dark current. At its peak at -0.2 V its value is 1.1×10^{10}

cmHz$^{1/2}$W^{-1}; meanwhile, Figure 3.2 shows that the detectivity of the state-of-the-art InAs/GaSb T2SL and HgCdTe devices operating at 77 K near 8-9 μm can be up to 4 times larger. Considering that the LWIR devices require substantial further optimisation in the barrier composition and bandpass filter compatibility, this result is still an acceptable starting point for future improvements.

Tellingly, D^* of the high-QE sample XV0576 is clearly compromised by its high dark currents, with a strong voltage-induced decrease revealing the underlying SRH mechanism that dominates J_d of this sample. Nevertheless, it reaches 5.3×10^{10} cmHz$^{1/2}$W^{-1} at the target operational bias of -0.1 V, a value comparable to, albeit about 2-3 times lower than, other systems in the 4-5 μm range as per Figure 3.2. In order to optimise this structure for detector applications, tackling the elevated J_d would be the first priority. The advantage of this step is evident in sample XV0650 which, despite its poorer responsivity and QE, demonstrates comparable and even superior D^* performance due to its lower and better-behaved J_d.

7.4 Conclusions

This Section presented work done to characterise the InAs/InAs$_{1-x}$Sb$_x$ nBn devices' properties. The dark current density J_d (Section 7.1) shows the expected diffusion-limited behaviour at temperatures above 140-180 K for the MWIR samples, but variations in activation energy E_a (7.1.2) in the LWIR structures point to unoptimised barrier compositions as the dominant property driving their current behaviour. Responsivity R (7.2.1) is found to be the highest at 1.70±0.11 A/W for the low-doped MWIR sample XV0576 at the operational temperature of 160 K and bias of -0.1 V, and predictably lower for samples with either higher doping or higher cut-off wavelengths. The corresponding peak internal and external quantum efficiencies QE (7.2.2) are 32.6±2.2% and 49.7±3.4% respectively. Specific detectivity D^* (7.3) is found to be $\sim 5 \times 10^{10}$ cmHz$^{1/2}$W^{-1} for two MWIR samples with otherwise very different J_d and R results, demonstrating the merit of optimising both of these parameters.

In Section 7.1.1, J_d for each sample is shown to display voltage-dependent behaviour at lower T (corresponding mostly to barrier tunnelling), then diffusion-limited characteristics as T increases. J_d of sample XV0650 is appreciably lower than that of XV0576 (which has a very similar structure) due to its 10-fold increase in n-doping. The data are then compared to Rule 07 and InAs/GaSb barrier detector data collated by Rhiger et al[79], and found to fit the trend of the barrier detectors. In Section 7.1.2 first it is shown that no surface currents occur in the devices. For some samples, Arrhenius plots demonstrate current densities lower than that for Rule 07, however this is correlated with voltage dependence of E_a, pointing to a presence of current-impeding potential barriers in the devices. The two samples with minimised E_a voltage dependence (XV0576 and XV0650) and so minimised potential barriers show diffusion-limited J_d behaviour that matches Rule 07 at higher T.

In Section 7.2, the responsivity results are first reported (7.2.1) for the MWIR samples XV0576 and XV0650, and the LWIR ones XV0552 and XV0548. An averaged $R(XV0576)$ at 160 K and -0.1 V bias is found to be 1.70±0.11 A/W (which is comparable to the proposed Teledyne detectors), while the peak $R(XV0650)$ is found to be 0.23 A/W, clearly affected by the increased n-doping. $R(XV0548)$ is $\sim$ 0.09 A/W at 77 K, most likely affected by barrier and bandpass filter misalignment.

External quantum efficiency results are reported for those same devices in Section 7.2.2: once again, XV0576 yields the highest result of (32.6±2.2)%, while samples XV0650 and XV0548 have EQE of (4.3±0.3)% and (0.26±0.07)% respectively. In Section 7.2.3 surface reflection R_s is estimated and used to calculate internal quantum efficiency IQE of the samples; resulting in a $\sim$ 50% increase from EQE for the MWIR samples, and $\sim$ 30% for the LWIR ones.

Finally, in Section 7.3 the J_d and the R data are combined to calculate specific detectivity D^* of the devices. Here, the advantage of lower J_d even in presence of poor responsivity becomes clear: sample XV0650 demonstrates D^* performance that matches and even exceeds that of sample XV0576, as both reach a value of $\sim 5 \times 10^{10}$ cmHz$^{1/2}$W^{-1} at operational temperature 160 K and bias -0.1 V. $D^*(XV0576)$ then degrades with bias due to increasing dark currents, while $D^*(XV0650)$ saturates. Meanwhile, sample XV0548 shows peak D^* of $\sim 1 \times 10^{10}$ cmHz$^{1/2}$W^{-1} at 77 K and -0.2 V, once again due to suppressed dark currents.

7.4.1 Future work

Dark current density J_d and its mechanisms are by far the most limiting parameter of the performance of the MWIR InAs/InAs$_{1-x}$Sb$_x$ detectors, and one with the most room for improvement. A simple optimisation of n-doping density between the already-known bounds of 6×10^{16} and 5×10^{17} cm^{-3} (dopant densities of XV0576 and XV0650 respectively) is expected to yield an improvement in the magnitude of J_d (the high cross-over temperature T_0 of XV0576, however, warrants further investigation). Next, two growth parameters: the substrate temperature during superlattice growth and group III/V growth ratio, which are currently optimised based on a combination of literature results, manufacturer recommendation and best practice (see Section 5.3), could be fine-tuned further.

It is evident that optimisation of the LWIR devices would return to the design stage: the valence band offset at the barrier-superlattice interface would first need to be minimised through a combination of Kronig-Penney-based modelling and iterative sample growth. Once potential barriers in the structure are eliminated, optimisation of J_d can proceed in the same fashion as for the MWIR devices. Growth on AlSb buffer layers will require additional work on the thickness and structure of the buffer, preferably extending it to an AlSb-based dislocation filter.

Quantum efficiency and responsivity can be improved in two ways: by increasing the d_{InAsSb}/d_{well} ratio (which improves absorption but faces strain-balancing restrictions), and by thinning the contact layer to minimise optical losses in it (although this improvement would be minor).

Chapter 8

Conclusions

The goal of this project was to test and develop the feasibility of InAs/InAs$_{1-x}$Sb superlattice-based nBn detectors for MWIR and LWIR detection purposes, and while further work is required to deliver state-of-the-art material, the presented devices are a good springboard for further development.

Growth of strain-balanced superlattices using molecular beam epitaxy was reported in Chapter 5. The samples grown can be generally split into two main categories: undoped superlattice layers epitaxially grown on GaAs substrates using GaSb and AlSb buffer layers, and the nBn devices proper, grown mostly on GaSb substrates and one based on an AlSb buffer layer. The device growth on the native GaSb substrates is predictably found (via XRD and TEM scanning) to provide superior crystalline quality, with the TEM images revealing no dislocations in the entire structure. Sb segregation length of $\lambda_{Sb} \sim 0.95$ nm is found at the superlattice interfaces, placing a lower limit on the structurally viable SLS layer thicknesses. TEM imagery of nBn growth on the AlSb buffer layer reveals threading and misfit dislocations, originating mostly from the AlSb interfaces.

In Chapter 6 understanding of the absorptive properties and the band structure of the InAs/InAs$_{1-x}$Sb superlattice was developed based on the undoped epitaxial SLS layers. The absorption coefficient α of the superlattices was characterised using Fourier Transform Infrared spectroscopy, and found to be of the same order of magnitude as bulk CMT material, as well as directly comparable to bulk III-V materials and the InAs/GaSb superlattice. The optical bandgap E_g was then extracted from the α data.

Using the Kronig-Penney model of a superlattice, this E_g dataset was then used to obtain the relationship between the Sb fraction x_{Sb} and the valence band position of InAs$_{1-x}$Sb$_x$, which will aid the design of superlattices in the future. In the process, understanding of the InAs/InAs$_{1-x}$Sb type-IIb band structure and its effect on SLS minibands was also developed. Evidence to support the direct nature of the band structure is also presented.

As part of the same Chapter, the spectral response of a series of nBn devices was characterised. In general, the MWIR nBn devices show strong absorption onsets, with signal that is detectable up to 280 K, which denotes good material quality. However, the n-doping dependence of the position of the MWIR maximum response is clear and warrants further optimisation. The LWIR nBn device grown on an AlSb buffer layer is also characterised, however its atypical band-edge absorption behaviour points either to poor crystallinity, instrumental factors or both; optimisation of AlSb-based device growth is crucial before it is considered a viable detector material. Finally, temperature dependence of the device bandgaps is shown to be relatively weak, which would help thermal stability of detectors derived from them.

Performance of the nBn detectors is reported in Chapter 7. Dark current density J_d measurements paint a complex picture of interdependence between the current mechanisms and magnitudes, and structural parameters of the devices: generally, the desirable diffusion-limited behaviour is achieved at higher temperatures for all samples, but further optimisation work needs to be carried out to extend this regime to target operational temperatures (160 K for MWIR devices and 77 K for LWIR). Inspection of voltage-dependent Arrhenius plots, and the resultant activation energies, reveals presence of non-negligible valence band offsets at the SLS-barrier interfaces of the LWIR devices that could lead to artificial suppression of J_d; two of the MWIR detectors, however, are shown to have well-aligned barriers, and which will serve as a starting point for optimisation of the LWIR ones.

Four devices are further tested to obtain external quantum efficiency QE, responsivity R and specific detectivity D^*. The highest QE is found to be $\sim 33\%$ in a low-doped MWIR sample with a well-aligned barrier but poor J_d; a structurally very similar sample, with a ten-fold increase in n-doping density shows notably improved J_d but a severely impacted QE of $\sim$ 4%, showing the need for fine-tuned n-doping. Responsivity values show a similar trend; it is important to note, however, that the responsivity of the best-performing MWIR device is comparable to the proposed Teledyne detectors[130]. The poor QE and R of the LWIR detectors, however, will require a back-to-the-basics approach beginning with an investigation of a barrier composition minimising the substantial valence band offset at its interface. Finally, the interplay between dark current density and responsivity becomes clearer when specific detectivity is analysed: both MWIR samples demonstrate matched D^* values despite their difference in QE, while the LWIR sample shows a result only one order of magnitude lower despite its severely impeded responsivity.

8.1 Future work

The partner company of this project, Leonardo, have committed to supporting its continuing development in order to deliver a viable alternative to CMT detectors. As such, future work will prioritise identification and optimisation of factors that determine device performance, mainly in the form of minimising J_d while maintaining high responsivity.

As discussed before, optimised n-doping densities are currently the simplest pathway to decreasing J_d in the MWIR detectors; a suitable balance between shortened carrier diffusion length and decreased dark current will need to be identified. There is reason to believe that the GaSb-absorber interface, due to its severely misaligned heterojunction band structure, forms a Schottky barrier and an effective electron source[177] that contributes to J_d in the absorber. A proposed solution exists in the form of a lattice-matched $AlAs_{1-x}Sb_x$ buffer layer, whose improved band structure alignment would disable this electron generation mechanism, and this approach is currently being investigated. The overall goal is to implement and test these structures in 2D arrays;

it is expected that once anti-reflection coating and double-pass architecture are implemented, an improvement in QE and responsivity will follow.

To improve GaSb-based LWIR devices, the first step must be to optimise the barrier alloy composition; once this is achieved, fine-tuning of other growth-related parameters will follow in the same manner as for the MWIR devices.

In order to deliver viable devices grown on mismatched GaAs substrates the buffer layer architecture will need to be expanded, likely incorporating superlattice-based dislocation filters designed to force dislocations to propagate away from the absorber interface and recombine[156]. Ultimately this could enable strain-balancing of LWIR superlattices on a_{AlSb}, a situation that promotes enhanced e1-hh1 wavefunction overlap and hopefully, increased absorption coefficients[119].

Appendix A

Theory of strain

It can be shown[33] that the strain tensor for the (001) lattice orientation reduces to the following form:

$$\epsilon_{001} = \epsilon_{\|} \begin{bmatrix} 1 & 0 & 0 \\ 0 & 1 & 0 \\ 0 & 0 & -2\frac{c_{12}}{c_{11}} \end{bmatrix} \tag{A.1}$$

where c_{11} and c_{12} are elastic constants. This determines the behaviour of pseudomorphically strained (001) epitaxial layers grown on (001) substrates as discussed in Section 2.1.1. The e_{zz} component results in out-of-plane strain equal to

$$\epsilon_{\perp} = -2\frac{c_{12}}{c_{11}}\epsilon_{\|} = \frac{a_{\perp}}{a} - 1 \tag{A.2}$$

Keeping in mind that $\epsilon_{\|}$ is simply ${}^{a_0}/_{a} - 1$, the above equation can be solved to find $\alpha_{\perp}$ as presented in Equation 2.2.

Volume change of a crystal due to strain induces changes in its electronic band structure, an effect which can be parametrised with the so-called hydrostatic deformation potential. The valence band hydrostatic deformation potential due to a change in volume Ω is[35]

$$a_v = \frac{dE_{v,av}}{d\ln\Omega} = dE_{v,av}\frac{d\Omega}{\Omega} \tag{A.3}$$

and similarly for the conduction band. The corresponding band gap deformation potential is equal to

$$a_g = a_c - a_v = \frac{d(E_c - E_{v,av})}{d\ln\Omega} \tag{A.4}$$

If the hydrostatic potential is known, the band shift becomes

$$\Delta E_{v,av} = a_v \frac{\Delta\Omega}{\Omega} \tag{A.5}$$

where the volume change can be obtained by taking the trace of the (001) strain tensor (Equation A.1):

$$\frac{\Delta\Omega}{\Omega} = \mathrm{Tr}(\epsilon_{001}) \tag{A.6}$$

in which case Equation A.5 becomes

$$\Delta E^{hy}_{v,av} = a_v(2\epsilon_{\parallel} + \epsilon_{\perp}) \tag{A.7}$$

The procedure for ΔE^{hy}_c is the same.

Thermal expansion of barrier and substrate materials

When an effective strain-balanced nBn structure is being designed, the thermal expansion of both the substrate and the barrier layers need to be taken into account in addition to the superlattice materials. These are[28], in units of Å:

$$\begin{aligned} a_{GaAs}(T) &= 5.65325 + 3.88 \times 10^{-5}(T - 300) \\ a_{GaSb}(T) &= 6.089292 + 4.72 \times 10^{-5}(T - 300) \\ a_{AlSb}(T) &= 6.1355 + 2.6 \times 10^{-5}(T - 300) \\ a_{AlAs}(T) &= 5.6611 + 2.9 \times 10^{-5}(T - 300) \end{aligned} \tag{A.8}$$

Appendix B

Sample summary

TABLE B.1: Grown on n-GaSb substrates unless otherwise stated.

nBn devices

ID	Type	d_{InAs} (Å)	d_{InAsSb} (Å)	Ratio	Cell repeats	d_{abs} (nm)	x_{Sb}
XV0161	MWIR	46	46.5	0.99	474	4384.5	0.178
XV0576	MWIR	58.4	74.7	0.78	320	4259.2	0.16
XV0650	MWIR	35.9	46.8	0.77	1010	8352.7	0.158
XV0208	LWIR	39.9	40.9	0.98	384	3102.72	0.33
XJ0292	LWIR	52.1	15.7	0.30	–	3300	0.40
XV0548	LWIR	66.2	34.4	1.92	365	3671.9	0.3
XV0552	LWIR	74.2	31.9	2.32	390	4137.9	0.31
QA504	LWIR	68.5	20.3	3.38	105	932.4	0.35
	MWIR	47.8	23.5	2.03	130	926.9	0.275

nBn devices cont'd

ID	Barrier	$d_{barrier}$ (nm)	Doping ($\times 10^{17}$ cm^{-3})	Comments
XV0161	$AlAs_{0.12}Sb_{0.88}$	46	0.6	
XV0576	$Al_{0.90}Ga_{0.10}As_{0.06}Sb_{0.94}$	110	0.6	
XV0650	$Al_{0.90}Ga_{0.10}As_{0.06}Sb_{0.94}$	110	5	
XV0208	$Al_{0.75}Ga_{0.25}Sb$	54	0.6	GaAs sub/ AlSb 1.1 μm
XJ0292	$Al_{0.58}Ga_{0.42}Sb$	51	0.6	
XV0548	$Al_{0.95}Ga_{0.05}Sb$	81	0.6	
XV0552	$Al_{0.78}Ga_{0.22}Sb$	80	0.6	
QA504	$Al_xGa_{1-x}Sb$	44	0.4	stepped x_{Al}; grown on VG V80-H

Epilayers									
ID	*Type*	*Buffer*	d_{buffer} *(nm)*	d_{InAs} (Å)	d_{InAsSb} (Å)	*Ratio*	*Cell repeats*	d_{abs} *(nm)*	x_{Sb}
XV0154	MWIR	GaSb	325	21	21.4	0.98	166	703.84	0.176
XV0159	MWIR	GaSb	325	68.7	70.3	0.98	55	764.5	0.178
XV0160	MWIR	GaSb	325	46.2	47.4	0.97	83	776.88	0.174
XV0232	LWIR	GaSb	590	47.1	14.1	3.34	109	667.08	0.31
XV0234	LWIR	GaSb	590	52	15.6	3.33	109	736.84	0.37
XV0235	LWIR	AlSb	551	18.9	16	1.18	208	725.92	0.41
XV0440	LWIR	GaSb	430	83.1	35.6	2.33	100	1187	0.3
XV0443	LWIR	GaSb	430	83.9	35.9	2.34	100	1198	0.29
XV0446	LWIR	GaSb	430	84.8	36.2	2.34	100	1210	0.275
XV0448	LWIR	AlSb	318	24	36	0.67	200	1200	0.29
XV0545	LWIR	GaSb	430	73.4	44.1	1.66	73	858	0.225
XV0547	LWIR	GaSb	430	70.5	30.9	2.28	73	740.2	0.257
XV0558	MWIR	GaSb	430	69.3	33.6	2.06	73	751.17	0.235
XV0560	MWIR	GaSb	430	48	14.1	3.36	109	679.1	0.31

Bibliography

[1] J. M. Marr and F. P. Wilkin. “A better presentation of Planck’s radiation law”. *American Journal of Physics* 80.5 (2012), pp. 399–405.

[2] R. Pogge. *An Introduction to Solar System Astronomy*. `http://www.astronomy.ohio-state.edu/~pogge/Ast161/Unit5/atmos.html`. Accessed on 09/12/2018.

[3] F. Rutz et al. “Imaging detection of CO_2 using a bispectral type-II superlattice infrared camera”. *11th International Conference on Quantitative InfraRed Thermography*. 2012.

[4] R. Scafutto and C. R. de Souza Filho. “Detection of Methane Plumes Using Airborne Midwave Infrared (3–5 μm) Hyperspectral Data”. *Remote Sensing* 10.8 (2018).

[5] A. Rogalski. “Infrared detectors: status and trends”. *Progress in Quantum Electronics* 27.2 (2003), pp. 59 –210.

[6] M. A. Kinch. *Fundamentals of Infrared Detectors*. SPIE Press, 2007.

[7] A. Rogalski. “HgCdTe infrared detector material: history, status and outlook”. *Reports on Progress in Physics* 68.10 (2005), p. 2267.

[8] P. Norton. “HgCdTe infrared detectors”. *Opto-Electronics Review* 10.3 (2002), pp. 159–174.

[9] E. A. Plis. “InAs/GaSb Type-II Superlattice Detectors”. *Advances in Electronics* 2014.3 (2014), p. 246769.

[10] C. Downs and T. E. Vandervelde. “Progress in Infrared Photodetectors Since 2000”. *Sensors* 13.4 (2013), pp. 5054–5098.

[11] *Regulation (EU) 2017/852 of the European Parliament and of the Council of 17 May 2017 on mercury, and repealing Regulation (EC) No 1102/2008*. `http://data.europa.eu/eli/reg/2017/852/oj`.

[12] A. Khoshakhlagh et al. "Optimization of InAs/GaSb type-II superlattice interfaces for long-wave ($\sim 8\ \mu$m) infrared detection". *Journal of Crystal Growth* 311.7 (2009), pp. 1901 –1904.

[13] S.P. Svensson et al. "Growth of type II strained layer superlattice, bulk InAs and GaSb materials for minority lifetime characterization". *Journal of Crystal Growth* 334.1 (2011), pp. 103 –107.

[14] P. M. Thibado et al. "Origins of interfacial disorder in GaSb/InAs superlattices". *Applied Physics Letters* 67.24 (1995), pp. 3578–3580.

[15] E. H. Steenbergen et al. "Significantly improved minority carrier lifetime observed in a long-wavelength infrared III-V type-II superlattice comprised of InAs/InAsSb". *Applied Physics Letters* 99.25 (2011), p. 251110.

[16] D. Donetsky et al. "Minority carrier lifetime in type-2 InAs/GaSb strained-layer superlattices and bulk HgCdTe materials". *Applied Physics Letters* 97.5 (2010), p. 052108.

[17] P. Martyniuk, M. Kopytko, and A. Rogalski. "Barrier infrared detectors". *Opto-Electronics Review* 22.2 (2014), pp. 127–146.

[18] P. Klipstein. ""XBn" barrier photodetectors for high sensitivity and high operating temperature infrared sensors". *Proc.SPIE*. Vol. 6940. 2008, pp. 6940 –6940 –12.

[19] E. F. Schubert. *Light-Emitting Diodes*. 2nd ed. Cambridge University Press, 2006.

[20] J. Singh. *Electronic and optoelectronic properties of semiconductor structures*. Cambridge University Press, 2003.

[21] G. Osbourn. "Strained-layer superlattices: A brief review". *IEEE Journal of Quantum Electronics* 22.9 (1986), pp. 1677–1681.

[22] M. P. C. M. Krijn. “Heterojunction band offsets and effective masses in III-V quaternary alloys”. *Semiconductor Science and Technology* 6.1 (1991), p. 27.

[23] J.W. Matthews and A.E. Blakeslee. “Defects in epitaxial multilayers: I. Misfit dislocations”. *Journal of Crystal Growth* 27 (1974), pp. 118 –125.

[24] A. P. Craig. “Lattice Mismatched Infrared Photodetectors”. PhD thesis. Lancaster University, 2015.

[25] R. People and J. C. Bean. “Calculation of critical layer thickness versus lattice mismatch for $\mathrm{Ge}_x\mathrm{Si}_{1-x}$/Si strained-layer heterostructures”. *Applied Physics Letters* 47.3 (1985), pp. 322–324.

[26] “Indium arsenide (InAs) lattice parameters, thermal expansion”. *Group IV Elements, IV-IV and III-V Compounds. Part a - Lattice Properties*. Ed. by O. Madelung, U. Rössler, and M. Schulz. Springer Berlin Heidelberg, 2001, pp. 1–6.

[27] “Indium antimonide (InSb), lattice parameter, thermal expansion”. *Group IV Elements, IV-IV and III-V Compounds. Part b - Electronic, Transport, Optical and Other Properties*. Ed. by O. Madelung, U. Rössler, and M. Schulz. Springer Berlin Heidelberg, 2002, pp. 1–5.

[28] I. Vurgaftman, J. R. Meyer, and L. R. Ram-Mohan. “Band parameters for III-V compound semiconductors and their alloys”. *Journal of Applied Physics* 89.11 (2001), pp. 5815–5875.

[29] C. Kittel. *Introduction to Solid State Physics*. 8th ed. Jonh Wiley & Sons, 2005.

[30] Y. S. Kim, K. Hummer, and G. Kresse. “Accurate band structures and effective masses for InP, InAs, and InSb using hybrid functionals”. *Phys. Rev. B* 80 (3 2009), p. 035203.

[31] Ioffe Institute. *InAs - Indium Arsenide*. `http://www.ioffe.ru/SVA/NSM/Semicond/InAs/`. Accessed on 09/12/2018.

[32] N. Bouarissa and H. Aourag. “Effective masses of electrons and heavy holes in InAs, InSb, GaSb, GaAs and some of their ternary compounds”. *Infrared Physics & Technology* 40.4 (1999), pp. 343 –349.

[33] Shun Lien Chuang. *Physics of Photonic Devices*. 2nd ed. John Wiley & Sons, 2009.

[34] M. Shen and W. Cao. “Electronic band-structure engineering of GaAs/$Al_xGa_{1-x}As$ quantum well superlattices with substructures”. *Materials Science and Engineering: B* 103.2 (2003), pp. 122 –127.

[35] C. G. Van de Walle. “Band lineups and deformation potentials in the model-solid theory”. *Phys. Rev. B* 39 (3 1989), pp. 1871–1883.

[36] Po-Wei Liu et al. “Photoluminescence and bowing parameters of InAsSb/InAs multiple quantum wells grown by molecular beam epitaxy”. *Applied Physics Letters* 89.20 (2006), p. 201115.

[37] D. Lackner et al. “Strain balanced InAs/InAsSb superlattice structures with optical emission to 10 μm”. *Applied Physics Letters* 95.8 (2009), p. 081906.

[38] Su-Huai Wei and Alex Zunger. “InAsSb/InAs: A type-I or a type-II band alignment”. *Phys. Rev. B* 52 (16 1995), pp. 12039–12044.

[39] P.T. Webster. “Growth, Optical Properties, and Optimization of Infrared Optoelectronic Materials”. PhD thesis. Arizona State University, 2016.

[40] E.H. Steenbergen. “Strain-balanced InAs-InAsSb Type-II Superlattices on GaSb Substrates for Infrared Photodetector Applications”. PhD thesis. Arizona State University, 2012.

[41] T. Schuler-Sandy et al. “Gallium free type II InAs/$InAs_xSb_{1-x}$ superlattice photodetectors”. *Applied Physics Letters* 101.7 (2012), p. 071111.

[42] P. T. Webster et al. “Measurement of InAsSb bandgap energy and InAs/InAsSb band edge positions using spectroscopic ellipsometry and photoluminescence spectroscopy”. *Journal of Applied Physics* 118.24 (2015), p. 245706.

[43] L. Gupta et al. "Temperature dependence of the fundamental band gap parameters in cadmium-rich ZnxCd1-xSe using photoluminescence spectroscopy". *Pramana* 61.4 (2003), pp. 729–737.

[44] R. Pässler and G. Oelgart. "Appropriate analytical description of the temperature dependence of exciton peak positions in GaAs/$Al_xGa_{1-x}As$ multiple quantum wells and the Γ8v-Γ6c gap of GaAs". *Journal of Applied Physics* 82.5 (1997), pp. 2611–2616.

[45] R. Pässler. "Temperature dependence of fundamental band gaps in group IV, III-V, and II-VI materials via a two-oscillator model". *Journal of Applied Physics* 89.11 (2001), pp. 6235–6240.

[46] S. R. Johnson and T. Tiedje. "Temperature dependence of the Urbach edge in GaAs". *Journal of Applied Physics* 78.9 (1995), pp. 5609–5613.

[47] Z. M. Fang et al. "Photoluminescence of InSb, InAs, and InAsSb grown by organometallic vapor phase epitaxy". *Journal of Applied Physics* 67.11 (1990), pp. 7034–7039.

[48] M. Y. Yen et al. "Long-wavelength photoluminescence of $InAs_{1-x}Sb_x$ (0<x<1) grown by molecular beam epitaxy on (100) InAs". *Applied Physics Letters* 52.6 (1988), pp. 489–491.

[49] S. P. Svensson et al. "Band gap of $InAs_{1-x}Sb_x$ with native lattice constant". *Phys. Rev. B* 86 (24 2012), p. 245205.

[50] S. R. Kurtz et al. "Ordering-induced band-gap reduction in $InAs_{1-x}Sb_x$ (x≊0.4) alloys and superlattices". *Phys. Rev. B* 46 (3 1992), pp. 1909–1912.

[51] J. I. Pankove. "Absorption Edge of Impure Gallium Arsenide". *Phys. Rev.* 140 (6A 1965), A2059–A2065.

[52] B. Bansal et al. "Alloying induced degradation of the absorption edge of $InAs_xSb_{1-x}$". *Applied Physics Letters* 90.10 (2007), p. 101905.

[53] J. Micallef and B. L. Weiss. "The refractive index of III-V semiconductor strained-layer superlattices". *Optical and Quantum Electronics* 23.6 (1991), pp. 669–684.

[54] M. N. Polyanskiy. *Refractive index database*. `https://refractiveindex.info`. Accessed on 10/12/2018.

[55] P. P. Paskov. "Refractive indices of InSb, InAs, GaSb, $InAs_xSb_{1-x}$, and $In_{1-x}Ga_xSb$: Effects of free carriers". *Journal of Applied Physics* 81.4 (1997), pp. 1890–1898.

[56] E. Rosencher and B. Vinter. *Optoelectronics*. Cambridge University Press, 2002.

[57] J. I. Pankove. *Optical Processes in Semiconductors*. Prentice-Hall electrical engineering series. Solid state physical electronics series. Prentice-Hall, 1971.

[58] M.W. Prairie and R.M. Kolbas. "A general derivation of the density of states function for quantum wells and superlattices". *Superlattices and Microstructures* 7.4 (1990), pp. 269 –277.

[59] I. Studenyak, M. Kranjec, and M. Kurik. "Urbach Rule in Solid State Physics". *International Journal of Optics and Applications* 4.3 (2014), pp. 76–83.

[60] S. Maimon and G. W. Wicks. "nBn detector, an infrared detector with reduced dark current and higher operating temperature". *Applied Physics Letters* 89.15 (2006), p. 151109.

[61] "Benefits and limitations of unipolar barriers in infrared photodetectors". *Infrared Physics & Technology* 59 (2013), pp. 152 –155.

[62] A. Rogalski, M. Kopytko, and P. Martyniuk. *Antimonide-based Infrared Detectors: A New Perspective*. SPIE Press, 2018.

[63] G. R. Nash and T. Ashley. "Reduction in Shockley–Read–Hall generation-recombination in AlInSb light-emitting-diodes using spatial patterning of the depletion region". *Applied Physics Letters* 94.21 (2009), p. 213510.

[64] P. Klipstein. "MWIR InAsSb XBn detectors for high operating temperatures". *Proc.SPIE*. Vol. 7660. 2010, pp. 7660 –7669.

[65] J.R. Pedrazzani. "Characteristics of InAs-Based nBn Photodetectors Grown by Molecular Beam Epitaxy". PhD thesis. University of Rochester, 2010.

[66] G. R. Savich et al. "Diffusion current characteristics of defect-limited nBn mid-wave infrared detectors". *Applied Physics Letters* 106.17 (2015), p. 173505.

[67] A. Rogalski, K. Adamiec, and J. Rutkowski. *Narrow-Gap Semiconductor Photodiodes*. SPIE Press, 2000.

[68] Z. Lin. "Study of Minority Carrier Lifetime and Transport in InAs/InAsSb type-II Superlattices Using a Real-Time Baseline Correction Method". PhD thesis. Arizona State University, 2016.

[69] C.H. Grein, M. E. Flatté, and H. Ehrenreich. "Comparison of ideal InAs/InAsSb and InAs/InGaSb superlattice detectors". *Electrochemical Society Proceedings*. Vol. 95. 1995, pp. 211–218.

[70] R J. Walters et al. "Design of an achievable, all lattice-matched multijunction solar cell using InGaAlAsSb". *Conference Record of the IEEE Photovoltaic Specialists Conference* (2011), pp. 000122–000126.

[71] E. S. Barr. "Historical Survey of the Early Development of the Infrared Spectral Region". *American Journal of Physics* 28.1 (1960), pp. 42–54.

[72] A. Rogalski. "Infrared detectors: an overview". *Infrared Physics & Technology* 43.3 (2002), pp. 187 –210.

[73] A. Rogalski. *Infrared Detectors*. Gordon and Breach Science Publishers, 2000.

[74] G. Vergara, M. Montojo, and M. Torquemada. "Polycrystalline lead selenide: the resurgence of an old infrared detector". *Opto-Electronics Review* 15.2 (2007), pp. 110–117.

[75] C. H. Grein, J. Garland, and M. E. Flatté. "Strained and Unstrained Layer Superlattices for Infrared Detection". *Journal of Electronic Materials* 38.8 (2009), pp. 1800–1804.

[76] B. Li et al. "Optical absorption above the energy band gap in $Hg_{1-x}Cd_xTe$". *Infrared Physics & Technology* 37.4 (1996), pp. 525 –531.

[77] K. Moazzami et al. "Detailed study of above bandgap optical absorption in HgCdTe". *Journal of Electronic Materials* 34.6 (2005), pp. 773–778.

[78] W.E. Tennant et al. "MBE HgCdTe Technology: A Very General Solution to IR Detection, Described by Rule "07", a Very Convenient Heuristic". *Journal of Electronic Materials* 37.9 (2008), pp. 1406–1410.

[79] D. R. Rhiger. "Performance Comparison of Long-Wavelength Infrared Type II Superlattice Devices with HgCdTe". *Journal of Electronic Materials* 40.8 (2011), pp. 1815–1822.

[80] W. E. Tennant. ""Rule 07" Revisited: Still a Good Heuristic Predictor of p/n HgCdTe Photodiode Performance?" *Journal of Electronic Materials* 39.7 (2010), pp. 1030–1035.

[81] A. Rogalski. "Recent progress in infrared detector technologies". *Infrared Physics & Technology* 54.3 (2011), pp. 136 –154.

[82] Teledyne Judson Technologies. *Indium Antimonide Detectors*. `http://www.teledynejudson.com/products/indium-antimonide-detectors`. Accessed on 11/12/2018.

[83] Hamamatsu Photonics. *InSb photovoltaic detectors*. `https://www.hamamatsu.com/eu/en/product/optical-sensors/infrared-detector/insb-photovoltaic-detector/index.html`. Accessed on 11/12/2018.

[84] I. Shtrichman. *Proc.SPIE*. Vol. 8353. 2012.

[85] C. S. Schnohr. "Compound semiconductor alloys: From atomic-scale structure to bandgap bowing". *Applied Physics Reviews* 2.3 (2015), p. 031304.

[86] A. Rogalski and K. Jóźwikowski. "Intrinsic carrier concentration and effective masses in InAs$_{1-x}$Sb$_x$". *Infrared Physics* 29.1 (1989), pp. 35 –42.

[87] G. B Stringfellow and P. E. Greene. "Liquid Phase Epitaxial Growth of InAsSb". *Journal of the Electrochemical Society* 118.5 (1971), pp. 805–810.

[88] S Elies et al. "Photoluminescence of MBE-grown InAs 1-x Sb x lattice matched to GaSb". *Journal of Physics D: Applied Physics* 26.1 (1993), p. 159.

[89] M. Razeghi. “Overview of antimonide based III-V semiconductor epitaxial layers and their applications at the center for quantum devices”. *Eur. Phys. J. AP* 23.3 (2003), pp. 149–205.

[90] Y. Lin et al. “Development of Bulk InAsSb Alloys and Barrier Heterostructures for Long-Wave Infrared Detectors”. *Journal of Electronic Materials* 44.10 (), pp. 3360–3366.

[91] P.S. Dutta. “III–V Ternary bulk substrate growth technology: a review”. *Journal of Crystal Growth* 275.1 (2005), pp. 106 –112.

[92] L. O. Bubulac et al. “Backside-illuminated InAsSb/GaSb broadband detectors”. *Applied Physics Letters* 36.9 (1980), pp. 734–736.

[93] Maxim Remennyy et al. “InAs and InAs(Sb)(P) (3-5 μm) immersion lens photodiodes for portable optic sensors”. *Proceedings of SPIE - The International Society for Optical Engineering* 6585 (2007).

[94] P.N. Brunkov et al. “InAsSbP/$\mathrm{InAs_{0.9}Sb_{0.1}}$/InAs DH photodiodes ($\lambda_{0.1}$ =5.2 μm, 300K) operating in the 77-353 K temperature range”. *Infrared Physics & Technology* 73 (2015), pp. 232 –237.

[95] L. Esaki and R. Tsu. “Superlattice and Negative Differential Conductivity in Semiconductors”. *IBM Journal of Research and Development* 14.1 (1970), pp. 61–65.

[96] G. A. Sai-Halasz, R. Tsu, and L. Esaki. “A new semiconductor superlattice”. *Applied Physics Letters* 30.12 (1977), pp. 651–653.

[97] “Two-dimensional electronic structure in InAs-GaSb superlattices”. *Solid State Communications* 26.9 (1978), pp. 589 –592.

[98] J. N. Schulman and T. C. McGill. “The CdTe/HgTe superlattice: Proposal for a new infrared material”. *Applied Physics Letters* 34.10 (1979), pp. 663–665.

[99] H. Mohseni et al. "Growth and characterization of type-II nonequilibrium photovoltaic detectors for long-wavelength infrared range". *Proceedings of SPIE - The International Society for Optical Engineering* 3948 (Apr. 2000), pp. 153–160.

[100] H. Mohseni and M. Razeghi. "Long-wavelength type-II photodiodes operating at room temperature". *Photonics Technology Letters, IEEE* 13 (June 2001), pp. 517 –519.

[101] E. A. Plis et al. "Performance of long-wave infrared InAs/GaSb strained layer superlattice detectors for the space applications". *Proceedings of SPIE - The International Society for Optical Engineering* (Sept. 2011).

[102] H. J. Haugan et al. "Growth of short-period InAs/GaSb superlattices". *Journal of Applied Physics* 100.12 (2006), p. 123110.

[103] M. Walther et al. "Growth of InAs/GaSb short-period superlattices for high-resolution mid-wavelength infrared focal plane array detectors". *Journal of Crystal Growth* 278.1 (2005), pp. 156 –161.

[104] W. Walukiewicz. "Defect Reactions at Metal-Semiconductor and Semiconductor-Semiconductor Interfaces". *Materials Research Society Symposium Proceedings*. Vol. 148. 1. 1989, pp. 156 –161.

[105] B. C. Connelly et al. "Investigation of Trap States in Mid-Wavelength Infrared Type II Superlattices Using Time-Resolved Photoluminescence". *Journal of Electronic Materials* 42.11 (2013), pp. 3203–3210.

[106] J. V. Li et al. "Minority carrier diffusion length and lifetime for electrons in a type-II InAs/GaSb superlattice photodiode". *Applied Physics Letters* 85.11 (2004), pp. 1984–1986.

[107] D. Zuo et al. "Direct observation of minority carrier lifetime improvement in InAs/GaSb type-II superlattice photodiodes via interfacial layer control". *Applied Physics Letters* 102 (Apr. 2013).

[108] X. B. Zhang et al. "Improved surface and structural properties of InAs/GaSb superlattices on (001) GaSb substrate by introducing an InAsSb layer at interfaces". *Applied Physics Letters* 90.13 (2007), p. 131110.

[109] G. C. Osbourn. "InAsSb strained-layer superlattices for long wavelength detector applications". *Journal of Vacuum Science & Technology B: Microelectronics Processing and Phenomena* 2.2 (1984), pp. 176–178.

[110] Zhang Y. H., R. H. Miles, and D. H. Chow. "InAs-InAs$_x$Sb$_{1-x}$ type-II superlattice midwave infrared lasers grown on InAs substrates". *IEEE Journal of Selected Topics in Quantum Electronics* 1.2 (1995), pp. 749–756.

[111] P Tang et al. "4-11 mu m infrared emission and 300 K light emitting diodes from arsenic-rich InAs$_{1-x}$Sb$_x$ strained layer superlattices". *Semiconductor Science and Technology* 10.8 (1995), p. 1177.

[112] Zhang Y.H. "InAs/InAs$_x$Sb$_{1-x}$ type-II superlattice midwave infrared lasers". *Optoelectronic Properties of Semiconductors and Superlattices: Antimonide-Related Strained-Layer Heterostructures*. CRC Press, 1997.

[113] A. D. Prins et al. "Evidence for a defect level above the conduction band edge of InAs/InAsSb type-II superlattices for applications in efficient infrared photodetectors". *Applied Physics Letters* 106.17 (2015), p. 171111.

[114] L. Höglund et al. "Influence of radiative and non-radiative recombination on the minority carrier lifetime in midwave infrared InAs/InAsSb superlattices". *Applied Physics Letters* 103.22 (2013), p. 221908.

[115] L. Höglund et al. "Influence of carrier concentration on the minority carrier lifetime in mid-wavelength infrared InAs/InAsSb superlattices". *Infrared Physics & Technology* 70 (2015), pp. 62 –65.

[116] Y. Lin et al. "Minority Carrier Lifetime in Beryllium-Doped InAs/InAsSb Strained Layer Superlattices". *Journal of Electronic Materials* 43.9 (2014), pp. 3184–3190.

[117] Y. Huang et al. "Epitaxial growth and characterization of InAs/GaSb and InAs/InAsSb type-II superlattices on GaSb substrates by metalorganic chemical vapor deposition for long wavelength infrared photodetectors". *Journal of Crystal Growth* 314.1 (2011), pp. 92 –96.

[118] P. C. Klipstein et al. "Modelling InAs/GaSb and InAs/InAsSb Superlattice Infrared Detectors". *Journal of Electronic Materials* 43.8 (2014), pp. 2984–2990.

[119] I. Vurgaftman et al. "Interband absorption strength in long-wave infrared type-II superlattices with small and large superlattice periods compared to bulk materials". *Applied Physics Letters* 108.22 (2016), p. 222101.

[120] A. M. Hoang et al. "High performance photodiodes based on InAs/InAsSb type-II superlattices for very long wavelength infrared detection". *Applied Physics Letters* 104.25 (2014), p. 251105.

[121] P. C. Klipstein et al. "Low SWaP MWIR detector based on XBn focal plane array". *Proc.SPIE*. Vol. 8704. 2013, pp. 8704 –8704 –12.

[122] J. B. Rodriguez et al. "nBn structure based on InAs/GaSb type-II strained layer superlattices". *Applied Physics Letters* 91.4 (2007), p. 043514.

[123] H. S. Kim et al. "Mid-IR focal plane array based on type-II InAs/GaSb strain layer superlattice detector with nBn design". *Applied Physics Letters* 92.18 (2008), p. 183502.

[124] G. Bishop et al. "nBn detectors based on InAs/GaSb type-II strain layer superlattice". *Journal of Vacuum Science & Technology B: Microelectronics and Nanometer Structures Processing, Measurement, and Phenomena* 26.3 (2008), pp. 1145–1148.

[125] P. Martyniuk and A. Rogalski. "Modelling of MWIR HgCdTe complementary barrier HOT detector". *Solid-State Electronics* 80 (2013), pp. 96–104.

[126] Małgorzata Kopytko et al. "High-operating temperature MWIR nBn HgCdTe detector grown by MOCVD". *Opto-Electronics Review* 21 (Dec. 2013).

[127] H. S. Kim et al. “Long-wave infrared nBn photodetectors based on InAs/InAsSb type-II superlattices”. *Applied Physics Letters* 101.16 (2012), p. 161114.

[128] A. Haddadi et al. “InAs/InAs$_{1-x}$Sb$_x$ type-II superlattices for high performance long wavelength infrared detection”. *Applied Physics Letters* 105.12 (2014), p. 121104.

[129] A. Haddadi et al. “Bias-selectable dual-band mid-/long-wavelength infrared photodetectors based on InAs/InAs$_{1-x}$Sb$_x$ type-II superlattices”. *Applied Physics Letters* 106.1 (2015), p. 011104.

[130] J. Kim et al. “HOT MWIR InAs/InAsSb T2SL discrete photodetector development”. *Proc.SPIE*. Vol. 10624. 2018, pp. 10624 –10624 –8.

[131] W. S. Knodle and R. Chow. “10 - Molecular Beam Epitaxy: Equipment and Practice”. *Handbook of Thin Film Deposition Processes and Techniques (Second Edition)*. Ed. by K. Seshan. Second Edition. William Andrew Publishing, 2001, pp. 381 –461.

[132] F. Rinaldi. “Basics of Molecular Beam Epitaxy (MBE)” (2002).

[133] Chang L.L. and Ploog K., eds. *Molecular Beam Epitaxy and Heterostructures*. Springer Netherlands, 1985.

[134] A.S. Bracker et al. “Surface reconstruction phase diagrams for InAs, AlSb, and GaSb”. *Journal of Crystal Growth* 220.4 (2000), pp. 384 –392.

[135] Downs A. J., ed. *Chemistry of Aluminium, Gallium, Indium and Thallium*. Springer Netherlands, 1993.

[136] *Vertex 70 User Manual*. 2nd ed. BRUKER OPTIK GmbH. 2013.

[137] P. R. Griffiths. *Fourier Transform Infrared Spectrometry*. 2nd ed. Chemical analysis ; v. 171. Wiley-Interscience, 2007.

[138] *Karl Suss MJB4 Mask Aligner*. `https://materials.princeton.edu/mnfl/the-tool-list/karl-suss-mjb4`. Accessed on 05/04/2018.

[139] Yurgens A. *Lab Demo: Physical Evaporation of Metals*. Chalmers University of Technology. 2004.

[140] M. A. Gosálvez and R. M. Nieminen. “Relation between macroscopic and microscopic activation energies in nonequilibrium surface processing”. *Phys. Rev. E* 68 (3), p. 031604.

[141] Hickmann F. *Wire Bonding Technology*. TPT. 2006.

[142] G. Machin et al. *MeP-K absolute primary radiometric thermometry*. Tech. rep. International Bureau of Weights and Measures (BIPM), 2012.

[143] A. P. Craig and Wagener M. private communication. Aug. 2017.

[144] QinetiQ Group plc. private communication. 2015.

[145] S. Liu et al. “Impact of substrate temperature on the structural and optical properties of strain-balanced InAs/InAsSb type-II superlattices grown by molecular beam epitaxy”. *Applied Physics Letters* 102.7 (2013), p. 071903.

[146] R. Fernandez. “RHEED oscillations of arsenic-controlled growth conditions to optimize MBE growth of III/V heterostructures”. *Journal of Crystal Growth* 116.1 (1992), pp. 98 –104.

[147] M. Stone. “Light sources for carbon dioxide, carbon monoxide and flame detection systems based on narrow gap III-V alloys”. PhD thesis. Lancaster University, 2006.

[148] R. Kaspi and K. R. Evans. “Sb-surface segregation and the control of compositional abruptness at the GaAsSb/GaAs interface”. *Journal of Crystal Growth* 175-176 (1997), pp. 838 –843.

[149] M.R Pillai et al. “Effect of Sb pre-deposition on the compositional profiles in MOVPE-grown InAsSb/InAs(111) multi-quantum wells”. *Journal of Crystal Growth* 208.1 (2000), pp. 79 –84.

[150] C. J. Reyner et al. “Characterization of GaSb/GaAs interfacial misfit arrays using x-ray diffraction”. *Applied Physics Letters* 99.23 (2011), p. 231906.

[151] R. Beanland. private communication. Apr. 2019.

[152] K. Muraki et al. “Surface segregation of In atoms during molecular beam epitaxy and its influence on the energy levels in InGaAs/GaAs quantum wells”. *Applied Physics Letters* 61.5 (1992), pp. 557–559.

[153] J. J. Harris et al. “Kinetic limitations to surface segregation during MBE growth of III–V compounds: Sn in GaAs”. *Applied Physics A* 33.2 (), pp. 87–92.

[154] Ayers E. A. *Heteroepitaxy of Semiconductors: Theory, Growth, and Characterization*. CRC Press, 2018.

[155] A. E. Romanov et al. “Threading dislocation reduction in strained layers”. *Journal of Applied Physics* 85.1 (1999), pp. 182–192.

[156] T. Ward et al. “Design rules for dislocation filters”. *Journal of Applied Physics* 116.6 (2014), p. 063508.

[157] S. J. Byrnes. *Multilayer optical calculations*. 2016. eprint: `arXiv:1603.02720[physics.comp-ph]`.

[158] “Optical Properties of Semiconductors”. *Handbook of Optics Volume II Devices Measurements and Properties Second Edition*. Ed. by Seiler D.G. Amirtharaj P.M. McGraw-Hill, 1994.

[159] M. Jaros. *Deep levels in semiconductors*. Hilger, 1982.

[160] *High Reflectors*. `http://www.kruschwitz.com/HR's.htm`. Accessed on 11/12/2018.

[161] *PLEXIGLASS SHEETS INFRARED TRANSMITTING*. `https://www.eplastics.com/plexiglass/acrylic-sheets/ir-transmitting`. Accessed on 11/12/2018.

[162] Bruker Optics. *Accurate Reflectance and Transmittance Measurements on Highly Refractive Materials*. Application Note.

[163] Z. Tian et al. “Influence of composition in InAs/GaSb type-II superlattices on their optical properties”. *Electronics Letters* 50 (Nov. 2014), pp. 1733–1734.

[164] R. Bhatt et al. “Urbach tail and bandgap analysis in near stoichiometric LiNbO3 crystals”. *physica status solidi (a)* 209.1 (), pp. 176–180.

[165] P. T. Webster et al. “Absorption properties of type-II InAs/InAsSb superlattices measured by spectroscopic ellipsometry”. *Applied Physics Letters* 106.6 (2015), p. 061907.

[166] Merzbacher E. *Quantum Mechanics*. 3rd ed. John Wiley & Sons, 1998.

[167] H. Helmers, C. Karcher, and A. W. Bett. “Bandgap determination based on electrical quantum efficiency”. *Applied Physics Letters* 103.3 (2013), p. 032108.

[168] M. Piccardo et al. “Localization landscape theory of disorder in semiconductors. II. Urbach tails of disordered quantum well layers”. *Phys. Rev. B* 95 (14 2017), p. 144205.

[169] S. Duman et al. “The effect of Sn doping Urbach Tail and optical absorbtion measurements of InSe crystal”. *Journal of Physics: Conference Series* 707.1 (2016), p. 012027.

[170] A. Shaker and A. Zekry. “A new and simple Model for Plasma and Doping induced Band Gap Narrowing”. *Journal of Electronic Devices,* Vol. 8 (2010).

[171] X. Shen. “Study of Structural, Optical and Electrical Properties of InAs/InAsSb Superlattices Using Multiple Characterization Techniques”. PhD thesis. Arizona State University, 2016.

[172] D. Olguin, M. Cardona, and A. Cantarero. “Electron–phonon effects on the direct band gap in semiconductors: LCAO calculations”. *Solid State Communications* 122.11 (2002), pp. 575 –589.

[173] B Klein et al. “Varshni parameters for InAs/GaSb strained layer superlattice infrared photodetectors”. *Journal of Physics D: Applied Physics* 44.7 (2011), p. 075102.

[174] O. Klin et al. “Progress with antimonide-based detectors at SCD”. *Proceedings of SPIE - The International Society for Optical Engineering* 7298 (2009).

[175] S.M. Sze. *Physics of Semiconductor Devices*. 2nd ed. Wiley-Interscience, 1981.

[176] *MODEL SR830 DSP Lock-In Amplifier*. Stanford Research Systems. 2011.

[177] D. Lackner et al. “Electrical and optical characterization of n-InAsSb/n-GaSb heterojunctions”. *Journal of Applied Physics* 107.1 (2010), p. 014512.